

# **Mesostrukturierte Metalloxide und Polyoxometallate mittels Ionogener Diblockcopolymere - Synthese, Charakterisierung und Anwendung**

## **Dissertation**

zur Erlangung des akademischen Grades eines  
**Doktors der Naturwissenschaft (Dr. rer. nat.)**

im Fach Chemie

an der Bayreuther Graduiertenschule für  
Mathematik und Naturwissenschaften

vorgelegt von

**Thomas Franz Lunkenbein**

geboren in Lichtenfels

Bayreuth, 2012



Die vorliegende Arbeit wurde in der Zeit von April 2009 bis Juni 2012 am Lehrstuhl für Anorganische Chemie I unter der Betreuung von Herrn Prof. Dr. Josef Breu angefertigt. Vollständiger Abdruck der von der Bayreuther Graduiertenschule für Mathematik und Naturwissenschaften der Universität Bayreuth genehmigten Dissertation zur Erlangung des akademischen Grades eines Doktors der Naturwissenschaften (Dr. rer. Nat.).

Dissertation eingereicht: 06.06.2012

Zulassung durch die Promotionskommission: 14.06.2012

Wissenschaftliches Kolloquium: 01.10.2012

Amtierender Dekan: Prof. Dr. Beate Lohnert

Prüfungsausschuss:

Prof. Dr. Josef Breu (Erstgutachter)

Prof. Dr. Axel H. E. Müller (Zweitgutachter)

Prof. Dr. Hans Keppler (Vorsitz)

Prof. Dr. Stephan Förster



Meinen Eltern und Geschwistern

## 愚公移山

*Der Mensch, der Berge versetzte, war derselbe,*

*der anfing, kleine Steine wegzutragen.*

-chinesisches Sprichwort-



# Inhaltsverzeichnis

<b>Glossar.....</b>	<b>ix</b>
<b>1. Summary.....</b>	<b>1</b>
<b>2. Zusammenfassung .....</b>	<b>5</b>
<b>3. Prolog.....</b>	<b>9</b>
<b>4. Einführung.....</b>	<b>11</b>
4.1    Nanomaterialien und Nanotechnologie .....	11
4.2    Mesostruktur, Mesophasen und Mesotechnologie .....	13
4.3    Templatgesteuerte Synthesen .....	16
4.4    Organische Template und strukturdirigierende Agentien .....	18
4.5    Anorganisch-Organische Hybridmaterialien.....	22
4.6    Polyoxometallate.....	25
<b>5. Problemstellung .....</b>	<b>31</b>
<b>6. Synopsis .....</b>	<b>33</b>
6.1    Kristalline TiO <sub>2</sub> Nanostrukturen mit hohem Aspektverhältnis.....	34
6.2    Packungsverhalten von zylindrischen Keggin POM Hybridmaterialien als Funktion des Aspektverhältnisses .....	38
6.3    Säurekatalysierte Zersetzung von Isopropanol durch unterschiedliche zylindrische Keggin POM-Hybridmaterialien .....	43
6.4    Direkte Herstellung von invers hexagonal geordneten Diblockcopolymer/ Keggin POM Nanokompositfilmen .....	48
6.5    Auf den Weg zu mesoporösem Keggin-Type Polyoxometallat – Eine Calcinierungsstudie - .....	53
6.6    Direkter Zugang zu porösen Molybdänoxycarbiden/ Kohlenstoff Nanokompositen.....	57

<b>7. Ergebnisse .....</b>	<b>63</b>
7.1    Darstellung des Eigenanteils .....	63
7.2    A Facile Polymer Templatting Route Toward High Aspect Ratio Crystalline Titania Nanostructures .....	69
7.3    High Surface Area Keggin-Type Polyoxometalate Nanorods and their Catalytic Performance in the Isopropanol Decomposition .....	109
7.5    Direct Synthesis of Inverse Hexagonally Ordered Diblock Copolymer/ Polyoxometalate Nanocomposite Films .....	131
7.6    Towards Mesoporous Keggin-Type Polyoxometalate –Systematic Removal of Organic Templates .....	171
7.7    Direct Access to Ordered Porous Molybdenum Oxycarbide/ Carbon Nanocomposites .....	197
<b>8. Referenz .....</b>	<b>223</b>
<b>9. Publikationsliste .....</b>	<b>229</b>
9.1    Publikationen .....	229
9.2    Posterbeiträge .....	234
<b>10. Danksagung .....</b>	<b>235</b>
<b>11. Erklärung des Verfassers .....</b>	<b>237</b>

# Glossar

°C	Grad Celsius
3D	3-dimensional
Å	Angström ( $1 \text{ Å} = 10^{-10} \text{ m}$ )
Abb.	Abbildung
$\text{Al}_2\text{O}_3$	Aluminiumoxid
bcc	body centered cubic (kubisch innenzentriert)
bzw.	beziehungsweise
CASH	combined assembly of soft and hard
CO	Kohlenstoffmonoxid
ca.	zirka
$\text{cm}^3$	Kubikzentimeter
cryo	cryogen
f	Volumenanteil in %
fcc	face centered cubic (kubisch flächenzentriert)
Fe	Eisen
FTIR	Fourier transformiert Infrarot
g	Gramm
griech,	griechisch
h	Stunde
H	magnetische Feldstärke
$\text{H}_2$	Wasserstoff
He	Helium
HCl	Salzsäure

HR	high resolution (Hochauflösung)
$\text{m}^2$	Quadratmeter
$\mu\text{m}$	Mikrometer ( $1 \mu\text{m} = 10^{-6} \text{ m}$ )
$\mu\text{mol}$	Mikromol
M41S	nanostrukturierte Mesoporöse Silicaphasen
min	Minute
$\text{MoO}_3$	Molybdäntrioxid
MS	Massenspektrometer
$\text{N}_2$	Stickstoff
nm	Nanometer ( $1 \text{ nm} = 10^{-9} \text{ m}$ )
NLDFT	nonlocal density functional theory
$\text{pp}_0^{-1}$	relativer Druck
PXRD	powder X-ray diffraction (Röntgenpulverdiffraktometrie)
REM	Rasterelektronenmikroskopie
$\text{RuO}_4$	Ruthenium-(VIII)-oxid
SAED	selected area electron diffraction
SAXS	small angle X-ray scattering (Kleinwinkelstreuung)
t	Zeit
TEM	Transmissionselektronenmikroskopie
THF	Tetrahydrofuran
TGA	thermogravimetrische Analyse
$\text{TiO}_2$	Titandioxid
UV	ultraviolett
u.v.m	und viele mehr
wt%	Gewichtsprozent

# 1. Summary

This thesis focuses on the synthesis, characterization, and application of mesostructured metal oxides and polyoxometalates templated by ionogene diblock copolymers. In particular three previously reported problems hampering the formation of mesostructured metal oxides were addressed.

Fast hydrolysis and condensation of reactive metal alkoxide-precursors foster the formation of large and unstructurable oxidic precursors. Furthermore, a simple and direct access to the desired morphology is often inhibited by the dynamic nature of the micelles formed by the template which is influenced by changes in pH, concentration, or ionic strength. Finally, the weak connection between the inorganic precursor and the organic template is attributed to weak attractive interactions between both materials and therefore limits the design of a periodic mesostructure. In general, hydrolysis, condensation, and hybrid formation have to proceed on the same time frame to reliably avoid macrophase separation.

To overcome this macrophase separation the department of AC I has recently developed a concept that addresses and solves all three problems. In the following these approaches are explained in the order mentioned above. Inorganic oligomeric clusters or pre-synthesized colloids replaced fast hydrolyzing and condensing metal alkoxides as inorganic precursors. Those clusters do not tend to condense since they occupy energetic minima on the condensation pathway toward extended oxidic structures. In addition, 1-dimensional core-crosslinked polymer brushes were employed for overcoming the dynamic nature of the micelles. Those rigid cylindrical polymer brushes were invariant against outer influences. Furthermore, those 1-dimensional nanoobjects exhibited ionizable coronas which were sufficiently basic to be easily protonated. Therefore, the strong Coulomb interactions formed guarantee a strong connection of the inorganic oxides to the organic templates.

Within this thesis the concept of charge-induced mesostructuring using molecular oxidic precursor was extended as presented hereafter.

Foremost, pre-synthesized rutile and anatase colloids were incorporated into 1-dimensional polymer structures. The crystal structure of rutile and anatase could be

## Summary

---

directed by the use of different acids (HCl: rutile; acetic acid: anatase) in the hydrolysis reaction of the titanium alkoxide precursor. Those TiO<sub>2</sub> polymorphs possessed positive zeta-potential at low pH-values. Hence, the template required negative charges at a pH around one. Therefore, in cooperation with the department MC II poly(styrenesulfonic acid-*block*-allylmethacrylate) (PSS-b-PAMA) were synthesized as cylindrical anionic antagonists. The PSS-corona is negatively charged even at low pH-values. The resulting 1-dimensional hybrid materials exhibited the same crystal structure as the precursor, a homogenous distribution of the nanoparticles in the polymer matrix, and a non-woven spaghetti-like microstructure with relatively high specific surface area after drying.

In a more detailed study the packing of the resulting 1-dimensional hybrid materials and their corresponding specific surface areas were investigated as a function of the length of the cylinders. In this study, cylindrical hybrid materials were used that consisted of heteropoly acid of the Keggin-Type polyoxometalate (Keggin POM) incorporated into 1-dimensional poly(butadiene-*block*-2-vinylpyridine) (PB-b-P2VP) polymer brushes. The aspect ratio of the 1-dimensional hybrid structures was found to vary only marginally with short sonication times. Furthermore, this short sonication resulted in a perfect dispersion of the anisotropic hybrid materials, and minimized the interparticular contact points within the microstructure. As a result, those pre-treated hybrid materials exhibited a maximum accessible surface area. An extension of the described synthesis protocol could be successfully applied toward Keggin POMs with varying charges, heteroatoms or metal cations. Catalysis tests of the hybrid cylinders revealed differences in the activity of the nanorods in the acidic catalyzed decomposition of isopropanol.

To enlarge the idea of charged-induced mesostructuring a new synthesis concept was developed yielding inverse hexagonally ordered polymer/Keggin POM mesophases. In this context poly(buadien-*block*-2-dimethylaminoethyl methacrylate) (PB-b-PDMAEMA) with a high degree of polymerization of the PB block was synthesized as organic template. Furthermore, the choice of solvent and the Keggin POM content were key factors within this process. To render this material interesting for diverse applications such as catalysis, the polymeric template has to be removed completely. Therefore, a systematical study was conducted. This study was conducted with thermal as well as aggressive methods. Amongst others the systematic head treatment studies showed that the mesostructure had been collapsed before the carbon was removed

completely. Aggressive methods, such as plasma etching, allowed successful access to the mesopores of microtome cut (< 50 nm) nanocomposite films. Addressing the heat treatment of the as-synthesized ordered polymer/ Keggin POM the oxidic walls were carburized resulting in ordered carbide/ carbon nanocomposites. Ordered carbide/ carbon nanocomposites can be considered interesting for catalysis or charge storage. For this purpose the polymeric template was not removed, but instead used as carbon source within the carburization reaction. Hence, the as-synthesized ordered mesophases gained direct and simple access to porous carbide/ carbon nanocomposites and showed catalytic activity in the decomposition of ammonia.

This work is a cumulative thesis. The detailed results are described in the attached publications.



## 2. Zusammenfassung

Das Ziel der vorliegenden Arbeit war es, Metalloxide und Polyoxometallate auf der Mesoebene mittels ionogener Diblockcopolymere zu strukturieren, zu charakterisieren und anwendungsspezifisch zu testen. Dabei wurden vor allem drei bisher bekannte Probleme, die mit der Mesostrukturierung von Metalloxiden einhergehen, umgangen.

Zum einen führt die schnelle Hydrolyse und Kondensation reaktiver Metallalkoxid-Precursoren zu unstrukturierbar großen Molekülen. Zum anderen ist oftmals ein direkter Zugang zu der gewünschten Morphologie aufgrund der mizellaren Dynamik des Templates, die von äußeren Einflüssen, wie pH-Wert, Konzentration oder Salzkonzentration abhängt, erschwert. Das dritte Problem ist die schlechte Anbindung des anorganischen Precursors an das organische Templat, was auf schwache, attraktive Wechselwirkungen zwischen beiden Materialien zurückzuführen ist. Generell müssen Hydrolyse, Kondensation und Hybridbildung zwingend synchron ablaufen, um eine Makrophasenseparation zuverlässig zu vermeiden.

Um diese Makrophasenseparation zu vermeiden, wurde am Lehrstuhl AC I ein neuartiges Konzept entwickelt, in dem alle drei Probleme adressiert und gelöst werden konnten. Diese Lösungsansätze werden nachfolgend entsprechend ihrer oben aufgeführten Reihenfolge erklärt. Zunächst wurden anionische oligomere Cluster oder pre-synthetisierte Kolloide als anorganische Precursoren verwendet, anstelle schnell hydrolysierer und kondensierender Metallalkoxide. Die Cluster besetzen energetische Minima auf dem Weg zu ausgedehnten Oxidstrukturen und neigen somit nicht zur Kondensation. Weiterhin konnte mit 1-dimensionalen kernquervernetzten Polymerbürsten die mizellare Dynamik umgangen werden, da die rigiden zylindrischen Polymerbürsten invariant gegenüber äußeren Einflüssen sind. Außerdem besitzen diese 1-dimensionalen Nanoobjekte ionisierbare Seitenarme, welche einfach protoniert werden können und somit über starke Coulomb-Wechselwirkungen eine stabile Anbindung der anorganischen Oxide an das organische Templat gewährleisten.

Dieses Konzept der ladungsinduzierten Mesostrukturierung mittels molekularer oxidischer Precursoren wurde innerhalb dieser Doktorarbeit weitergeführt, deren Ergebnisse nachfolgend kurz dargestellt werden.

Zuerst wurde am Beispiel von pre-synthetisierten Rutil- und Anatas-Kolloiden gezeigt, dass nicht nur anionische oligomere Cluster, sondern auch Kolloide in 1-dimensionale Poylmerstrukturen eingelagert werden können. Die Kristallstruktur von Rutil und Anatas konnte durch Verwendung unterschiedlicher Säuren (HCl: Rutil; Essigsäure: Anatas) bei der Hydrolyse des Titanalkoxid-Precursors gezielt eingestellt werden. Diese TiO<sub>2</sub>-Polymorphe besitzen bei niedrigen pH-Werten eine positive Oberflächenladung. Polystyrolsulfonsäure-*block*-polyallylmethacrylat (PSS-b-PAMA) wurde in Zusammenarbeit mit dem Lehrstuhl MCII als zylindrischer anionischer Antagonist synthetisiert. Die PSS-Seitenarme sind selbst bei niedrigen pH-Werten noch negativ geladen. Die resultierenden 1-dimensionalen Hybridmaterialien besaßen dieselbe Kristallstruktur wie der Precursor, eine homogene Verteilung der Nanopartikel in der Polymermatrix und nach Trocknung eine verschlungene, spaghetti-ähnliche Mikrostruktur mit relativ hoher spezifischer Oberfläche.

In einer detaillierteren Studie wurde zusätzlich der Einfluss der Länge der zylindrischen Template auf die Packung der 1-dimensionalen Nanoobjekte und auf die daraus resultierende spezifische Oberfläche untersucht. Dabei wurden zylindrische Hybridmaterialien aus Heteropolysäuren des Keggin-Typ Polyoxometallates (Keggin POM), die in 1-dimensionale Polybutadien-*block*-poly(2-vinylpyridin) (PB-b-P2VP) Polymerbürsten eingelagert wurden, verwendet. Hierbei zeigte sich insbesondere, dass eine kurze Ultraschallbehandlungsdauer das Aspektverhältnis der 1-dimensionalen Strukturen nur gering verändert, die Dispersion der anisotropen Hybridmaterialien perfektioniert und die interpartikulären Kontaktpunkte innerhalb der Mikrostruktur minimiert. Als Ergebnis wurde hierfür die maximal zugängliche spezifische Oberfläche erhalten. Eine Ausweitung dieses Syntheseprotokolls auf Keggin POMs mit unterschiedlicher Ladung, Heteroatomen und Metallkationen konnte auch erfolgreich durchgeführt werden. Katalysetests dieser Hybridzylinder offenbarten dabei Unterschiede in der Aktivität dieser Nanostäbchen in der sauer katalysierten Zersetzung von Isopropanol.

Angliedernd an die ladungsinduzierten Mesostrukturierung wurde ein neues Synthesekonzept zu invers hexagonal geordneten Polymer/ Keggin POM Mesostrukturen erarbeitet. Als organisches Templat wurde Polybutadien-*block*-poly(2-dimethylaminoethylmethacrylat) (PB-b-PDMAEMA) mit einem hohen Polymerisationsgrad des PB-Blockes synthetisiert. Als weitere Schlüsselfaktoren erwiesen sich neben

diesem hohen Polymerisationsgrad des PB-Blockes die Wahl des Lösungsmittel und der Keggin POM-Anteil. Um dieses Material auch für Anwendungen wie der Katalyse ansprechend zu machen, muss das polymere Templat am besten vollständig entfernt werden, um eine möglichst hohe Zugänglichkeit der aktiven Zentren zu gewährleisten. Dies wurde sowohl thermisch als auch mit aggressiveren Methoden versucht. Zum einen wurde durch systematische Studien zur thermischen Entfernung des Templates gezeigt, dass die Mesostruktur kollabiert bevor der Kohlenstoff komplett entfernt werden kann. Zum anderen wurde durch aggressivere Methoden, wie Plasmaätzen, erfolgreich der Zugang zu den Mesoporen an Ultradünnschnitten (<50 nm) realisiert. An die thermische Behandlung reihte sich auch die Umwandlung der geordneten Mesphasen in geordnete Carbid/ Kohlenstoff-Nanokomposite an. Letztere sind für Katalyse oder Ladungsspeicherung auch wissenschaftlich interessant. Für die Umwandlung der geordneten oxidischen Mesphasen in Carbid/ Kohlenstoff Nanokomposite wurde nicht versucht das polymere Templat in den Poren zu entfernen, sondern es wurde zum ersten Mal als Kohlenstoffquelle in der Carbidisierungsreaktion verwendet. Folglich lieferten die hergestellten geordneten Mesphasen einen direkten und einfachen Zugang zu porösen Carbid/ Kohlenstoff Nanokompositen und zeigten katalytische Aktivität in der Zersetzung von Ammoniak.

Diese Arbeit ist eine kumulative Dissertation. Die detaillierten Ergebnisse werden in den angehängten Publikationen beschrieben.



### 3. Prolog

Humanologen befassen sich mit dem Verständnis der menschlichen Natur und Psyche. Psychologen untersuchen das Verhalten und den Geisteszustand einer einzelnen Person. Soziologen analysieren das Verhalten einer großen gesellschaftlichen Gruppe. Wer aber untersucht das Verhalten von drei Personen?

Dieses Beispiel kann man analog auch auf chemische und physikalische Abläufe in der Makro- und Nanowelt übertragen. Die makroskopische Welt wird durch die klassische Newton'sche Mechanik dominiert, wohingegen das Verhalten einzelner Atome auf quantenmechanischen Prozessen und Abläufen beruht. Das Bindeglied zwischen beiden Technologien, nämlich das Zusammenwirken von Atomen, wird als Mesotechnologie (griech.: mesos = Mitte, dazwischen) bezeichnet.

In einer Zeit, in der das Weltbild geprägt ist von miniaturisierten und dennoch immer leistungsfähigeren Geräten, ist die Mesotechnologie nicht mehr wegzudenken. So postulierte bereits 1965 *Gordon Moore*, Mitbegründer der Computerchip Firma Intel und Urheber des Mooreschen Gesetzes, dass sich die Prozessordichte alle zwei Jahre verdoppeln werde.<sup>[1]</sup> Allerdings war die Entwicklung elektronischer Geräte und Speichermedien nicht der einzige Schauplatz, der im Laufe der Jahre im Zuge fortschreitender Miniaturisierung an Komplexität gewann. Auch die Nachfrage nach immer leistungsfähigeren und robusteren Katalysatoren führte zur Erforschung neuartiger Systeme auf der Nano- bzw. Mesoebene.

In Afrika meint man, viele kleine Leute an vielen kleinen Orten, die viele kleine Dinge tun, können das Gesicht der Welt verändern. In ähnlicher Weise können nur durch das Zusammenwirken einzelner partikulärer Nanosysteme, zum Beispiel durch Selbstanordnung, die heutigen komplexen Aufgabenstellungen bewerkstelligt werden.

Mit Hilfe der Mesotechnologie werden aus diesen nanoskopischen Einzelbausteinen durch kontrollierte Anordnung mesoskopische Objekte aufgebaut und somit für die oben genannten Anwendungsbeispiele maßgeschneidert.



## 4. Einführung

### 4.1 Nanomaterialien und Nanotechnologie

„There is plenty of room at the bottom“, mit diesem berühmtem Ausspruch erkannte *Richard Philips Feynman* bereits 1959 die Bedeutung der Nanotechnologie.<sup>[2]</sup> Dieser „Platz am Boden“ der Materialchemie hat in den folgenden 50 Jahren nicht nur die Art der Forschung verändert, sondern auch zu einer rapiden Entwicklung hochentwickelter, elektronischer und optischer Geräte sowie neuartiger Medikamente geführt, die das gesellschaftliche Leben deutlich vereinfachen.<sup>[3-6]</sup> Grund genug, um in diesem Abschnitt auf die Besonderheiten der Nanotechnologie einzugehen.

Was versteht man unter dem Begriff „nano“? Ordnet man zum Beispiel zehn Wasserstoff- oder fünf Siliziumatome nacheinander auf einer geraden Linie an, so beträgt deren Ausdehnung ungefähr ein Nanometer.<sup>[3]</sup> Als physikalische Größe ist ein Nanometer ein Billionstel Meter. Das Präfix „nano“ wurde vom griechischen Wort „nannos“ adaptiert, was so viel wie Zwerg bedeutet. So sind Nanomaterialien kleinste Festkörper, deren Größenordnung in mindestens einer Dimension unter 100 nm liegen.<sup>[7,8]</sup> Generell behandelt die Nanotechnologie die struktur- und größenkontrollierte Synthese, die Charakterisierung und die Eigenschaft von Materialien auf der atomaren und molekularen Ebene.<sup>[2,9]</sup>

Gestaltselektive Synthesen von Nanomaterialien oder Nanostrukturen erlauben anwendungsspezifisch maßgeschneiderte Materialien zu realisieren, die sich über mehrere Dimensionen erstrecken können.<sup>[7]</sup> Dabei ermöglichen verschiedenste Syntheseprotokolle die Herstellung von einfachen Nanopartikeln,<sup>[10]</sup> Nanokapseln,<sup>[11]</sup> Nanodrähten,<sup>[12]</sup> Nanoröhren,<sup>[13]</sup> 2-dimensionalen Anordnungen von Nanopartikeln<sup>[14]</sup> oder 3-dimensionalen Supergittern.<sup>[15]</sup>

Die physikalischen und chemischen Eigenschaften solcher Nanomaterialien können sich signifikant vom korrespondierenden Bulk-Materials unterscheiden.<sup>[7,16]</sup> Aufgrund ihrer sehr geringen Größe liegen Nanomaterialien im Bereich der kritischen Größe für makroskopisch physikalische Phänomene. Unterschreiten solche Materialien diese Größe, treten zum Beispiel neue Merkmale in der elektronischen Struktur auf, die auf diesen Größeneffekt oder „Quantum Dot“-Effekt zurückzuführen sind. Insbesondere

bewirken die nanoskopischen Strukturen eine Erhöhung des Oberflächen-/Volumenverhältnis, wodurch mehr Atome an der Oberfläche oder in oberflächennahen Positionen sitzen. So können makroskopisch metallisch leitende Substanzen im Größenbereich zwischen 1 und 2 nm zu Isolatoren werden oder plötzlich katalytische Eigenschaften zeigen.<sup>[17,18]</sup> Weiterhin besitzen solche Nanomaterialien großenabhängige, plasmonische und magnetische Eigenschaften (Abb. 1).<sup>[19]</sup> Letztere können zum Beispiel, wenn sie geeignet modifiziert sind, in der Krebstherapie eingesetzt werden, um an das karzinogene Gewebe „anzudocken“ und somit zu einer gezielten Therapie führen.

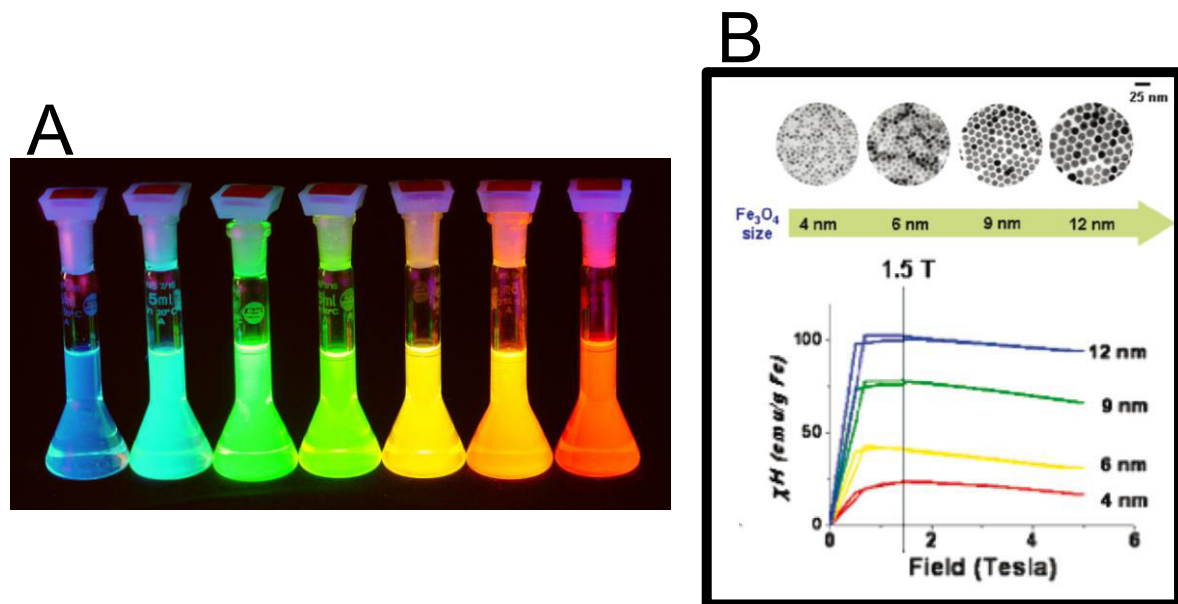


Abb. 1: Darstellung des Größeneffektes: A) Fluoreszenz von CdSe-CdS Kern-Schale Nanopartikel mit unterschiedlichen Durchmessern im Bereich von 1,7 nm (blau) bis 6 nm (rot).<sup>[20]</sup> B) Fe<sub>3</sub>O<sub>4</sub>-Nanopartikel unterschiedlicher Größe (oben) und die dazugehörige großenabhängige Magnetisierung (unten).<sup>[19]</sup>

## 4.2 Mesostruktur, Mesophasen und Mesotechnologie

Die Frage nach dem Unterschied zwischen der Nano- und Mesowelt kann nur durch eine genauere Betrachtung beantwortet werden. Antwortversuche waren schon in der Antike verankert. Bereits *Aristoteles* definierte die Physik als das Phänomen, in der die Annahme einer bestimmten Gestalt für jegliche Art von Materie die treibende Kraft darstellte.<sup>[21]</sup> Heutzutage sind Begriffe wie „Nano“ oder „Meso“ längst nicht mehr nur Fachbegriffe, die ausschließlich in chemischen Fachzeitschriften auftauchen, sondern sind auch längst Teil des öffentlichen Lebens.<sup>[22]</sup>

„Meso“ hat viele Bedeutungen, die sich zum einen auf eine Längenskala, zum anderen aber auch auf ein Prinzip beziehen lassen. Die „International Union of Pure and Applied Chemistry“ teilte poröse Materialien in drei großenabhängige Systeme ein. Mikroporöse Substanzen besitzen Poren mit einem Durchmesser kleiner als 2 nm. Mesoporöse Materialien weisen Poren zwischen 2 und 50 nm auf. Von Stoffen mit Makroporen spricht man, wenn die Porengröße 50 nm überschreitet.<sup>[23]</sup> Diese Einteilung der Porengrößen wurden durch Konvention willkürlich gesetzt. In der Chemie organischer Moleküle und mesostrukturierter Hybride sind Mesphasen allgegenwärtig. Der Begriff „Meso“ dehnt sich hier aber über einen größeren Bereich von bis zu 500 nm aus.<sup>[21]</sup> Die Mesoskala ist also zwischen der Mikro- und der Makroskala angeordnet und stellt folglich eine bestimmte Größenordnung dar.

Ein anderes Verständnis von „Meso“ setzt diesen Begriff nicht mit einer bestimmten Längenskala gleich, sondern sieht darin eher eine Art Arbeitsprinzip: „Meso“ ist somit irgendwo zwischen molekularer und Festkörperchemie, zwischen einer diskreten molekularen und kontinuierlichen Ordnung oder zwischen einer Bindungsknüpfung und einem Strukturaufbau basierend auf physikalischen Wechselwirkungen anzusiedeln.<sup>[21,24]</sup> Generell ist eine Mesophase definiert durch die Selbstanordnung von Nanomaterialien in größere geordnete Strukturen. Das gezielte Beeinflussen von nanoskopischen Bausteinen einhergehend mit einer Strukturkontrolle auf der Mesoskala entwickelte sich zu einer vielversprechenden und ästhetischen Methode in der Materialchemie.<sup>[6,25]</sup>

Der gezielte Aufbau von Mesostrukturen mit maßgeschneiderten Eigenschaften ist daher größtenteils nicht auf die Ausbildung kovalenter Bindungen im Zuge chemischer Reaktionen zurückzuführen, sondern auf die kontrollierte Selbstanordnung von Nanopartikeln auf der Mesoebene. Die Mesotechnologie schlägt dabei eine Brücke zwischen der Molekül- und der Materialchemie. Mesotechnologie kann auch als die Kunst verstanden werden, die Bindungen, Wechselwirkungen und Molekulanordnungen kontrolliert und reproduzierbar manipuliert.<sup>[21]</sup>

Es bleibt noch zu klären, was unter dem Begriff „kontrolliert“ in diesem Zusammenhang genau zu verstehen ist. Zum einen wollen Chemiker insbesondere die Größe, Gestalt und Oberfläche von funktionellen Materialien anwendungsspezifisch und vorherbestimmt einstellen. Vor allem soll hierbei die Morphologie und Ordnung zweier unterschiedlicher Komponenten auf der Mesoskala über kooperative Selbstanordnung vorhersagbar sein (siehe Synthese von 3D optischen Metamaterialien<sup>[26]</sup>). Somit ergäbe sich eine große Bandbreite an chemischen und physikalischen Synthesestrategien, die eine kontinuierliche und gezielte Einstellung von ungeordneten bis hinzu geordneten Mesostrukturen erlaubten.<sup>[21]</sup>

Hybridmaterialien, in denen organische und anorganische Komponenten durch Selbstanordnungsprozesse kontrolliert ineinander integriert wurden, zeigen eine signifikante Verbesserung der Eigenschaften bezogen auf die der einzelnen Komponenten.<sup>[24]</sup> Zum Beispiel entdeckte man vor etwa 1200 Jahren zufällig, dass die Kombination aus Indigo und Palygorskit, einem natürlichen Schichtsilicat, ein Hybridmaterial ergab, dass die alten Maya-Stämme aufgrund seiner Farbstabilität für ihre Fresken benutzten (Abb. 2). Dieser Farbstoff wird als „Maya Blue“ bezeichnet.<sup>[27]</sup>

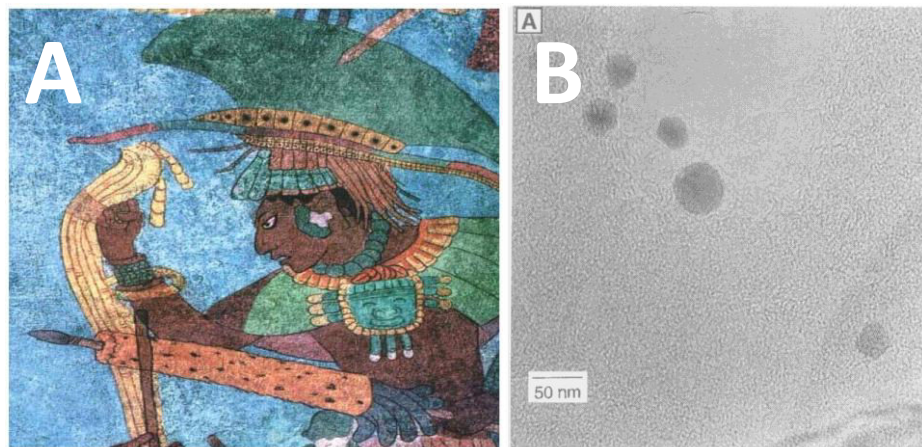


Abb. 2: A) Bildnis eines Maya Kriegers. Die Abbildung wurde computerbearbeitet. B) TEM-Aufnahme eines synthetischen „Maya Blue“-Hybridmaterial. Die schwarzen Punkte sind Nanokristalle innerhalb des Indigo/Palygorskит-Matrix.<sup>[27,28]</sup>

## 4.3 Templatgesteuerte Synthesen

Die kontrollierte Darstellung und Anordnung von Objekten auf der Nano- bzw. Mesoebene kann durch „top-down“ und/oder „bottom-up“ Prozesse erreicht werden.<sup>[29-31]</sup> In einem „top-down“-Prozess werden aus makroskopischen Materialien durch mechanische Zerkleinerungsprozesse, wie Mahlen, Ätzen oder Abrieb, Nanostrukturen erzeugt.<sup>[3]</sup> Die so hergestellten Materialien sind vergleichsweise teuer und aufwendig in ihrer Herstellung. Daneben bietet der „bottom-up“-Ansatz einen günstigen und einfachen Prozess, um hochgeordnete Strukturen durch Selbstanordnung von nanoskopischen Bausteinen aufzubauen.<sup>[30]</sup> Die Anordnung von nanopartikulären Bausteinen in geordnete Mesostrukturen durch diesen „bottom-up“-Prozess kann zu neuen Materialien mit attraktiven Eigenschaften führen.<sup>[32-34]</sup>

Insbesondere Materialien mit hoher Porosität und hoher zugänglicher Oberfläche sind von sehr großem industriellem aber auch akademischem Interesse. Solch geordneten und/oder porösen Materialien können durch eine templatgesteuerte Synthese erhalten werden.<sup>[25,35,36]</sup> Eine Templatierung erlaubt letztendlich eine hohe Strukturkontrolle und dadurch die Synthese von Materialien mit maßgeschneiderten Eigenschaften.<sup>[37]</sup> Hierbei unterscheidet man zwischen Exo- und Endotemplat.<sup>[35]</sup>

Exotemplate sind poröse Festkörper, die als Templat für einen anderen Festkörper dienen. Nach der Entfernung des Festkörpergerüsts werden feinverteilte Nanodrähte oder poröse Materialien erhalten. Die Art des resultierenden Materials ist abhängig von den 3-dimensionalen Verbindungen innerhalb des Exotemplates.<sup>[35]</sup> Eine exakte Nachbildung dieser Gerüstfestkörper wird als Nanocasting bezeichnet.<sup>[38]</sup> Die Entfernung solcher Exotemplate ist vergleichsweise aufwändig, weil das Templat meist aus mesoporösem Silica besteht, welches temperaturresistent ist und nur durch aggressive und toxische Flusssäure weggeätzt werden kann.

Bei der Herstellung von porösen Materialien hat sich vor allem die templatgesteuerte „bottom-up“-Synthese (Endotemplatierung) mit organischen Molekülen bewährt.<sup>[39]</sup> Endotemplate sind organische Template, wie Tenside oder Blockcopolymere, die zur Reaktionsmischung gegeben werden. Diese Template bilden Strukturen aus, wechselwirken mit den anorganischen Precursor und hinterlassen, nach ihrer meist thermischen Entfernung, einen porösen Feststoff.<sup>[35]</sup>

Durch eine scheinbar uneingeschränkte Anzahl von Templayen konnten in den letzten Jahren eine noch nie dagewesene Vielfalt an Morphologien über mehrere Größenordnungen beginnend im Nanometerbereich bis in den Mikrometermaßstab dargestellt werden.<sup>[34,40-42]</sup> Für viele Anwendungen ist eine geordnete Struktur nicht zwingend erforderlich, solange eine hohe Oberfläche zugänglich ist.<sup>[43]</sup> Vielmehr dienen geordnete Mesoporen hauptsächlich zum Stofftransport in katalytischen Prozessen oder für Superkapazitäten. Solche geordnet poröse Materialien besitzen zudem einen gravierenden Nachteil gegenüber ungeordneten Systemen, da sie eine verhältnismäßig geringere Oberfläche besitzen.<sup>[21,44,45]</sup>

## 4.4 Organische Template und strukturdirigierende Agentien

Für die Synthese von anorganisch-organischen Hybridmaterialien sind nicht alle organischen Moleküle geeignet. Fraglich ist folglich, was ein organisches Molekül für die Verwendung als Templat oder strukturdirigierendes Agens qualifiziert?

In der Regel werden für die Mesostrukturierung oberflächenaktive Substanzen wie Tenside oder amphiphile Diblockcopolymere verwendet.<sup>[39,46-48]</sup> Amphiphile Moleküle oder Tenside, die aus einer polaren Kopfgruppe und einer unpolaren Alkylkette bestehen, bilden in Lösungsmitteln, das für eine Domäne nicht selektiv ist, Mizellen aus. Diese mizellaren Morphologien sind ein energetischer Kompromiss aus den sterischen Ansprüchen langer Alkylketten und den abstoßenden Kräften geladener Kopfgruppen. Die Konzentration der Tenside im geeigneten Lösungsmittel muss für die Mizellbildung oberhalb der kritischen Mizellkonzentration (KMK) liegen.<sup>[39,49]</sup> Zusätzlich kann die mizellare Struktur durch Änderungen des Lösungsmittel, der Temperatur oder der Salzkonzentration beeinflusst werden.<sup>[47,50]</sup> In Lösung können Sphären, Zylinder, Lamellen u.v.m. realisiert werden (Abb. 3).

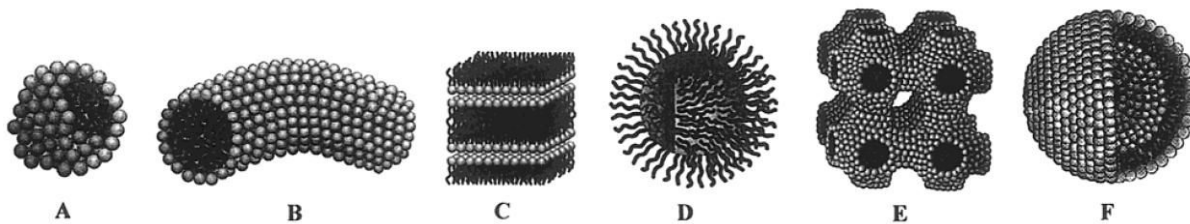


Abb. 3: Mizellare Strukturen (A = Sphären, B = Zylinder, C = Lamellen, D = inverse Mizelle, E = bikontinuierliche Netzwerke, F = Liposomen).<sup>[51]</sup>

Letztendlich ergibt die vorgegebene mizellare Struktur des Tensides und die Anbindung der anorganischen Nanopartikeln an die Kopfgruppe die finale Hybridstruktur. Der Nachteil bei der Verwendung von Tensiden als strukturdirigierendes Agens liegt in der limitierten Porengröße und Wandstärke der resultierenden Hybridmaterialien. Insbesondere dünne Wände gewährleisten wenig Strukturstabilität in katalytischen Prozessen.<sup>[48]</sup> Einen Ausweg aus diesen

geometrischen Restriktionen liefern amphiphile supramolekulare Template wie Blockcopolymere. Ähnlich wie Tenside können diese in Lösung Mizellen ausbilden.<sup>[52,53]</sup>

Ein amphiphiles Diblockcopolymer ist ein Polymer, das aus einem hydrophilen Block A und einem hydrophoben Block B besteht, die kovalent miteinander verbunden sind.<sup>[47,54,55]</sup> Im Bulk tritt aufgrund der Unmischbarkeit der beiden Polymerblöcke eine Mikrophasenseparation in A- und B- reiche Domänen auf, die durch eine beträchtliche innere Oberfläche voneinander getrennt sind.<sup>[56]</sup> Ein wichtiger Parameter hierbei ist der Florry-Huggins Wechselwirkungsparameter  $\chi$ . Dieser gibt direkt die Mischbarkeit ( $\chi < 0$ ) oder Unmischbarkeit ( $\chi > 0$ ) der beiden Blöcke A und B an. Im Bulk treten oberhalb des Inkompatibilitätsparameters  $N\chi > 10,5$  ( $N$ : Polymerisationsgrad) unterschiedliche Morphologien auf. Je nach Volumenanteil eines Blockes können kubisch dicht gepackte Sphären (bcc oder fcc), hexagonal geordnete Zylinder, Lamellen oder gyroidale Strukturen verwirklicht werden (Abb. 4).<sup>[47]</sup>

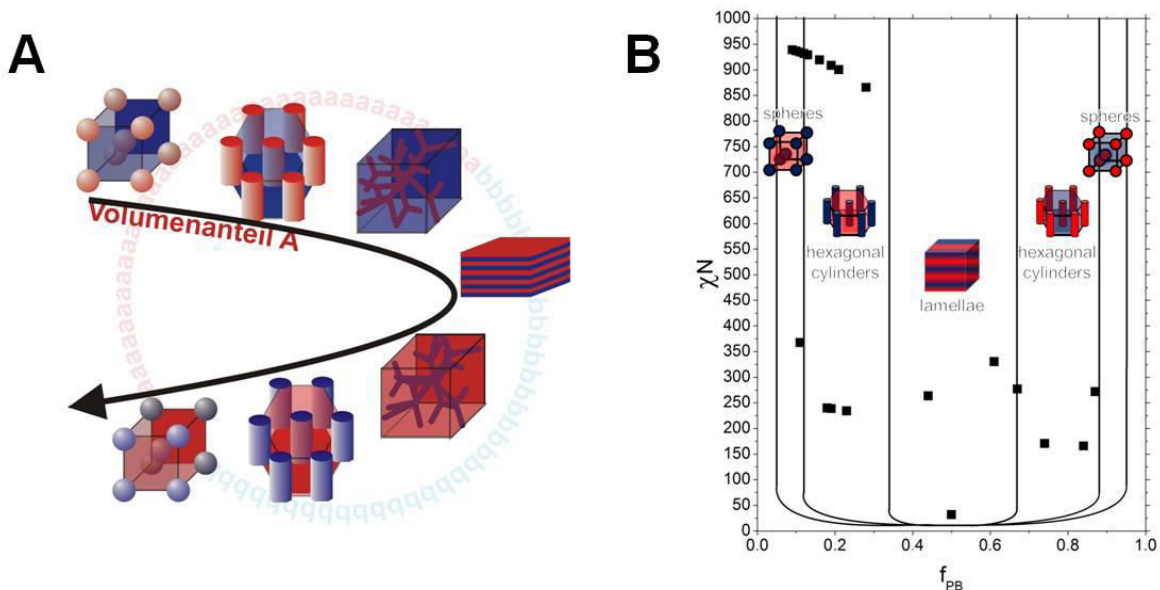


Abb. 4: A) Mögliche Morphologien eines Diblockcopolymers. B) Phasendiagramm von PB-b-P2VP.

Dieser einfache Zugang zu einer Vielzahl verschiedener Morphologien mit definierter Größe und Gestalt begründet das stetig wachsende Interesse an Diblockcopolymeren für die Verwendung als strukturdirigierende Agentien von anorganischen Nanopartikeln und Kolloiden.<sup>[40,41,57-59]</sup>

Während man sich zu Beginn der Mesostrukturierung auf geladene (kationische) supramolekulare Tensidphasen konzentriert hat, wie zum Beispiel bei den hexagonal geordneten, mesoporösen M41S-Phasen, fokussierte man sich bei den Blockcopolymer-Phasen auf ungeladene Systeme.<sup>[60,61]</sup> Letztere verschaffen zwar mehr Flexibilität hinsichtlich Porengröße und Wandstärke, aber die Kompositbildung muss auf relativ schwache Wasserstoffbrücken vertrauen.

Dagegen bietet die Verwendung von ionisierbarer, amphiphiler Diblockcopolymere, wie PSS-b-PAMA, PB-b-P2VP, oder PB-b-PDMAEMA (Abb. 5), einen entscheidenden Vorteil. Ersteres ist über den ganzen pH-Bereich negativ geladen, wohingegen die letzten beiden durch einfache Protonierung oder Quaternisierung der tertiären Aminogruppen positiv geladen werden kann. So zeigten Yelamanchili *et al.*, dass zum einen die als Precursoren verwendeten Heteropolysäuren in der Lage sind, diese Polymere zu protonieren. Zu anderen verhindern die resultierenden Coulomb-Wechselwirkungen zwischen den Polyoxometallat-Anionen und den kationischen Templayen zuverlässig eine Makrophasensegregation.<sup>[40]</sup>

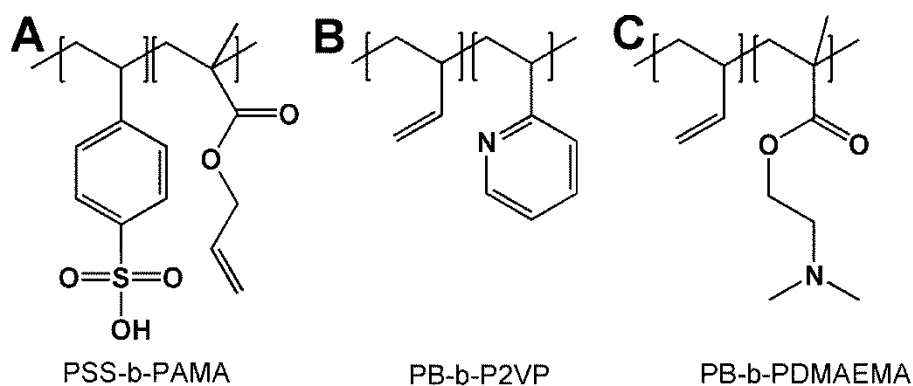


Abb. 5: Idealisierte Strukturen ionisierbarer Diblockcopolymere. (A) PSS-b-PAMA, (B) PB-b-P2VP und (C) PB-b-PDMAEMA.

Auch bei Diblockcopolymeren ist die Morphologie in Lösung abhängig von dem pH-Wert, der Konzentration, der Temperatur, dem Lösungsmittel oder der Ionenstärke. Diese Faktoren können getrieben durch die mizellare Dynamik zur Umwandlung oder zum Auflösen der Morphologien führen.<sup>[50]</sup> Demzufolge ist der Zugang zu anorganisch-organischen Hybridmaterialien mit gewünschter Morphologie erschwert.

## 4.5 Anorganisch-Organische Hybridmaterialien

Mit der Entwicklung der ersten geordneten mesoporösen Silica- Materialien (M41S-Phasen) in den Laboratorien der „Mobile Oil Cooperation“ wurde 1992 ein neuer Zweig in der Materialwissenschaft gegründet.<sup>[61]</sup> Nach der Ausweitung dieses Konzeptes auf Blockcopolymere konnte eine gewisse Flexibilität in der Einstellung des Porendurchmessers und der Wandstärke generiert werden.<sup>[60,61]</sup> Dies führte zu einem gesteigerten Forschungsinteresse an mesoporösen Materialien, insbesondere an mesoporösen Übergangsmetallociden. In diesem Abschnitt soll kurz auf den Stand der Forschung, die auftretenden Probleme und Perspektiven von mesostrukturierten Metallociden eingegangen werden.

Generell bilden sich diese geordneten Oxidphasen in den meisten Fällen mittels eines Flüssigkristall-Templat-Mechanismus um Mizellen und verschiedener lyotroper Phasen von Tensiden oder Diblockcopolymeren aus.<sup>[62]</sup> Selbst kleinste Änderungen in den Reaktionsbedingungen können als Folge der mizellaren Dynamik in ungewünschten Strukturen resultieren. Die sich daraus ergebende Einschränkung in den Variationsmöglichkeiten der Reaktionsparameter macht die Ausweitung des Synthesekonzepts auf mesoporöse Metallocide mühsam. Metallocide sind daher so interessant, weil sie variable Oxidationsstufen und die Fähigkeit besitzen ihre d-Orbitale mit Elektronen zu besetzen. Diese Eigenschaften machen diese Materialgruppe interessant für ein breites Anwendungsspektrum angefangen bei der Katalyse,<sup>[63,64]</sup> über Photo-/Elektrochromie<sup>[65-69]</sup> und Ferroik,<sup>[70]</sup> bis hin zur Sensorik<sup>[71,72]</sup>.

Es können aber nur vereinzelt mesoporöse Metallocide (Titan, Zirconium, Vanadium,<sup>[57]</sup> Mangan, Wolfram<sup>[73]</sup> oder Niob.<sup>[74]</sup>) über das Endotemplatverfahren oder indirekt über das Exotemplatverfahren hergestellt werden. Die Gründe hierfür finden sich in der vergleichsweisen schnellen Hydrolyse und Kondensation der verwendeten Metalalkoxid-Vorstufen oder einer schlechten attraktiven Wechselwirkung zwischen Templat und anorganischen Precursor. Hydrolyse, Kondensation, Kompositbildung und Selbstorganisation müssen aber zwingend auf einer Zeitskala ablaufen. Ist das nicht der Fall, sind die mesoporösen Metallocide oft schlecht geordnet und erweisen sich als thermisch labil.

Eine Ausweitung des Konzepts der templatgesteuerten Strukturierung auf weitere mesoporöse Übergangsmetallocide wurde zumindest für Filme nach der Erfindung des „Evaporation-Induced Self-Assembly“-Prozesses (EISA) erhalten.<sup>[75,76]</sup> Die kooperative Anordnung zwischen organischen Templat und anorganischen Precursor erfolgt durch sukzessives Verdampfen des Lösungsmittels. Dabei ist die Selbstanordnung konzentrationsgesteuert.

Weiterhin wäre für poröse Materialien, die einen optimalen Stofftransport gewährleisten müssen, ein ideales Poresystem am besten hierarchisch aufgebaut.<sup>[77]</sup> Mikroporen in den Wänden von Mesoporen sorgen für Gestaltselektivität der katalysierten Reaktionen. Zusätzlich bewirken die Mesoporen einen erhöhten Stofftransport zu den katalytisch aktiven Zentren (Abb. 6).

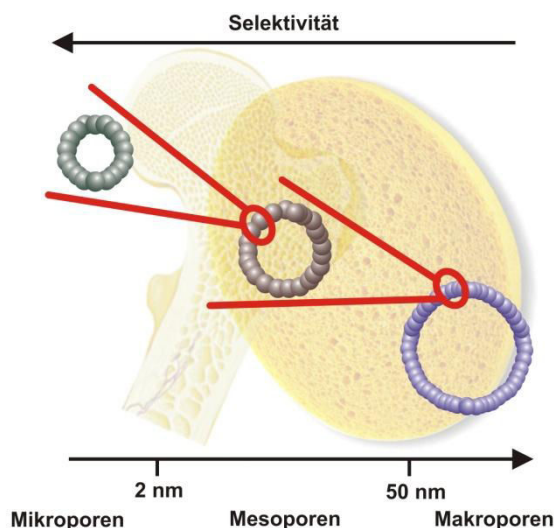


Abb. 6: Schematische Darstellung hierarchischer Porosität.

Neben der hierarchischen Porosität gewinnt auch der Aspekt der Kristallinität immer mehr an Bedeutung. Die Kristallinität der Porenwände erhöht nicht nur die thermische und mechanische Stabilität, sondern beeinflusst auch alle kooperativen Phänomene. Zusätzlich käme das Auftreten von speziellen elektronischen Strukturen und Gitterdefekten hinzu, die häufig für katalytische Anwendungen notwendig sind und in amorphen Materialien fehlen.<sup>[78]</sup> Zum Beispiel ist amorphes mesoporöses TiO<sub>2</sub> photokatalytisch weniger aktiv als kristalliner Anatas.<sup>[57]</sup> Templatgesteuerte Synthesen führen in der Regel zu amorphen Hybridmaterialien. Postsynthetische Kristallisierungsversuche laufen bei Temperaturen über 500 °C ab, wobei auf der einen

Seite das Templat zwar entfernt werden kann, auf der anderen Seite aber verschiedenste Redoxprozesse oder Phasenumwandlungen einen Kollaps der Mesostruktur verursachen.<sup>[66,78]</sup> Die thermisch induzierte Umwandlung der Kristallstruktur führt zwar zu dem Verlust der Porosität, allerdings ergäbe sich aus der Polymorphie auch ein breiteres Eigenschaftsspektrum. Um den Kollaps zu umgehen wurden Kontrolle bzw. Synthese der Kristallstruktur und die Mesostrukturierung in zwei separate Schritte unterteilt, wodurch Flexibilität gewonnen werden konnte (kolloidale Route). Das gezielte Einstellen der Kristallstruktur wurde anhand mesoporöser, metastabiler Al<sub>2</sub>O<sub>3</sub>- und TiO<sub>2</sub>-Polymorphe gezeigt.<sup>[79,80]</sup>.

Neben der Kristallinität ist für die meisten Anwendungen alleine die zugängliche Oberfläche entscheidend.<sup>[43]</sup> Deshalb sind auch 1-dimensionale Objekte mit hohem Aspektverhältnis, wie Nanoröhren und Nanostäbe generell als Template für die Mesostrukturierung von Übergangsmetalloxiden interessant.<sup>[40]</sup>

Zusammenfassend zeigt der oben aufgezeigte Weg zu anorganisch-organischen Hybridmaterialien die generelle Machbarkeit solcher Mesostrukturen. Daraus wird aber auch ersichtlich, dass die bisherigen Syntheseansätze noch mit Problemen behaftet sind. Ein Weg um die aufgezeigten Probleme hinsichtlich Kondensation und Hybridbildung zu umgehen, könnte in der Verwendung von Polyoxometallaten (POM) liegen. Diese oligomeren anorganischen Cluster befinden sich im energetischen Minimum auf den Weg zu kondensierten Oxidstrukturen. Dadurch wird eine schnelle Weiterkondensation, wie sie bei Metallalkoxiden beobachtet wird, wirkungsvoll umgangen.

## 4.6 Polyoxometallate

Metallkationen, Oxo-Anionen und polymere Oxidstrukturen sind in wässriger Lösung über eine Reihe pH-abhängiger Hydrolysereaktionen miteinander verknüpft (Abb. 7).

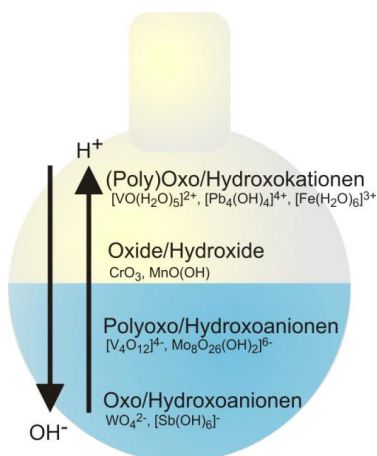
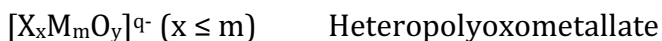


Abb. 7: Beispielhafte Darstellung pH-abhängiger Hydrolysereaktionen in Anlehnung an Referenz [81].

Die Löslichkeit der meisten bekannten Metalloxide und Polyoxosalze ist auf wenige Lösungsmittel begrenzt. Diesbezüglich bilden Isopoly- oder Heteropolyoxometallate der frühen Übergangselemente eine wichtige Ausnahme. Beide unterscheiden sich in ihrer Strukturformel:



Dabei steht X für das Heteroatom und M für das Metallatom in seiner höchsten Oxidationsstufe ( $d^0$  oder  $d^1$ ).

Im gesamten Periodensystem sind nur fünf Übergangsmetalle, Molybdän (VI), Wolfram (VI), Niob (V), Tantal (V) und Vanadium (V), in der Lage Polyoxoanionen-Cluster aufzubauen, von denen nur zwei - nämlich Molybdän und Wolfram - umfangreich erforscht wurden.<sup>[81]</sup> Es stellt sich somit die Frage welche Eigenschaft ein Metallatom haben muss, um Polyoxometallate auszubilden?

Neben den geeigneten Kationenradien muss das zur Verfügung stehende Metallkation ein guter Akzeptor für die  $p\pi$ -Elektronen des Sauerstoffs sein. Die Fähigkeit  $p\pi$ -Elektronen aufzunehmen nimmt mit zunehmendem Kationenradius ab. Für die Ausbildung eines POM-Clusters müssen aber beide Faktoren gleichzeitig erfüllt sein. Es gibt Kationen, die eine hohe bis sehr hohe Affinität zu den  $p\pi$ -Elektronen des Sauerstoffs zeigen, aber für eine notwendige oktaedrische Koordination zu klein sind (z.B.  $\text{Cr}^{6+}$ -Ionen). Daneben gibt es Kationen, die eine hinreichende Größe haben, aber eine schlechte Affinität zu den Elektronen des Sauerstoffs besitzen (z.B.  $\text{Te}^{6+}$ -Ionen).[81] Im Gegensatz zu  $\text{Cr}^{6+}$  können  $\text{V}^{5+}$ ,  $\text{Mo}^{6+}$  oder  $\text{W}^{6+}$  eine oktaedrische Koordination realisieren (Abb. 8A).[82]

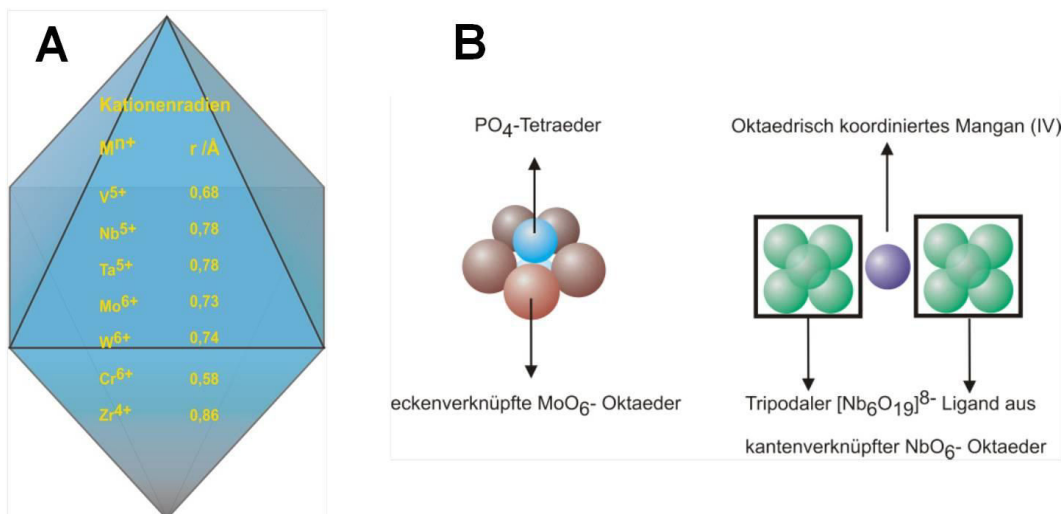


Abb. 8: A) Effektive Kationenradien nach Shannon und Prewitt. Eine oktaedrische Koordination wird im Bereich zwischen 0,65 und 0,80 Å realisiert.[83] Die aufgeführten  $\text{Cr}^{6+}$ - und  $\text{Zr}^{4+}$ -Kationen sind nicht mehr in der Lage eine oktaedrische Koordination zu verwirklichen. B) Schematische Darstellung von primären (links) und sekundären (sekundären) Heteroatomen (nach Referenz [81]).

Nachfolgend wird der Aufbau eines Hetropolyoxometallats generell beschrieben. Polyoxomolybdate und Polyoxowolframate bestehen aus verzerrten Sauerstoffoktaedern. In den Lücken befinden sich die Metallatome. Die Oktaeder sind miteinander über gemeinsame Ecken oder Kanten verknüpft. Die Metallatome sind in Richtung des terminalen Sauerstoffs des Oktaeders verschoben. Aus der daraus

resultierenden Verkürzung der M-O-Bindungen entstehen die für diesen Strukturtyp notwendigen und charakteristischen Metall-Sauerstoff- $\pi$ -Bindungen. Diese terminalen, nicht verbrückenden Sauerstoffatome sind nicht-basisch, regulieren die Protonierung und verhindern eine Weiterpolymerisation bzw. Kondensation des Polyaniongerüstes.<sup>[81]</sup> Anders als zum Beispiel bei porösem TiO<sub>2</sub>, bei dem die Kondensation über  $\mu$ -Hydroxy-Gruppen erfolgt, muss bei den POMs zur Ausbildung eines Netzwerkes ein Vernetzer in Form von La<sup>3+</sup>- oder Cs<sup>+</sup>-Ionen eingearbeitet werden.<sup>[57,84,85]</sup>

Im Gegensatz zu den fünf Metallkationen, die fähig sind Polyoxo-Strukturen aufzubauen, sind mittlerweile 67 Elemente bekannt, die als Heteroatom in die verschiedenen Metalloxidcluster eingebettet werden können. Hierbei wird zwischen primären („zentralen“) und sekundären („peripheren“) Heteroatomen unterschieden. Primäre Heteroatome sind für die Stabilität der Struktur des POMs essentiell. Sekundäre Heteroatome sind außerhalb der Heteropolyoxo-Anionen. Das Polyoxo-Anion ist davon unabhängig stabil (Abb. 8B).

Die Koordination des Heteroatoms innerhalb oder außerhalb des Metallclusters ist variabel und hängt vom Heteroatom selbst ab. So können sowohl tetraedrische, oktaedrische, kubische und ikosaedrische Koordinationen für das Heteroatom realisiert werden (Abb. 9).

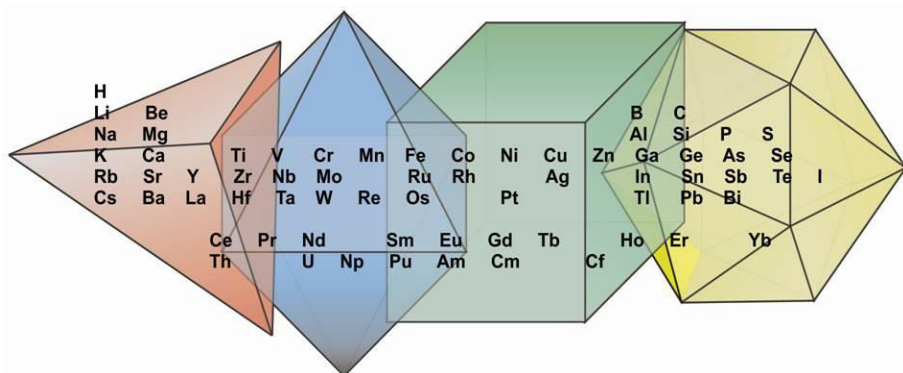


Abb. 9: Mögliche Polyeder der bisher als Heteroatome eingesetzten Elemente (nach Referenz [81]).

Eines der bekanntesten Heteropolyoxometallat-Strukturmotive ist der Keggin-Typ (Keggin POM). Dieses POM wurde 1826 zum ersten Mal von Berzelius synthetisiert und

besitzt die allgemeine Summenformel  $[XM_{12}O_{40}]^{n-}$ .<sup>[86]</sup> Die Struktur des *1,4,1,9,2,5,2,6,3,7,3,8,4,10,5,10,6,11,7,11,8,12,9,12-dodeca-μ-oxo-μ12-(tetraoxo-phosphato-01.4.9,02.5.6,03.7.8,010.11.12)-tetrakis-[tri-μ-oxo-tri(oxomolybdat)](3-)*-Anions wurde 1933 durch *J.F. Keggin* röntgendiffraktometrisch aufgeklärt.<sup>[87,88]</sup> Dessen pseudosphärische Struktur besteht aus einem Heteroatom-Sauerstoff-Tetraeder umgeben von zwölf ecken- bzw. kantenverknüpften Molybdän-Sauerstoff-Oktaedern (Abb. 10).

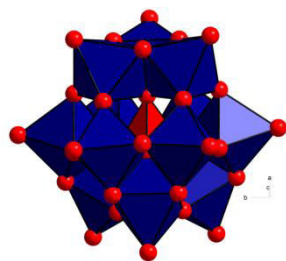


Abb. 10: Struktur des Keggin- Anions; rotes Polyeder:  $XO_4$ -Tetraeder; blaue Polyeder:  $MO_6$ -Oktaeder.

Daneben existieren eine Reihe zusätzlicher Heteropolyoxometallat-Strukturtypen, wie der Silverton-Typ  $[XM_{12}O_{42}]$ , Dawson-Typ  $[X_2M_{18}O_{62}]$ , Waugh-Typ  $[XM_9O_{32}]$  und Anderson-Typ  $[XM_6O_{24}]$ .<sup>[81]</sup>

Keggin POMs besitzen interessante und vielfältige chemische, physikalische und elektronische Eigenschaften,<sup>[89,90]</sup> die ihren Einsatz in der Katalyse und Elektrochemie rechtfertigen.<sup>[90-94]</sup> Allerdings ist die Zugänglichkeit zum katalytisch aktiven Zentrum der reinen Keggin POMs begrenzt, da diese anorganischen Oxide grundsätzlich eine sehr geringe Oberfläche besitzen.<sup>[91]</sup> Daher ist die Erhöhung der spezifischen Oberfläche durch geeignete Strukturierungsmethoden ein sehr stark umforschtes Gebiet.

Das Einarbeiten der Keggin POMs in funktionelle Architekturen und Materialien ist allerdings schwierig. Gelingt es, die hydrophilen Anionen mit hydrophoben, organischen Materialien ladungsvermittelt zu kombinieren, ist die Stabilisierung der resultierenden Hybridmaterialien dennoch limitiert.<sup>[91,95]</sup>

So konnten zum Beispiel die hydrophilen und hochgeladenen Keggin POM Einheiten in hydrophobe organische Matrizen eingebracht werden, indem die anorganischen

Gegenionen durch kationische Tenside ausgetauscht oder kovalent angebunden werden, was wiederum zu der Etablierung der so genannten „Surfactant Encapsulated Polyoxometalate Cluster“ (SEC) führte.<sup>[96-103]</sup>

Für gewöhnlich sind diese tensidären POMs sphärische Nanoobjekte, die sich in organischem Medium lösen lassen und in einem zusätzlichen Arbeitsschritt in funktionale Mesostrukturen mit erhöhter katalytischer Aktivität überführt werden können.<sup>[104]</sup> So konnte bereits eine Vielzahl von Strukturen, wie „Zwiebeln“, „Würmer“, „Honigwaben“, hexagonal geordnete Zylinder, „Scheiben“, „Röhren“ u.v.m.<sup>[105]</sup> generiert werden (Abb. 11).

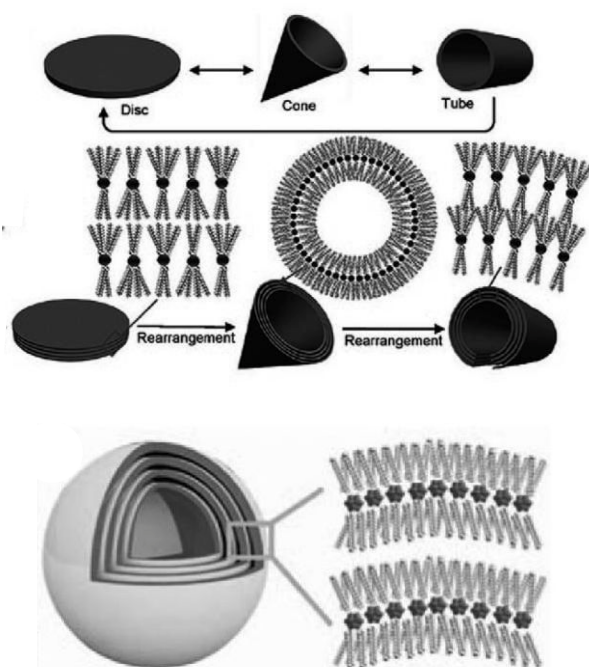


Abb. 11: Typische Darstellung der SECs und ihre Selbstanordnung in unterschiedlichste Nanoobjekte. Oben: Platten-, Kegel- und Röhren-Struktur. Unten: Zwiebel-Struktur.<sup>[105]</sup>

Eine Ausdehnung dieses Konzeptes auf amphiphile Diblockcopolymere resultierte in der Verwirklichung von einzelnen, mizellaren, vesikulären und wurmartigen Nanoobjekten.<sup>[106,107]</sup> Darauf aufbauend konnten mit kernquervernetzten Diblockcopolymeren durch Selbstanordnung von diskreten, wurmartigen Nanohybridien verschlungene spaghetti-ähnliche Mesostrukturen aufgebaut werden.<sup>[40]</sup>



## 5. Problemstellung

Das Ziel dieser Arbeit war es, Übergangsmetallocide und Polyoxometallate mittels ionogener Diblockcopolymere in definierte Strukturen zu überführen, zu charakterisieren und auf ihre Anwendbarkeit in der Katalyse zu testen. Dabei wurde der Fokus vor allem auf den Ausbau des bereits am Lehrstuhl AC 1 erarbeiteten Prinzips der ladungsinduzierten Strukturierung von anionischen oligomeren Clustern mittels ionisierbarer 1-dimensionaler Diblockcopolymeren gelegt.

Darauf aufbauend lag ein Forschungsschwerpunkt in der Übertragung dieses Konzeptes auf pre-synthetisierte Nanokristalle. Diese besitzen bei niedrigen pH-Werten eine positive Oberflächenladung und sollten daher in negativ geladene 1-dimensionale Polyelektrolyte eingelagert werden. Ein Vorteil für die Verwendung dieser kolloidalen Partikel ist, dass das Polymorph durch die Synthesebedingungen bei der Hydrolyse der korrespondierenden Precursoren gezielt eingestellt werden kann. Diese Überlegung wurde am Beispiel des Polymorphismus von  $\text{TiO}_2$  überprüft.

Des Weiteren wurde im Hinblick auf die bereits etablierte Synthese von 1-dimensionalen Polymer/ Keggin POM Hybridmaterialien versucht dieses System genauer zu verstehen. Insbesondere das Verhalten der spezifischen Oberflächen dieser zylindrischen Hybridmaterialien stand zunächst im Mittelpunkt der Forschung, da dieser Faktor maßgeblich für katalytische Anwendungen ist. Besonderer Fokus wurde hierbei auf den Einfluss des Aspektverhältnisses gelegt und dieses systematisch untersucht. Ebenso musste geklärt werden, ob die entwickelten Polymer/ Keggin POM Nanostäbe auch wegen ihrer hohen spezifischen Oberfläche katalytische Aktivität besitzen, da dies einer der Hauptgründe für die Strukturierung war. Hierzu wurden verschiedene 1-dimensionale Hybridmaterialien, die sich in Ladung, Heteroatom und Metallkation der Heteropolysäure unterscheiden, in der sauer katalysierten Zersetzung von Isopropanol getestet.

Abweichend von den rigiden 1-dimensionalen Systemen wurde versucht einen Syntheseweg zu entwickeln, der es ermöglicht, direkt periodisch geordnete, invers hexagonale Polymer/ Keggin POM Mesphasen herzustellen. Solche bikontinuierlichen Phasen wurden in der Literatur mit Diblockcopolymeren bisher noch nicht beschrieben.

## Problemstellung

Die Schwierigkeit liegt hierbei in der Anbindung des hydrophoben Templates an die hydrophilen POM-Anionen und zugleich in der ungenügenden Lösungsstabilität solcher organophilierten POM-Anionen. Diese Faktoren sind allerdings für die Ausbildung hochgeordneter Mesphasen essentiell. In vorherigen Arbeiten des Lehrstuhl AC I zeigte sich, dass eine Anbindung dieser oligomeren Cluster an organische Template über attraktive Coulomb-Wechselwirkung generell funktioniert. Eine ladungsgesteuerte Anbindung der Keggin POM-Einheiten an das organische Templat wäre auch hier erfolgversprechend. Außerdem wurde ein maßgeschneidertes Diblockcopolymer entwickelt, dessen hydrophober Block deutlich länger als der hydrophile Block ist. Dieser Ansatz ist aus der Tensidchemie bekannt und kann in einem geeigneten Lösungsmittel die benötigte mizellare Stabilität versprechen, was letztendlich über einen EISA-Prozess zur Ausbildung der geordneten Mesphasen führt.

Eine anschließende Entfernung des organischen Templates aus den invers hexagonal geordneten Mesphasen, entweder thermisch oder mechanisch z.B. über Plasmaätzen, brächte die volle Funktionalität und zugängliche Oberfläche solcher Materialien zum Vorschein und wäre für katalytische Anwendungen essentiell. Neben Übergangsmetallociden haben sich aber auch Übergangsmetallcarbide in katalytischen Reaktionen bewährt. Daher wurde unter der Annahme, dass das polymere Templat als Kohlenstoffquelle in der Carbidisierungsreaktion dienen könnte, in weiteren Experimenten die Umwandlung dieser periodischen Mesostrukturen in geordnete Carbid-Phasen untersucht. Dies gewährleiste somit einen direkten Zugang zu porösen Carbiden. Diese Probleme wurden im Rahmen dieser Arbeit ebenso untersucht.

## 6. Synopsis

Diese Dissertation enthält sechs Publikationen, wobei sich die Veröffentlichungen in zwei thematische Blöcke unterteilen lassen: 1-dimensionale zylindrische und invers hexagonal geordnete Mesostrukturen. Innerhalb eines Blockes wurden die Veröffentlichungen von der Synthese hin zur Anwendung aufgereiht. In allen Fällen erfolgt die Hybridbildung über Coulomb-Wechselwirkung zwischen organischem Templat und anorganischem Precursor.

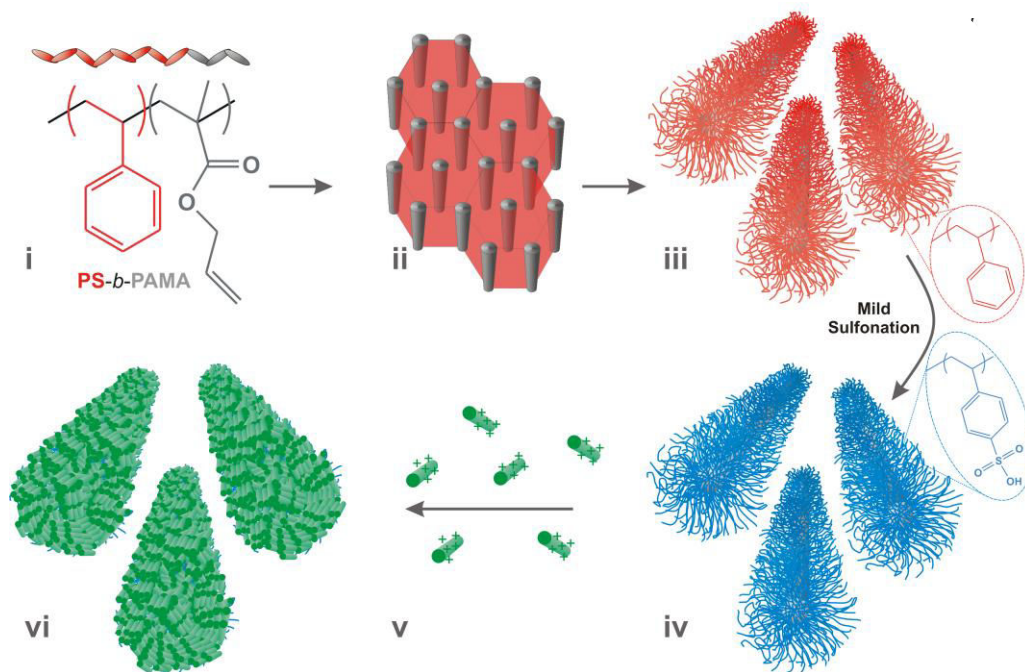
Zunächst wurde das Prinzip der kolloidalen Route auf 1-dimensionale Mesostrukturen übertragen. Die wasserlöslichen und negativ geladenen zylindrischen Template wurden anschließend mit oberflächlich positiv geladenen pre-synthetisierten Rutil- oder Anatas-Kolloiden beladen. Die erhaltenen 1-dimensionalen Mesostrukturen zeigten dieselbe Kristallstruktur wie der Precursor (**7.2**). Weiterhin wurden mit positiv geladenen 1-dimensionalen Templayen zylindrische Keggin POM Hybridmaterialien aus wässriger Suspension mit verschiedenen Aspektverhältnissen hergestellt. Dies führte nach Trocknung zu unterschiedlich dicht gepackten Mikrostrukturen. Es zeigte sich, dass diese Packung maßgeblich für das Verhalten der spezifischen Oberfläche als Funktion des Aspektverhältnisses verantwortlich ist (**7.3**). Eine Ausweitung dieses Strukturierungsprinzips auf andere Keggin POMs wurde erfolgreich durchgeführt. Weiterhin zeigten die resultierenden Zylinderstrukturen hohe spezifische Oberflächen und besaßen katalytische Aktivität in der säurekatalysierten Zersetzung von Isopropanol (**7.4**).

Das Einbringen von Keggin POM-Anionen in positiv geladene Diblockcopolymere erwies sich als äußerst effektiv. So konnten in Abhängigkeit des Keggin POM-Anteiles zum ersten Mal invers hexagonal geordnete Mesophasen über einen EISA-Prozess hergestellt werden. Es zeigte sich, dass das Lösungsmittel und die Löslichkeit des hydrophoben Blockes eine Schlüsselrolle im Strukturierungsprozess einnehmen (**7.5**). Der Erhalt dieser geordneten Mesostrukturen mit geöffneten Mesoporen konnte durch Plasmaätzen an Ultradünnnschnitten erfolgreich dargelegt werden (**7.6**). Auch eine Umwandlung solcher Mesophasen in hierarchisch poröse, katalytisch aktive Carbide wurde erfolgreich praktiziert (**7.7**). Diese Ergebnisse werden im Folgenden umfangreich dargestellt.

## 6.1 Kristalline TiO<sub>2</sub> Nanostrukturen mit hohem Aspektverhältnis

Nanostrukturierte Metalloxide mit hohem Aspektverhältnis wie Nanodrähte oder Nanoröhren sind aufgrund ihrer großenabhangigen optischen und elektronischen Eigenschaften von besonderem wissenschaftlichem Interesse.

Die Arbeit zeigt eine generelle Methode auf, um nanokristalline Metalloxide in 1-dimensionale Mesostrukturen zu überführen. Das in diesem Kapitel beschriebene Synthesekonzept unterstreicht die generelle Anwendbarkeit der kolloidalen Route.



Schema 1: PS-*b*-PAMA (i) mikrophasensepariert in (ii) hexagonal geordnete Zylinder. (iii) Die UV-kernquervernetzten zylindrischen Polymerbürsten mit PAMA-Kern und PS-Bürsten wurden redispersiert und (iv) sulfoniert. Die somit negativ geladenen zylindrischen Polyelektrolytbürsten wurden mit (v) positiv geladenem pre-synthetisierten Rutil Nanokristallen beladen. Dies führte zur Bildung von anisotropen Metalloxid/ Polymer Nanodrähten (vi).

Zunächst wurde PSS-b-PAMA als wasserlösliches 1-dimensionales Polymertemplat, wie in Schema 1i – iv gezeigt, hergestellt. Der Schlüsselschritt war die Umwandlung von 1-dimensionalen kernquervernetzten PS-b-PAMA mit einer PS-Corona in zylindrische, wasserlösliche PSS-b-PAMA Polyelektrolytbürsten durch milde Sulfonierung (Abb. 12).

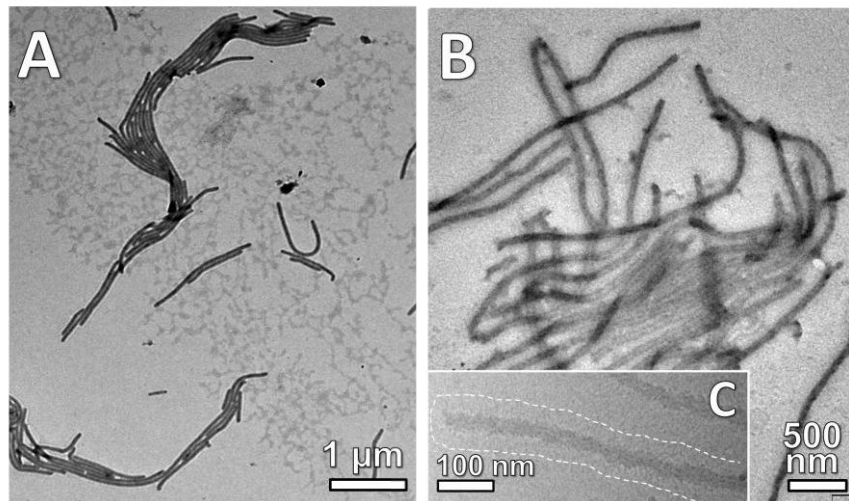


Abb. 12: TEM Aufnahmen der kernquervernetzten, zylindrischen Polymerbürsten und ihrer sulfonierten Analoga: (A) RuO<sub>4</sub>- markiertes PS-b-PAMA aus THF und (B) PSS-b-PAMA aus Wasser. (C) Cryo-TEM Ausschnitt von PSS-b-PAMA in Wasser

Die negativ geladenen Polyelektrolytbürsten wurden als Templat für die Herstellung von 1-dimensionalen, mesostrukturierten Rutil- bzw. Anatas-Nanokristallen herangezogen. Die unterschiedlichen, an der Oberfläche positiv geladenen TiO<sub>2</sub>-Polymorphe wurden jeweils vor der Hybridbildung separat synthetisiert. Die Kristallstruktur von Rutil und Anatas konnte durch die Verwendung unterschiedlicher Säuren (HCl: Rutil; Essigsäure: Anatas) bei der Hydrolyse des TiO<sub>2</sub>-Precursors gezielt eingestellt werden (Abb. 13 Aa und Ba).

Die anschließende Hybridbildung erfolgte über elektrostatische Anziehung zwischen dem positiv geladenen anorganischen Precursor und dem negativ geladenen organischen Templat unter Erhalt der vorgegebenen Kristallinität der Nanopartikel (Abb. 13). Die gute Verteilung der Nanokristalle in der Polymermatrix wurde durch HR-TEM Aufnahmen nachgewiesen (Abb. 14 A und B). Zusätzliche SAED-Messungen der

anisotropen Polymer/ Rutil Hybridstrukturen bestätigen die Phasenzuordnung durch PXRD-Messungen (Abb. 14 C).

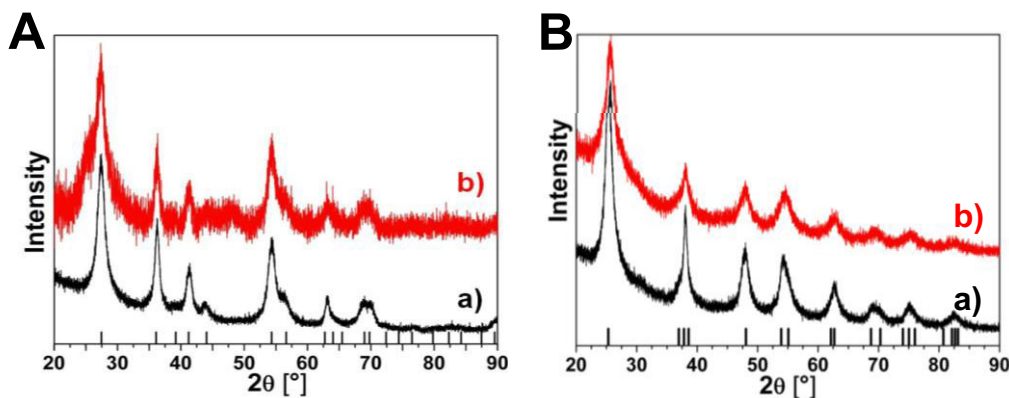


Abb. 13: Röntgendiffraktogramme des (A) Rutil-Precursors (a) sowie des anisotropen Polymer/ Rutil Hybridmaterials und (B) des Anatas-Precursors (a) sowie der anisotropen Polymer/ Anatas Hybridmaterialien.

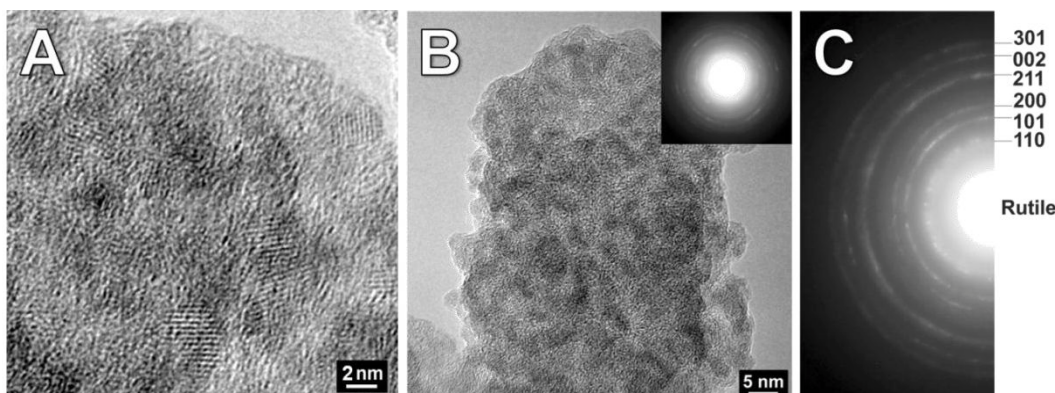


Abb. 14: (A) und (B) HR-TEM-Aufnahmen der anisotropen Rutil Hybride. (C) SAED-Messung der Rutil Nanodrähte.

Die flexiblen anisotropen Hybrimaterialien bilden nach der Trocknung verschlauft spaghettiforme Mikrostrukturen (Abb. 15 A-D) aus. Das interpartikulär poröse Geflecht besitzt eine spezifische Oberfläche von 66 m<sup>2</sup>/g. Nach der thermischen Entfernung des Templates bleibt die Mikrostruktur erhalten (Abb. 15 E-F).

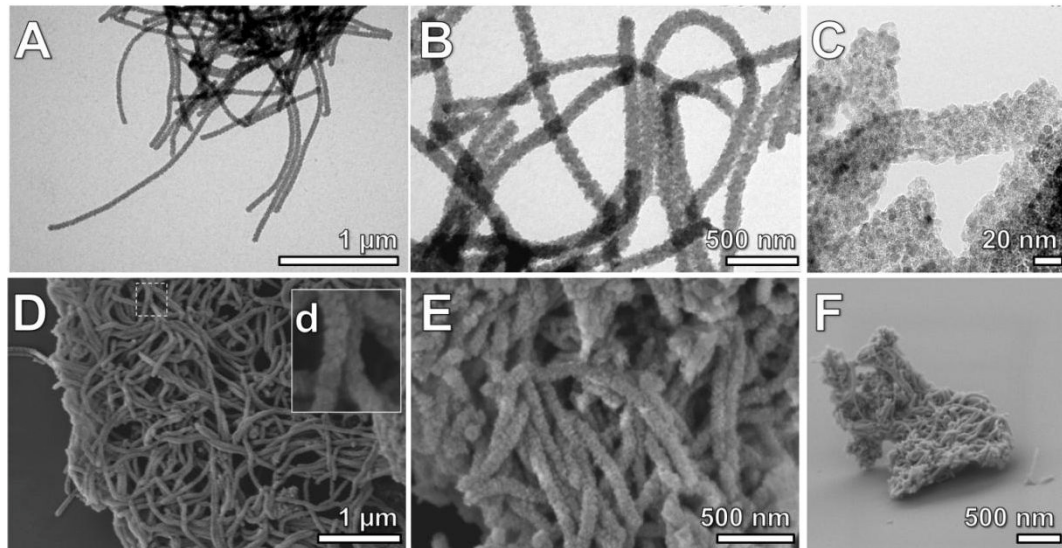


Abb. 15: TEM-Aufnahmen der synthetisierten Rutil-Zylinder (A-D) und nach der Entfernung des Templates (E-F).

Die Ergebnisse zeigen die generelle und einfache Machbarkeit von 1-dimensional Hybridmaterialien unter Verwendung von pre-synthetisierten Metalloxid-Kationen. Am Beispiel zweier Polymorphe von  $\text{TiO}_2$ , Rutil und Anatas, konnten diese ladungsvermittelt und selektiv in eine 1-dimensionale Matrix eingebracht werden.

## 6.2 Packungsverhalten von zylindrischen Keggin POM Hybridmaterialien als Funktion des Aspektverhältnisses

Die verschlauften Spaghetti-ähnlichen Hybridmaterialien, besitzen zwar hohe Oberfläche, allerdings wurde hier auf beeinflussende Faktoren, wie Oberflächenrauigkeit oder interpartikuläre Packung der Mikrostrukturen nicht eingegangen. Letztere hängt mit der Länge der zylindrischen Hybridmaterialien zusammen. In einer detaillierteren Studie wurde in der nachfolgenden Arbeit die Änderung der spezifischen Oberfläche als Funktion des Aspektverhältnisses der 1-dimensionalen Hybridmaterialien untersucht. Hierbei wurden Keggin POMs (Molybdophosphorsäure,  $H_3[PMo_{12}O_{40}]$ ) als geladene, anorganische Precursoren verwendet. Als Templat wurden kernquervernetzte PB-b-P2VP-Nanostäbe mit ionisierbaren P2VP-Seitenarmen verwendet. Zuvor wurden die PB-b-P2VP-Zylinder in wässriger HCl dispergiert und die Länge über Ultraschallbehandlung eingestellt (Abb. 16, Tabelle 1). Schon nach einminütiger Behandlung zeigte sich eine signifikante Verkürzung der mittleren Partikellänge (Abb. 16 B). Die Anisotropie und das Aspektverhältnis nahmen mit zunehmender Ultraschalldauer (Abb. 16 C-D) ab. Nach zehn Minuten überstieg der Anteil an Partikeln mit annähernd sphärischer Morphologie den der anisotropen Zylinder (Abb. 16E). Die durchschnittlichen Längen der Zylinder sind in Tabelle 1 dargestellt.

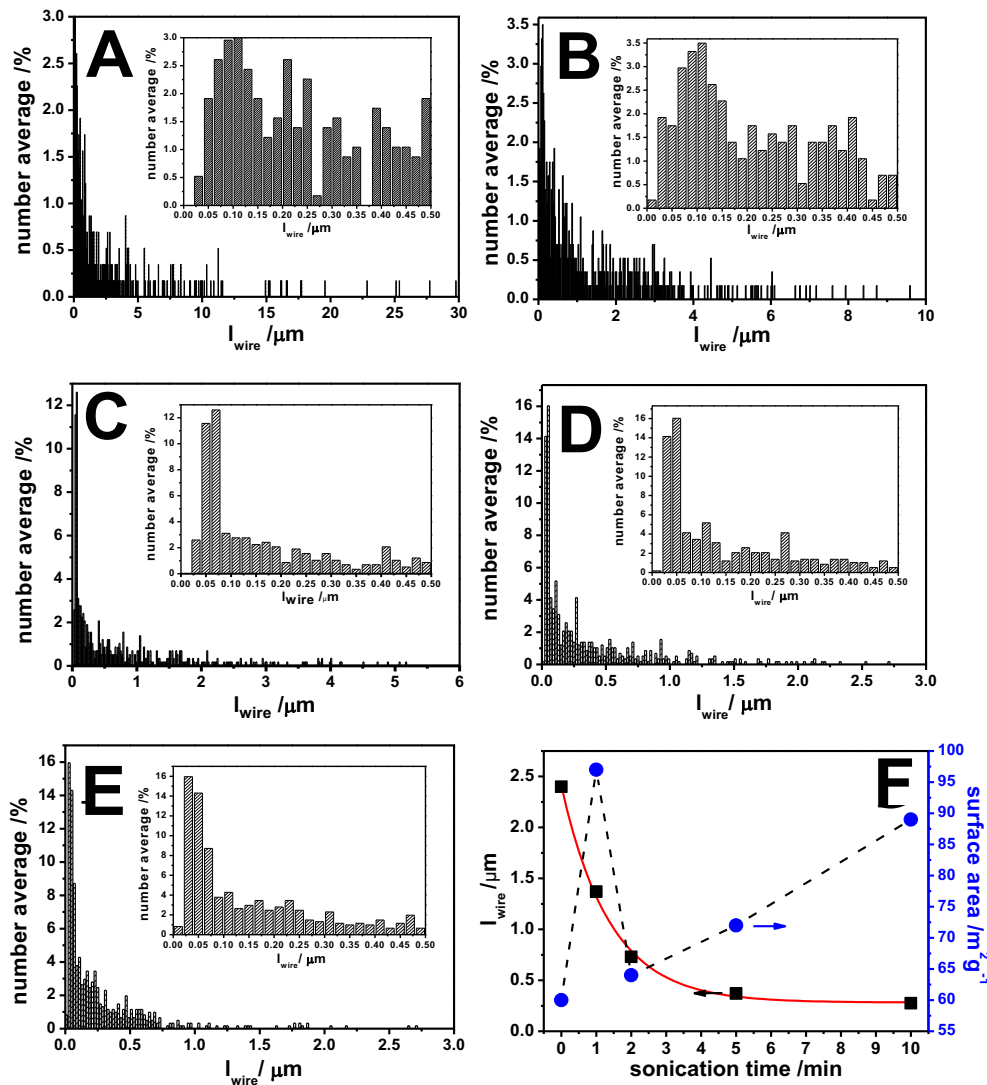


Abb. 16: Längenverteilung der zylindrischen PB-b-P2VP-Mizellen für unterschiedliche Ultraschalldauer: A) 0 min, B) 1min, C) 2 min, D) 5 min, und E) 10 min. F) Entwicklung der mittleren Zylinderlängen und der spezifischen Oberfläche der zylindrischen PB-b-P2VP/ Keggin POM-Hybridmaterialien als Funktion der Beschallungsdauer.

Tabelle 1: Charakteristika der zylindrischen Polymermizellen und des zylindrischen PB-b-P2VP/ Keggin POM-Hybridmaterials

zylindrische PB-b-P2VP/Keggin POM Hybride	Ultraschalldauer /min	Durchschnittslänge /µm	Aspektverhältnis α	Oberfläche /m <sup>2</sup> /g
hybrid 1	0	2.40	120	60
hybrid 2	1	1.37	68.5	97
hybrid 3	2	0.73	36.5	64
hybrid 4	5	0.37	18.5	72
hybrid 5	10	0.28	14.0	89

Nach Einstellung der Zylinderlänge erfolgte die Hybridbildung über Coulomb-Wechselwirkungen zwischen den positiv geladenen Polymerbürsten und den anionischen Keggin POM-Einheiten. Die einzelnen zylindrischen Hybridmaterialien ordnen sich in verschlungene Spaghetti-ähnliche Mikrostrukturen an (Abb. 17).

Die so erhaltenen unterschiedlich langen PB-b-P2VP/ Keggin POM Hybridmaterialien besaßen entsprechend ihrer Ultraschallbehandlungsdauer spezifische Oberflächen von 60, 97, 64, 72 bzw. 89 m<sup>2</sup>/g (Abb. 16, Tabelle 1). Das Verhalten der Oberflächen konnte nicht mit der Oberflächengleichung für Zylinder (Gleichung 1) erklärt werden.

$$A = \frac{L+r}{L+\frac{4}{3}r} \cdot \frac{2}{r \cdot \rho_{\text{composite}}} \quad (1)$$

wobei L als Länge der Zylinder, r der Zylinderradius und ρ die Dichte der zylindrischen PB-b-P2VP Keggin POM Materialien ist. Gleichung 1 zeigt eine geringe Abhängigkeit der spezifischen Oberfläche von der Zylinderlänge. Auch weichen der theoretische Erwartungswert und der experimentelle Befund stark voneinander ab. Dies soll an folgendem Beispiel verdeutlicht werden. Angenommen alle Zylinder besäßen einen einheitlichen Radius und konstante Dichte so würde man beim Übergang von Hybrid 2 zu Hybrid 3 (Tabelle 1) eine Erhöhung der spezifischen Oberfläche um einen Faktor von 1.4 erhalten. Im Gegensatz zu dem theoretisch erwartenden Werten zeigt der experimentell erhaltene Wert eine drastische Minimierung der Oberfläche.

Genaue Betrachtungen zeigten, dass das Oberflächenverhalten dieser Mikrostrukturen in erster Linie nicht von der Erhöhung der Endkappen abhängig ist, sondern von Faktoren wie Oberflächenrauigkeit, Größe der interpartikulären Poren und 40

daraus resultierend vom Grad des Interpartikelkontakte. Dies wurde durch REM-Aufnahmen bestätigt (Abb. 17). So zeigte sich, dass ein kurze Ultraschallbehandlungszeit von einer Minute zu einer besseren Dispersion innerhalb der verschlauften Spaghetti-ähnlichen Mikrostrukturen führte (Abb. 17 C und D), was die Oberfläche zunächst erhöhte. Kürzere anisotrope Hybridzylinder packen dichter als ihre langen Analoga (Abb. 17 E und F). Dies führte zu einer Minimierung der Oberfläche. Letztendlich wurde die Oberfläche durch fast sphärische Hybridmaterialien wieder erhöht (Abb. 17 G und J). Diese fungieren als Abstandshalter zwischen den verbleibenden anisotropen Zylindern und verhindern dadurch eine dichte Packung.

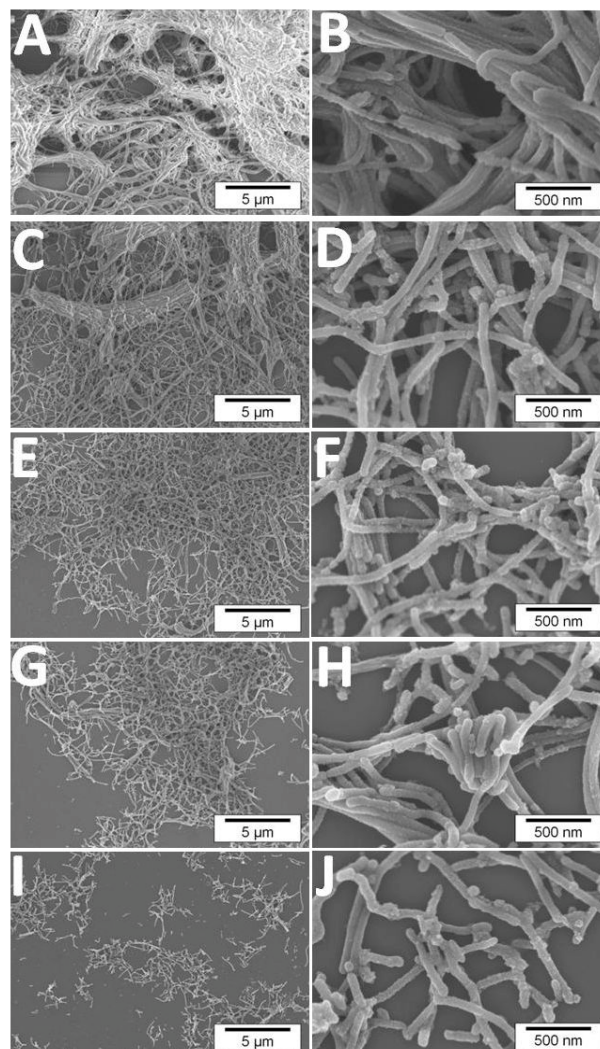


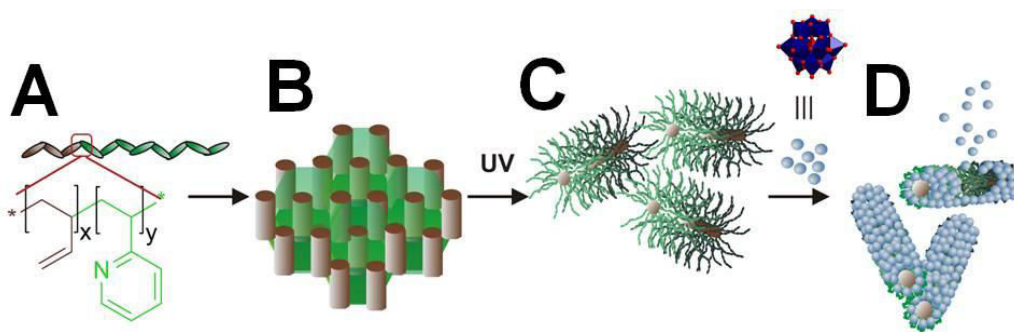
Abb. 17: REM-Aufnahmen von zylindrischen PB-b-P2VP/ Keggin POM-Hybridmaterialien bei unterschiedlichen Vergrößerungen. Durchschnittslänge der PB-b-P2VP-Zylinder: A), B) 2.40  $\mu\text{m}$ , C), D) 1.53  $\mu\text{m}$ , E), F) 0.73  $\mu\text{m}$ , G), H) 0.37  $\mu\text{m}$ , and I), J) 0.28  $\mu\text{m}$ .

Die Studie zeigt, dass die Länge kernquervernetzter Polymerzyliner mittels Ultraschallbehandlung eingestellt werden kann. Die spezifische Oberfläche der korrespondierenden Polymer/ Keggin POM Hybridmaterialien hängt vor allem von der Packung der anisotropen Hybridmaterialien und somit vom Grad der interpartikulären Kontakte ab.

## 6.3 Säurekatalysierte Zersetzung von Iso-propanol durch unterschiedliche zylindrische Keggin POM-Hybridmaterialien

Die Untersuchungen der Katalyseeigenschaften unterschiedlicher 1-dimensionaler Keggin POM Hybridmaterialien wurden in Zusammenarbeit mit der Abteilung für Anorganische Chemie des Fritz-Haber-Instituts der Max-Planck-Gesellschaft zu Berlin durchgeführt. Dabei wurde das bewährte Prinzip der templatgesteuerten, ladungsinduzierten Strukturierung von Keggin POMs weiter ausgebaut. Ausgehend von 1-dimensionale kernquervernetzten PB-b-P2VP Polymerbürsten wurden Heteropolysäuren des Keggin-Typs, die sich in Ladung, Heteroatom und Metallkation unterscheiden in das Templat eingelagert: Molybdophosphorsäure ( $H_3PMo_{12}O_{40}$ ), Molybdokieselsäure ( $H_4SiMo_{12}O_{40}$ ) und Wolframatophosphorsäure ( $H_3PW_{12}O_{40}$ ). Die Aminofunktion der P2VP-Seitenarme ist basisch genug, um von den starken Heteropolysäuren *in-situ* protoniert zu werden. Die daraus resultierenden attraktiven Coulomb-Wechselwirkungen zwischen den Keggin POM-Anionen und den protonierten, positiv geladenen Polymerzylinern förderten die Hybridbildung (Schema 2).

Das Ziel war, die Zugänglichkeit der sauren Zentren des Keggin POMs nach der Hybridbildung anhand der sauerkatalysierten Zersetzung von Isopropanol zu testen



Schema 2: A) PB-b-P2VP (B) mikrophasensepariert in hexagonal geordnete PB-Zylinder in einer P2VP-Matrix. (C) 1-dimensionale Polymerbürsten mit P2VP-Seitenarmen nach UV-Vernetzung und Dispergierung. (D) Einlagerung von Keggin POM-Einheiten in das zylindrische Polymertemplat und Bildung von 1-dimensionalen PB-b-P2VP/ Keggin POM-Hybridmaterialien.

Die hergestellten, diskreten, zylindrischen PB-b-P2VP/ Keggin POM Hybridmaterialien ordnen sich nach Trocknung in verschlungene Spaghetti-ähnliche Volumenstrukturen an, wie durch REM-Aufnahmen belegt wurde (Abb. 18). N<sub>2</sub>-Physisorptionsmessungen ergaben hohe spezifische Oberflächen der hergestellten Hybridmaterialien der Molybdophosphor-, Molybdokiesel- und Wolframatophosphorsäure (Tabelle 2). Diese sind 10-bis-20mal höher als die Oberflächen der korrespondierenden kristallinen Heteropolysäuren ( $3 \text{ m}^2/\text{g}$ ).

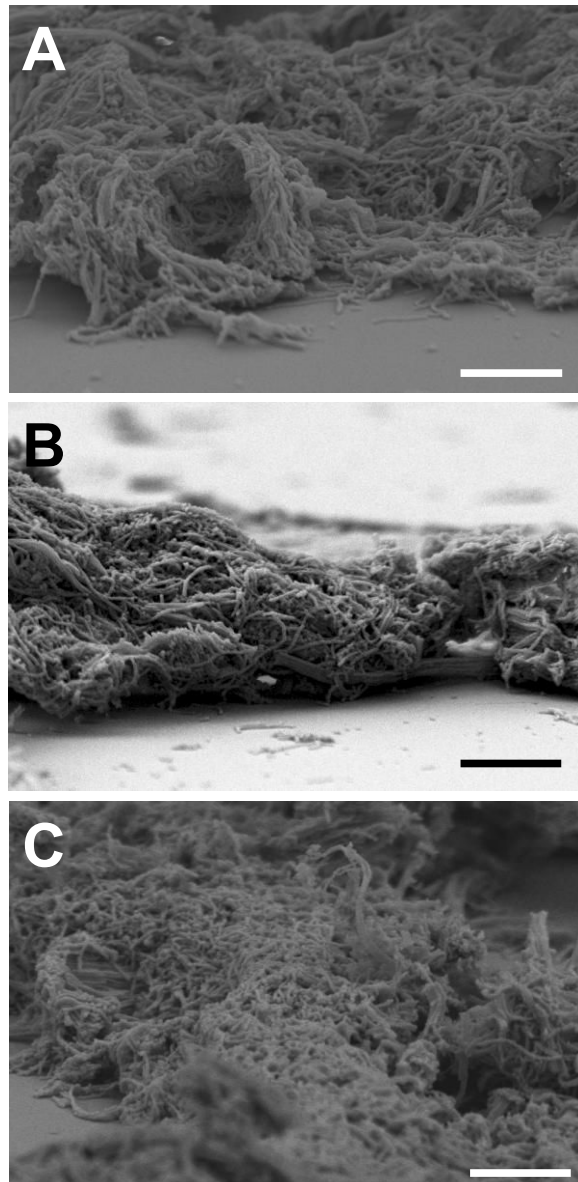


Abb. 18: REM-Aufnahmen der 1-dimensionalen PB-b-P2VP/ Keggin POM Hybridstrukturen nach Trocknung: A)  $H_3[PMo_{12}O_{40}]$ , B)  $H_4[SiMo_{12}O_{40}]$  und C)  $H_3[PW_{12}O_{40}]$ . Maßstab: 2  $\mu m$ .

Pulverdiffraktometrische Untersuchungen zeigten, dass sämtliche zylindrische Hybridmaterialien im Gegensatz zu ihren kristallinen Vorstufen amorph waren. Dies ist ein Beleg für eine gute Verteilung der Keggin POM-Anionen in der Polymermatrix. Mittels FTIR-Messungen konnte die intakte Keggin-Struktur nach der Einlagerung nachgewiesen werden.

Tabelle 2: Eigenschaften der zylindrischen PB-b-P2VP/ Keggin POM Hybridmaterialien.

Keggin POM	Wasseranteil des Precursors pro Formeleinheit	Spezifische Oberfläche /m <sup>2</sup> /g	Isopropanol Umsatz /%	Propylen Selektivität /%
H <sub>3</sub> PMo <sub>12</sub> O <sub>40</sub>	27	62	2.6	81
H <sub>4</sub> SiMo <sub>12</sub> O <sub>40</sub>	29	50	1.7	82
H <sub>3</sub> PW <sub>12</sub> O <sub>40</sub>	28	32	0.3	89

Die hergestellten 1-dimensionalen Polymer/ Keggin POM-Hybridmaterialien wurden anschließend in der sauerkatalysierten Zersetzung von Isopropanol getestet. Isopropanol zersetzt sich in Gegenwart von sauren Zentren zu Propylen und wird in der Anwesenheit von basischen Zentren zu Aceton oxidiert. Im Beisein von redox-aktiven Katalysatoren jedoch kann Isopropanol ebenso direkt zu Aceton oxidiert werden.<sup>[108]</sup> POMs sind in der Katalyse bifunktionell, da sie sowohl Brönstedt acide Zentren als auch redox-aktive Zentren besitzen. Die Aktivität der synthetisierten Hybridmaterialien in der Zersetzungsreaktion des Alkohols war gering (Tabelle 2). Bei niedrigen Temperaturen überwog die Redox-Chemie der Heteropolysäuren, wohingegen nach Überschreiten einer Aktivierungstemperatur die säurekatalysierte Reaktion sukzessive zunahm. Die Aktivität in der Zersetzung von Isopropanol nahm mit zunehmender Oberfläche der Hybridmaterialien in der Reihenfolge von H<sub>3</sub>PW<sub>12</sub>O<sub>40</sub> (0.3 %) < H<sub>3</sub>PMo<sub>12</sub>O<sub>40</sub> (1.3 %) < H<sub>4</sub>SiMo<sub>12</sub>O<sub>40</sub> (1.7 %) zu. Die Selektivität für Propylen stieg in der Reihenfolge H<sub>3</sub>PMo<sub>12</sub>O<sub>40</sub> (73 %) < H<sub>4</sub>SiMo<sub>12</sub>O<sub>40</sub> (82 %) < H<sub>3</sub>PW<sub>12</sub>O<sub>40</sub> (89 %) zu (Abb. 19).

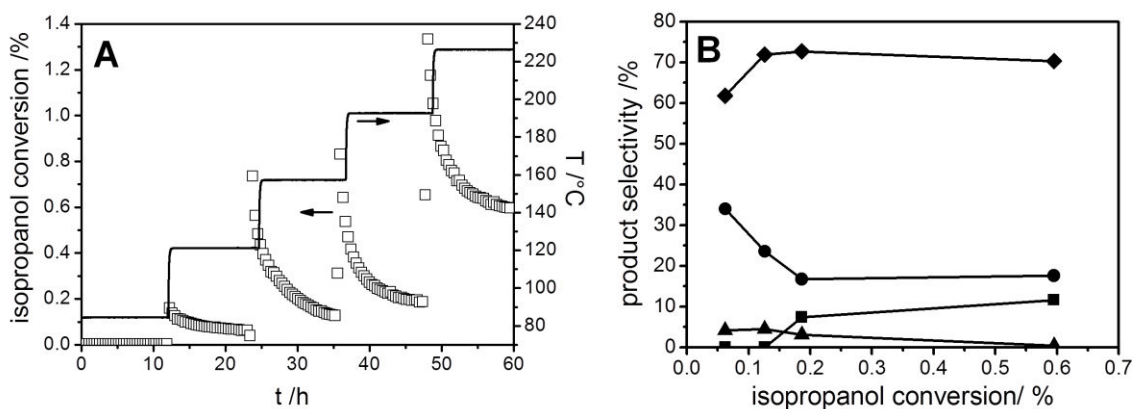
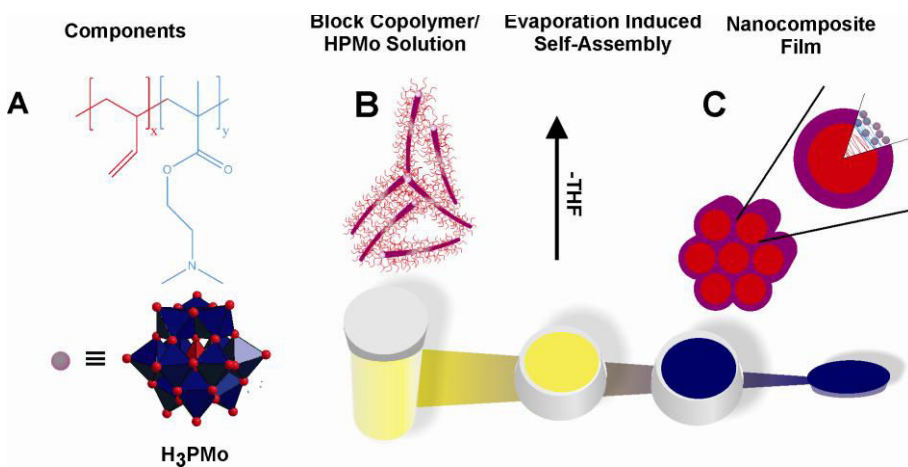


Abb. 19 Katalytische Aktivität von 1-dimensionalen PB-b-P2VP/  $\text{H}_3[\text{PMo}_{12}\text{O}_{40}]$  Hybridmaterialien in der Gasphasenzersetzung von Isopropanol: A) Isopropanol Umsatz als Funktion der Zeit und Temperatur und B) Selektivität unter stationären Bedingungen: Propylen (Raute), Aceton (Kreise), Propan (Quadrate) und Diisopropylether (Dreiecke).

Insgesamt wurden unterschiedliche 1-dimensionale PB-b-P2VP/ Keggin POM Hybridmaterialien mit hoher spezifischer Oberfläche hergestellt und ihre Aktivität in der Zersetzung von Isopropanol getestet. Die getesteten Materialien zeigten geringe Aktivität, was auf eine erschwerte Zugänglichkeit der sauren Zentren deuten lässt. Eine Erklärung hierfür würde der grundlegende Mechanismus der Hybridebildung liefern, der vor allem in der attraktiven Coulomb-Wechselwirkung zwischen Templat und anorganischem Precursor begründet ist. Hierfür werden die basischen Aminofunktionen der P2VP-Seitenarme *in-situ* durch die Heteropolysäure protoniert. Die in der Strukturierung involvierten Protonen können aber gleichzeitig nicht für die Katalyse zur Verfügung stehen.

## 6.4 Direkte Herstellung von invers hexagonal geordneten Diblockcopolymer/ Keggin POM Nanokompositfilmen

Angliedernd an die ladungsinduzierte Mesophasen wurde ein neues Synthesekonzept zu invers hexagonal geordneten Polymer/ Keggin POM-Mesostrukturen erarbeitet. Invers hexagonal geordnete POM-Mesophasen, (Polymerzylinder umgeben von einer POM Matrix) sind selbst für Tensidsysteme selten und wurden für Diblockcopolymere noch nicht gefunden. Theoretisch wären solche bikontinuierlichen Morphologien robust und besäßen erhöhte Protonenleitfähigkeit.<sup>[95]</sup> Ausgehend von PB-b-PDMAEMA als ionogenes Diblockcopolymer und H<sub>3</sub>[PMo<sub>12</sub>O<sub>40</sub>] als anorganischer Precursor sollte gezielt eine Synthese zu invers hexagonal geordneten Mesphasen über einen EISA-Prozess entwickelt werden (Schema 3).



Schema 3: Direkte Synthese von hexagonal geordneten PB-b-PDMAEMA/ Keggin POM Nanokompositfilmen: A) chemische Strukturen von PB-b-PDMAEMA (oben) und Keggin POM (unten). B) Mizellbildung in Lösung durch die hohe Löslichkeit des PB-Blockes in THF. C) Invers hexagonal geordnete PB-b-PDMAEMA/ Keggin POM-Nanokompositfilme mit PB-Zylindern in einer PDMAEMA/ Keggin POM-Matrix.

Die Schwierigkeit liegt hierbei in der Anbindung des hydrophoben Templates an die hydrophilen POM-Anionen und zugleich in der ungenügenden Lösungsstabilität solcher organophilierten POM-Anionen. Um hochgeordnete invers hexagonal PB-b-PDMAEMA Keggin POM-Nanokompositfilme zu erhalten, muss eine Makrophasenseparation zwischen den beiden beteiligten Komponenten zuverlässig verhindert werden. Daher mussten die oben aufgeführten zwei Faktoren kontrolliert werden.

Zum einen wechselwirkten die Keggin POM-Anionen über die Coulomb-Wechselwirkung selektiv mit den PDMAEMA-Domänen des Diblockcopolymers. Zum anderen gewährleistete der hohe Polymerisationsgrad und die gute Löslichkeit des PB-Blockes in THF einen auch bei hohen Konzentrationen lösungstablen PB-b-PDMAEMA/Keggin POM-Komplex (Abb. 20).

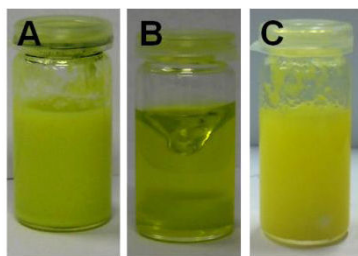


Abb. 20: Fotoaufnahmen von A) PDMAEMA Homopolymer in Gegenwart von Keggin POM in THF, B) PB-b-PDMAEMA mit Keggin POM in THF und C) PB-b-PDMAEMA mit Keggin POM in Aceton. Beide Diblockcopolymer-Blöcke und das Keggin POM-Molekül besitzen gute bis sehr gute Löslichkeit in THF ( $\chi_{\text{PDMAEMA-THF}} = 0.003$ ,  $\chi_{\text{PB-THF}} = 0.11$  gegenüber  $\chi_{\text{PB-Aceton}} = 0.36$ ).

Des Weiteren wurde die Mizellbildung in THF als Funktion des Keggin POM-Anteiles mittels cryo-TEM-Aufnahmen verfolgt (Abb. 21). Mit zunehmender Keggin POM-Konzentration wurden mizellare (Abb. 21 A), bikontinuierliche Netzwerk- (Abb. 21 B) und vesikuläre Phasen (Abb. 21 C) durchlaufen. Die Verknüpfungsmuster in Abb. 21 B sind typisch für Netzwerke.<sup>[109]</sup>

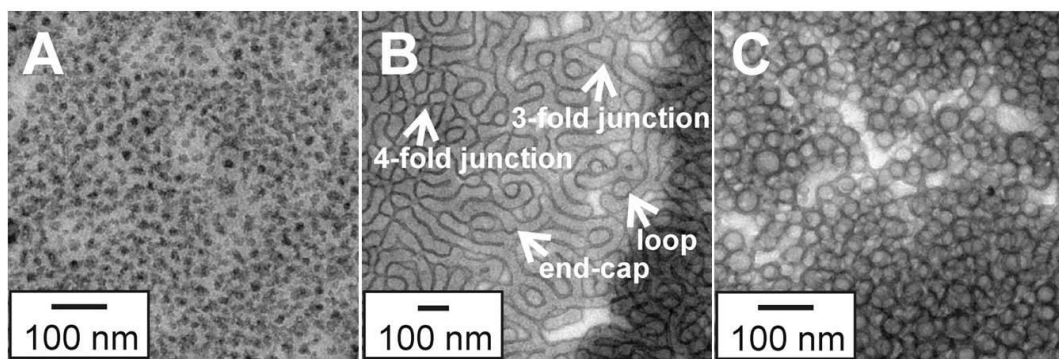


Abb. 21: Cryo-TEM-Aufnahmen aus THF für verschiedene PB-b-PDMAEMA/ Keggin POM-Verhältnisse: A) 3.23, B) 1.08 und C) 0.54.

Nach Verdampfen des Lösungsmittels bei 32 % relativer Luftfeuchte und bei Raumtemperatur erhielt man homogene, röntgenamorphe Filme. Diese Filme zeigten in den FTIR-Messungen eine intakte Keggin-Struktur. Strukturelle Zuordnung mittels SAXS-Messungen und TEM-Aufnahmen (Abb. 22) von Mikrotomschnitten der Kompositfilme ergaben ungeordnete Systeme für geringe Keggin POM Beladungen (Abb 22 A). Bei einer Erhöhung des Keggin POM Anteils auf 61 wt % (Abb. 22 B) bzw. 70 wt % (Abb. 22 C) wurden hexagonal geordnete PB-b-PDMAEMA/ Keggin POM-Filme erhalten. Für höhere Keggin POM-Anteile nimmt die Ordnung wieder ab (Abb. 23 D-F). Zusätzliche SAXS-Messungen bestätigten die elektronenmikroskopischen Beobachtungen.

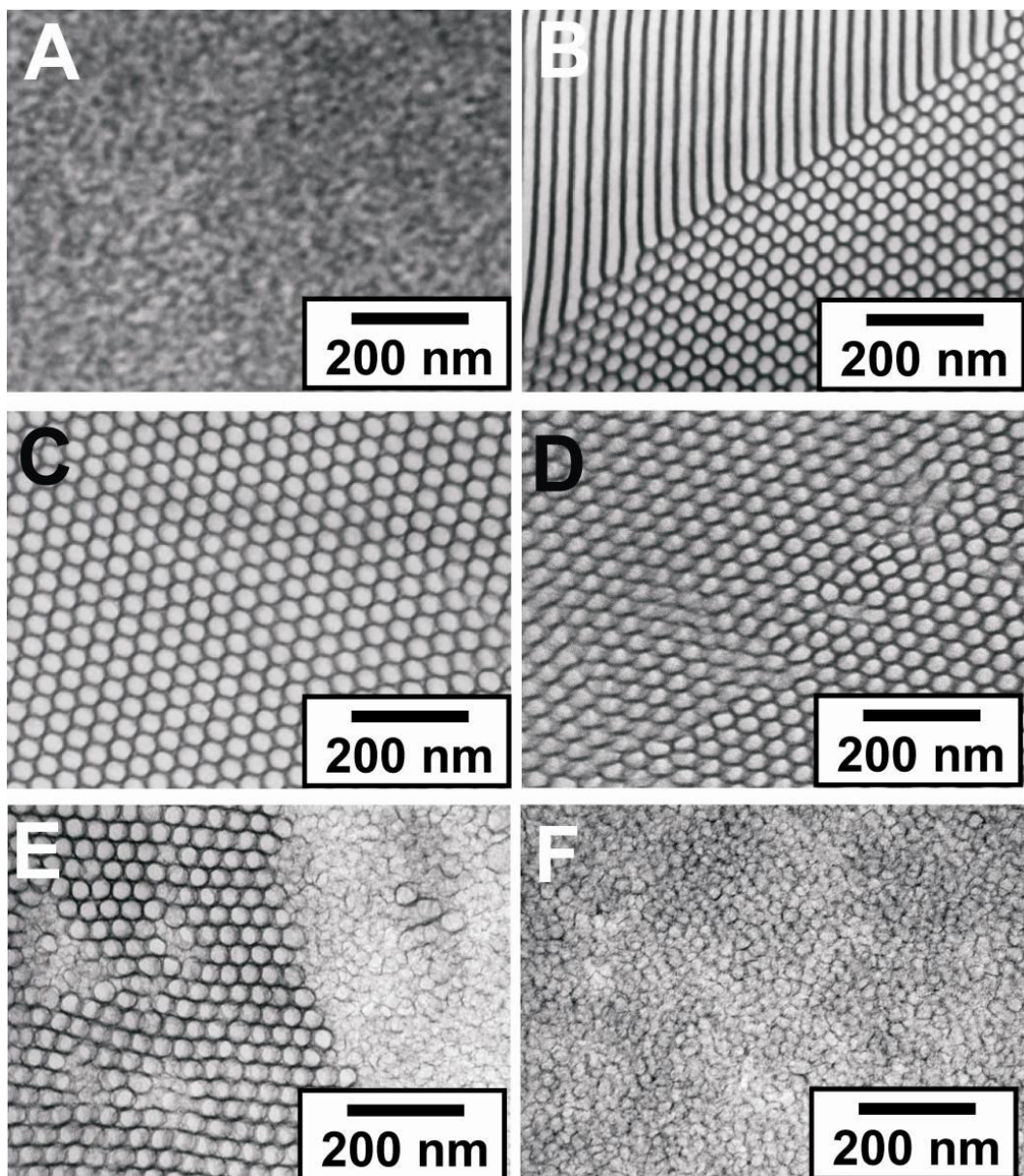


Abb. 22: Repräsentative TEM-Aufnahmen der PB-b-PDMAEMA/ Keggin POM Nanokompositfilme für unterschiedliche Keggin POM-Beladungen: A) 44 wt %, B) 61 wt %, C) 70 wt %, D) 76 wt %, E) 80 wt % und F) 83 wt %.

Weitere Charakteristika der Hybridfilme wie Porendurchmesser, Wandstärke oder Zusammensetzung sind in Tabelle 3 zusammengefasst.

Tabelle 3: PB-b-PDMAEMA/ Keggin POM Nanokompositfilme

Probe	Keggin	wt % Keggin	Block-copolymer	H <sup>+</sup> /N <sup>a</sup>	r <sup>b</sup>	M <sup>c</sup>	d <sub>spacing</sub> <sup>d</sup> /nm	A <sup>e</sup> /nm	B <sup>f</sup> /nm	f <sub>S,calc</sub> <sup>g</sup>	f <sub>S,TEM</sub> <sup>h</sup>
POM1	H <sub>3</sub> PMo	28	PB-b-PDMAEMA	0.46	6.52	M/D	31	nd	nd	0.22	nd
POM2	H <sub>3</sub> PMo	44	PB-b-PDMAEMA	0.93	3.23	M/D	29	nd	nd	0.27	nd
POM3	H <sub>3</sub> PMo	54	PB-b-PDMAEMA	1.39	2.16	M/D	nd	nd	nd	0.31	nd
POM4	H <sub>3</sub> PMo	61	PB-b-PDMAEMA	1.85	1.62	Hex	42	28.9±2.7	7.9±1.1	0.35	0.44
POM5	H <sub>3</sub> PMo	70	PB-b-PDMAEMA	2.78	1.08	Hex	45	32.4±2.5	10.2±1.7	0.42	0.48
POM6	H <sub>3</sub> PMo	76	PB-b-PDMAEMA	3.71	0.81	Hex	51	35.6±2.8	9.2±2.1	0.47	0.43
POM7	H <sub>3</sub> PMo	80	PB-b-PDMAEMA	4.63	0.65	Hex/D	45	32.0±3.9	6.8±1.5	0.52	0.38
POM8	H <sub>3</sub> PMo	83	PB-b-PDMAEMA	5.59	0.54	Hex/D	31	nd	nd	0.56	nd
POM9	H <sub>3</sub> PMo	70	PB-b-P2VP	1.57	1.91	Hex	39	27.0±1.6	8.98±1.1	0.46	0.49
POM10	H <sub>3</sub> PW	79	PB-b-P2VP	1.61	1.86	Hex	41	29.9±2.1	9.11±1.3	0.46	0.47

<sup>a</sup> Molares Verhältnis zwischen H<sup>+</sup> und DMAEMA Einheiten.

<sup>b</sup> Molares Verhältnis von DMAEMA Einheiten zu H<sub>3</sub>PMo.

<sup>c</sup> Morphologie der mesostrukturierten Filme: M: mikellar, D: ungeordnet, Hex: invers hexagonal

<sup>d</sup> bestimmt durch SAXS Messungen

<sup>e</sup> PB Zylinderdurchmesser aus den TEM Bildern.

<sup>f</sup> Dicke der PDMAEMA/H<sub>3</sub>PMo aus den TEM Abbildungen.

<sup>g</sup> Berechneter solvophobischer Volumenanteil

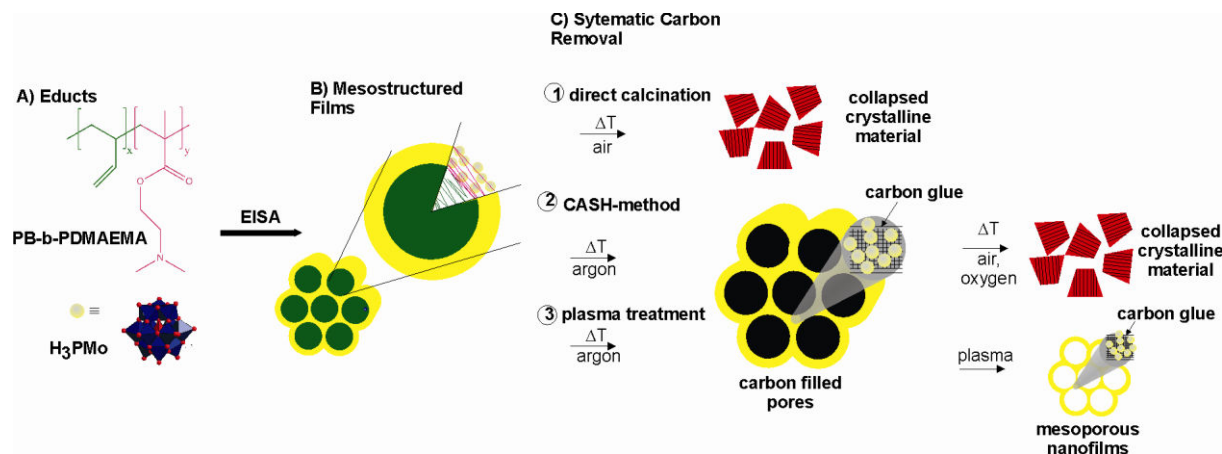
<sup>h</sup> Solvophobisches Volumen aus TEM Messungen

Zusammenfassend wurde folglich dargelegt, dass die Kombination aus PB-b-PDMAEMA und Keggin POM in THF stabile Mizellen über den gesamten Konzentrationsbereich ausbildete. Langsames Verdampfen des Lösungsmittels ergab invers geordnete hexagonale Mesphasen. So konnten zum ersten Mal, direkt und auf einfache Art, invers hexagonal geordnete Diblockcopolymer/ POM Hybridmaterialien hergestellt werden.

## 6.5 Auf den Weg zu mesoporösem Keggin-Type Polyoxometallat – Eine Calcinierungsstudie -

Um die Funktionalität und Oberflächen der hergestellten hexagonal geordneten Keggin POM Mesphasen in seiner vollen Bandbreite auszunutzen und für Anwendungen interessant zu machen, muss das Polymertemplat aus den Mesoporen komplett entfernt werden. Daher wurde in der nachfolgenden Studie systematisch das Entfernen des organischen Templates untersucht. Dabei wurden über 20 unterschiedliche Calcinierungsbedingungen angewandt, die sich aus der Variation von Calcinierungsatmosphäre, -temperatur und -zeit zusammensetzten.

Die Ergebnisse dieser Untersuchungen sind in Schema 4 zusammengefasst. Direkte Calcinierung der PB-b-PDMAEMA/ Keggin POM Nanokomposite an Luft führte zur sofortigen Zersetzung und Bildung von ungeordnetem und kristallinem MoO<sub>3</sub> (Schema 4c, Weg 1). Daraufhin wurde ein alternativer Weg in Betracht gezogen, der aus einer zweistufigen thermischen Behandlung des Kompositen bestand (CASH-Methode; Schema 4c, Weg 2): Zuerst wurden Teile des sp<sup>2</sup>-hybridisierten Kohlenstoffs in Argonatmosphäre zu amorphem Kohlenstoff reduziert. Der *in-situ* gebildete Kohlenstoff „verklebte“ die Keggin POM Einheiten in den Wänden untereinander und verhinderte so einen strukturellen Kollaps der Mesostruktur. Durch eine anschließende Calcinierung in Luft oder Sauerstoffatmosphäre bei unterschiedlichen Temperaturen und Haltezeiten sollte der Kohlenstoff restlos unter Strukturerhalt entfernt werden. Weiterhin wurde versucht den Kohlenstoff über Plasmaätzen zu entfernen (Schema 4c, Weg 3). Die nachfolgenden Betrachtungen beziehen sich auf Weg 2 und Weg 3.



Schema 4: Schematische Übersicht der Calcinierungsstudien: (A) Edukte; (B) Selbstanordnung zu invers hexagonal geordneten PB-b-PDMAEMA/ Keggin POM-Nanokompositfilme. (C) Systematische Entfernung des Polymertemplates direkt an Luft (Weg 1), zweistufige thermische Behandlung (Weg 2) oder durch Argoncalcinierung und anschließende Plasmabehandlung (Weg 3).

Nach jedem Calcinierungsschritt einer zuvor in Argonatmosphäre thermisch behandelten Probe wurde der Massenverlust der Probe als eine weitere Charakterisierungsmethode bestimmt. Trägt man diesen Massenverlust gegen die Calcinierungszeit auf, erhält man im Einklang mit pulverdiffraktometrischen Untersuchungen Existenzbereiche, in denen amorphe (A), halbkristalline (SC) und kristalline (C) Phasen bestehen (Abb. 23). Darüber hinaus wurde mittels TEM-Aufnahmen und SAXS-Messungen nachgewiesen, dass für kristalline Proben die geordnete Mesophase verschwand (Abb. 24 grauer Bereich). Raman-Messungen zeigten für alle calcinierten Kompositproben die Gegenwart von amorphem Kohlenstoff. Löslichkeitsexperimente des calcinierten Materials ergaben, dass sich über 70 % in Wasser lösten. Dies ließ auf eine ungenügende Kondensation der Keggin POM Cluster untereinander schließen.

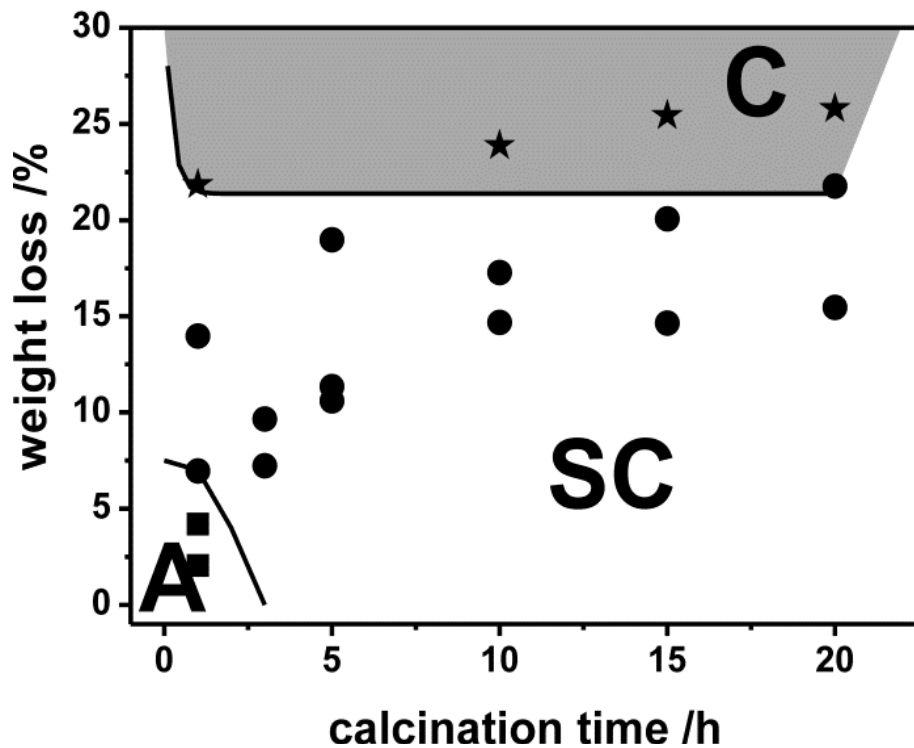


Abb. 23: Existenzbereiche unterschiedlicher Kristallisationsgrade als Funktion des Gewichtsverlustes und der Calcinierungsduer. Quadrate: amorphe Phase (A), Kreise: halbkristallines Material (SC), Sterne: kristalliner Komposit (C). Der grau hinterlegte Bereich zeigt den Verlust der geordneten Mesostruktur an.

Alternativ wurde durch mechanische Methoden wie Plasmaätzen eine Zugänglichkeit zu dem geordneten Mesoporen erreicht. Am Beispiel von Ultradünnsschnitten ( $< 50 \text{ nm}$ ) des vorher in Argonatmosphäre thermische behandelten Komposites konnte dies mit H-O-Plasma gezeigt werden (Abb. 24 A-E). Allerdings lassen Kontrastmodulationen auf den plasmabehandelten Kompositmaterialien auf ein „Verkleben“ der Wände durch Kohlenstoff schließen (Abb. 24 C). Diese Methode konnte nicht auf die geordneten Bulk Komposit-Filme übertragen werden. Hier zeigten REM-Aufnahmen, dass lange Plasmabehandlung von Bulk-Komposit-Filmen zu einer sukzessiven Zerstörung der äußeren Zylinderflächen und letztendlich der gesamten Mesostruktur führt (Abb. 24 F).

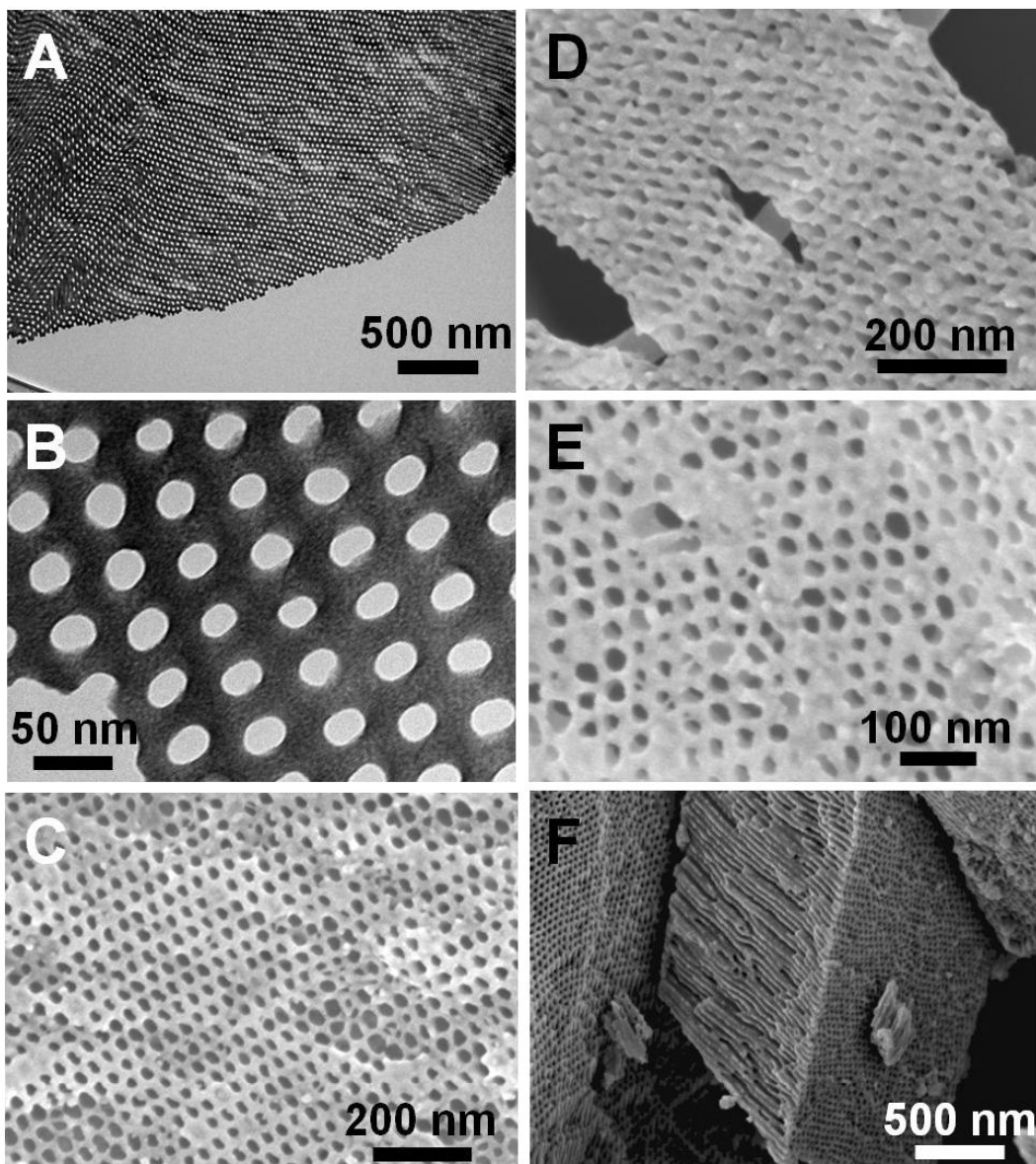


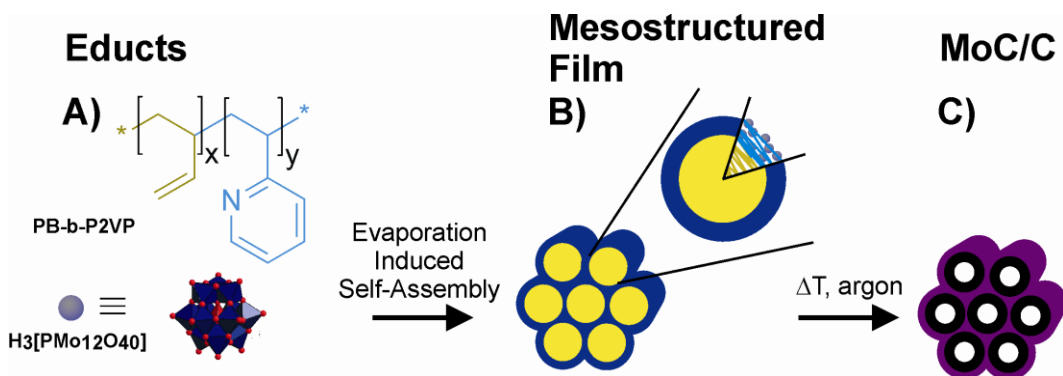
Abb. 24: Elektronenmikroskopische Aufnahmen von H<sub>2</sub>O-Plasma behandelten Proben:  
A) und B) TEM-Aufnahmen und C) – E) REM Aufnahmen dünner Filme bei unterschiedlichen Vergrößerungen. F) Repräsentatives REM-Bild einer Plasma geätzten Bulk Probe.

Zusammenfassend „verklebte“ der *in-situ* gebildete Kohlenstoff die einzelnen Keggin POM Einheiten und verhinderte so zuverlässig den Kollaps der Mesostruktur. Anschließende Calcinierung in oxidativer Atmosphäre führte entweder zur Bildung von ungeordneten, kristallinen Materialien und/ oder hinterließ einen hohen Kohlenstoffanteil im Material. Durch Plasmabehandlung konnte an Ultradünnsschnitten die geordneten Poren unter Strukturerhalt geöffnet werden.

## 6.6 Direkter Zugang zu porösen Molybdänoxycarbiden/ Kohlenstoff Nanokompositen

Weiterhin wurde in Zusammenarbeit mit der Abteilung für Anorganische Chemie des Fritz-Haber-Instituts der Max-Planck-Gesellschaft zu Berlin gezeigt, dass hexagonal geordneten PB-b-P2VP/ Keggin POM-Mesphasen in geordnete Oxycarbid/ Kohlenstoff-Komposite überführt werden können. Diese Kompositmaterialien sind vor allem für Anwendungen wie die der Katalyse oder Ladungsspeicherung in Superkapazitäten interessant.

Ausgehend von invers hexagonal geordneten PB-b-P2VP/ Keggin POM-Mesphasen wurde eine direkte Synthese hin zu Molybdänoxycarbide/ Kohlenstoff-Kompositen entwickelt. Hierzu wurde das vergleichsweise reich an  $sp^2$ -hybridisiertem Kohlenstoff Diblockcopolymer PB-b-P2VP verwendet. Im Gegensatz zu anderen Syntheseprotokollen diente dieses Polymer neben seiner Eigenschaft als strukturdirigierendes Agens auch gleichzeitig als Kohlenstoffquelle für die Carbidisierung, welche durch relativ milde thermische Behandlung in Argonatmosphäre erfolgte (Schema 5).



Schema 5: Skizze des Syntheseweges zu hexagonal geordneten Molybdänoxycarbid/Kohlenstoff-Nanokompositen.

Die generelle Umwandlung der Komposite in geordnete Carbid-Phasen kann mit TEM-Aufnahmen visualisiert werden (Abb. 25). Die hochgeordneten hexagonalen PB-b-P2VP/ Keggin POM Mesophasen (Abb. 25 A) weisen eine hohe Verteilung der Keggin POMs in der P2VP-Matrix auf (Abb. 25 B). Nach thermischer Behandlung in Argonatmosphäre bleibt die geordnete Mesostruktur erhalten. In den Porenwänden bildeten sich 4 nm große Nanopartikel (Abb. 25 C und D). Diese Nanopartikel konnten pulverdiffraktometrisch einer fcc Carbid-Phase ( $\text{MoC}_{1-x}$  oder  $\text{MoO}_x\text{C}_y$ ) zugeordnet werden. (Siehe hierzu auch Abb. 25 F: Der Gitterebenenabstand von 2.4 Å entspricht der (111) Ebene in fcc Carbid-Phasen). Die exakte Phasenzuordnung mittels Elementaranalyse, TGA-MS und HR-TEM ließ einen Schluss auf das Oxycarbid zu. Die dazugehörige HR-TEM Aufnahme (Abb. 26 E) zeigte eine Zickzack-Struktur, die Fehlstellen in der [010] Zonenachse zugeordnet werden kann und typisch für das Molybdänoxycarbid ist.<sup>[110]</sup>

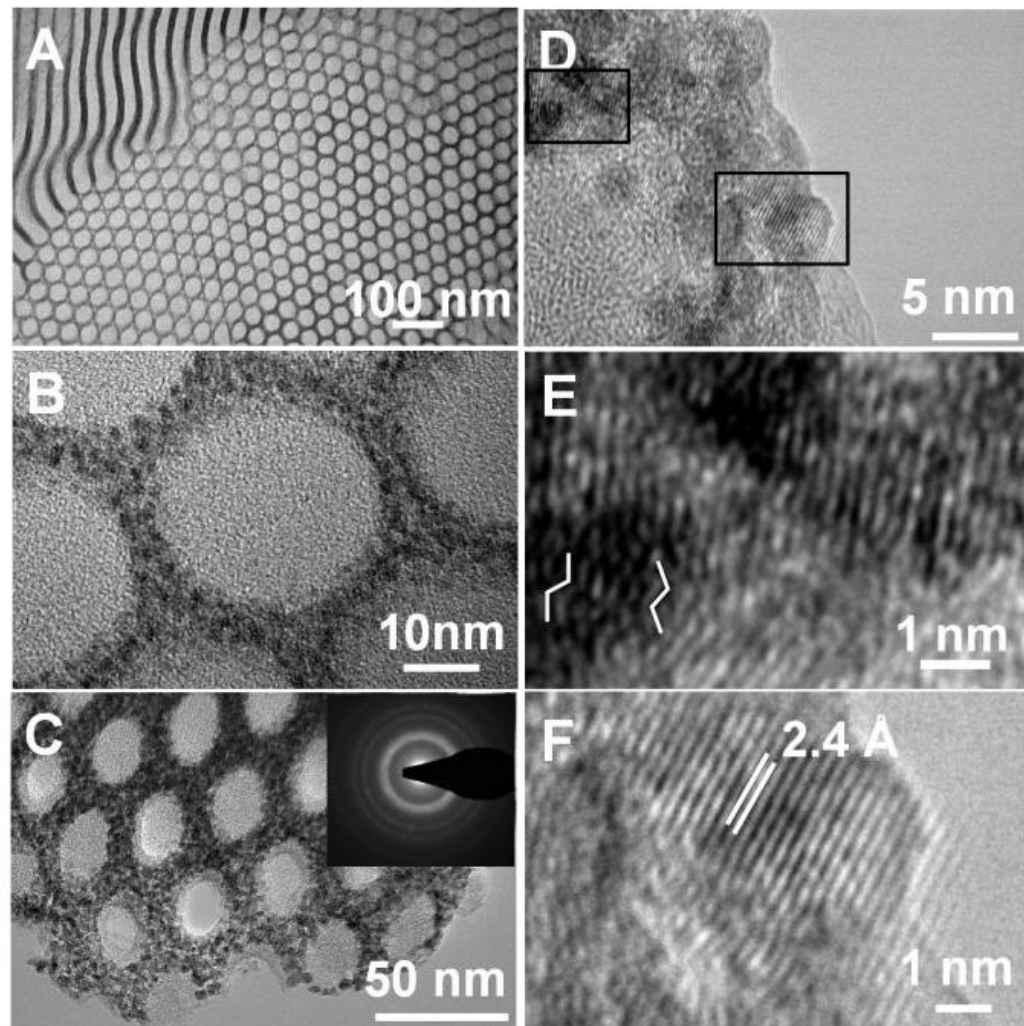


Abb. 25: Repräsentative TEM Aufnahmen des PB-b-P2VP/ Keggin POM Nanokompositen (A und B) und des korrespondierenden Oxycarbid/ Kohlenstoff Materials bei unterschiedlichen Vergrößerungen (C-F).

Weitere physikalische Charakterisierungsmethoden, wie Stickstoff-Physisorptions-experimente (Abb. 25 A) offenbarten eine Typ I Isotherme mit H4 Hysterese. Die spezifische Oberfläche betrug  $133 \text{ m}^2/\text{g}$ . Zusätzliche NLDFT Analyse der Stickstoff-Physisorption Isotherme (Abb. 25 B) zeigte ein mikro- und mesoporöses Material mit einem gesamt Porenvolumen von  $0.085 \text{ cm}^3/\text{g}$  (davon  $0.043 \text{ cm}^3/\text{g}$  rückführbar auf Mikroporen). Eine Raman-Messung offenbarte deutlich die Gegenwart von überschüssigem, amorphem Kohlenstoff (Abb. 25 C), der die Porenwände auskleidet, sie stabilisiert und die Oxycarbide-Nanopartikel einhüllt. Diese Annahme konnte auch durch CO-Chemisorptions-Messungen bestätigt werden (Abb. 27 D). Nach Vorbehandlung der Oxycarbide bei  $450^\circ\text{C}$  bzw.  $600^\circ\text{C}$  konnte eine messbare CO- Aufnahme ( $84 \mu\text{mol/g}$

bzw.  $165 \mu\text{mol/g}$ ) gemessen werden. Hierbei wurde reduktiv Kohlenstoff entfernt und Teile des Oxycarbids in Carbide überführt.

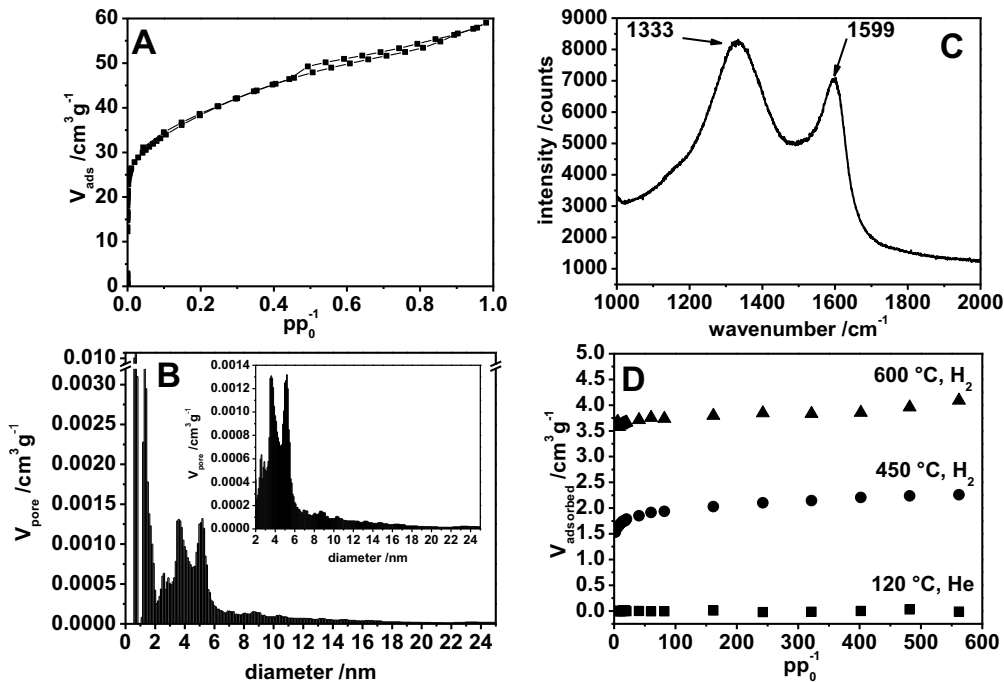


Abb. 26: A) Stickstoff-Physisorptionsisotherme des Oxycarbid/Kohlenstoff Nanokomposit und die dazugehörige NLDFT Analyse (B). (C) Raman-Messung und (D) Chemisorptions-Messungen desselben Komposit für unterschiedliche Vorbehandlungen: Quadrate: He und  $120 \text{ }^\circ\text{C}$ ; Kreise:  $\text{H}_2$  und  $450 \text{ }^\circ\text{C}$ ; Dreiecke:  $\text{H}_2$  und  $600 \text{ }^\circ\text{C}$ .

Die katalytische Aktivität des MoC/C Nanokomposites nach der Aktivierung in  $\text{H}_2$ -Atmosphäre wurde in der Zersetzung von Ammoniak getestet (Abb. 27). Die Auswertung des Arrhenius-Plotes (Abb. 27 B) ergab eine Aktivierungsenergie von 37 kcal/mol.

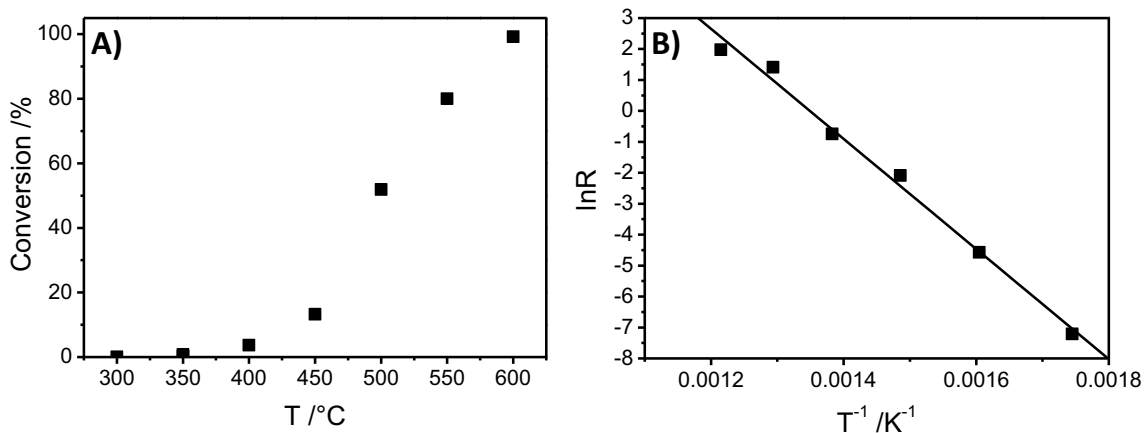


Abb. 27: Zersetzung von Ammoniak über MoC/C Nanokomposite: A) Umsatz-Temperatur-Diagramm und B) der dazugehörige Arrhenius-Plot.

Die vorliegende Arbeit zeigt, dass die hexagonal geordneten PB-b-P2VP/ Keggin POM Nanokomposite direkt und einfach unter Beibehalt der periodischen Struktur in Oxycarbid/ Kohlenstoff Nanokomposite umgewandelt werden können. Aktivierung der katalytisch aktiven Zentren erfolgte über Vorbehandlung in H<sub>2</sub>-Atmosphäre. Neben der gezeigten Katalyse wären solche hierarchisch poröse Materialien auch für Superkapazitoren interessant.



## 7. Ergebnisse

### 7.1 Darstellung des Eigenanteils

Die Ergebnisse, die in dieser Dissertation vorgestellt werden, wurden in Zusammenarbeit mit anderen Kooperationspartnern erhalten und bei den unten aufgeführten Journals eingereicht oder in ihnen veröffentlicht. Nachfolgend wird der Anteil aller Co-Autoren an den unterschiedlichen Veröffentlichungen genau dargelegt.

#### Kapitel 7.2

Diese Arbeit wurde im Journal *Small* unter den Titel

#### **A Facile Polymer Templating Route Toward High Aspect Ratio Crystalline Titania Nanostructures**

von Markus Müllner, Thomas Lunkenbein, Nobuyoshi Miyajima, Josef Breu\* und Axel H. E. Müller\*

angenommen. Die Arbeit wurde in Zusammenarbeit mit dem Lehrstuhl MCII verwirklicht.

Mein Eigenanteil setzte sich aus der Synthese der Rutil Nanokristalle, ihrer Mesostrukturierung und Charakterisierung zusammen. Darüber hinaus führte ich fast alle elektromikroskopischen Untersuchungen durch und war auch an der Diskussion und der Korrektur des Manuskripts beteiligt.

Markus Müllner synthetisierte das Templat, unterstützte bei der Mesostrukturierung, verfasste das Manuskript und stand für wissenschaftliche Diskussionen zur Verfügung.

- Nobuyoshi Miyajima steuerte eine HR-TEM- Aufnahme bei.
- Josef Breu und Axel H. E. Müller standen für Diskussionen und Korrekturen des Manuskripts zur Verfügung

Mein geschätzter Eigenanteil: ca. 50 %.

### Kapitel 7.3

Diese Arbeit wurde in der *Zeitschrift für Physikalische Chemie* unter den Titel

#### **Packing of Cylindrical Keggin-Type Polyoxometalate Hybrid Micelles as a Function of Aspect Ratio**

von Thomas Lunkenbein, Martin Schieder, Carina Bojer, Axel H. E. Müller und Josef Breu\*

eingereicht.

Ich führte die Synthese und Charakterisierung des Templates und des Hybridmaterials durch. Des Weiteren verfasste ich das Manuskript.

Ferner:

- Martin Schieder half bei Korrekturen und wissenschaftlichen Diskussionen
- Carina Bojer führte als studentische Hilfskraft unter meiner Aufsicht Experimente durch
- Axel H. E. Müller steuerte die Monomere und das Equipment zur Herstellung des Templates bei.
- Josef Breu war involviert in wissenschaftlichen Diskussionen und der Korrekturen des Manuskripts.

Mein Eigenanteil war ca. 85 %.

### Kapitel 7.4

Das Maunskript wurde in Zusammenarbeit mit dem Fritz-Haber-Institut der Max-Planck-Gesellschaft zu Berlin verfasst und wird in *Langmuir* unter dem Titel

#### **High Surface Area Keggin-Type Polyoxometalate Nanorods and their Catalytic Performance in the Isopropanol Decomposition**

von Thomas Lunkenbein, Klaus Friedel-Ortega, Ram Sai Yelamanchili, Annette Trunschke, Robert Schlögl, Josef Breu\*

eingereicht werden.

Ich synthetisierte und charakterisierte das Templat und das Hybridmaterials und führte Katalyseexperimente durch. Des Weiteren verfasste ich das Manuskript und stand für wissenschaftliche Diskussionen zur Verfügung.

Ferner:

- Klaus Friedel-Ortega wies mich in die Katalyseapparatur ein und führte einige Experimente selbst durch. Er stand für wissenschaftliche Diskussionen zur Verfügung.
- Ram Sai Yelamanchili führte Vorexperimente durch
- Annette Trunschke, Robert Schlögl und Josef Breu standen für wissenschaftliche Diskussionen zur Verfügung und beteiligten sich an der Korrektur des Manuskripts.

Mein Eigenanteil war ca. 75 %.

## Kapitel 7.5

Die Arbeit wurde im *Journal of the American Chemical Society* unter den Titel

### **Direct Synthesis of Inverse Hexagonally Ordered Diblock Copolymer/Polyoxometalate Nanocomposite Films**

von Thomas Lunkenbein, Marleen Kamperman,\* Zihui Li, Hiroaki Sai, Carina Bojer, Markus Drechsler, Stephan Förster, Ulrich Wiesner, Axel H.E. Müller, und Josef Breu\* eingereicht.

Ich koordinierte, entwickelte und führte sämtliche Experimente zur Herstellung und Charakterisierung des Hybridmateriale durch. Darüber hinaus verfasste ich das Manuskript und stand für wissenschaftliche Diskussionen zur Verfügung.

Ferner:

- Zihui Li und Hiroaki Sai führten die SAXS- Messungen durch.
- Carina Bojer führte als studentische Hilfskraft unter meiner Aufsicht Experimente durch.
- Markus Drechsler führte die cryo-TEM Messungen durch.
- Stephan Förster fittete die SAXS-Kurven und stand für wissenschaftliche Diskussionen zur Verfügung.
- Marleen Kamperman, Axel H. E. Müller, Ulrich Wiesner und Josef Breu unterstützten mit wissenschaftlichen Diskussionen und Korrekturen des Manuskripts.

Mein Eigenanteil belief sich auf ca. 80 %.

## Kapitel 7.6

Diese Arbeit wurde für *Chemistry an Asian Journal* unter dem Titel

### **Towards Mesoporous Keggin-Type Polyoxometalate –Systematic Removal of Organic Templates**

von Thomas Lunkenbein, Marleen Kamperman, Martin Schieder, Sebastian With, Zihui Li, Stephan Förster, Ulrich Wiesner und Josef Breu\*

vorbereitet.

Ich habe die Experimente durchgeführt, das Manuskript geschrieben und stand für wissenschaftliche Diskussionen zur Verfügung.

Ferner:

- Martin Schieder, damals Praktikant, führte unter meiner Anweisung Experimente durch.
- Sebastian With und Zihui Li trugen die SAXS- Messungen bei.
- Marleen Kamperman, Stephan Förster, Ulrich Wiesner und Josef Breu halfen mit wissenschaftlichen Diskussionen und Korrekturen des Manuskripts.

Mein Eigenanteil betrug ca. 80 %.

## Kapitel 7.7

Diese Arbeit wird unter den Titel

### **Direct Access to Ordered Porous Molybdenum Oxycarbide/Carbon Nanocomposites**

von Thomas Lunkenbein, Dirk Rosenthal, Torsten Otremba, Zihui Li, Hiroaki Sai, Carina Bojer, Ulrich Wiesner, Annette Trunschke, Robert Schlögl und Josef Breu\*

in *Angewandte Chemie- International Edition* eingereicht.

Ich führte die Experimente und Charakterisierung durch, schrieb das Manuskript und beteiligte mich an wissenschaftlichen Diskussionen.

Ferner:

- Dirk Rosenthal führte die CO-Chemisorptionsmessungen durch und beteiligte sich an der Korrektur des Manuskriptes.
- Torsten Otremba führte die katalytische Zersetzung von Ammoniak durch.
- Zihui Li und Hiroaki Sai waren für die SAXS-Messungen verantwortlich.
- Carina Bojer, eine studentische Hilfskraft, führte unter meiner Aufsicht Experimente durch.
- Ulrich Wiesner, Annette Trunschke, Robert Schlögl und Josef Breu unterstützten mit wissenschaftlichen Diskussionen und Korrekturen des Manuskripts.

Mein Eigenanteil lag bei ca. 75 %.



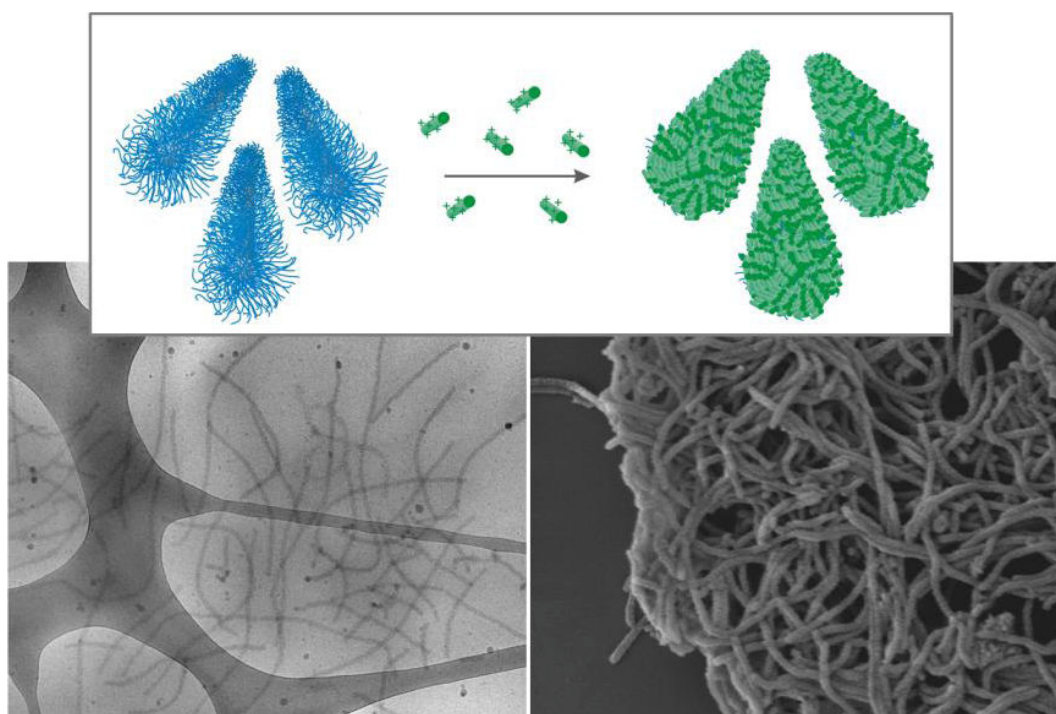
## 7.2 A Facile Polymer Templating Route Toward High Aspect Ratio Crystalline Titania Nanostructures

Markus Müllner,<sup>1</sup> Thomas Lunkenbein,<sup>2</sup> Nobuyoshi Miyajima,<sup>3</sup> Josef Breu<sup>2,\*</sup> and Axel H. E. Müller<sup>1,\*</sup>

<sup>1</sup>Lehrstuhl für Makromolekulare Chemie II, Universität Bayreuth, 95440 Bayreuth, Germany

<sup>2</sup>Lehrstuhl für Anorganische Chemie I, Universität Bayreuth, 95440 Bayreuth, Germany

<sup>3</sup>Bayerisches Geoinstitut, Universität Bayreuth, 95440 Bayreuth, Germany



### Abstract

High aspect ratio rutile and anatase hybrid nanowires are produced *via* a template-directed process using a novel cylindrical polyelectrolyte brush template. Loading the highly negatively charged 1D templates with pre-synthesized TiO<sub>2</sub> nanocrystals, results in the fabrication of soluble crystalline TiO<sub>2</sub> hybrid nanowire.

**Keywords.** block copolymer, cylindrical polymer brush, templating, hybrid nanostructures, titania

## Introduction.

There has been a growing interest in the manipulation of the architecture of materials, which is motivated by application-based objectives in various research areas covering chemistry, biology, physics and materials science. Nanomaterials are promising candidates for solving major problems of nowadays society, such as sustainable energy,<sup>[1]</sup> information storage,<sup>[2]</sup> water treatment,<sup>[3]</sup> etc. Especially one-dimensional (1D) nanostructures of metal oxides, like nanowires or nanotubes, have been under close investigation due to their size-dependent optical and electronical properties, which allow them to be used in catalysis, separation, or photovoltaic applications.<sup>[4]</sup> Among the many metal oxides used in these fields are the polymorphs of titania ( $\text{TiO}_2$ ).  $\text{TiO}_2$  is a semiconductor and well-known for its applications in the field of photocatalysis and photo-electrochemistry due to its excellent optical transmittance and high refractive index.<sup>[1a, 5]</sup> Crystalline titania (in its anatase and rutile polymorphs) is of considerable interest as it finds further use in sensors and dye-sensitized solar cells.<sup>[6]</sup> Each polymorph of  $\text{TiO}_2$  has different physical properties and, consequently, the ability to control its crystal structure is of great interest.<sup>[7]</sup>

Several strategies for achieving 1D inorganic nanomaterials have been reported ranging from hydrothermal growth<sup>[8]</sup> and electrospinning<sup>[9]</sup> to template chemistry.<sup>[4a, 10]</sup> Well-defined templates, in particular, allow the fabrication of tailor-made materials with specific shapes and structural properties.<sup>[10a, 10b, 11]</sup> An important class of organic templates derives from 1D organic structures, in particular cylindrical polymer brushes (CPBs).<sup>[10c, 12]</sup> CPBs refer to both molecular brushes (having a single macromolecule as backbone) and brushes obtained from block copolymers. Molecular CPBs are synthesized via grafting approaches<sup>[13]</sup> and give 1D nanoobjects with very uniform length and diameter, which have been used as templates for the synthesis of various 1D hybrid materials, such as  $\text{CdS}$ ,<sup>[14]</sup>  $\text{CdSe}$ ,<sup>[15]</sup>  $\text{Fe}_2\text{O}_3$ ,<sup>[14, 16]</sup>  $\text{SiO}_2$ <sup>[17]</sup> nanowires and nanotubes.<sup>[18]</sup> However, when ionic side-chains of a molecular CPB interact with oppositely charged multivalent ions or colloids they are prone to collapse.<sup>[19]</sup> Earlier attempts to synthesize  $\text{TiO}_2$  nanowires based on the interaction of poly(2-hydroxyethyl methacrylate) brushes with  $\text{Ti(OBu)}_4$  led to amorphous material only.<sup>[20]</sup> As an alternative to the rather complex molecular brush synthesis and behavior, crosslinking cylindrical bulk morphologies of block copolymers can be applied to form 1D templates with a rigid core.<sup>[12b, 21]</sup> Organic-inorganic 1D hybrid nanomaterials obtained from CPB

templates show many advantages with respect to colloidal stability, functionality, flexibility, and producibility.<sup>[10c]</sup>

The hybrid formation can occur via two possible ways; the in-situ formation of inorganic material from soluble molecular precursors within the template<sup>[15]</sup> or the infiltration of pre-synthesized inorganic nanoparticles (colloidal route).<sup>[22]</sup> In-situ generation of nanoparticles within a 1D template may lead to insufficient or inhomogeneous filling of the template or poor control of nanoparticle size,<sup>[15]</sup> whereas pre-synthesized nanoparticles can be more easily characterized and homogenously infiltrated leading to better defined hybrid nanostructures.<sup>[13, 16]</sup>

Within this context, extensive efforts have been devoted to obtain highly crystalline hybrid nanomaterials, as they bear superior properties when compared to amorphous or low crystalline hybrids.<sup>[23]</sup> However, as-made hybrid materials of TiO<sub>2</sub> are often amorphous and additional high temperature treatment is required to obtain highly crystalline materials<sup>[20, 24]</sup> which again bears the risk of losing solubility and the hybrid morphology.<sup>[23b]</sup>

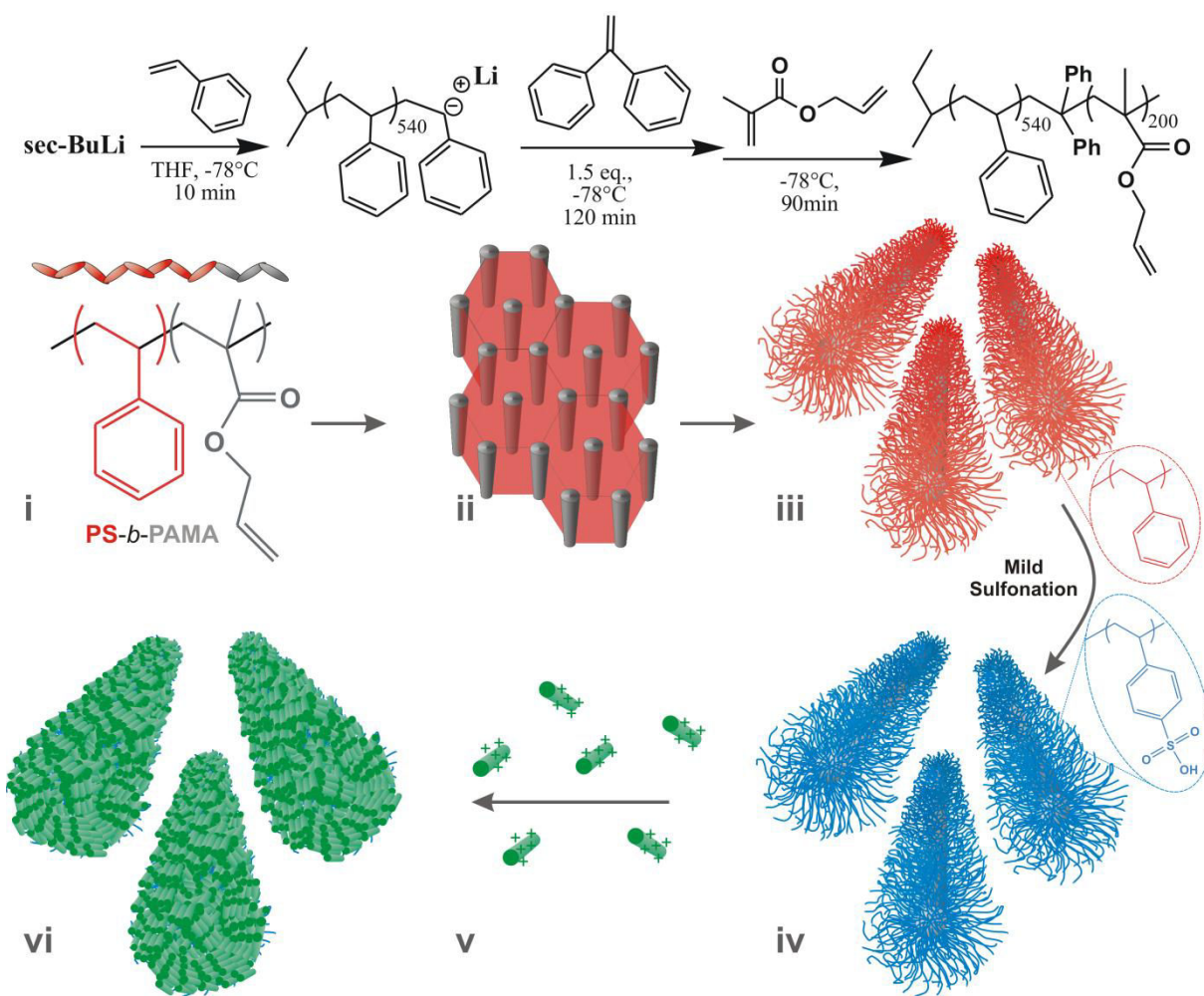
Herein, we demonstrate a novel synthesis concept that can be applied for structuring metal oxides, which we apply to the synthesis of rutile and anatase nanowires with high aspect ratio. To the best of our knowledge, this is the first report on a rigid, water-soluble 1D template that is strongly negatively charged at very low pH. By mildly sulfonating cylindrical polyelectrolyte brushes, obtained from the bulk morphology of polystyrene-*block*-poly(allyl methacrylate) block copolymers, very long and robust organic templates can be produced for the fabrication of anisotropic TiO<sub>2</sub> nanostructures. The phase-pure crystallinity of TiO<sub>2</sub> is adjusted prior to the hybrid formation during production of positively charged colloidal nanocrystals in an aqueous and mild approach. In turn, the hybrid nanostructures are soluble, highly crystalline and produced at low temperatures (60 °C). Additionally, they can serve as precursors for the pyrolytic formation of purely inorganic nanowires. With the presented system, it is possible to realize nanoscale structuring of metal oxides in a facile manner.

## Results and Discussion

### Synthesis of the 1D template brush

Poly(allyl methacrylate) (AMA) was chosen for the crosslinkable and cylinder-forming block, as it is reported that the allyl group undergoes crosslinking in the presence of radicals.<sup>[25]</sup> Using sequential anionic polymerization, we obtained a well-defined diblock copolymer polystyrene-*block*-poly(allyl methacrylate) (PS-*b*-PAMA). For details see supporting Information, S1-S4. <sup>1</sup>H-NMR, showed the absence of crosslinking (Figure S2). The composition of the diblock copolymer, as determined by a combination of size exclusion chromatography and <sup>1</sup>H-NMR, is PS<sub>69</sub>PAMA<sub>31</sub><sup>81</sup>, (subscripts are the weight fractions and the superscript refers to the total number-average molecular weight, M<sub>n</sub>, of 81 kg·mol<sup>-1</sup>) with a polydispersity index of 1.06 (Figure S1). The film casting of PS<sub>69</sub>PAMA<sub>31</sub><sup>81</sup> from toluene resulted in hexagonally packed cylinders of PAMA segments in a PS matrix (see transmission electron microscopy (TEM) images in Figure S3). The diameter of the PAMA cylinders was 22 ± 2 nm, as determined by TEM measurements. The cylindrical morphology was preserved by co-casting 10 wt% of a photoinitiator and crosslinking of the allyl groups by irradiation of the polymer film with UV light for four hours.

After crosslinking, the polymer film was re-dispersed in THF to obtain single cylindrical polymer brushes with a PS corona (see Scheme 1,iii). The diameter of the dispersed cylinders was 60-65 nm in the dry state (measured by TEM). The lengths of the cylinders varied from only 200 nm up to 5 μm. The wide length distribution results from the domain size distribution of the cast bulk film. The very long cylinders can be shortened by sonication but we chose not to modify them.



**Scheme 1.** Top: sequential anionic polymerization of polystyrene-*b*-block-poly(allyl methacrylate) (PS-*b*-PAMA). Below: PS-*b*-PAMA (**i**) microphase-separates into (**ii**) hexagonally packed cylinders. (**iii**) The UV-crosslinked cylindrical polymer brushes with PAMA core and PS corona are redispersed and (**iv**) sulfonated into cylindrical polyelectrolyte brushes with a poly(styrenesulfonic acid) corona. (**v**) Positively charged and pre-synthesized titania nanocrystals are then infiltrated to produce (**vi**) anisotropic metal oxide -polymer brush hybrid nanowires.

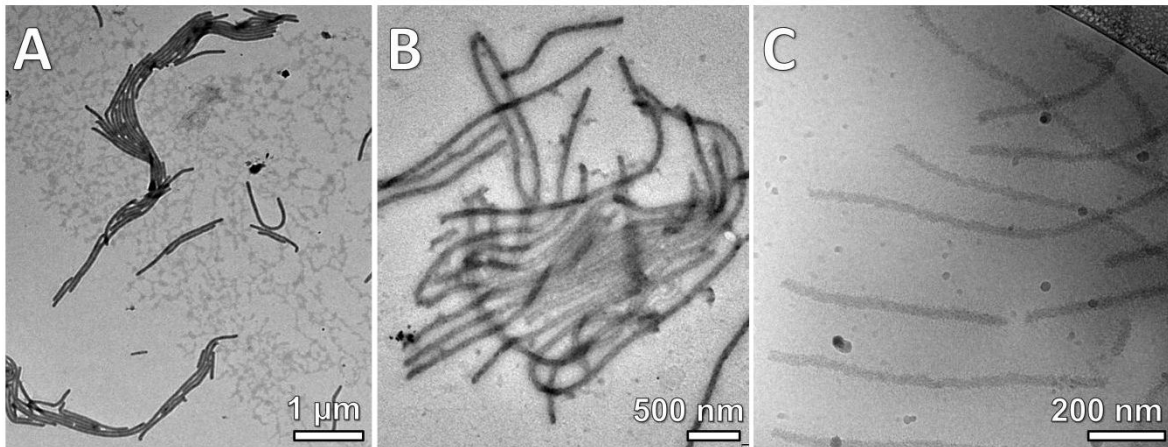


**Figure 1.** TEM micrographs of core-crosslinked cylindrical polymer brushes and their sulfonated analogues: **(A)** RuO<sub>4</sub>-stained PS-*b*-PAMA (from THF) and **(B)** PSS-*b*-PAMA (from water). **(C)** Cryo-TEM micrograph of PSS-*b*-PAMA in water.

Next, the PS corona was sulfonated to poly(styrenesulfonic acid) (PSS), which is a strong anionic polyelectrolyte (Scheme 1, iv). Mild sulfonation with acetyl sulfonate<sup>[26]</sup> in dichloroethane led to a degree of sulfonation of 81 % and hence the transformation of most of the PS corona into PSS. After sulfonation, the crosslinked core remained around 25 nm in diameter (see dark cylinders in Figure 1C). From the distance of cylinders in cryogenic TEM (cryo-TEM; Figure 1C), the length of the PSS side-chains is estimated to be below 100 nm. The PSS side chains consist of 540 monomer units, which leads to a contour length of 135 nm (0.25 nm per monomer unit). The actual length of the polyelectrolyte chains in water is assumed to be quite stretched due to the high charge density and the resulting high osmotic pressure of the dissociated protons. However, it is known that polyelectrolyte chains in aqueous solution are rarely fully extended.<sup>[27]</sup> The PSS grafts allow excellent dispersion of the polymer brushes in water and guarantee a high and satisfactory amount of negative charges even at low pH values for the infiltration of positively charged TiO<sub>2</sub> nanocrystals.

Note that the block copolymer polystyrene-*b*-polybutadiene, which also produces PS cylinders but with a polybutadiene core, did not survive the mild sulfonation conditions. This phenomenon highlights the superior properties of the PS-*b*-PAMA block copolymer template.

### Synthesis of crystalline TiO<sub>2</sub> nanocolloids

As for the crystals, both the size and the chemical nature of the surface of the colloid are essential. Therefore, we have developed a modified low-temperature, non-hydrothermal synthesis route for both colloidal rutile and anatase which are only electrostatically stabilized.<sup>[22]</sup> The titania nanocrystals were synthesized using acidic water as the reaction medium and titanium tetra(*n*-butoxide) as the precursor. Under these conditions, well-defined nanocrystals were obtained under very mild conditions at 60 °C in two hours. The apparent hydrodynamic diameter was ~8 nm for the rutile nanocrystals (Figure 2C) and ~14 nm for the anatase ones (Figure S6E). Cryo-TEM images (Figures 2A, B) verify the presence of pre-synthesized rutile nanocrystals in water. While the original precursor dispersions were stable, some agglomeration of the nanocrystals occurred due to decreased electrostatic repulsion upon transfer and dilution for the dynamic light scattering (DLS) measurement (see white circle, Figure 2B). However, the intensity-weighted hydrodynamic diameter distribution in Figure 2C (solid line) overemphasizes the few larger agglomerates. The phase purity of the nanocrystals was confirmed by powder X-ray diffraction (PXRD) (see Figure 3A for rutile and Figure S6D for anatase).

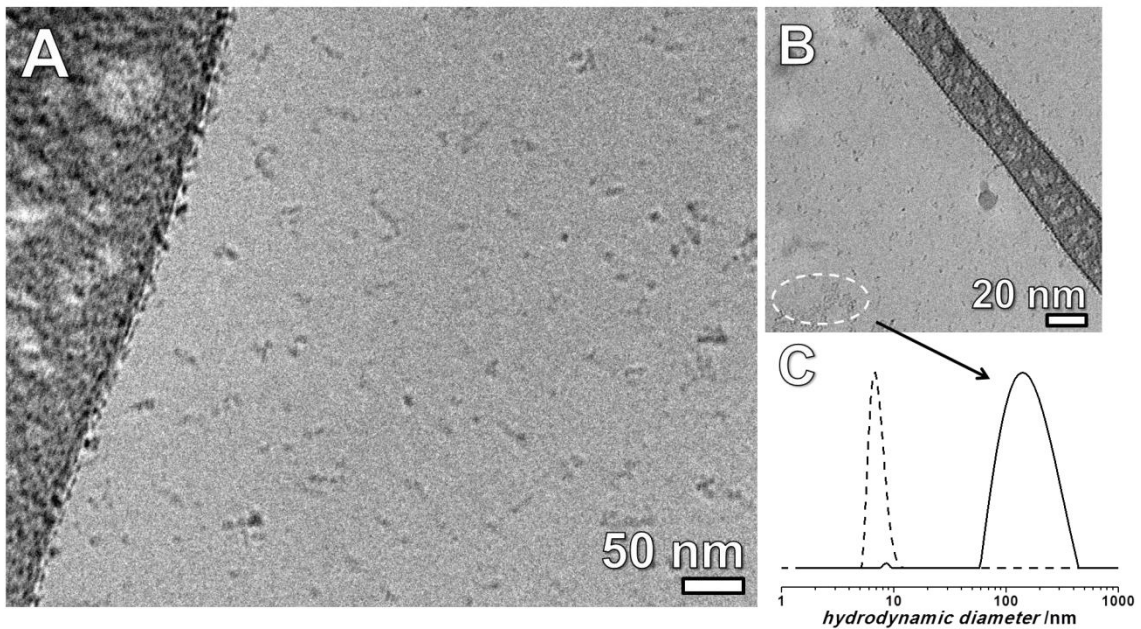


**Figure 2. (A, B)** Cryo-TEM micrograph of rutile nanocrystals in water. They can be found aligned at the edge of the lacey grid. **(C)** Hydrodynamic diameter distribution (from DLS) of rutile nanocrystals in acidic water: number-weighted plot (dashed line) and intensity-weighted plot (solid line). Large hydrodynamic diameters derive from the agglomeration of nanocrystals, as can be seen in **(B)** (white circle).

#### Synthesis of crystalline 1D TiO<sub>2</sub> hybrid nanowires

It is well known that the surface potential of oxides critically depends on pH.<sup>[28]</sup> Freshly prepared colloidal suspensions of rutile or anatase nanocrystal precursors were used for the TiO<sub>2</sub> hybrid nanowire synthesis. Since titania is quite acidic with a point of zero charge below 5, rutile and anatase only possess a positively charged surface at very low pH values.<sup>[22, 28]</sup> Contrary to other polyelectrolytes, like poly(meth)acrylic acid, our PSS template still bears a significant negative charge at very low pH values. The resulting strong Coulomb interactions with the PSS polyanions control the supramolecular assembly of the nanocrystals into the corona of the template brushes, leading to crystalline organic-inorganic TiO<sub>2</sub> nanowires. Figure 3A shows the PXRD pattern of the as-synthesized rutile composite (top curve). The polymeric template itself is amorphous and only contributes to the background in the PXRD. Therefore, it was subtracted from the PXRD trace. The rutile reflexes seen in the PXRD of the precursors reappear in the pattern of the hybrid material. The same can be found when anatase colloids were used

instead of rutile. The corresponding hybrid material exhibits the anatase crystal structure as it was pre-determined by the colloids (Figure S6). Thus, the intercalation of the crystalline  $\text{TiO}_2$  colloids into the brush template led to the successful fabrication of soluble hybrid materials with a pre-determined shape, size and crystallinity. The full width of half maximum (FWHM) of the rather broad reflexes in the powder diffraction translate to rather small crystal sizes of infiltrated nanocrystals, as verified by DLS (see precursor hydrodynamic diameter distribution in Figure 2C (rutile) and Figure S6E (anatase)).

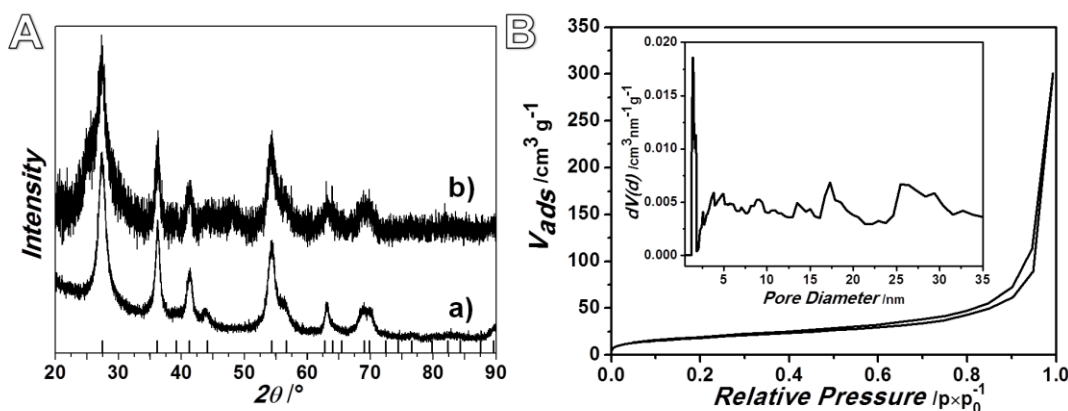


**Figure 3.** **(A)** Powder XRD patterns of **a)** as-synthesized rutile precursor (bottom curve) and **b)** as-synthesized rutile hybrid material (top curve). The ticks on the x-axis indicate expected rutile reflexes. **(B)**  $N_2$ -sorption isotherms of as-synthesized rutile nanowires, including pore diameter distribution.

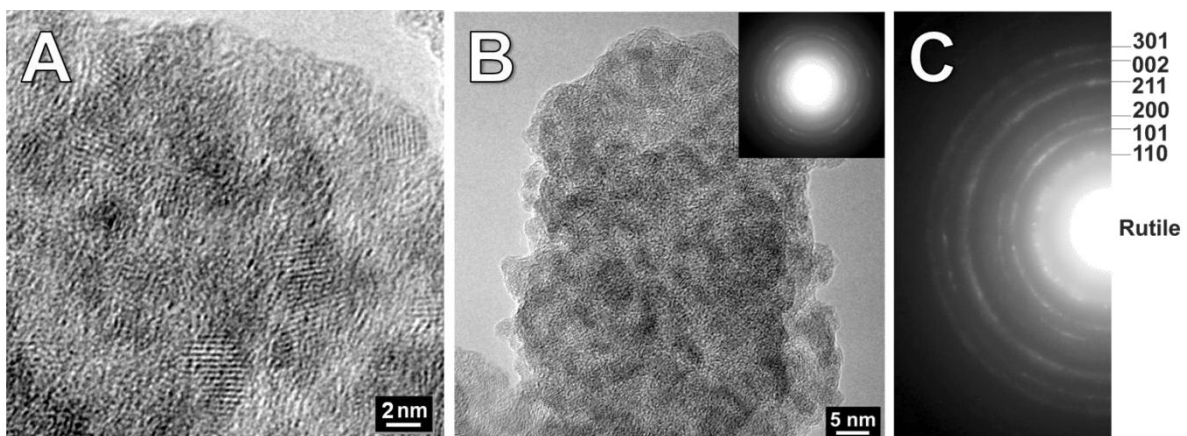


**Figure 4.** **(A, B)** High-ResolutionTEM micrographs of as-synthesized rutile nanostructures and **(C)** the corresponding SAED indexing and verification of rutile crystal structure.

To verify the PXRD pattern and to further underline the crystallinity of the hybrid nanowires, we performed high resolution TEM (HR-TEM) measurements. The HR-TEM micrographs clearly indicate that the inorganic part of the hybrid material is built up through the embedment of crystalline colloids. SAED indexing verified that the embedded colloids exhibit rutile crystal structure (Figure 4).

Both TEM (Figure 5A–C) and scanning electron microscopy (SEM) images (Figure 5D–F) are in line with the proposed mechanism of the hybrid formation. The diameter of the composite nanowires was around 55 nm. This means that the polyelectrolyte corona contracts during the infiltration step due to electrostatic interaction between the polyanion and the positively charged nanocolloids; similar to an interpolyelectrolyte complex (IPEC) formation.<sup>[29]</sup> In contrast to molecular brushes, it does not collapse. High aspect ratio nanostructured rutile and anatase hybrid materials, which are soluble in polar solvents and water, were produced by this infiltration method (Figure 5 and Figure S6). The hybrid nanowires survive harsh ultrasound without fracturing and do not fall apart in salt or at higher pH. The well-dispersed nanowires form non-woven spaghetti-like networks upon drying. Due to the anisotropic shape, the dry composite material provides both a highly porous mesostructure in combination with a comparatively large surface area. The surface area of the dried rutile hybrid material was  $66 \text{ m}^2 \cdot \text{g}^{-1}$ , as determined by Brunauer-Emmett-Teller (BET) analysis of  $\text{N}_2$ -sorption isotherms (Figure 3B). Although thermogravimetric analysis (TGA) determines a weight

content of  $\text{TiO}_2$  of around 50 % (Figure S5) the hybrid material remains highly flexible. The remaining 50% organic material provides a certain ductility to the hybrid.

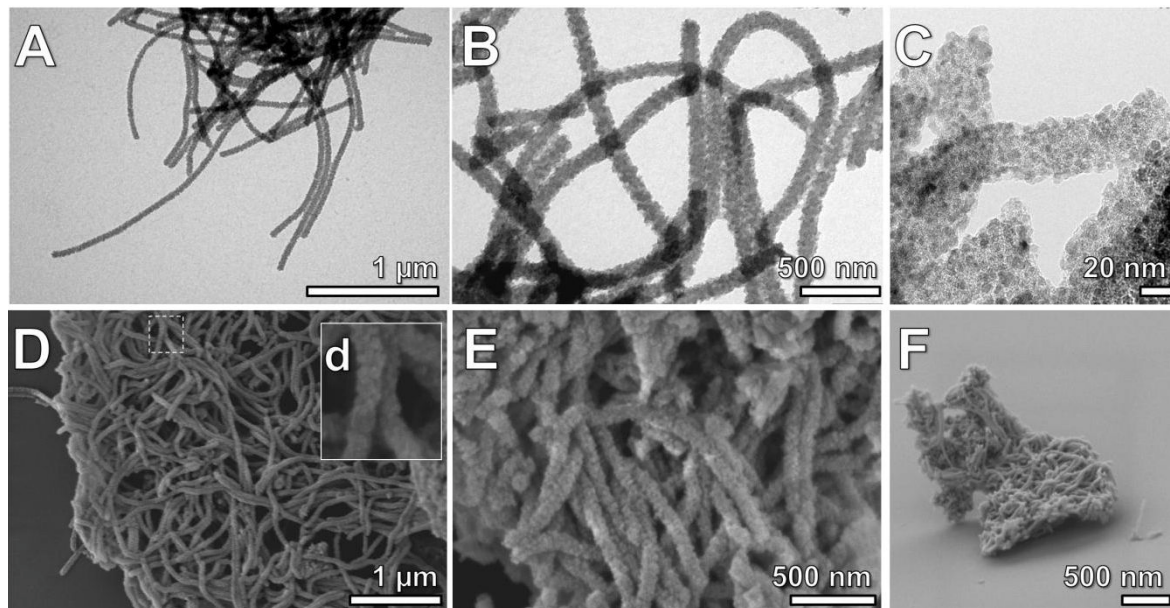


**Figure 5.** (A-C) TEM micrographs of as-synthesized anisotropic rutile nanostructures, (D) SEM micrographs of as-synthesized rutile nanowires, and (E, F) calcined rutile nanowires on a tilted sample stage ( $75^\circ$  viewing angle).

After step-wise calcination, first in argon atmosphere and then in air, all polymeric material was destroyed but the cylindrical shape of the former hybrid material was preserved (Figure 5E, F).

### Conclusion

In conclusion, our mild, template-directed approach produces soluble 1D crystalline  $\text{TiO}_2$  nanowires with high aspect ratio and high surface area at rather low temperatures. The nanowires disperse well in polar solvents and arrange into porous non-woven mesostructures with high surface area upon drying, which keep their shape after calcination. Hence, deposition of single  $\text{TiO}_2$  nanowires onto substrates or producing well-defined layers is easy. This particular material may give rise to various applications, such as catalytically active filter systems, energy storage devices, or in particular in photovoltaics, as anatase finds wide-spread use in dye-sensitized solar cells.<sup>[30]</sup> Insufficient contacts between  $\text{TiO}_2$  particles in photovoltaic devices still limit the

electron transport and hence lower the efficiency of solar cells. On the basis of that fact, we assume that our materials, with their increased aspect ratios and networks structures, might introduce additional electron pathways, when compared to the corresponding spherical materials.

Our novel cylindrical template with PAMA core and PSS corona is unique in two ways: (i) it is water-soluble and negatively charged over the full pH range, and (ii) due to the crosslinked PAMA core it is rigid enough to prevent collapse upon interaction with the titania nanocrystals.

We are convinced that our colloidal route can be generally used to produce many other anisotropic metal oxide hybrids of any known and desired polymorphic crystal structure, as the only prerequisite is the availability of small and positively charged nanocrystals, where the pH of hybrid formation may be freely adjusted to the particular metal oxide of arbitrary point of zero charge.<sup>[28]</sup>

**Acknowledgment:** This work was funded by the Collaborative Research Center (SFB) 840 within project A7. M. M. and T. L. contributed equally to this work and acknowledge BayEFG for a scholarship and the international graduate school of the ENB "Structures, Reactivity and Properties of Metal Oxides" for a fellowship, respectively.

**Supporting Information** is available on the WWW under <http://www.small-journal.com> or from the author.

## References

- [1] a) M. Grätzel, *Nature* **2001**, *414*, 338; b) B. O'Regan, M. Grätzel, *Nature* **1991**, *353*, 737; c) A. S. Arico, P. Bruce, B. Scrosati, J.-M. Tarascon, W. van Schalkwijk, *Nat. Mater.* **2005**, *4*, 366.
- [2] a) G. S. D. Beach, C. Nistor, C. Knutson, M. Tsoi, J. L. Erskine, *Nat. Mater.* **2005**, *4*, 741; b) S. S. P. Parkin, M. Hayashi, L. Thomas, *Science* **2008**, *320*, 190.
- [3] a) Q. Li, S. Mahendra, D. Y. Lyon, L. Brunet, M. V. Liga, D. Li, P. J. J. Alvarez, *Water Res.* **2008**, *42*, 4591; b) J.-Y. Bottero, J. Rose, M. R. Wiesner, *Integr. Environ. Assess. Manage.* **2006**, *2*, 391.
- [4] a) Y. Xia, P. Yang, Y. Sun, Y. Wu, B. Mayers, B. Gates, Y. Yin, F. Kim, H. Yan, *Adv. Mater.* **2003**, *15*, 353; b) J. Weber, R. Singhal, S. Zekri, A. Kumar, *Inter. Mater. Rev.* **2008**, *53*, 235.

- [5] X. Chen, S. S. Mao, *Chem. Rev.* **2007**, *107*, 2891.
- [6] a) N. Bahadur, K. Jain, R. Pasricha, Govind, S. Chand, *Sensor Actuat- B: Chem.* **2010**, *159*, 112; b) L. F. O. Furtado, A. D. P. Alexiou, L. Gonçalves, H. E. Toma, K. Araki, *Angew. Chem. Int. Ed.* **2006**, *45*, 3143; c) C. S. Karthikeyan, M. Thelakkat, *Inorg. Chim. Acta* **2008**, *361*, 635; d) J. C. Brendel, Y. Lu, M. Thelakkat, *J. Mater. Chem.* **2010**, *20*, 7255.
- [7] a) J. Y. Ying, C. P. Mehnert, M. S. Wong, *Angew. Chem. Int. Ed.* **1999**, *38*, 56; b) D. V. Bavykin, J. M. Friedrich, F. C. Walsh, *Adv. Mater.* **2006**, *18*, 2807.
- [8] a) X. Wang, Y. Li, *J. Am. Chem. Soc.* **2002**, *124*, 2880; b) X. Jiaqiang, C. Yuping, C. Daoyong, S. Jianian, *Sens. Actuat. B: Chem.* **2006**, *113*, 526; c) G. Shen, P.-C. Chen, K. Ryu, C. Zhou, *J. Mater. Chem.* **2009**, *19*, 828.
- [9] a) P. Viswanathamurthi, N. Bhattacharai, H. Y. Kim, D. R. Lee, *Nanotechnology* **2004**, *15*, 320; b) D. Li, Y. Xia, *Nano Lett.* **2003**, *3*, 555; c) H. Dong, D. Wang, G. Sun, J. P. Hinestroza, *Chem. Mater.* **2008**, *20*, 6627.
- [10] a) H.-W. Liang, S. Liu, S.-H. Yu, *Adv. Mater.* **2010**, *22*, 3925; b) J. Yuan, A. Walther, A. H. E. Müller, *Phys. Stat. Sol. B* **2010**, *247*, 2436; c) J. Yuan, A. H. E. Müller, *Polymer* **2010**, *51*, 4015.
- [11] a) P. S. Chinthamanipeta, Q. Lou, D. A. Shipp, *ACS Nano* **2011**, *5*, 450; b) I. Botiz, S. B. Darling, *Mater. Today* **2010**, *13*, 42.
- [12] a) M. Antonietti, S. Förtser, *Top. Curr. Chem.* **2003**, *266*, 1; b) R. S. Yelamanchili, A. Walther, A. H. E. Müller, J. Breu, *Chem. Commun.* **2008**, 489; c) F. H. Schacher, T. Rudolph, M. Drechsler, A. H. E. Müller, *Nanoscale* **2010**, *3*, 288.
- [13] M. Zhang, A. H. E. Müller, *J. Polym. Sci. Part A: Polym. Chem.* **2005**, *43*, 3461.
- [14] M. Zhang, M. Drechsler, A. H. E. Müller, *Chem. Mater.* **2004**, *16*, 537.
- [15] J. Yuan, M. Drechsler, Y. Xu, M. Zhang, A. H. E. Müller, *Polymer* **2008**, *49*, 1547.
- [16] Y. Xu, J. Yuan, B. Fang, M. Drechsler, M. Müllner, S. Bolisetty, M. Ballauff, A. H. E. Müller, *Adv. Funct. Mater.* **2010**, *20*, 4182.
- [17] a) J. Yuan, Y. Xu, A. Walther, S. Bolisetty, M. Schumacher, H. Schmalz, M. Ballauff, A. H. E. Müller, *Nat. Mater.* **2008**, *7*, 718; b) Y. Xu, J. Yuan, A. H. E. Müller, *Polymer* **2009**, *50*, 5933.

- [18] M. Müllner, J. Yuan, S. Weiß, A. Walther, M. Förtsch, M. Drechsler, A. H. E. Müller, *J. Am. Chem. Soc.* **2010**, *132*, 16587.
- [19] a) L-T. Yan, Y. Xu, M. Ballauff, A. H. E. Müller, A. Böker, *J. Phys. Chem. B* **2009**, *113*, 5104; b) Y. Xu, S. Bolisetty, M. Drechsler, B. Fang, J. Yuan, L. Harnau, M. Ballauff, A. H. E. Müller, *Soft Matter* **2009**, *5*, 379.
- [20] J. Yuan, Y. Lu, F. Schacher, T. Lunkenbein, S. Weiss, H. Schmalz, A. H. E. Müller, *Chem. Mater.* **2009**, *21*, 4146.
- [21] a) X. Yan, G. Liu, F. Liu, B. Z. Tang, H. Peng, A. B. Pakhomov, C. Y. Wong, *Angew. Chem. Int. Ed.* **2001**, *40*, 3593; b) Q. Lou, P. S. Chinthamani, D. A. Shipp, *Langmuir* **2011**, *27*, 15206.
- [22] R. S. Yelamanchili, Y. Lu, T. Lunkenbein, N. Miyajima, L.-T. Yan, M. Ballauff, J. Breu, *Small* **2009**, *5*, 1326.
- [23] a) B. Ohtani, Y. Ogawa, S.-i. Nishimoto, *J. Phys. Chem. B* **1997**, *101*, 3746; b) Lee, M. Christopher Orilall, S. C. Warren, M. Kamperman, F. J. DiSalvo, U. Wiesner, *Nat. Mater.* **2008**, *7*, 222.
- [24] a) J. Lee, C. M. Orilall, S. C. Warren, M. Kamperman, F. J. DiSalvo, U. Wiesner, *Nat. Mater.* **2008**, *7*, 222; b) Y. Mao, S. S. Wong, *J. Am. Chem. Soc.* **2006**, *128*, 8217; c) H. Zhang, M. Finnegan, J. F. Banfield, *Nano Lett.* **2000**, *1*, 81.
- [25] A. Matsumoto, S. Asai, H. Aota, *Macromol. Chem. Phys.* **2000**, *201*, 2735.
- [26] T. Saito, B. D. Mather, P. J. Costanzo, F. L. Beyer, T. E. Long, *Macromolecules* **2008**, *41*, 3503.
- [27] M. Balastre, F. Li, P. Schorr, J. Yang, J. W. Mays, M. V. Tirrell *Macromolecules*, **2002**, *35*, 9480.
- [28] a) S. Fazio, J. Guzmán, M. T. Colomer, A. Salomoni, R. Moreno, *J. Eur. Ceram. Soc.* **2008**, *28*, 2171; b) M. Kosmulski, *J. Colloid Interf. Sci.* **2006**, *298*, 730.
- [29] Y. Xu, O. V. Borisov, M. Ballauff, A. H. E. Müller, *Langmuir* **2010**, *26*, 6919.
- [30] a) J. Bandara, K. Willinger, M. Thelakkat, *Phys. Chem. Chem. Phys.* **2011**, *13*, 12906; b) J. T. Park, J. H. Koh, J. A. Seo, J. H. Kim, *J. Mater. Chem.* **2011**, *21*, 1787.

## Supporting Information

### S1. Experimental Part

**Materials.** *sec*-Butyllithium (1.3 M solution in hexane, Acros) was used without further purification. THF (Fluka) was distilled from CaH<sub>2</sub> and K. Subsequently, the solvent was directly transferred into a glass reactor (Büchi). Styrene (Acros) was stirred over Bu<sub>2</sub>Mg for 2 h and afterwards condensed on a vacuum line. Allyl methacrylate (ABCR) was stirred over trioctylaluminium for 40 min and afterwards also condensed on a vacuum line with dynamic vacuum aperture. 1,1-Diphenylethylene (DPE, Aldrich) was distilled from *sec*-butyllithium. The photoinitiator [diphenyl(2,4,6-trimethylbenzoyl)phosphine oxide] (Lucirin TPO®) was provided by BASF. Titanium tetra(*n*-butoxide) (Aldrich), acetic anhydride (Fluka), hydrochloric acid (37% HCl), acetic acid and sulfuric acid (98% H<sub>2</sub>SO<sub>4</sub>) were used as received.

**Synthesis of polystyrene-*b*-poly(allyl methacrylate).** PS-*b*-PAMA was synthesized via sequential living anionic polymerization in THF (400 mL) at low temperatures<sup>[1]</sup> in the presence of alkoxides to stabilize the living chain end. The alkoxides were obtained by reacting 4 mL of *sec*-BuLi with THF at -20 °C and slowly warming to room temperature over night. In the following, styrene (21 g, 0.2 mol) was injected via syringe into the septum-sealed reactor vessel and initiated with *sec*-butyllithium (0.2 mL, 0.28 mmol) at -78 °C. The polymerization was allowed to proceed for 15 min at -78 °C. Before the polymerization of the second block, the polystyrene end chains were end-capped with DPE (0.25 mL, 1.4 mmol) at -78 °C for 1 h in order to attenuate the reactivity of the anions; otherwise, attack of the ester moiety of the allyl methacrylate (AMA) would occur. AMA (9 g, 0.07 mol) was injected via syringe into the reaction vessel and was polymerized for 90 min at -78 °C. Finally the reaction was quenched through the addition of 3 mL of deoxygenated isopropanol. The polymer was then purified by precipitation into cold isopropanol and freeze-dried from dioxane.

**Film Casting and Crosslinking.** A film of diblock copolymer was cast from toluene with an additional amount of 10 wt% photoinitiator (Lucirin TPO®). After crosslinking, the resulting fixed self-organized structures were re-dissolved in THF by stirring for at least one week. The re-dispersion can be sped up by sonication, which will, however, lead to shorter polymer cylinders. In this way, core-shell cylindrical polymer brushes with a polystyrene corona and a poly(allyl methacrylate) core were produced in a large

quantity. The crosslinking procedure did not change the morphology of the bulk structure. Crosslinking of the as-cast polymer film was carried out with a UV-lamp (Hoehnle VG UVAHAND 250 GS with cut-off at 300nm) for 4 h.

**Sulfonation of the PS corona.** The PS-*b*-PAMA cylinders (~1 g) were dispersed in dichloroethane (DCE; 50 mL) and deoxygenated by bubbling argon for 15 min. While bubbling, the dispersion was heated to 50°C and 2.5 M of freshly prepared acetyl sulfate solution (10-15 mL) was added slowly. The acetyl sulfate solution was prepared according to literature.<sup>[2]</sup> The sulfonation process was allowed to proceed for 24 h until a few milliliters of MeOH were added. DCE was distilled off on a rotary evaporator. The sulfonated brushes were washed several times with MilliQ water using a centrifuge, in order for the polymer brushes to be recollected. The degree of sulfonation achieved by this mild method was 81%. This was determined by the elemental analysis of sulfur (theoretical value at 100 % sulfonation of PS to PSS: 13.9 %; experimental value: 11.2 %). Interestingly we found that PSS-*b*-PB remained a brownish-black precipitate in water, while the white PSS-*b*-PAMA readily and completely dissolved in water.

**Synthesis of crystalline TiO<sub>2</sub> nanocolloids.** Rutile was previously produced in the presence of HCl,<sup>[3]</sup> whereas anatase was already produced in the presence of acetic acid.<sup>[4]</sup> Herein, the mild synthesis of rutile or anatase nanocrystals was performed in acidic water at 60 °C while continuously stirring by the drop-wise addition of titanium (IV) *n*-butoxide (2 mL) to 5 mL of a 2 M HCl (in case of rutile) or 2M acetic acid (in case of anatase) solution. After 2 h, the stirring was stopped and the required amount of suspension of nanocrystals was taken out via Eppendorf pipette for the hybrid formation.

**Synthesis of crystalline TiO<sub>2</sub> hybrid nanowires.** A template brush suspension (12 mL, c = 1 g L<sup>-1</sup>) was adjusted to pH 1 by adding 2M HCl. The acidic brush suspension was then added drop-wise to 160 µL of the as-prepared rutile crystal suspension in a glass vial under stirring (60 °C). For the fabrication of anatase hybrid nanowires, the same template brush suspension (pH 1) was added drop-wise to 180 µL of the anatase crystal suspension. However, it is not possible to reach pH 1 with acetic acid; consequently, the pH of the anatase colloid suspension was adjusted to pH 1 by adding 2M H<sub>2</sub>SO<sub>4</sub> prior to the addition of the template brushes.

In both cases, the hybrid formation was stopped after 2h of stirring at 60 °C. Immediately, the resulting hybrid materials were centrifuged and washed several times with water and methanol until they were dried in air or freeze-dried from water. The dry hybrid materials were then used for further characterization and experiments.

## S2. Methods

**Transmission electron microscopy (TEM).** Ultrathin (30-80 nm) samples for TEM were cut from the as-cast and crosslinked polymer films with a Reichert-Jung Ultracut E equipped with a diamond knife. TEM micrographs were taken on a Zeiss CEM 902 operating at 80 kV. In order to enhance the electron density of the poly(allyl methacrylate) phase, the samples were stained with OsO<sub>4</sub>. For TEM samples coming from solution, a droplet of a dilute solution (0.05 g L<sup>-1</sup>) of THF or water was dropped onto a copper grid (200 mesh) coated with carbon film. The liquid was then blotted and the sample allowed to dry at room temperature for a short time. In the case of water, the copper grid was treated with plasma for about 15 sec in order to enhance the wetting. High resolution TEM (HR-TEM) was carried out on a Philips CM20FEG TEM operated at 200 kV using carbon lacey TEM grids.

**Cryogenic Transmission Electron Microscopy (Cryo-TEM).** Cryo-TEM was conducted by dropping the aqueous dilute solution on a hydrophilized lacey TEM grid, where most of the liquid was removed with blotting paper, leaving a thin film stretched over the grid holes. The specimens were shock frozen by rapid immersion into liquid ethane and cooled to approximately 90 K by liquid nitrogen in a temperature controlled freezing unit (Zeiss Cryobox, Zeiss NTS GmbH, Oberkochen, Germany). After the specimens were frozen, the remaining ethane was removed using blotting paper. The specimen was inserted into a cryo-transfer holder (CT3500, Gatan, München, Germany) and transferred to a Zeiss EM922 EF-TEM instrument operated at 200 kV.

**Scanning electron microscopy (SEM).** SEM images were taken from a high resolution scanning electron microscope (LEO 1530 FESEM) with field emission cathode. A magnification in the range from 20x to 900000x can be achieved. All samples were investigated from a silicon wafer and sputtered with platinum prior to measurement.

**Molecular characterization of the block copolymer.** Size exclusion chromatography (SEC) with THF as eluent was performed on an apparatus equipped with PSS SDVgel columns (30 x 8 mm, 5 mm particle size) with  $10^5$ ,  $10^4$ ,  $10^3$ , and  $10^2$  Å pore sizes using RI and UV detection ( $\lambda = 254$  nm) at a flow rate of 1.0 mL/min. The calibration was based on polystyrene standards and toluene was used as an internal standard. Proton nuclear magnetic resonance ( $^1\text{H-NMR}$ ) spectra were recorded on a Bruker AC-300 spectrometer at room temperature in  $\text{CDCl}_3$  in order to determine the polymer composition. The molecular weight of PAMA was calculated from the number-average molecular weight,  $M_n$ , of the PS precursor obtained by THF-SEC and the ratio of characteristic NMR signals.

**Composite characterization.** Powder X-ray diffraction (PXRD) measurements were performed at 25 °C on a Panalytical XPERT-PRO diffractometer in reflection mode using  $\text{CuK}\alpha$  radiation.  $\text{N}_2$  physisorption was conducted at 77 K on a Quantachrome Autosorb 1 instrument. Prior to the measurements, the samples were degassed at 403 K for 24 h. Calcination was done in a tube furnace. First, the sample was calcined within a nitrogen atmosphere at a heating rate of 3 K min $^{-1}$  from 30 °C to 650 °C. The heating procedure was sectioned into three parts: from 30 °C to 300 °C (3 K min $^{-1}$ ), isotherm at 300 °C for 5 h, and then from 300 °C to 650 °C (3 K min $^{-1}$ ). The material was again calcined in air at a heating rate of 3K/min from 30 °C to 550 °C.

### S3. SEC of $\text{PS}_{69}\text{PAMA}_{31}^{81}$ diblock copolymer

SEC measurements were performed to determine the molecular weight distribution of the PS precursor and the diblock copolymer. SEC was calibrated with PS standards, which allowed the precise determination of the number-average molecular weight ( $M_n$ ) of the PS block. Polydispersity indices were 1.02 (PS) and 1.06 ( $\text{PS}_{540}-b-\text{PAMA}_{200}$ ).

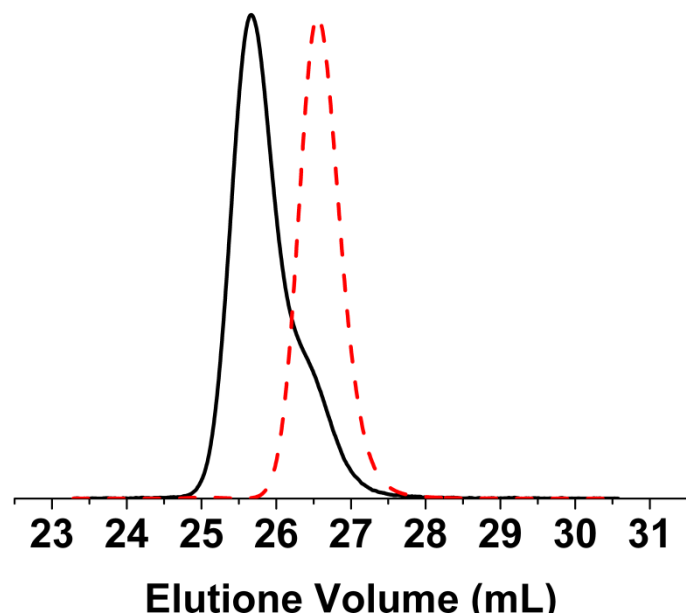


**Figure S1.** SEC traces of PS homopolymer (red dashed line) and PS<sub>69</sub>PAMA<sub>31</sub><sup>81</sup> diblock copolymer (black solid line).

**S4.  $^1\text{H-NMR}$  of  $\text{PS}_{69}\text{PAMA}_{31}^{81}$** 

A  $^1\text{H-NMR}$  measurement in  $\text{CDCl}_3$  was performed to determine the compositions of the diblock copolymer. Knowing the  $M_n$  of the PS block from SEC, the characteristic PS peaks at around 7 ppm were compared to the characteristic signals of the PAMA block. Figure S4 shows the attribution of the respective protons of the diblock copolymer. Comparison of the two allyl protons (Figure S2(b)) at 5.4 ppm with the two protons at 4.5 ppm (Figure S2(d)) gave a ratio of 1:1 and thus revealed that the allyl bond was indeed not affected by anionic polymerization.

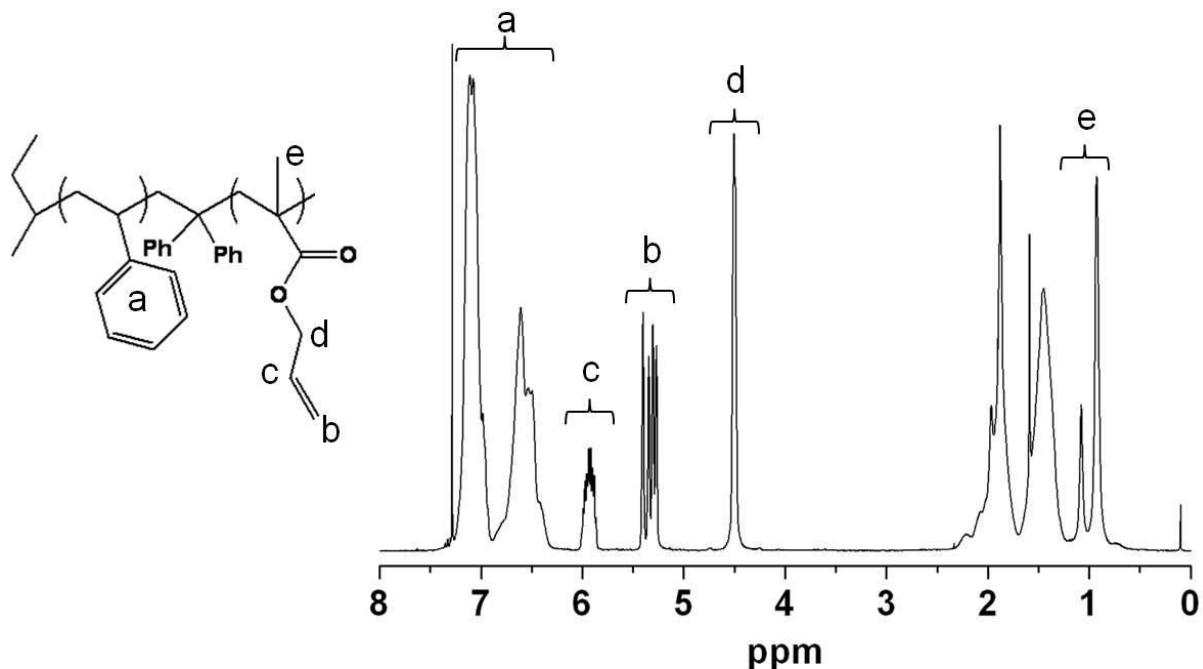


**Figure S2.**  $^1\text{H-NMR}$  spectra of diblock copolymer  $\text{PS}_{69}\text{PAMA}_{31}^{81}$  in  $\text{CDCl}_3$ .

## S5. Bulk morphology

Thin cut films of non-crosslinked polymer films revealed hexagonally packed PAMA cylinders in a PS matrix. After co-casting a photo-crosslinker and crosslinking under UV light, the micrographs remained unchanged.

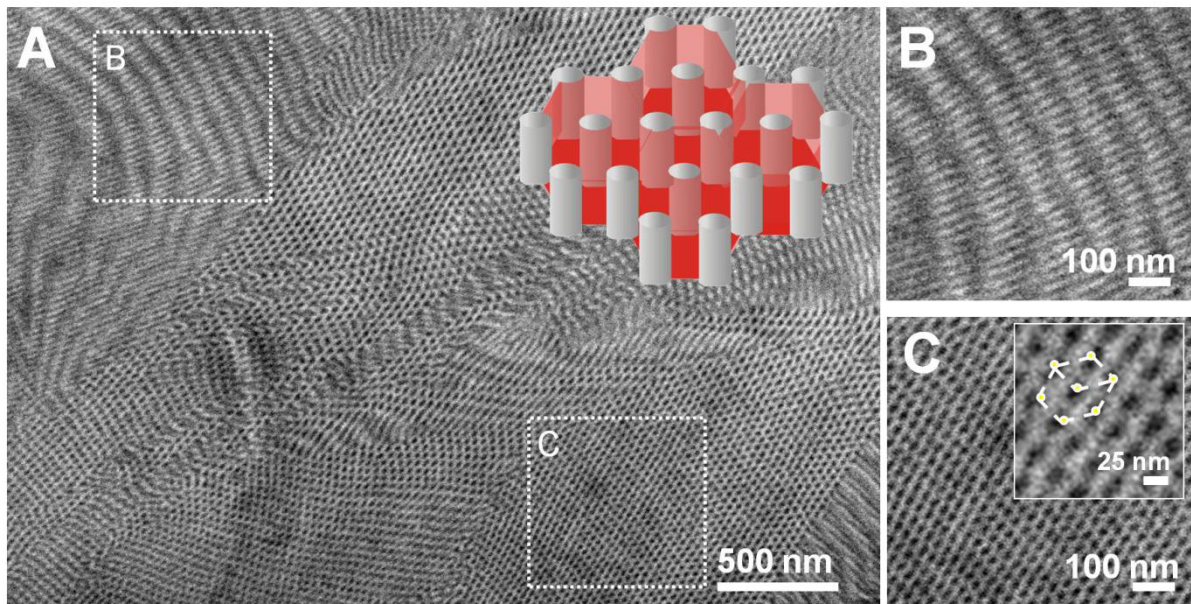


**Figure S3.** (A) TEM micrograph of  $\text{PS}_{69}\text{PAMA}_{31}^{81}$  cast film from toluene. (B) and (C) are magnifications of the insets in (A) and highlight the lying and standing PAMA cylinders, respectively. The double-bond containing cylinders were stained with  $\text{OsO}_4$  to increase contrast.

**S6. SEM of argon calcined rutile nanowires**

SEM of argon calcined rutile nanowires highlights the porosity and stability of calcined rutile nanowires. The images clearly show the anisotropic shape of the rutile nanostructures (Figures S4A/B). Through sample stage tilting, it was possible to further underline the intact worm-like structures (Figures S4C/D).

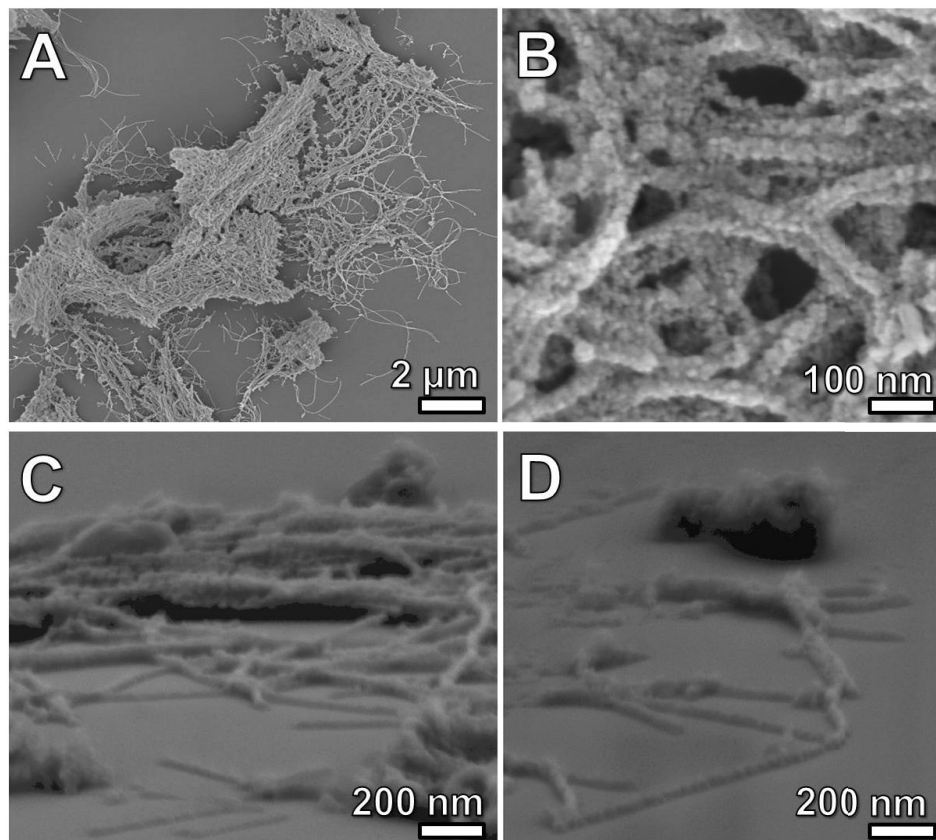


**Figure S4.** (A/B) SEM images of argon calcined rutile nanostructures at different magnifications and (C/D) with tilted sample stage ( $75^\circ$  angle of view).

### S7. Thermogravimetric analysis of rutile nanostructures

Thermogravimetric analysis (TGA) of rutile nanostructures revealed the inorganic  $\text{TiO}_2$  content of the hybrid material. Calcination from 30 °C to 650 °C at a heating rate of 10 K min<sup>-1</sup> and a subsequent isotherm for 2 h at 650 °C removed 51 % of organic material and only left  $\text{TiO}_2$  behind. The composition of the hybrid materials is consequently around 50:50 in weight content.

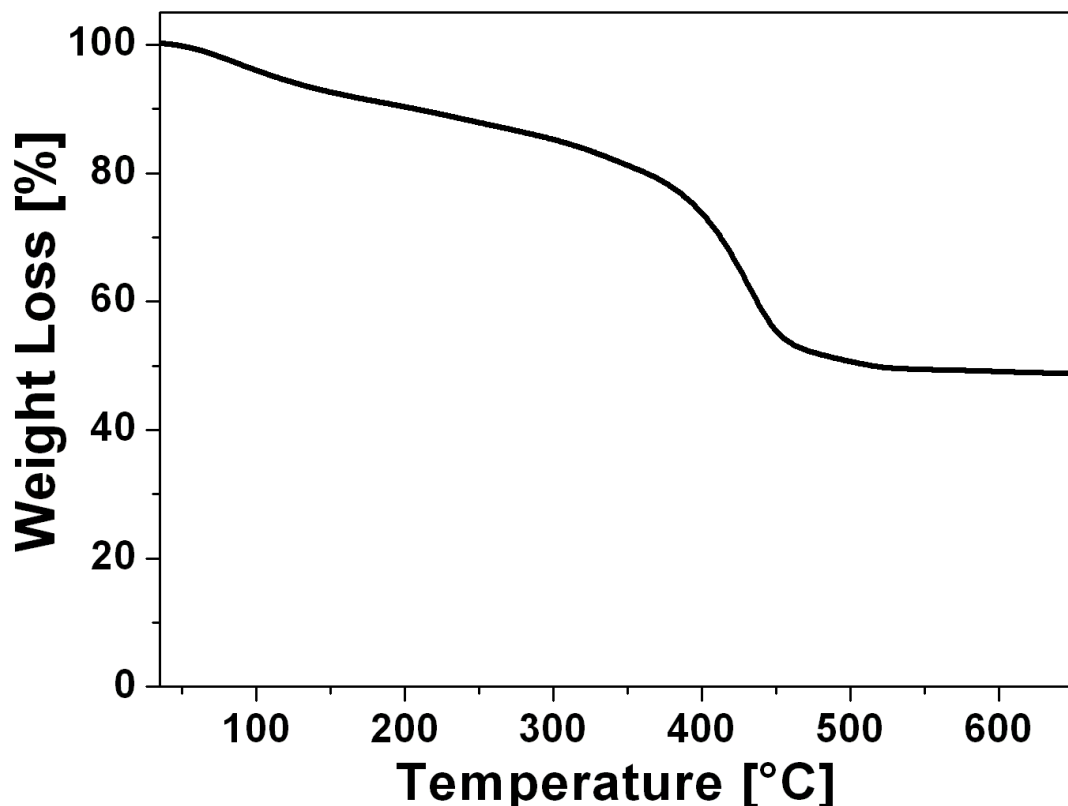


**Figure S5.** TGA measurement of rutile nanostructures in air.

## S8. Crystalline anatase nanowires from pre-synthesized crystalline anatase colloids

We also applied the colloidal route to produce crystalline anatase nanostructures. Similar to the synthesis of crystalline rutile nanocrystals, crystalline nanocolloids of anatase were successfully synthesized prior to hybrid formation. It is reported that titanium tetra(*n*-butoxide) forms anatase crystals with acetic acid.<sup>[4]</sup> Therefore, we synthesized these colloids in 2M acetic acid. Phase purity of the anatase colloids was determined by PXRD (see the black bottom curve in Figure S6D). The size of anatase nanocrystals was measured by DLS in 2M HCl in order to supply sufficient surface charge. Nanocolloids with an apparent hydrodynamic diameter of around 14 nm were observed. The large signal at around 110 nm is attributed to the agglomeration of nanocolloids. As larger object scatter more light, the signal at around 100 nm is greatly enhanced in the intensity-weighted DLS plot (Figure S6E).

After infiltration of the oppositely charged anatase nanocrystals into the template brush corona at pH 1, crystalline nanowires with a high aspect ratio were obtained (Figure S6A). When compared to the rutile nanostructures in the main manuscript, these nanostructures look quite identical. However, these nanostructures differ in crystallinity, as it is possible to adjust the crystal structure through the infiltrated nanocrystals. Consequently, when anatase nanocolloids were used, the corresponding hybrid material consisted of crystals of the same polymorph as the nanocolloids, as can be seen and verified by PXRD (see red top curve in Figure S6D). The HR-TEM micrographs in Figure S6B/C show the crystal lattices of as-prepared anatase hybrid nanowires.

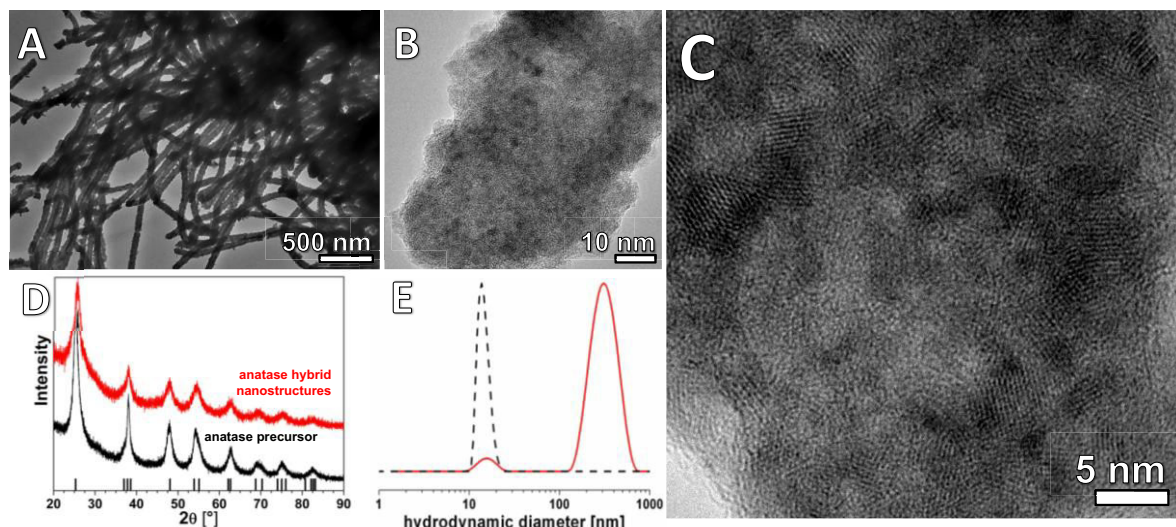


**Figure S6.** (A) TEM micrograph of as-synthesized anatase hybrid nanowires. (B/C) HR-TEM micrographs of as-synthesized anatase hybrid nanowire. (D) PXRD pattern of anatase nanocrystals (black bottom pattern) and as-synthesized anatase hybrid nanostructures (red top pattern). The ticks on the x-axis indicate all anatase reflexes. (E) DLS measurement of anatase nanocrystals in 2M HCl: number-weighted plot (black dashed line) and unweighted plot (red solid line).

## References

- [1] F. Schacher, M. Müllner, H. Schmalz, A. H. E. Müller, *Macromol. Chem. Phys.* **2009**, *210*, 256.
- [2] T. Saito, B. D. Mather, P. J. Costanzo, F. L. Beyer, T. E. Long, *Macromolecules* **2008**, *41*, 3503.
- [3] R. S. Yelamanchili, Y. Lu, T. Lunkenbein, N. Miyajima, L.-T. Yan, M. Ballauff, J. Breu, *Small* **2009**, *5*, 1326.
- [4] S. Li, G. Ye, G. Chen, *J. Phys. Chem. C* **2009**, *113*, 4031.

## 7.3 Packing of Cylindrical Keggin-Type Polyoxometalate Hybrid Micelles as a Function of Aspect Ratio

*Thomas Lunkenbein,<sup>1</sup> Martin Schieder,<sup>1</sup> Carina Bojer,<sup>1</sup> Axel H. E. Müller,<sup>2</sup> and Josef Breu<sup>1,\*</sup>*

<sup>1</sup>Lehrstuhl für Anorganische Chemie I, Universität Bayreuth, 95440 Bayreuth, Germany

<sup>2</sup>Lehrstuhl für Makromolekulare Chemie II, Universität Bayreuth, 95440 Bayreuth, Germany

### Abstract

The packing of cylindrical Keggin-Type polyoxometalate hybrid micelles and its influence on specific surface area was studied as function of aspect ratio. Core-crosslinked cylindrical poly(butadiene-block-2-vinylpyridine) (PB-b-P2VP) micelles were used as templates for mesostructuring phosphomolybdic acid ( $H_3PMo_{12}O_{40}$ ). Prior to hybrid formation the length of the cylindrical PB-b-P2VP micelles was adjusted by sonication. Depending on the aspect ratio of the cylinders a remarkable and unexpected evolution of specific surface areas was observed. The changes in the specific surface area could be explained by a series of scanning electron microscopy and transmission electron microscopy images and were related to the packing of the 1D nanoobjects.

**Keywords.** surface area, sonication, anisometric hybrid, non-woven, self-assembly

## Introduction.

Cylindrical micelles of polymers have attracted considerable attention over a wide area of applications. For instance, in medicine cylindrical micelles are utilized in flow-intensive drug delivery, since they perfectly orient in a flowing stream.[1] In the field of engineering cylindrical micelles have been used as compatibilizer,[2,3] and as additives that increase the toughness of epoxy resins.[4] Furthermore cylindrical aggregates of peptide-amphiphiles have been used as fibrous templates in the direct biomineralization of hydroxyapatite.[5]

However, reports on cylindrical micelles as templates for inorganic transition metal oxides are scarce.[2,6] Normally, the mesostructure adopted by diblock copolymer/inorganic oxide hybrid materials is governed by reaction conditions during self-organization and hybrid formation. Hence micelle transformation of these supramolecular soft templates represents a major obstacle on the way to a desired mesostructure of the resulting hybrid material. Polymer micelles are very sensitive to changes in pH, temperature, solvent, and ionic strength.[6,7] Consequently, in many cases the conditions essential for the formation of the desired template structure do not overlap with the requirements for the controlled assembly of the inorganic precursors around the template. Pre-designed core-crosslinked cylindrical micelles are invariant and allow for extensive variation of reaction conditions during hybrid formation.[8,7]

The length of the cylindrical micelles is determined by the domain sizes of the corresponding bulk morphology and the degree of crosslinking reaction. As-synthesized core-crosslinked cylindrical micelles are several micrometers in length. The length of the cylindrical micelles may, however, be easily adjusted post cross-linking. For instance, sonication of suspensions of cylindrical micelles induces fracture and shorter cylinders of a few hundred nanometers are obtained.[9-11] The aspect ratio of the 1D nanoobjects may be controlled to a certain degree by sonication time and power. This method therefore provides rigid cylindrical micelles of various length/aspect ratio which can subsequently be used for templating of inorganic transition metal oxides such as Keggin-Type polyoxometalates (Keggin POMs).

Keggin POMs possess interesting and versatile chemical, physical, and electronical properties,[12,13] giving way to applications in catalysis, electrochemistry, and host-guest chemistry.[14-17] However, the accessibility of active sites for pure acids or salts is

limited, because of low surface area of these inorganic materials.[14] Increasing the specific surface area by appropriate techniques that structure Keggin POMs on the mesoscale is therefore a major focus in current polyoxometalate chemistry.

Incorporation of the hydrophilic and highly charged Keggin POM units into hydrophobic organic materials may be achieved by replacing the inorganic counterions with cationic surfactants to form so-called surfactant encapsulated polyoxometalate clusters (SEC).[18-23] The SECs usually are spherical nanoobjects with no appreciable aspect ratio. They are however soluble in organic solvents and upon drying close packed structures of hybrid materials are obtained. Additional fabrication steps ensure discrete nanoarchitectures that show enhanced catalytic performances.[24]

We have previously obtained 1D nanohybrids materials applying core-crosslinked cylindrical micelles carrying an aminofunction in the corona and combining this template with heteropolyacids as inorganic precursor.[6] Coulomb interactions between the *in-situ* protonated polymer corona and the anionic Keggin POM units assure hybrid formation. Due to the large aspect ratios, upon casting the suspensions, singular cylindrical polymer/Keggin POM nanohybrids arrange into non-woven spaghetti-like networks with high surface area. Here, we now study the formation of these disordered mesostructures in more detail. In particular, the influence of the length of the cylindrical templates on packing of the 1D nanoobjects and the resulting specific surface area is considered.

## Experimental Part

*Synthesis of poly(butadiene-block-2-vinylpridine) (PB-*b*-P2VP) diblock copolymer.* The PB-*b*-P2VP diblock copolymer was synthesized via sequential anionic polymerization in tetrahydrofuran (THF) as described elsewhere.[7] THF- gel permeation chromatography was used to determine the molecular weight of the polybutadiene (PB) block and the polydispersity index (PDI) of the final diblock copolymer. THF was HPLC grade (Aldrich), and measurements were conducted at room temperature (RT) and at flow rates of 0.5 mL/min. A <sup>1</sup>H-NMR spectrum was recorded to calculate the composition of the diblock copolymer. The final diblock copolymer has a molecular weight of 60 kg/mol and a P2VP weight content of 81 wt %.

*Core-crosslinking.* The cylindrical PB-b-P2VP micelles were produced by the selective crosslinking of the cylinder morphology. The latter formed in the bulk phase by casting a solution of the PB-b-P2VP precursor (10 wt %) in CHCl<sub>3</sub> which also contained 10 wt % of the UV initiator Lucirin TPO. Crosslinking of the bulk film was achieved by UV radiation (cut-off: < 350 nm) for 2 h on each side.

*Sonication.* 40 mL of as-synthesized cylindrical PB-b-P2VP micelles were dispersed in 1 molar (M) hydrochloric acid (HCl, 1 g/L) and placed under a Branson model-250 digital sonifier equipped with 1/8 in. diameter tapered microtip (200 W at 10 % amplitude).

*Preparation of cylindrical PB-b-P2VP/H<sub>3</sub>PMo hybrid micelles.* Phosphomolybdic acid [H<sub>3</sub>[PMo<sub>12</sub>O<sub>40</sub>], H<sub>3</sub>PMo, p.a.] was obtained from Aldrich. X-ray diffraction showed it to be a mixture of different hydrated phases. Therefore, it was recrystallized from water and stored at 86 % relative humidity (RH) in order to assure a defined stoichiometry.[25] Under these conditions a crystalline material was obtained containing 27 water molecules per formula unit as confirmed by thermogravimetric analysis (TGA). The pH value was kept below 1.5. Below this pH H<sub>3</sub>PMo exists as the predominant species.[14,26] The amount of added H<sub>3</sub>PMo was calculated on the basis of the content of amine functions within the diblock copolymer. An 1.5fold excess of H<sub>3</sub>PMo was added to assure a complete grafting of H<sub>3</sub>PMo over the cylindrical PB-b-P2VP micelles. 20 mL of 4•10<sup>-3</sup> M H<sub>3</sub>PMo (pH = 1.2) in water was added dropwise to 20 mL of a solution of core-crosslinked cylindrical PB-b-P2VP micelles in 1 M HCl (1g/L, pH = 0) under continuous stirring at room temperature. With the addition of the H<sub>3</sub>PMo solution to the polymer dispersion, greenish precipitates were produced. The pH of the final cylindrical hybrid micelles dispersion was 0.5. The resultant precipitate was stirred for additional 2 h. The precipitate was then washed several time with deionized water to remove the chloride anions. Finally the sample was freeze-dried.

*Characterization.* Brightfield transmission electron microscopy (TEM) images were performed on a Leo 922 operated at an acceleration voltage of 200 kV. Cylindrical micelles and cylindrical hybrid micelles were diluted to 0.1 gL<sup>-1</sup> in 1 M HCl solution and ethanol, respectively and a droplet was placed on a carbon coated copper grid.

Field emission scanning electron microscopy (SEM) was performed using a LEO Gemini microscope equipped with a field emission cathode. The acceleration voltage was

set to 3 kV. Samples were dispersed in ethanol and droped on a silica waver. Prior to measurements the sample on the waver was sputtered with a 1.3 nm Pt layer.

Powder X-ray diffraction (PXRD) patterns were obtained using nickel filtered Cu-K $\alpha$  radiation ( $\lambda = 1.54187 \text{ \AA}$ ) on a Bragg-Brentano-type diffractometer (XPERT-PRO, PANalytical B.V.) equipped with an X'Celerator Scientific RTMS detector. All patterns were analyzed using Panalytical's Highscore Plus software.

Fourier-Transformed Infrared (FTIR) measurements were conducted on a Perkin Elmer Spectrum 100 equipped with an attenuated total reflection (ATR) unit.

N<sub>2</sub> physisorption experiments were conducted at 77 K on a Quantachrome Autosorb 1 instrument. Prior to measurements, the samples were degassed at 373 K for 24 h.

## Results and Discussions.

Bulk PB-b-P2VP was first dissolved in acidic aqueous solution. The electrostatic repulsion between adjacent protonated P2VP coronas assisted the dispersion of the polymeric cylinders in aqueous solutions. Furthermore the length of the pristine cylindrical micelles was adjusted by sonication. Subsequent hybrid formation led to a variety of cylindrical PB-b-P2VP/H<sub>3</sub>PMo hybrid micelles that assemble into non-woven spaghetti-like networks upon drying. The evolution of the surface area of the cylindrical hybrid micelles as function of sonication and thus of average cylinder length was studied.

*Sonication of cylindrical PB-b-P2VP micelles.* TEM images of the core-crosslinked cylindrical PB-b-P2VP micelles before and after 10 min of ultrasound treatment are shown in Figure 1. The diameter of the PB core is approximately 20 nm and the P2VP corona extends ca. 35 nm around the PB-core (Fig. 1). The total diameter of the polymeric wires is ca. 90 nm. As expected, ultrasound treatment of the cylindrical PB-b-P2VP micelles (1 gL<sup>-1</sup>) at five different exposure times (0 min, 1 min, 2 min, 5 min, and 10 min) in acidic aqueous solution lead to significant fracture of cylindrical micelles. The length of more than 500 cylindrical PB-b-P2VP micelles was obtained from TEM images. The corresponding histograms are shown in Figure 2. The insets zoom into the length distribution below 500 nm. The average length of the cylindrical micelles at different sonication times is given in Table 1.

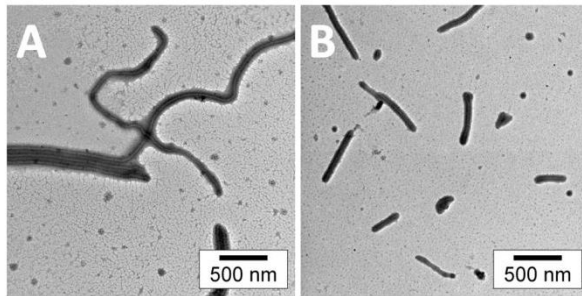


**Fig. 1.** TEM images of cylindrical micelles of core-crosslinked PB-b-P2VP without ultrasound treatment (A) and after 10 min of sonication (B).

**Table 1.** Characteristics of cylindrical polymer micelles and cylindrical PB-b-P2VP/H<sub>3</sub>PMo hybrid micelles

cylindrical PB-b-P2VP/H <sub>3</sub> PMo hybrid micelles	sonication time /min	average length /μm <sup>a</sup>	aspect ratio $\alpha^c$	surface area /m <sup>2</sup> /g <sup>b</sup>
hybrid 1	0	2.40	120	60
hybrid 2	1	1.37	68.5	97
hybrid 3	2	0.73	36.5	64
hybrid 4	5	0.37	18.5	72
hybrid 5	10	0.28	14.0	89

<sup>a</sup> as obtained from TEM measurements.

<sup>b</sup> 5 point BET analysis.

<sup>c</sup> ratio of average length of the cylindrical micelles to the width of the PB core.

Pristine cylindrical PB-b-P2VP micelles (without sonication) showed a rather broad length distribution (Fig. 2A) ranging from short cylindrical micelles to highly anisometric PB-b-P2VP micelles with lengths exceeding 30 μm. The average length of the cylindrical micelles was determined to be 2.40 μm. After 1 min of sonication treatment (Fig. 2B) the cylindrical PB-b-P2VP micelles became already significantly shorter and the average length dropped to 1.53 μm. The average length continues to decrease monotonically with extension of sonication. Interestingly, the length distribution narrows with prolonged sonication and pronounced maxima are observed (Fig. 2C-D) that nevertheless were gradually shifted towards shorter rods. With decreasing average length, the anisometric nature was diminished, the average aspect ratios shrunk, and the number of micelles approaching a more spherical shape increased.

# Packing of Cylindrical Keggin-Type Polyoxometalate Hybrid Micelles as a Function of Aspect Ratio

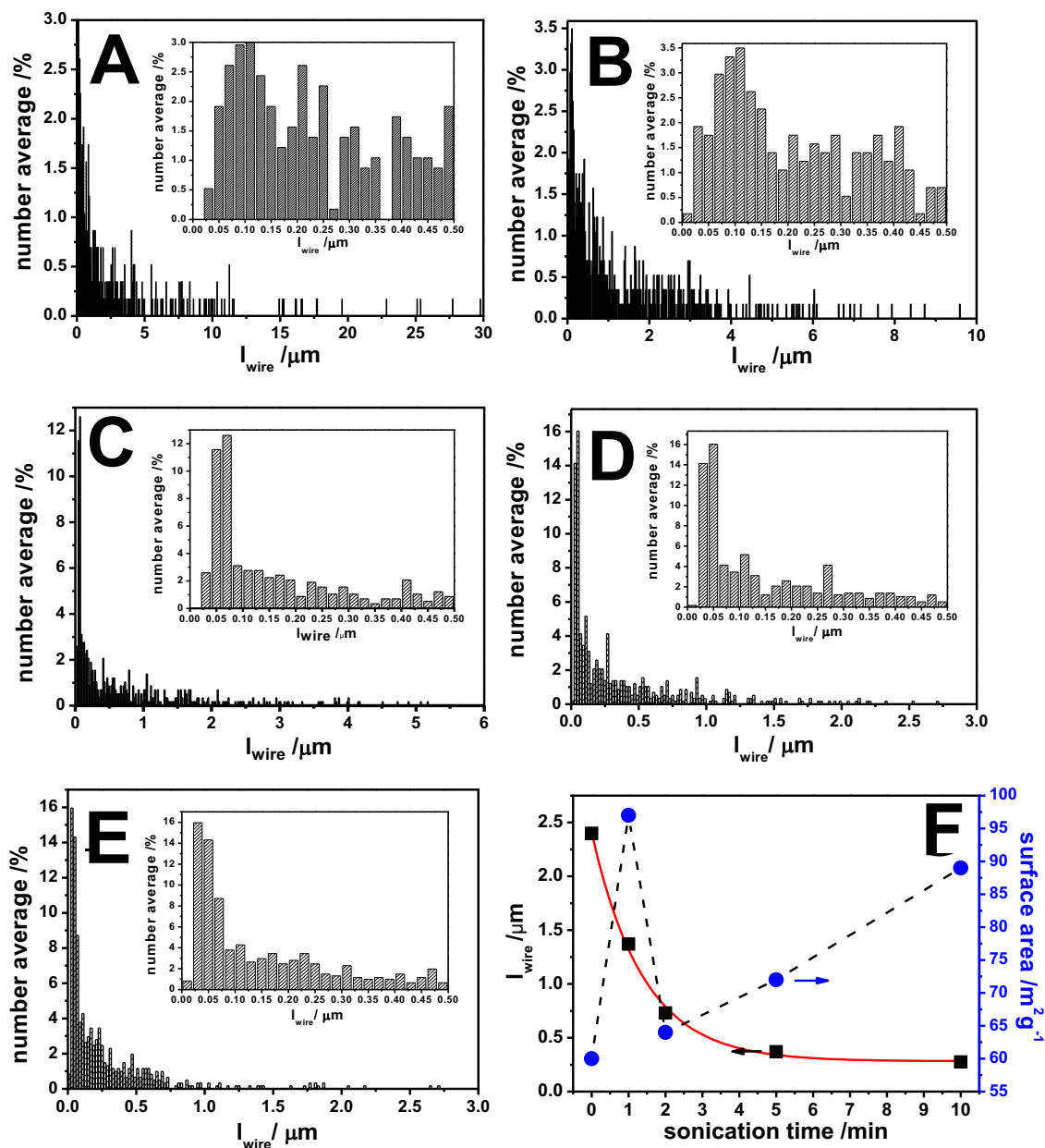


**Fig. 2.** Length distribution of cylindrical PB-b-P2VP micelles for different sonication times: A) 0 min, B) 1 min, C) 2 min, D) 5 min, and E) 10 min. F). Evolution of average length of cylindrical micelles (black squares) and specific surface area of cylindrical PB-b-P2VP/H<sub>3</sub>PMo hybrid micelles (blue circles) as function of sonication time.

After 10 min of sonication treatment (Fig. 2E, average length: 0.28  $\mu\text{m}$ ) the number of almost spherical particles surmounted the anisotropic cylindrical micelles and became the dominating species. All together these results suggested a rapid and efficient fracture of core-crosslinked cylindrical PB-b-P2VP micelles by sonication. The average 100

length followed an exponential decay and asymptotically approached a plateau value of ca. 0.27 µm (Fig. 2F). This suggests that particles with high aspect ratio showed higher sensitivity to ultrasound due to increased fragility of the micelles to shear stress. Selective fracture of longer micelles consequently resulted in a decrease of the number of cylindrical micelles exhibiting larger aspect ratios (Table 1). Shorter micelles produced by fracture possess higher resistance to impact of sonication energy.

*Cylindrical PB-b-P2VP/H<sub>3</sub>PMo hybrid micelles.* Subsequent to sonication, the cylindrical PB-b-P2VP micelles differing in length were converted into cylindrical hybrid materials and the influence of the aspect ratio on the microstructure of the cylindrical hybrid micelles was studied. Cylindrical hybrid micelles were characterized by a combination of PXRD, FTIR, N<sub>2</sub> sorption, SEM, and TEM. The labeling of cylindrical PB-b-P2VP/H<sub>3</sub>PMo hybrid micelles follows the labeling of templates given in Table 1. The PXRD patterns (Fig. 3) showed amorphous materials regardless of sonication times which is an indication for a homogeneous dispersion of the H<sub>3</sub>PMo units in the P2VP corona.

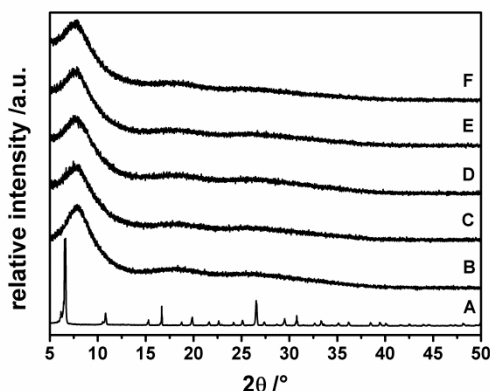


**Fig. 3.** PXRD patterns of (A) pristine H<sub>3</sub>PMo, (B) hybrid 1, (C) hybrid 2, (D) hybrid 3, (E) hybrid 4, and (F) hybrid 5.

FTIR measurements (Fig. 4) confirmed the integrity of H<sub>3</sub>PMo units after hybrid formation. H<sub>3</sub>PMo exhibits four characteristic bands, which are a fingerprint of the Keggin structure.[27,28] There are four kinds of oxygen atoms in H<sub>3</sub>PMo giving rise to the following frequency assignments:  $\nu_{as}$  (Mo-O<sub>d</sub>) – 960 cm<sup>-1</sup>,  $\nu_{as}$  (Mo-O<sub>b</sub>-Mo) – 870 cm<sup>-1</sup>,  $\nu_{as}$  (Mo-O<sub>c</sub>-Mo) – 785 cm<sup>-1</sup>, and  $\nu_{as}$  (P-O<sub>a</sub>) – 1065 cm<sup>-1</sup>. The FTIR spectra of hybrid 1 to 5

represent superpositions of the spectra of commercial H<sub>3</sub>PMo (Fig. 4A) and the PB-b-P2VP polymer template, which clearly indicates that the H<sub>3</sub>PMo structure stayed intact during hybrid formation. However, a shift in frequencies was observed for both corner and edge shared Mo-O-Mo vibrations involving the oxygens concerned in the protonation of PMo<sup>3-</sup> anions. In comparison to commercial H<sub>3</sub>PMo the vibrations shift to higher wavenumbers as a result of the change in the environment of the PMo<sup>3-</sup> anions dispersed in the polymer matrix. This indicates the presence of Coulomb interactions with the template.

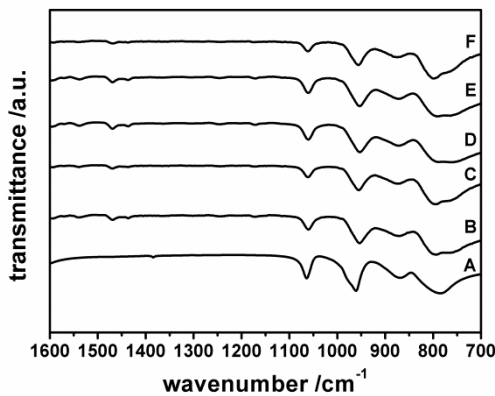


**Fig. 4.** FTIR spectra of (A) pristine H<sub>3</sub>PMo, (B) hybrid 1, (C) hybrid 2, (D) hybrid 3, (E) hybrid 4, and (F) hybrid 5.

*Evolution of surface areas with aspect ratio.* The N<sub>2</sub> physisorption measurements of hybrid 1, 2, 3, 4, and 5 revealed high surface areas of 60, 97, 64, 72, and 89 m<sup>2</sup>g<sup>-1</sup> (Table 1), respectively. Remarkably, the evolution of surface areas as function of sonication time showed a maximum for hybrid 2 followed by a pronounced decrease for hybrid 3 and a subsequent steady increase to hybrid 5 (Fig. 2F). This unexpected development of surface area could not be explained by the surface generated by the additional caps of shorter rods. The specific surface area (A) of cylinders is given by equation (eq.) 1.

$$A = \frac{L+r}{L + \frac{4}{3}r} \cdot \frac{2}{r \cdot \rho_{\text{composite}}} \quad (2)$$

where  $L$  is the length of the cylinder,  $r$  the corresponding radius, and  $\rho$  the density of the cylindrical PB-b-P2VP/H<sub>3</sub>PMo hybrid micelles.

Eq. 1 shows only a slight dependence of the surface area on the length of the cylinders. For instance, assuming a uniform radius of all rods and constant density, the specific surface area would be expected to increase by a factor of 1.4 on going from hybrid 2 to the shorter hybrid 3 while contrary to expectations, the experimentally observed surface area indeed decreased drastically.

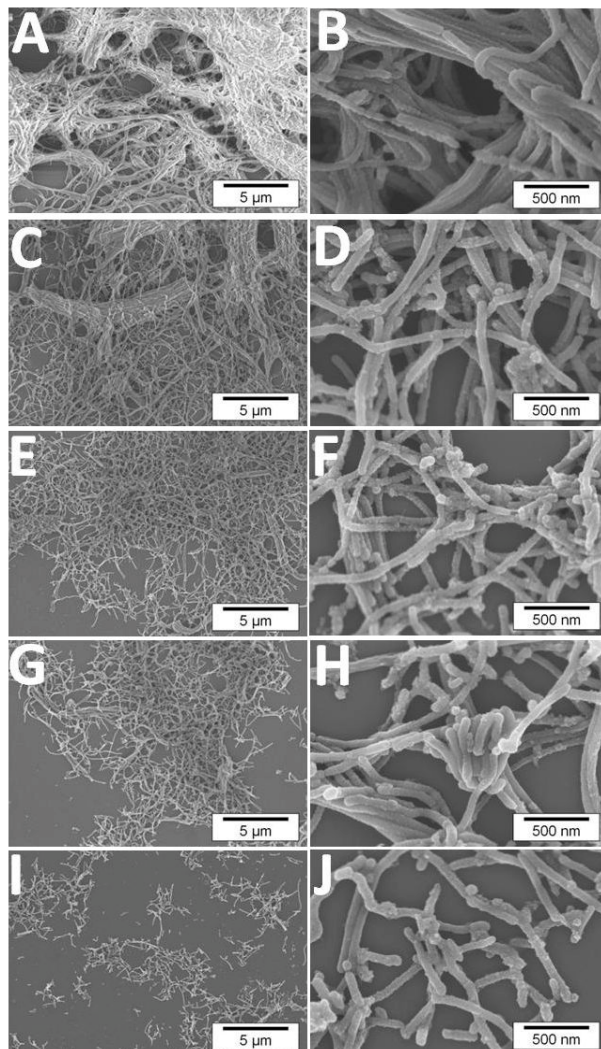


**Fig. 5.** SEM images of cylindrical PB-b-P2VP/H<sub>3</sub>PMo hybrid micelles at different magnifications. Average length of the PB-b-P2VP cylindrical templates: A), B) 2.4  $\mu\text{m}$ , C), D) 1.53  $\mu\text{m}$ , E), F) 0.73 mm, G), H) 0.37  $\mu\text{m}$ , and I), J) 0.28  $\mu\text{m}$ .

Clearly, the observed trend of surface areas of such non-woven spaghetti-like hybrid micelles is not primarily determined by the number of caps but is influenced by factors such as surface roughness, the size of interparticular pores [29], and thus the degree of inter-particle contact points. The evolution of surface area can be explained by the microstructures observed by SEM (Fig. 5) and TEM (Fig. 6) images.

Hybrid 1 exhibited long cylinders that arrange into dense packed aggregates (Fig. 5A and B). Many rods run in parallel and the high content of contact points of neighbouring cylinders (Fig. 5B) hampered the accessibility of outer surfaces resulting in a relative low surface area of  $60 \text{ m}^2/\text{g}$ . Hybrid 2 was treated with ultrasound for 1 min. This led to a shorter average cylinder length but with still relative high aspect ratio (Table 1). Ultrasound, however, also destroyed the densely packed aggregates. Rather, the cylindrical PB-b-P2VP/H<sub>3</sub>PMo hybrid micelles assemble into a highly dispersed non-woven spaghetti-like microstructure (Fig. 5C and D). This microstructure features only a few contact points assuring a high surface area of  $97 \text{ m}^2/\text{g}$ . For hybrid 3 the cylinder length distribution showed a shift to short still anisometric cylinders but with low aspect ratio (Fig. 2C). These shorter rods presumably were below the entanglement length and therefore could realize denser packed microstructures (Fig. 5E and F). This in turn increases the amount of contact area which no longer is accessible to the probe gas and consequently a decrease in surface area ( $64 \text{ m}^2/\text{g}$ ) was observed. Further extension of sonication time (5 min, hybrid 4) resulted in a mixture of short cylinders with low aspect ratio and increasing volume fractions of approximately spherical micelles. This ensued the formation of dense packed cylindrical hybrid micelles with high contact points and low surface area as well as low aspect ratio hybrid micelles exhibiting low contact points and higher surface area. The hybrid micelles with an aspect ratio approaching 1 are expected to act as spacer between the cylinders (Fig. 5G and H) hamper their dense packing and thus leading to an increase of surface area ( $72 \text{ m}^2/\text{g}$ ) as compared to hybrid 3. Further increase in surface area ( $89 \text{ m}^2/\text{g}$ ) for hybrid 5 was caused by the surmounting share of low aspect ratio particles that prevent any direct contacts of parallel rods (Fig. 5I and J). With excessive ultrasound treatment the morphology approaches spherical hybrid micelles. As a result of their geometry dense packed spheres exhibit the lowest degree of contact points and provide a high degree of voids accessible to the probe gas. To our knowledge the surface area of cylindrical PB-b-P2VP/H<sub>3</sub>PMo hybrid micelles exceeded the specific surface area of the corresponding Cs-

salt ( $78 \text{ m}^2/\text{g}$ ) [30] for the first time. Thus the surface area reported here is expected to be the highest obtained for organic/ $\text{H}_3\text{PMo}$  hybrid materials.

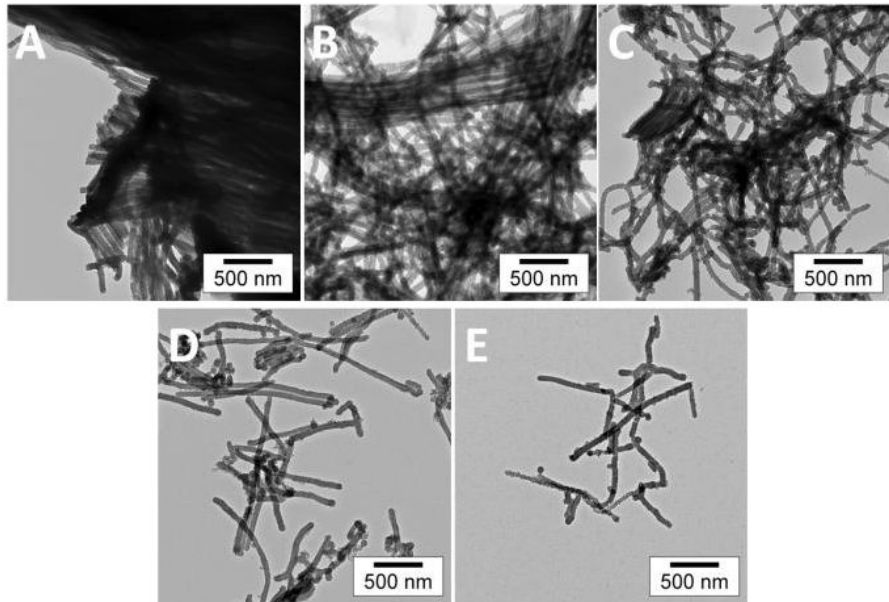


**Fig. 6.** TEM micrographs of cylindrical PB-b-P2VP/ $\text{H}_3\text{PMo}$  hybrid micelles. Average lengths of the cylindrical PB-b-P2VP micelles: A)  $2.4 \mu\text{m}$ , B)  $1.53 \mu\text{m}$ , C)  $0.73 \mu\text{m}$ , D)  $0.37 \mu\text{m}$ , and E)  $0.28 \mu\text{m}$ .

TEM micrographs (Fig. 6) corroborated the structural features seen in SEM images. The surface roughness of all cylindrical PB-b-P2VP/ $\text{H}_3\text{PMo}$  hybrid materials was similar which is in agreement with an homogeneous grafting of  $\text{H}_3\text{PMo}$  units over the polymeric cylindrical micelles.

All together these results showed that the maximum in surface area observed for cylindrical PB-b-P2VP/ $\text{H}_3\text{PMo}$  hybrid micelles is determined by a delicate balance between length of the cylinders and their dispersion in non-woven spaghetti-like networks. The observed non-woven spaghetti-like microstructures are obtained by precipitation of the hybrid micelles. Therefore the influence of the precipitation kinetics might induce a slight variation of the absolute values of surface areas observed, but the trend observed as function of aspect ratio is always preserved.

## Conclusion.

In conclusion, we showed that the length of cylindrical PB-b-P2VP micelles could be adjusted easily by sonication. We also observed an interesting evolution of surface area of cylindrical PB-b-P2VP/H<sub>3</sub>PMo hybrid micelles. The changes in surface area were not primarily affected by the different lengths of the cylindrical hybrid micelles but rather by the packing of their non-woven spaghetti-like mesostructures. It was found that short sonication (1 min) decreased the aspect ratio of cylindrical hybrid micelles only slightly, while fostering perfect dispersion, and thus a non-woven microstructure with few inter-particle contact points could be obtained providing the highest accessible surface area.

**Acknowledgements.** This work was supported by the Deutsche Forschungsgemeinschaft (DFG) within the Collaborative Research Center (SFB) 840. T. L. thanks the international graduate school of the ENB “Structures, Reactivity and Properties of Metal Oxides” for a fellowship.

## References

1. P. Dalheimer, F. S. Bates, D. E. Discher, *Macromolecules* **36** (2003) 6873.
2. M. Zhang, A. H. E. Müller, *J. Polym. Sci. A Polym. Chem.* **43** (2005) 3461.
3. T. M. Ruhland, A. H. Gröschel, A. Walther, A. H. E. Müller, *Langmuir* **27** (2011) 9807.
4. J. M. Dean, N. E. Verghese, H. Q. Pham, F. S. Bates, *Macromolecules* **36** (2003) 9267.
5. J. D. Hartgerink, E. Beniash, S. I. Stupp, *Science* **294** (2001) 1684.
6. R. S. Yelamanchili, A. Walther, A. H. E. Müller, J. Breu, *Chem. Commun.* (2008) 489.
7. A. Walther, A. S. Goldmann, R. S. Yelamanchili, M. Drechsler, H. Schmalz, A. Eisenberg, A. H. E. Müller, *Macromolecules* **41** (2008) 3254.
8. A. Walther, A. Goldel, A. H. E. Müller, *Polymer* **49** (2008) 3217.
9. G. Guerin, H. Wang, I. Manners, M. A. Winnik, *J. Am. Chem. Soc.* **130** (2008) 14763.
10. M. Ballauff, B. A. Wolf, *Macromolecules* **14** (1981) 654.
11. X. Yan, G. Liu, H. Li, *Langmuir* **20** (2004) 4677.
12. M. T. Pope, A. Müller, *Angew. Chem. Int. Ed.* **30** (1991) 34.

13. M. T. Pope, A. Müller: Polyoxometalate Chemistry From Topology via Self-Assembly to Applications, Kluwer Academic Publishers, Dordrecht (2001).
14. J. B. Moffat: Metal-Oxygen Clusters - The Surface and Catalytic Properties of Heteropoly Oxometalates, Kluwer Academic/Plenum Publishers, New York (2001).
15. D. E. Katsoulis, Chem. Rev. **98** (1998) 359.
16. K. Nomiya, H. Murasaki, M. Miwa, Polyhedron **5** (1986) 1031.
17. M. Misono, Catal. Rev. Sci. Eng. **29** (1987) 269.
18. W. Li, W. Bu, H. Li, L. Wu, M. Li, Chem. Commun. (2005) 3785.
19. H. Li, W. Qi, W. Li, H. Sun, W. Bu, L. Wu, Adv. Mater. **17** (2005) 2688.
20. Y. L. Wang, W. Li, L. X. Wu, Langmuir **25** (2009) 13194.
21. S. Polarz, B. Smarsly, M. Antonietti, Chem. Phys. Chem. **2** (2001) 457.
22. Y. K. Han, Z. J. Zhang, Y. L. Wang, N. Xia, B. Liu, Y. Xiao, L. X. Jin, P. Zheng, W. Wang, Macromol. Chem. Phys. **212** (2011) 81.
23. X. K. Lin, Y. L. Wang, L. X. Wu, Langmuir **25** (2009) 6081.
24. A. Nisar, Y. Lu, J. Zhuang, X. Wang, Angew. Chem. Int. Ed. **50** (2011) 3187.
25. O. Nakamura, I. Ogino, T. Kodama, Solid State Ionics **3-4** (1981) 347.
26. G. B. McGarvey, J. B. Moffat, J. Mol. Catal. **69** (1991) 137.
27. C. Rocchicciolieltcheff, M. Fournier, R. Franck, R. Thouvenot, Inorg. Chem. **22** (1983) 207.
28. C. Rocchicciolieltcheff, A. Aouissi, M. Bettahar, S. Launay, M. Fournier, J. Catal. **164** (1996) 16.
29. S. Eichhorn, W. Sampson, J. R. Soc. Interface **7** (2010) 641.
30. G. I. Park, I. K. Song, W. Y. Lee, J. Mol. Catal. A **168** (2001) 115.

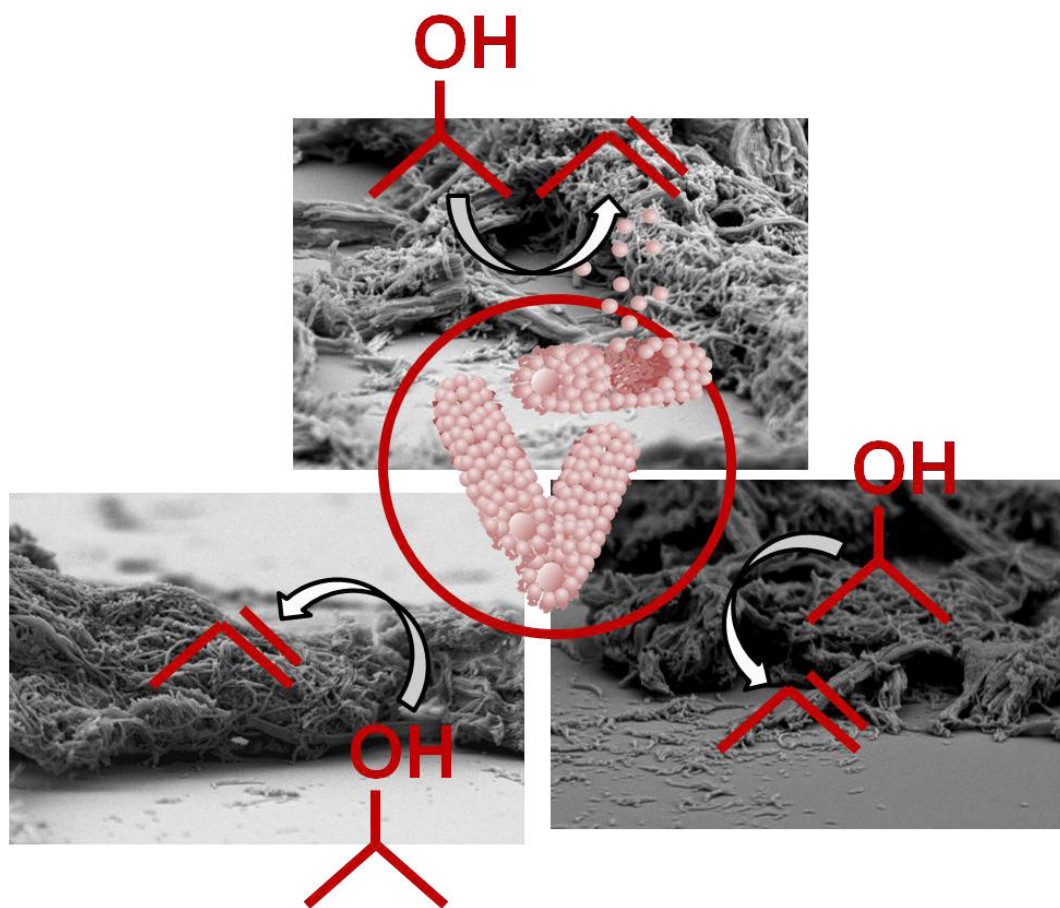


## 7.3 High Surface Area Keggin-Type Polyoxometalate Nanorods and their Catalytic Performance in the Isopropanol Decomposition

Thomas Lunkenbein<sup>1</sup>, Klaus Friedel-Ortega<sup>2</sup>, Ram Sai Yelamanchili<sup>1</sup>, Annette Trunschke<sup>2</sup>, Robert Schlögl<sup>2</sup>, and Josef Breu<sup>1,\*</sup>

<sup>1</sup>Lehrstuhl für Anorganische Chemie I, Universität Bayreuth, 95440 Bayreuth, Germany.

<sup>2</sup>Abteilung für Anorganische Chemie, Fritz-Haber-Institut der Max-Planck-Gesellschaft, 14195 Berlin, Germany.



**Abstract.**

The preparation of high surface area Keggin-Type polyoxometalate nanocomposites templated cylindrical ionizable diblock copolymers and their catalytical performance in isopropanol decomposition was studied. Core-crosslinked cylindrical poly(butadiene-block-2-vinylpyridine) nanorods were used as templates for mesostructuring phosphomolybdic acid ( $H_3PMo$ ), silicomolybdic acid ( $H_4SiMo$ ), and phosphotungstic acid ( $H_3PW$ ). The resulting 1-dimensional nanocomposites were catalytical active in the decomposition of isopropanol following the order  $H_3PW < H_3PMo < H_4SiMo$ . Over acid sites isopropanol decomposes to propylene. The selectivity toward propylene production was also investigated and followed the trend:  $H_3PMo < H_4SiMo < H_3PW$ .

**Keywords.** Polyoxometalate, self-assembly, Coulomb-interaction, catalysis, mesostructuring

## Introduction.

Synthesis of organic-inorganic nanocomposites using organic templates has attracted world wide attention due to the ability of organics like surfactants or block copolymer to self-assemble into a variety of nanostructures with well-defined shape and size.<sup>[1-4]</sup> In particular, block copolymers allow easy control of organic-inorganic hybrid morphology down to the nanometer scale.<sup>[4,5]</sup> Since macroscopic properties crucially depend on both composition and morphology, properties can thus be tailored by combining principles of self-assembly, polymer, colloidal, and inorganic chemistries resulting in nanocomposites with a variety of functionalities and properties.<sup>[4-7]</sup> However, the dynamics observed between different micelle structures, represent a major obstacle using these supramolecular soft templates. Polymer micelles are very sensitive to the reaction conditions. Changes in pH, temperature, solvent, ionic strength can lead to micelle transformation.<sup>[8,9]</sup> Consequently, in many cases the conditions required for the formation of the desired template structure do not match with those requirements for the controlled assembly of an inorganic precursors around the template.

For instance, Keggin-type heteropolyoxometalates (Keggin POM), possess fascinating properties.<sup>[10-15]</sup> The properties of the POMs, particularly of the Keggin-type, depend mainly on the nature of the counter cation and the composition of the Keggin POM anion.<sup>[10-12]</sup> Due to their high ion conductivity, electron density, rapid and reversible oxidative-reductive processes Keggin POMs are of interest in a variety of technological applications such as high performance catalysts, sensor devices and electrodes.<sup>[11-15]</sup> Commercial Keggin POMs possess relatively small surface areas.<sup>[11]</sup> Due to these small surface areas the accessibility to the active sites is hampered and as a result the applications of Keggin POMs are limited.<sup>[10,11]</sup> For many of these applications, it would therefore be highly desirable to increase the surface area of these compounds by shaping them into a mesostructured morphology.

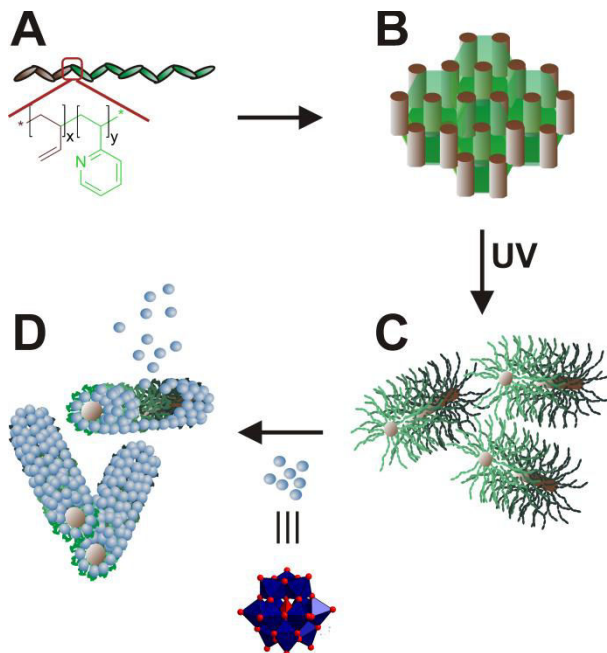
Until now, the surface area of the Keggin POMs was increased following two approaches: Firstly, Mesoporous silica materials like MCM-41, SBA-15 with high surface areas (ca. 800–1000 m<sup>2</sup>g<sup>-1</sup>) were used as supports for the dispersion of Keggin POM.<sup>[16-23]</sup> Among many other factors, the activity of supported Keggin POMs depends crucially on the strength of interaction of this cluster with the surface sites. For instance, with aluminosilicate supports, both the number and the average acid strength of the Brönsted acid sites of the Keggin POMs decrease.<sup>[16]</sup> In brief, while the accessible surface area of

Keggin POMs may indeed be increased by these high surface area supports, limitations arise from low Keggin POM loading, leaching of the active sites into the reaction medium and detrimental interactions with the supports.

Secondly, Keggin POM nanocomposites have been synthesized using surfactants or polymers as soft templates. [11,23-28] For instance, the hydrophilic and highly charged Keggin POM units were incorporated into hydrophobic organic materials by replacing the inorganic counterions with cationic surfactants to form the so-called surfactant encapsulated polyoxometalate clusters (SEC).<sup>[29-34]</sup> The SECs usually are spherical nanoobjects with no aspect ratio. These SECs are however soluble in organic solvents and upon drying close packed structures of hybrid materials are obtained that yield in discrete nanoarchitectures with enhanced catalytic performances.<sup>[35,36]</sup> This charge induced self assembly in turn might suggest that high surface area materials might be accessible by taking advantage of Coulomb interactions between inorganic precursor and soft template.

Earlier, we have reported the synthesis of PB-P2VP/[SiMo<sub>12</sub>O<sub>40</sub>]<sup>4-</sup> nanocomposites (PB-P2VP = poly(butadiene-*block*-2-vinylpyridine)) using core-crosslinked PB-P2VP block copolymer nanorods as templates.<sup>[8]</sup> In the present report, the expansion of the synthesis strategy to different Keggin POMs is discussed. Keggin POMs with different charge and metal centers were used to study the general applicability of this approach. In addition, we studied the influence of calcinations on morphology and surface area. Scheme 1 summarizes our approach for the synthesis of pre-designed Keggin POM nanostructures. Firstly, a block copolymer is synthesized which microphase-separates into a well-defined cylindrical or spherical bulk structure. Generally, adjusting the volume fractions and molecular weight of the block copolymer allows a facile tunability of the dimensions and shapes of the desired polymeric template. Secondly, the dynamics of the polymeric nanostructures are frozen by crosslinking the core.<sup>[8,37]</sup> Thereby nanostructures are obtained that are resistant to changes in reaction conditions such as different pH and solvent conditions. Thirdly, the pyridine moieties in the corona are basic enough to be protonated *in situ* upon addition of the Keggin POMs which are heteropoly acids. Fourthly, by this quaternization a strong Coulomb interaction between the cationic soft template and the anionic inorganic precursors is triggered and the organic-inorganic nanocomposite precipitates.

The effect of mesostructuring and enhanced surface area on the accessibility of active sites of the as-synthesized PB-P2VP/Keggin POM composites was subsequently studied in the decomposition reaction of isopropanol. The decomposition of isopropanol over acidic sites renders the formation of propylene or diisopropyl ether, whereas over basic sites acetone is observed.<sup>[38]</sup>



Scheme 1: Schematic illustration towards Keggin POM nanowires. A) PB-*b*-P2VP diblock copolymer: The degree of polymerization is denoted by  $x$  and  $y$  for the PB- ( $x=214$ ) and P2VP-block ( $y=469$ ), respectively. B) Cylindrical bulk morphology with PB cylinders embedded in a P2VP matrix. C) After UV crosslinking dispersion in THF results in PB core-crosslinked worm-like polymeric nanowires. D) Grafting over of Keggin POM leads to polymeric Keggin POM nanowires.

## Experimental Part

*Synthesis of polymer templates.* A well-defined PB-P2VP block copolymer with 19 wt-% PB and a molecular weight of 60 kg/mol was synthesized by anionic polymerization as reported elsewhere.<sup>[9]</sup> The synthesis of the polybutadiene-poly(2-vinylpyridine) diblock copolymers (PB-P2VP) was accomplished via sequential living anionic polymerization in THF. According to NMR and GPC, coupled to a multi-angle laser light scattering detector, the polymer synthesized is  $\text{PB}_{19}\text{P2VP}_{81}^{60}$ . The subscript numbers denote the mass fraction in percent, and the superscripts give the number-average

molecular weight in kg/mol. For core-crosslinking of the block copolymer in the bulk state, a 10 wt% solution of PB-P2VP in chloroform was allowed to evaporate slowly in the presence of 10 wt% of Lucirin TPO, corresponding to the amount of polymer. After complete evaporation of the solvent and film annealing, the films were crosslinked on a UV lamp (cut-off < 350 nm) for 2 h. Subsequently, soxhlet extraction was performed in THF and the insoluble product was dispersed in THF in order to obtain soluble PB-P2VP core-crosslinked cylinders.

*Synthesis of Keggin POM nanocomposites.* 20 mL core-crosslinked worm-like PB-P2VP, polymer solution in THF (0.5 wt%) was added to 20 mL of  $5 \cdot 10^{-3}$  M Keggin POM (e.g.;  $H_3PMo_{12}O_{40} \cdot 27 H_2O$ ) in THF with continuous stirring for 2 h. With the addition of polymer solution to Keggin POM solution, coloured precipitates were produced. In this way coloured precipitates were produced by grafting coloured Keggin POMs over the polymer templates. The resultant precipitate was stirred for additional 2 h. The precipitate was washed 3 times with deionized water and freeze-dried.

*Catalysis Studies.* The decomposition of 2-propanol over supported heteropoly acids was carried out at ambient pressure in a fixed bed quartz U-shaped reactor (6 mm i. d.), kept in a tubular furnace attached to a temperature control unit. In a typical experiment, 25 mg of sample material (255-350  $\mu m$ ) were loaded into the reactor and heated thereafter in a nitrogen stream at 358 K for 2 h. Before catalytic testing, the inert gas was passed with a flow rate of 27.5 mLn/min through a saturator containing isopropanol at 293 K, which resulted in 4.2 % alcohol in the gas mixture. The temperature was held constant for 12 h time-on-stream before it was stepwise changed between 358 and 498 K. Concentrations of reactants and products were determined using an on-line gas chromatograph (Agilent 6890, HP-FFAP and HP-Plot columns).

*Instruments and measurements.* Transmission electron microscopy (TEM) was performed on a Zeiss CEM 922 and Philips CM200 LaB6 microscope at accelerating voltages of 200 kV and samples for TEM analysis were prepared by sonicating the samples in ethanol for 2 min followed by depositing one drop on a holey carbon film supported by a copper grid using a Pasteur pipette. Prior to measurements PB-P2VP nanowires where stained with  $I_2$  in order to visualize the core-corona structure.  $I_2$  preferentially interacts with the P2VP side arms.

Field-emission scanning electron microscopy (FESEM) was performed using a LEO Gemini microscope equipped with a field emission cathode. Infrared (IR) spectroscopy data was collected on a Brucker IFS66V using KBr pellets.

Powder X-Ray Diffraction (PXRD) patterns were obtained using nickel filtered Cu-K $\alpha$  radiation ( $\lambda = 1.54187 \text{ \AA}$ ) on a Bragg-Brentano-type diffractometer (XPERT-PRO, PANalytical B.V.) equipped with an X'Celerator Scientific RTMS detector. All patterns were analyzed using Panalytical's Highscore Plus software.

Nitrogen physisorption was conducted at 77 K on a Quantachrome Autosorb 1 instrument. Prior to the measurements, the samples were degassed at 120 °C for 24 h.

## Results and Discussions

*Polymer Templates.* The weight fractions are chosen in such a way that the diblock copolymer forms a cylindrical morphology in the bulk state with PB-cylinders embedded in a P2VP matrix. The unsaturated PB-cores were crosslinked using a commercial photoinitiator to lock the cylindrical structure. The core-crosslinked cylinders exhibit worm-like morphologies when dissolved in THF.

These rigid, core-crosslinked worm-like polymer nanostructures were examined by transmission electron microscopy (TEM). Images are shown in Figure 1A. The core-corona structure of the polymer template was revealed due to the different electron penetrability of the PB core and P2VP/I<sub>2</sub> corona. In case of the worm-like polymer template, the diameter of the PB core is approximately 20 nm and the P2VP corona extends ca. 35 nm around the PB-core (Figure 1A). The total diameter of the wormlike polymeric rods is ca. 90 nm.

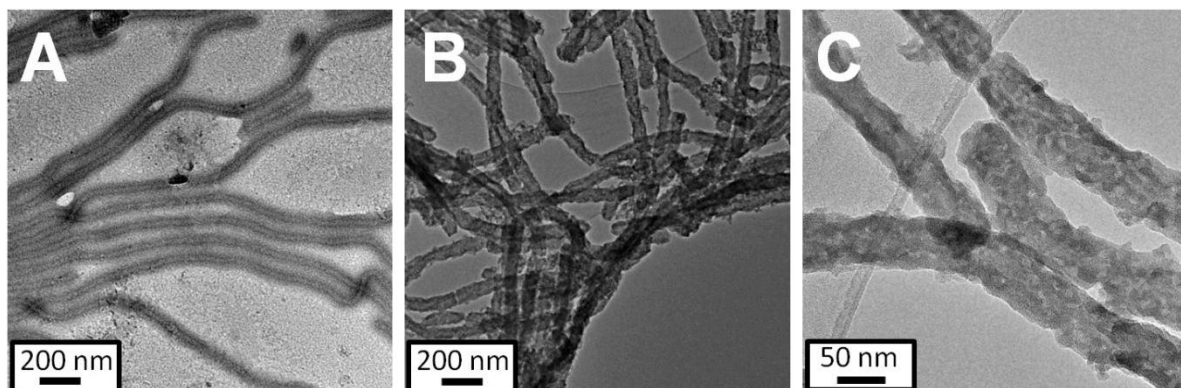


Figure 1: Representative bright-field TEM images of core-crosslinked PB-P2VP nanowires after contrasting with  $I_2$  (A) and PB-P2VP / $H_3PMo$  nanowires at different magnifications (B,C).

*Polymer-Keggin POM nanocomposites.* In an earlier report, we proved the applicability of our novel approach by grafting  $[SiMo_{12}O_{40}]^{4-}$  ions on core-crosslinked PB-P2VP block copolymer nanowires.<sup>[8]</sup> The resultant Keggin POM nanocomposites showed high surface areas and good dispersion of the Keggin POM over polymer nanowires. Similarly, in this report the polymer-Keggin POM nanocomposites are synthesized by adding the PB-P2VP polymer template solution to different Keggin POM solutions (e.g.,  $H_3PMo_{12}O_{40}$ ), also in THF. When neutral polymer templates in THF are added to the Keggin POM solution which is a heteropolyacid the 2-vinylpyridine units in the template corona will be protonated. The anionic POMs then assemble driven by strong Coulomb interactions between the cationic 2-vinylpyridinium units and the anionic Keggin POMs. The polymer-Keggin POM nanocomposites are labeled as  $BV/H_nXY$  ( $n=3,4$ ;  $X=P,Si$ ;  $Y=Mo,W$ ; see Table 1). The polymer-Keggin POM nanocomposites were characterized by using a combination of TEM, FESEM,  $N_2$  sorption measurements, PXRD, and IR measurements. For the sake of clarity, we concentrate on  $BV/H_3PMo$  nanowires, if not mentioned explicitly. The results obtained for  $BV/H_4SiMo$  and  $BV/H_3PW$  nanowires are listed in Table 1 and are presented in the supplementary information and will be addressed when appropriate.

TEM images of  $BV/H_3PMo$  nanowires are shown in Figure 1 B and C. In comparison to the pure polymer template (Figure 1A) the surface of the cylindrical nanocomposite

appeared rough. This implies the grafting of Keggin POM anions over the rigid cationic template.

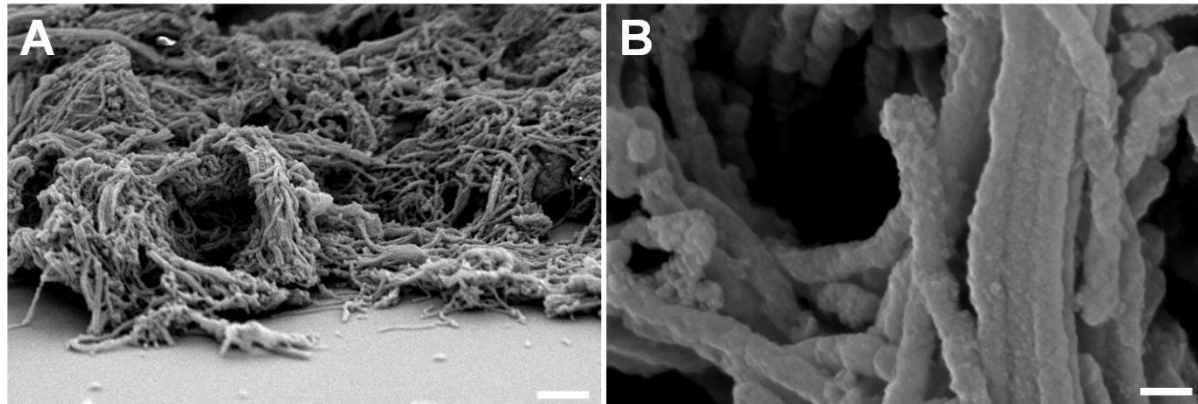


Figure 2: FESEM images at different magnification typical for non-woven spaghetti-like BV/HPMo nanowires. The scale bars are 1  $\mu\text{m}$  (A) and 100 nm (B), respectively. In (A) the stage was tilted by 75°.

The images obtained by FESEM investigations were in line with the TEM observations were (Figure 2 and Figure SI 1). Among the rough surface the FESEM images (Figure 2A) revealed that the cylindrical BV/H<sub>3</sub>PMo nanowires self-assembled into non-woven spaghetti-like microstructures. The Coulomb interactions rendered the assembly very robust. When core-crosslinked polymer nanowires were dispersed in THF solution by prolonged stirring the length of the nanowires as observed in the bulk was preserved in the solution.

Table 1. Properties of the polymer-Keggin POMs nanocomposites.

Keggin POM	Water content of the precursor per formula unit	Surface area /m <sup>2</sup> g <sup>-1</sup> <sup>a</sup>	Isopropanol conversion /%	Propylene selectivity /%
H <sub>3</sub> PMo <sub>12</sub> O <sub>40</sub>	27	62	1.3	73
H <sub>4</sub> SiMo <sub>12</sub> O <sub>40</sub>	29	50	1.7	82
H <sub>3</sub> PW <sub>12</sub> O <sub>40</sub>	28	32	0.3	89

[a] 5 point BET

The recorded N<sub>2</sub> sorption isotherm of BV/H<sub>3</sub>PMo nanowires is presented in Figure 3. The type IV isotherms showed a H3 hysteresis indicating inter-particular wedge-shaped mesopores. 5 point BET analysis revealed high surface areas for the developed Keggin POM nanocomposites. BV/H<sub>3</sub>PMo, BV/H<sub>4</sub>SiMo and BV/H<sub>3</sub>PW nanowires exhibited surface areas of 62, 50, and 32 m<sup>2</sup>g<sup>-1</sup>, respectively, whereas the commercially available corresponding crystalline Keggin POMs only have surface areas of 4, 3, and 4 m<sup>2</sup>/g. Approximately 10 to 20 times increase in surface areas was observed.

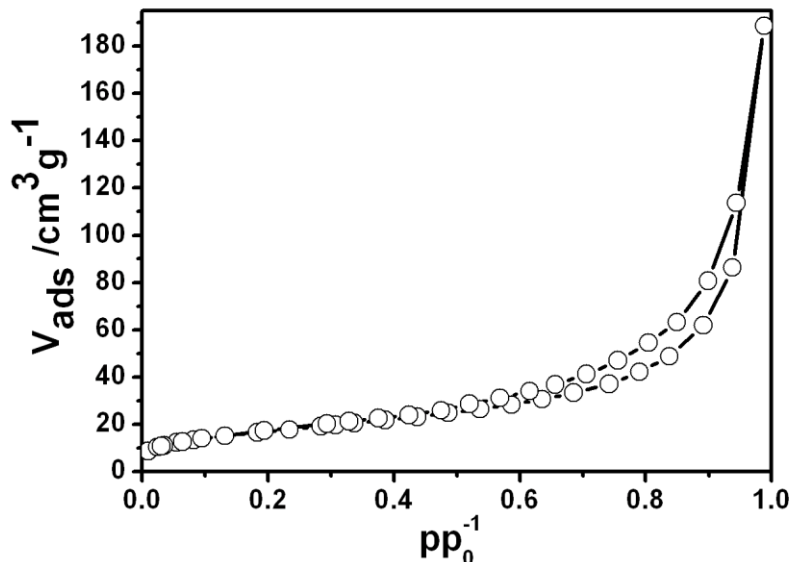


Figure 3: Nitrogen physisorption isotherm of BV/H<sub>3</sub>PMo nanowires.

In addition, wide-angle powder XRD patterns of the commercial Keggin POMs and the as-synthesized nanocomposites were recorded (see Figure 4). In contrast to the commercial Keggin POMs, PXRD patterns of the nanocomposites were amorphous which also indicated that the Keggin POM anions were well dispersed in the polymer matrix.

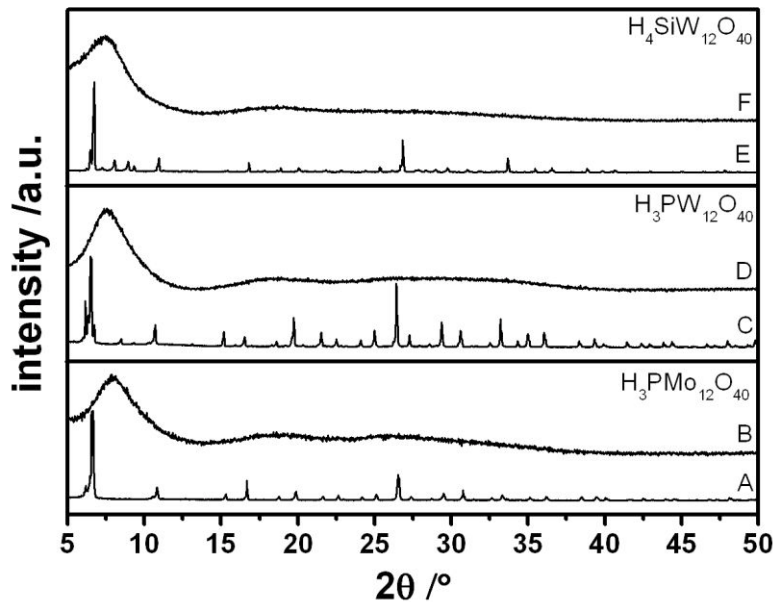


Figure 4: PXRD patterns of parent  $\text{H}_3\text{PMo}_{12}\text{O}_{40}$  (A),  $\text{H}_3\text{PW}_{12}\text{O}_{40}$  (C),  $\text{H}_4\text{SiMo}_{12}\text{O}_{40}$  (E) and the corresponding composite nanowires (B), (D) and (F), respectively.

The grafting of Keggin POM anions over polymer templates was further verified by IR analysis. IR spectra of the commercial Keggin POMs, and the Keggin POM nanocomposites are shown in Figure 5. It has been widely reported that the Keggin-type POMs show four characteristic bands, which are the fingerprint of the Keggin structure.<sup>[11,39]</sup> There are four kinds of oxygen atoms in Keggin POMs, e.g.; in  $\text{H}_3\text{PMo}_{12}\text{O}_{40}$  these 4 characteristic bands were at  $\nu_{\text{as}}$  ( $\text{Mo}-\text{O}_d$ ) –  $960 \text{ cm}^{-1}$ ,  $\nu_{\text{as}}$  ( $\text{Mo}-\text{O}_b-\text{Mo}$ ) –  $870 \text{ cm}^{-1}$ ,  $\nu_{\text{as}}$  ( $\text{Mo}-\text{O}_c-\text{Mo}$ ) –  $785 \text{ cm}^{-1}$ , and  $\nu_{\text{as}}$  ( $\text{P}-\text{O}_a$ ) –  $1065 \text{ cm}^{-1}$  whereas  $\text{H}_3\text{PW}_{12}\text{O}_{40}$  exhibits these characteristic bands at  $\nu_{\text{as}}$  ( $\text{W}-\text{O}_d$ ) –  $990 \text{ cm}^{-1}$ ,  $\nu_{\text{as}}$  ( $\text{W}-\text{O}_b-\text{W}$ ) –  $890 \text{ cm}^{-1}$ ,  $\nu_{\text{as}}$  ( $\text{W}-\text{O}_c-\text{W}$ ) –  $810 \text{ cm}^{-1}$ , and  $\nu_{\text{as}}$  ( $\text{P}-\text{O}_a$ ) –  $1080 \text{ cm}^{-1}$ . For  $\text{H}_4\text{SiMo}_{12}\text{O}$  these 4 characteristic bands were observed at  $\nu_{\text{as}}$  ( $\text{Mo}-\text{O}_d$ ) –  $952 \text{ cm}^{-1}$ ,  $\nu_{\text{as}}$  ( $\text{Mo}-\text{O}_b-\text{Mo}$ ) –  $794 \text{ cm}^{-1}$ ,  $\nu_{\text{as}}$  ( $\text{Mo}-\text{O}_c-\text{Mo}$ ) –  $864 \text{ cm}^{-1}$ , and  $\nu_{\text{as}}$  ( $\text{Si}-\text{O}_a$ ) –  $902 \text{ cm}^{-1}$ . The IR spectra of the different Keggin POM nanocomposites correspond well to the superposition of the spectra of the commercial Keggin POMs and PB-P2VP polymer templates, which is an indication that the Keggin structure stayed intact when being grafted around the polymer template. However, there is a shift observed in the frequencies for corner and edge shared Mo-O-Mo, and W-O-W vibrations which are the basal oxygens involved in the grafting of Keggin POM anions over

cylindrical PB-P2VP. Both vibrations shifted to higher wave numbers indicating a change in the degree of protonation of the Keggin POMs dispersed in the polymer matrix.

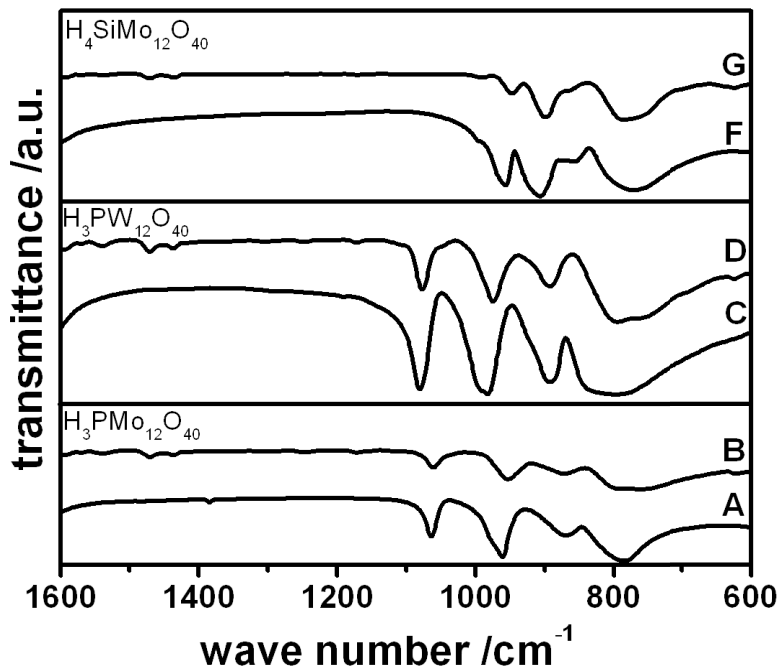


Figure 5: IR-spectra of pristine  $\text{H}_3\text{PMo}_{12}\text{O}_{40}$  (A),  $\text{H}_3\text{PW}_{12}\text{O}_{40}$  (C),  $\text{H}_4\text{SiMo}_{12}\text{O}_{40}$  (E) and the corresponding composite nanowires (B), (D) and (F), respectively.

*Decomposition of Isopropanol.* As mentioned in the introduction, HPAs especially of the Keggin Type, are widely used in acid-base catalysis. During nanocomposite formation parts of the acid sites were involved in the protonation of the pyridine units and might not contribute to the acidic strength of the nanocomposite. To answer the question whether acidic sites of the cylindrical nanocomposite could take part in the catalytic reactions vapor-phase decomposition of isopropanol was conducted as a model reaction. Isopropanol decomposes into propylene or diisopropyl ether over acidic sites, whereas over basic centers acetone is formed. However, acetone could also be produced by the oxidation of isopropanol in the presence of HPA.<sup>[38]</sup> Therefore, catalytic tests of the anisotropic composites were performed in the temperature range between 85 and 225 °C. In the present study all three BV/Keggin POM nanowires (BV/ $\text{H}_3\text{PMo}$ , BV/ $\text{H}_4\text{SiMo}$ , BV/ $\text{H}_3\text{PW}$ ) show similar catalytic behavior in the conversion of isopropanol

(Figure 6 and Figure SI 2). The temperature profile and the conversion of isopropanol are illustrated in Figure 6A. In detail, BV/H<sub>3</sub>PMo nanowires showed a maximum in isopropanol conversion of 1.3 % at 225 °C. Furthermore, the decomposition of isopropanol increased for each temperature step, followed by a subsequent exponential decrease during dwelling. These results imply that for longer time on stream the access to the acidic active sites was blocked, whereas increasing the temperature induced the reactivation of the catalytical active centers. Most likely, the blocking of the active sites was related to absorption of the reactant or products on the acidic sites of the Keggin POM unit. It is well known that polar molecules such as isopropanol or acetone can strongly absorb onto Keggin POM units forming solvated or pseudoliquid phase species. For instance an uptake of 6.3 isopropanol molecules per Keggin POM formula unit has been reported.<sup>[40]</sup> In Figure 6B the product selectivity at steady state conditions is shown. Our catalytic studies on Keggin POMs nanocomposites showed that propylene and acetone were the pre-dominantly decomposition products of isopropanol. With increasing isopropanol conversion the propylene content reached 73 %, whereas the acetone moiety monotonically decreased to 18 %. Furthermore propane and diisopropyl ether were formed. An increase in temperature shifted the selectivity toward propylene indicating a more favorable decomposition of isopropanol over acidic sites in agreement with results published earlier.<sup>[41]</sup> The formation of acetone was considered to be a result of isopropanol oxidation accompanied by a reduction of the Keggin clusters which has a stronger influence at lower temperatures. In line with this observation, the BV/H<sub>3</sub>PMo nanowires showed a color change from green to blue after the catalytic tests which is consistent with a partially reduction of the Keggin units forming the so called molybdenum blues (see Figure SI 3).

The selectivity for propylene increased in the order of BV/H<sub>3</sub>PMo (73 %) < BV/H<sub>4</sub>SiMo (82 %) < BV/H<sub>3</sub>PW (89 %). Beside, the maximum conversion of isopropanol increased in the series: BV/HPW (0.3 %) < BV/HPMo (1.3 %) < BV/HSiMo (1.7 %).

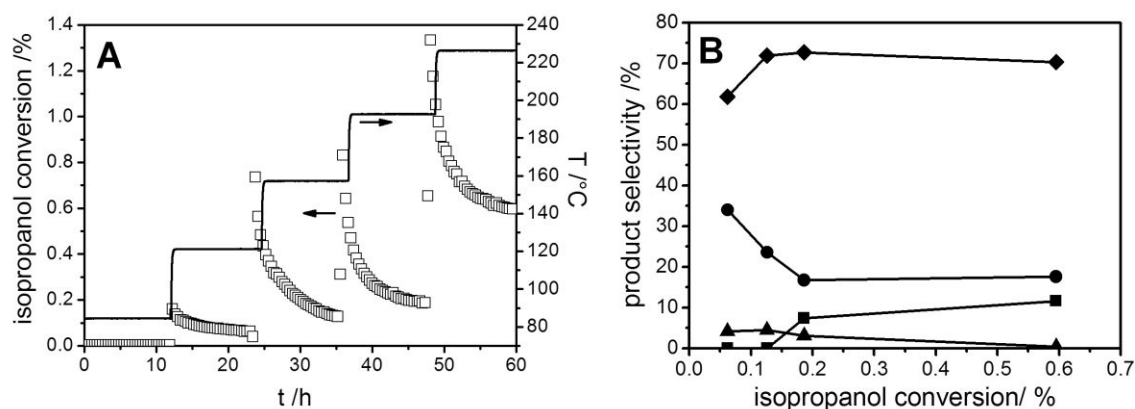


Figure 6: Typical catalytic performance of BV/HPMo nanocomposite in the vapor-phase decomposition of isopropanol: A) Isopropanol conversion versus time and temperature and B) product selectivity at steady-state conditions. The following decomposition products were obtained: triangles: disiopropyl ether, squares: propane, circles: acetone, rhombus: propylene.

It should be mentioned that during catalysis, the anisotropic nature of the nanocomposite and structure of the Keggin unit were retained (Figure SI 4 and 5).

### Conclusion.

In summary we explored the grafting of different Keggin POMs ( $\text{H}_3\text{PMo}$ ,  $\text{H}_4\text{SiMo}$ ,  $\text{H}_3\text{PW}$ ) over ionizable core-crosslinked PB-b-P2VP nanorods. All PB-b-P2VO/ Keggin POM nanorods self-assembled into non-woven spaghetti-like microstructures and possessed high surface area compared to the pristine HPAs. Furthermore, they show activity in the acid catalysed decomposition of isopropanol and high selectivity for the corresponding decomposition product propylene in the order  $\text{HPW} < \text{HPMo} < \text{HSiMo}$  and  $\text{HPMo} < \text{HSiMo} < \text{HPW}$ , respectively.

**Acknowledgment.** This work was supported by the Deutsche Forschungsgemeinschaft (DFG) within the Collaborative Research Center (SFB) 840. T. L. thanks the international graduate school of the ENB “Structures, Reactivity and Properties of Metal Oxides” for a fellowship.

**Supporting Information.** Supporting Information is available in the www.

## References

- [1.] F. Hoffmann, M. Cornelius, J. Morell, M. Fröba, *Angew. Chem. Int. Ed.* **2006**, *45*, 3216-3251.
- [2.] R. Ulrich, J. W. Zwanziger, S. M. De Paul, A. Reiche, H. Leuninger, H. W. Spiess, U. Wiesner, *Adv. Mater.* **2002**, *14*, 1134-1137.
- [3.] Z. Huang, W. Bensch, W. Sigle, P. A. van Aken, L. Kienle, T. Vitoya, H. Modrow, T. Ressler, *J. Mater. Sci.* **2008**, *43*, 244-253.
- [4.] S. Förster, *Colloid Chemistry 1* **2003**, *226*, 1-28.
- [5.] A. C. Finnefrock, R. Ulrich, A. Du Chesne, C. C. Honeker, K. Schumacher, K. K. Unger, S. M. Gruner, U. Wiesner, *Angew. Chem. Int. Ed.* **2001**, *40*, 1207.
- [6.] F. Schüth, *Angew. Chem. Int. Ed.* **2003**, *42*, 3604-3622.
- [7.] S. A. Davis, M. Breulmann, K. H. Rhodes, B. Zhang, S. Mann, *Chem. Mater.* **2001**, *13*, 3218-3226.
- [8.] R. S. Yelamanchili, A. Walther, A. H. E. Müller, J. Breu, *Chem. Commun.* **2008**, *4*, 489-491.
- [9.] A. Walther, A. S. Goldmann, R. S. Yelamanchili, M. Drechsler, H. Schmalz, A. Eisenberg, A. H. E. Müller, *Macromolecules* **2008**, *41*, 3254-3260.
- [10.] M.T.Pope and A.Müller, *Polyoxometalate Chemistry From Topology via Self-Assembly to Applications*, Kluwer Academic Publishers, Netherlands **2001**.
- [11.] J.B.Moffat, in *Metal-Oxygen Clusters - The Surface and Catalytic Properties of Heteropoly Oxometalates*, Kluwer Academic / Plenum Publishers, New York **2001**.
- [12.] C. Rocchicciolideltcheff, A. Aouissi, M. Bettahar, S. Launay, M. Fournier, *J. Catal.* **1996**, *164*, 16-27.
- [13.] K. Okamoto, S. Uchida, T. Ito, N. Mizuno, *J. Am. Chem. Soc.* **2007**, *129*, 7378-7384.
- [14.] K. Nomiya, H. Murasaki, M. Miwa, *Polyhedron* **1986**, *5*, 1031-1033.
- [15.] D. E. Katsoulis, *Chem. Rev.* **1998**, *98*, 359-387.
- [16.] T. Blasco, A. Corma, A. Martinez, P. Martinez-Escolano, *J. Catal.* **1998**, *177*, 306-313.

- [17.] C. T. Kresge, M. E. Leonowicz, W. J. Roth, J. C. Vartuli, J. S. Beck, *Nature* **1992**, 359, 710-712.
- [18.] C. F. Shi, R. W. Wang, G. S. Zhu, S. L. Qiu, J. Long, *Eur. J. Inorg. Chem.* **2005**, 4801-4807.
- [19.] L. Yang, Y. T. Qi, X. D. Yuan, H. Shen, J. Kim, *J. Mol. Catal. A: Chem.* **2005**, 229, 199-205.
- [20.] S. Y. Yu, L. P. Wang, B. Chen, Y. Y. Gu, J. Li, H. M. Ding, Y. K. Shan, *Chem. A Eur. J.* **2005**, 11, 3894-3898.
- [21.] D. Y. Zhao, J. L. Feng, Q. S. Huo, N. Melosh, G. H. Fredrickson, B. F. Chmelka, G. D. Stucky, *Science* **1998**, 279, 548-552.
- [22.] D. Y. Zhao, Q. S. Huo, J. L. Feng, B. F. Chmelka, G. D. Stucky, *J. Am. Chem. Soc.* **1998**, 120, 6024-6036.
- [23.] P. M. Rao, A. Wolfson, S. Kababya, S. Vega, M. V. Landau, *J. Catal.* **2005**, 232, 210-225.
- [24.] H. S. Yun, M. Kuwabara, H. S. Zhou, I. Honma, *Thin Solid Films* **2007**, 515, 2842-2846.
- [25.] G. G. Janauer, A. Doble, J. D. Guo, P. Zavalij, M. S. Whittingham, *Chem. Mater.* **1996**, 8, 2096-2101.
- [26.] A. Stein, M. Fendorf, T. P. Jarvie, K. T. Müller, A. J. Benesi, T. E. Mallouk, *Chem. Mater.* **1995**, 7, 304-313.
- [27.] A. Taguchi, T. Abe, M. Iwamoto, *Adv. Mater.* **1998**, 10, 667-669.
- [28.] R. F. Zhang, C. Yang, *J. Mater. Chem.* 2008, 18, 2691-2703.
- [29.] W. Li, W. Bu, H. Li, L. Wu, M. Li, *Chem. Commun.* **2005**, 3785-3787.
- [30.] H. Li, W. Qi, W. Li, H. Sun, W. Bu, L. Wu, *Adv. Mater.* **2005**, 17, 2688-2692.
- [31.] Y. L. Wang, W. Li, L. X. Wu, *Langmuir* **2009**, 25, 13194-13200.
- [32.] S. Polarz, B. Smarsly, M. Antonietti, *Chem. Phys. Chem.* **2001**, 2, 457-461.
- [33.] Y. K. Han, Z. J. Zhang, Y. L. Wang, N. Xia, B. Liu, Y. Xiao, L. X. Jin, P. Zheng, W. Wang, *Macromol. Chem. Phys.* **2011**, 212, 81-87.

- [34.] X. K. Lin, Y. L. Wang, L. X. Wu, *Langmuir* **2009**, *25*, 6081-6087.
- [35.] A. Nisar, Y. Lu, J. Zhuang, X. Wang, *Angew. Chem. Int. Ed.* **2011**, *50*, 3187-3192.
- [36.] G. Maayan, R. Popovitz-Biro, R. Neumann, *J. Am. Chem. Soc.* **2006**, *128*, 4968-4969.
- [37.] R. K. O'Reilly, C. J. Hawker, K. L. Wooley, *Chem. Soc. Rev.* **2006**, *35*, 1068-1083.
- [38.] A. Gervasini, A. Auroux, *J. Catal.* **1991**, *131*, 190-198.
- [39.] C. Rocchicciolieltcheff, M. Fournier, R. Franck, R. Thouvenot, *Inorg. Chem.* **1983**, *22*, 207-216.
- [40.] D. E. Katsoulis, *Chem. Rev.* **1998**, *98*, 359-387.
- [41.] D. Park, S. Lee, J. Lee, S. Song, H. Kim, J. Song, I. Song, *Catal. Lett.* **2008**, *126*, 308-312.

**Supporting Information.**

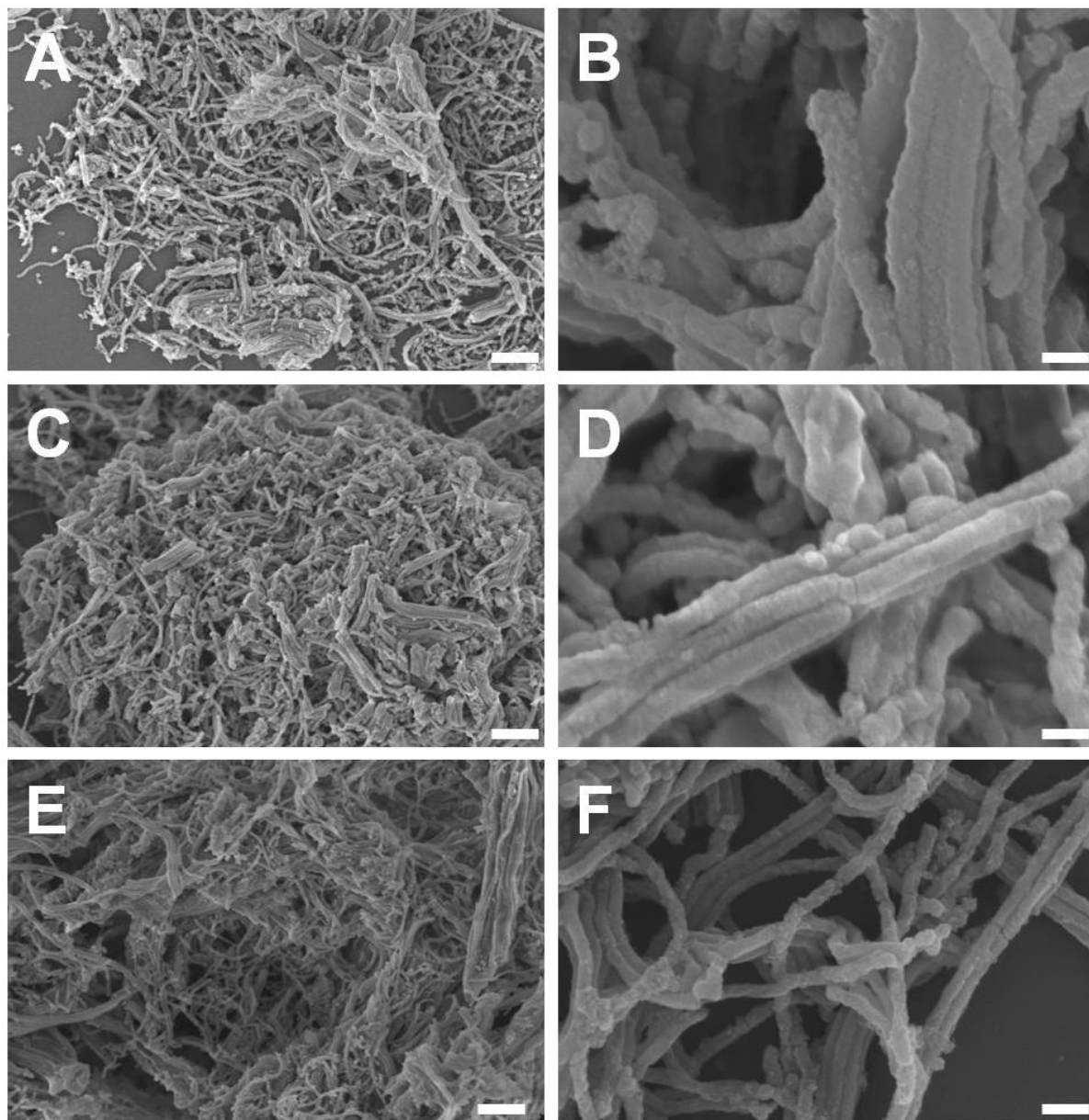


Figure SI 1: SEM images of BV/Keggin POM nanowires at different magnification: A) and B) H<sub>3</sub>PMo, C) and D) H<sub>4</sub>SiMo, E) and F) H<sub>3</sub>PW.

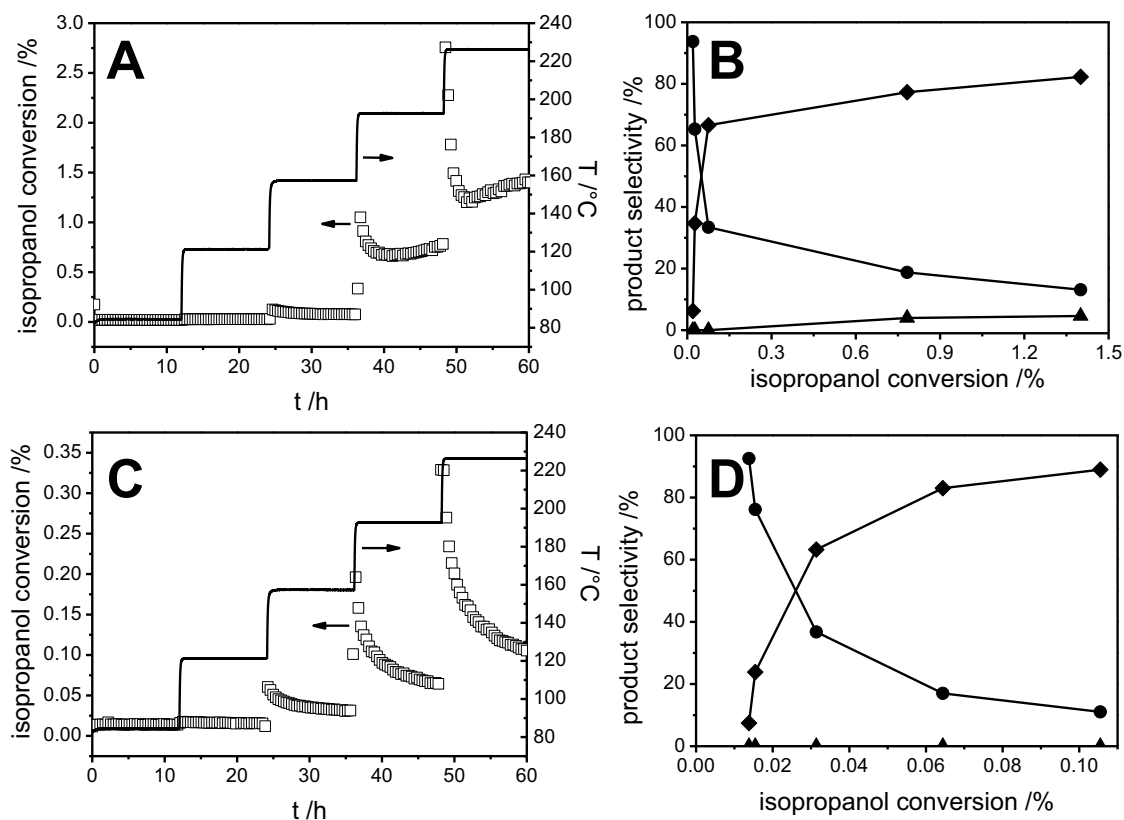


Figure SI 2: Typical catalytic performance of  $\text{BV}/\text{H}_4\text{SiMo}$  (A and B) and  $\text{BV}/\text{H}_3\text{PW}$  nanowires (C and D) in the vapor-phase decomposition of isopropanol: A) Isopropanol conversion versus time and temperature and B) product selectivity at steady-state conditions for  $\text{BV}/\text{H}_4\text{SiMo}$  nanowires. C) Isopropanol conversion versus time and temperature and D) product selectivity at steady-state conditions for  $\text{BV}/\text{H}_3\text{PW}$  nanowires. The following decomposition products were obtained: disiopropyl ether (triangles), propane (squares), acetone (circles), propylene (rhombus).

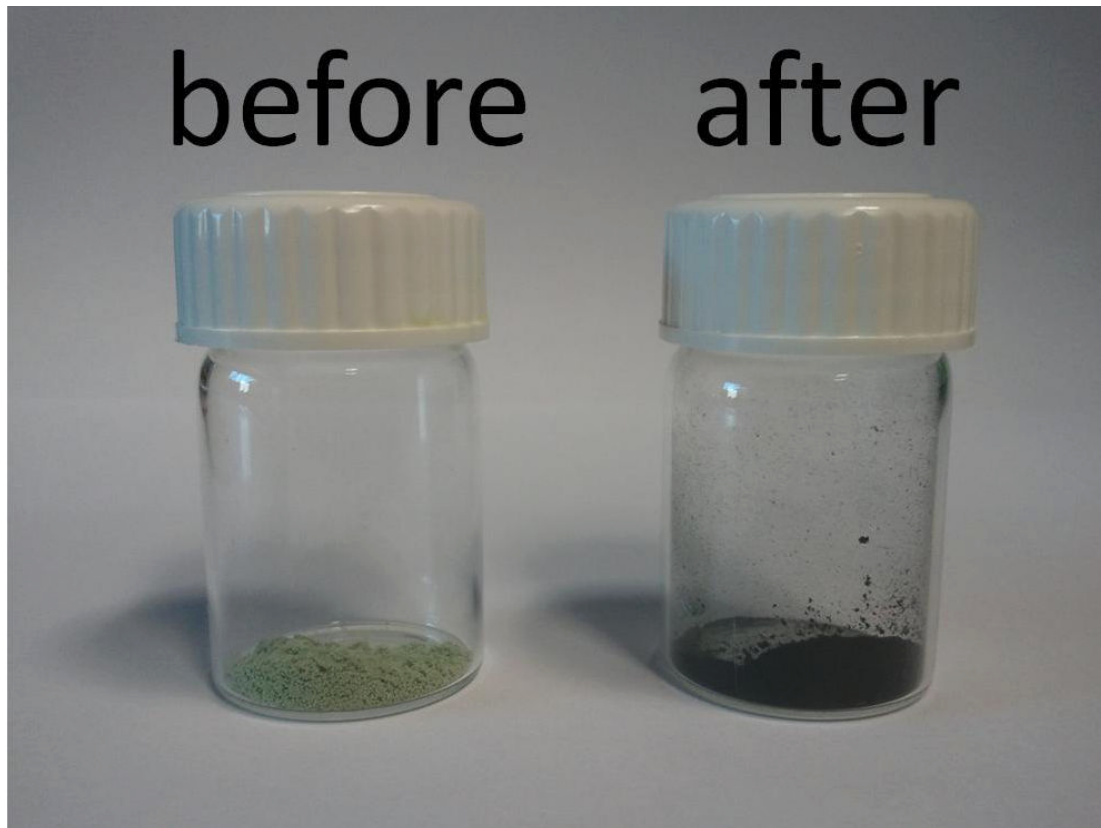


Figure SI 3: BV/H<sub>3</sub>PMo nanowires bevor (left) and after (right) catalytic tests.

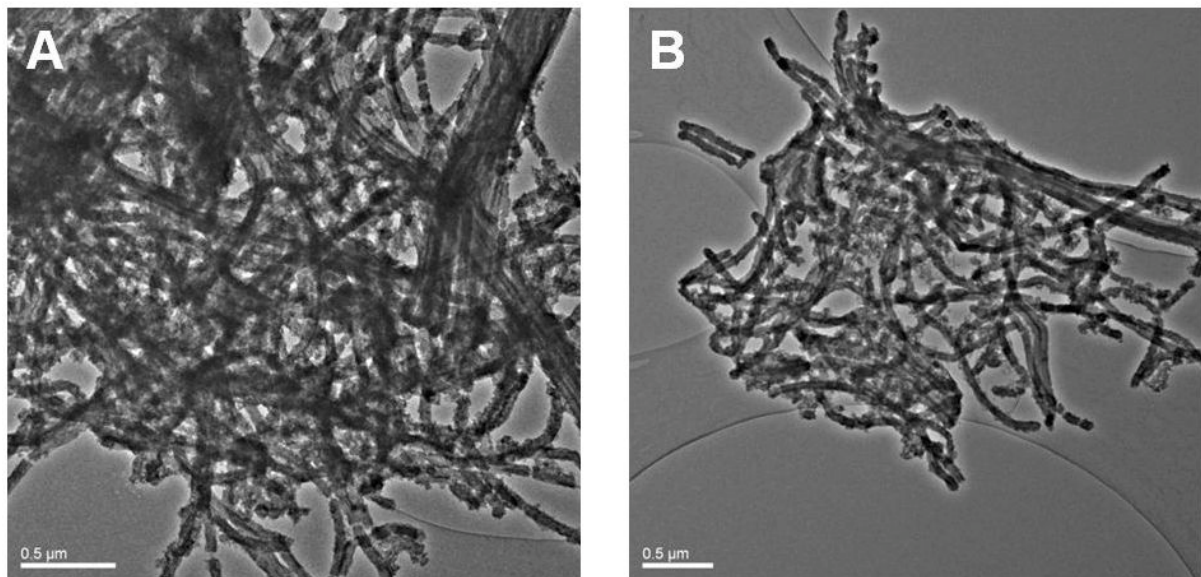


Figure SI 4: TEM images of BV/ H<sub>3</sub>PMo nanowires before (A) and after (B) catalytic tests. The wire-like shape was retained.

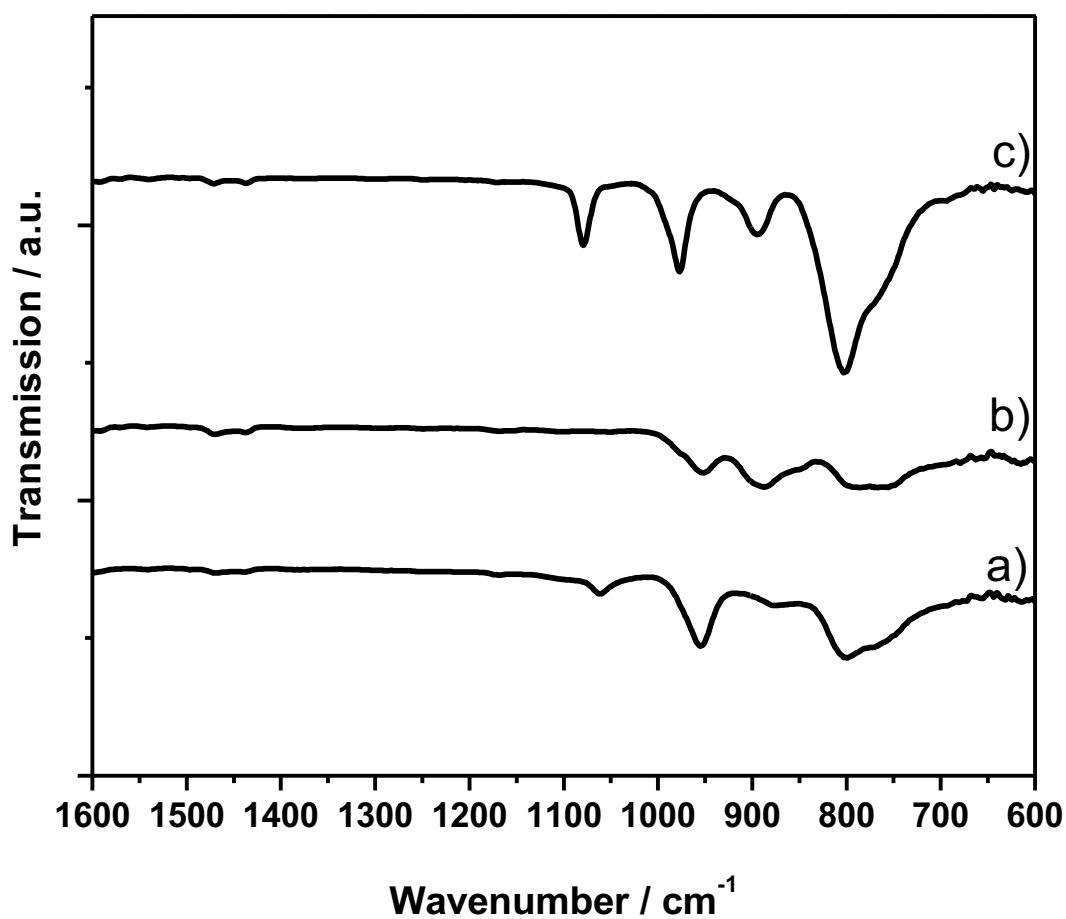


Figure SI 5: IR spectra of BV/ Keggin POM nanowires after catalytic tests: a) H<sub>3</sub>PW, b) H<sub>4</sub>SiMo, c) H<sub>3</sub>PMo.

## 7.5 Direct Synthesis of Inverse Hexagonally Ordered Diblock Copolymer/Polyoxometalate Nanocomposite Films

Thomas Lunkenbein,<sup>1</sup> Marleen Kamperman,<sup>2,\*</sup> Zihui Li,<sup>3</sup> Carina Bojer,<sup>1</sup> Markus Drechsler,<sup>4</sup> Stephan Förster,<sup>5</sup> Ulrich Wiesner,<sup>3</sup> Axel H.E. Müller,<sup>4</sup> and Josef Breu<sup>1,\*</sup>

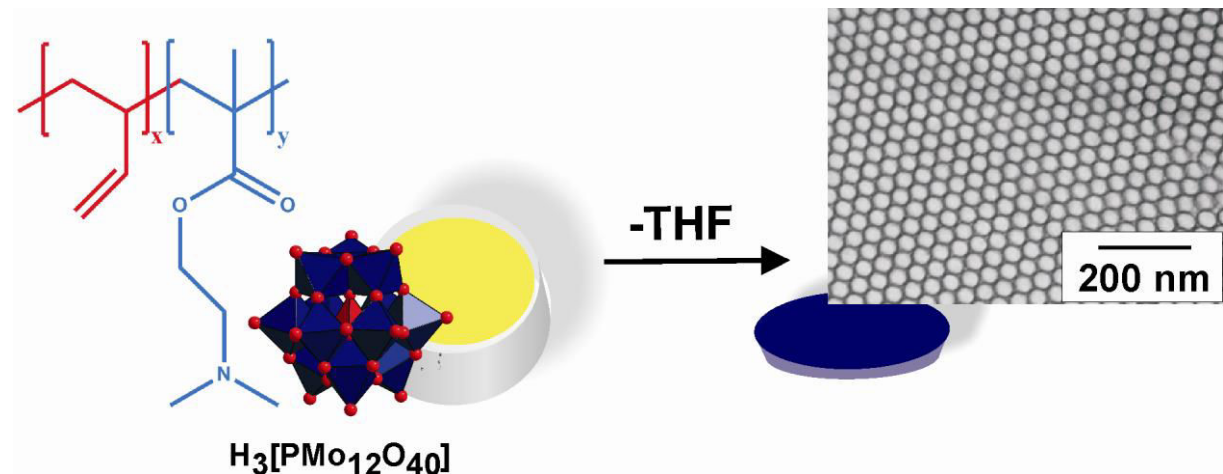
<sup>1</sup>Lehrstuhl für Anorganische Chemie I, Universität Bayreuth, 95440 Bayreuth, Germany

<sup>2</sup>Physical Chemistry and Colloid Science Wageningen University, NL-6703 HB Wageningen, Netherlands

<sup>3</sup>Materials Science & Engineering Cornell University Ithaca, NY 14853, USA

<sup>4</sup>Lehrstuhl für Makromolekulare Chemie II, Universität Bayreuth, 95440 Bayreuth, Germany

<sup>5</sup>Lehrstuhl für Physikalische Chemie I, Universität Bayreuth, 95440 Bayreuth, Germany



**Abstract.**

Nanostructured inverse hexagonal polyoxometalate composite films were cast directly from solution using poly(butadiene-block-2-(dimethylamino)ethyl methacrylate) (PB-b-PDMAEMA) diblock copolymers as structure directing agents for phosphomolybdic acid ( $H_3[PMo_{12}O_{40}]$ ,  $H_3PMo$ ).  $H_3PMo$  units are selectively incorporated into the PDMAEMA domains due to electrostatic interactions between protonated PDMAEMA and  $PMo^{3-}$  anions. Long solvophilic PB chains stabilized the PDMAEMA/ $H_3PMo$  aggregates in solution and reliably prevented macrophase separation. The choice of solvent is crucial. It appears that all three components, both blocks of the diblock copolymer as well as  $H_3PMo$ , have to be soluble in the same solvent which turned out to be tetrahydrofuran, THF. Evaporation induced self-assembly resulted in highly ordered inverse hexagonal nanocomposite films as observed from transmission electron microscopy and small angle X-ray scattering. This one-pot synthesis may represent a generally applicable strategy for integrating polyoxometalates into functional architectures and devices.

**Keywords.** Polyoxometalate, hexagonal, diblock copolymer, evaporation induced self-assembly, electrostatic interaction

## Introduction

Polyoxometalates (POMs) are early transition metal oxide clusters of distinct charge, size, and shape.<sup>1-5</sup> In particular Keggin-type heteropolyoxometalates (Keggin POMs) have found wide-spread application in fields of catalysis, electrochemistry and host guest chemistry as a consequence of their structural, chemical and electronical diversity.<sup>3;6-10</sup> However, integration of Keggin POMs into ordered hybrid architectures remains challenging. When combining highly hydrophilic POMs with hydrophobic organic structure directing agents, stabilization of the resulting hybrid materials in solvents that would allow controlled self assembly is difficult. To meet this challenge, several strategies were developed to manipulate the surface properties of POMs.<sup>11;12</sup> For instance, phase transfer of POMs into hydrophobic solvents was accomplished by exchanging the counterions with cationic molecular surfactants generating so-called surfactant encapsulated polyoxometalate clusters.<sup>13-21</sup> Polarz *et al.* applied a smart approach where the structure directing surfactants were covalently attached to POM head groups.<sup>22;23</sup> In a separate step, these organophilic POMs could then be processed into thin hexagonally ordered films using e.g. Langmuir-Blodgett techniques.

Discrete micellar, vesicular and worm-like nanoobjects were obtained when amphiphilic diblock copolymers were used to generate hybrid materials.<sup>24;25</sup> With core-crosslinked diblock copolymers non-woven structures could be fabricated from discrete worm-like nanohybrids.<sup>26</sup> Direct preparation of ordered nanostructured diblock copolymer/Keggin POM films as is well established for instance for inverse hexagonal TiO<sub>2</sub> films<sup>27</sup> has not been reported. Most likely this is related to the difficulties encountered in stabilizing hybrid materials of strongly interacting Keggin POM anions and organic cations at high concentrations and high Keggin loadings. Hexagonally packed cylinder structures (POMs segregated in the matrix surrounding cylinders, see Scheme 1) and bicontinuous morphologies would, however, be of particular interest, because of increased robustness and proton conductivity.<sup>28</sup> Moreover, those morphologies can easily be transformed to porous metal carbides.<sup>29</sup>

Here we describe a generally applicable strategy for producing inverse hexagonally ordered diblock copolymer/POM nanocomposite films by simple evaporation of the solvent similar to the evaporation induced self-assembly (EISA) processes reported earlier.<sup>30;31</sup>

## Experimental Part

*Synthesis of Poly(butadiene-block-2-(dimethylamino)ethyl methacrylate) (PB-b-PDMAEMA) diblock copolymer.* The diblock copolymer PB-b-PDMAEMA was synthesized by sequential living anionic polymerization in tetrahydrofuran (THF) as published elsewhere.<sup>32</sup> THF- gel permeation chromatography (GPC) was used to determine the molecular weight of the first block (polybutadiene, PB) using a PB calibration curve. The polydispersity index (PDI) of the diblock copolymer was determined by Salt- GPC in the presence of 0.25 wt % tributylammonium bromide and THF as eluent. In both cases THF was HPLC grade (Aldrich), and measurements were conducted at room temperature (RT) and at flow rates of 0.5 mL/min. <sup>1</sup>H-NMR was used to determine the chemical composition of the diblock copolymer. The resulting PB-b-PDMAEMA polymer had a molar mass of 29 kg/mol, a weight fraction of 22 wt % of PDMAEMA, and a PDI of 1.03.

*Synthesis of composites.* Phosphomolybdic acid ( $\text{H}_3[\text{PMo}_{12}\text{O}_{40}]$ ,  $\text{H}_3\text{PMo}$ , p.a.) was obtained from Aldrich. X-ray diffraction showed it to be a mixture of different hydrated phases. Therefore, it was recrystallized from water and stored at 86 % relative humidity (RH) in order to assure a defined stoichiometry.<sup>33</sup> Under these conditions a crystalline material was obtained containing 27 water molecules per formula unit as confirmed by thermogravimetric analysis (Figure SI 1). THF (p.a., Aldrich) was distilled to remove the stabilizer. In a typical block copolymer/ $\text{H}_3\text{PMo}$  nanocomposite synthesis, 0.1 g of the block copolymer was dissolved in THF (approx. 2 mL). The solution of the polymer was filtered (0.2  $\mu\text{m}$ , TEFLO<sup>N</sup>) and added to a separate solution of  $\text{H}_3\text{PMo}$  in 3 mL THF at RT under continuous stirring. After 30 min, the clear yellowish solution was poured into a TEFLO<sup>N</sup> petri dish (diameter: 3.2 cm) which was placed in an exsiccator kept at 32 % RH and RT (Figure SI 2). The Petri dish was covered by a hemispherical glass cap to control the evaporation rate of the solvent during EISA. Following this procedure, films with different  $\text{H}_3\text{PMo}$  content were prepared, as listed in Table 2.

*Characterization of the composite solution.* For cryogenic transmission electron microscopy (*cryo*-TEM) studies, a drop of the solution in THF was put on a lacey carbon filmed TEM copper grid. Most of the liquid was removed with blotting paper, leaving a thin liquid film stretched over the lace. The specimens were instantly vitrified by rapid immersion into liquid nitrogen in a temperature controlled freezing unit (Zeiss Cryobox, Zeiss NTS GmbH, Oberkochen, Germany). The frozen specimens were inserted to a Zeiss

EM 922 OMEGA EF-TEM using a cryo transfer holder (CT3500, Gatan, München, Germany) and kept at temperatures around 90 K. The transmission electron microscope was operated at an acceleration voltage of 200 kV. Zero-loss filtered images ( $\Delta E = 0$  eV) were taken under reduced dose conditions (100–1000 e/nm<sup>2</sup>). All images were registered digitally by a bottom mounted CCD camera system (Ultrascan 1000, Gatan) combined and processed with a digital imaging processing system (Gatan Digital Micrograph 1.8).

*Characterization of inverse hexagonally ordered films.* Small angle X-ray scattering (SAXS) data were collected at the Cornell High Energy Synchrotron Source (CHESS) applying a CCD 2-D detector. X-ray energies of 1.378 Å and 1.252 Å were used and the sample-to-detector distance was 352.02 cm and 371.58 cm, respectively. The fitting of the SAXS data was accomplished with the program SCATTER by Förster et al.<sup>34,35</sup>

Brightfield transmission electron microscopy (TEM) images were taken on a Zeiss CEM902 and a Zeiss EM922Omega operated at an acceleration voltage of 80 kV and 200 kV, respectively. As-synthesized composite films were microtomed under cryogenic conditions and placed on a lacey carbon filmed copper grid.

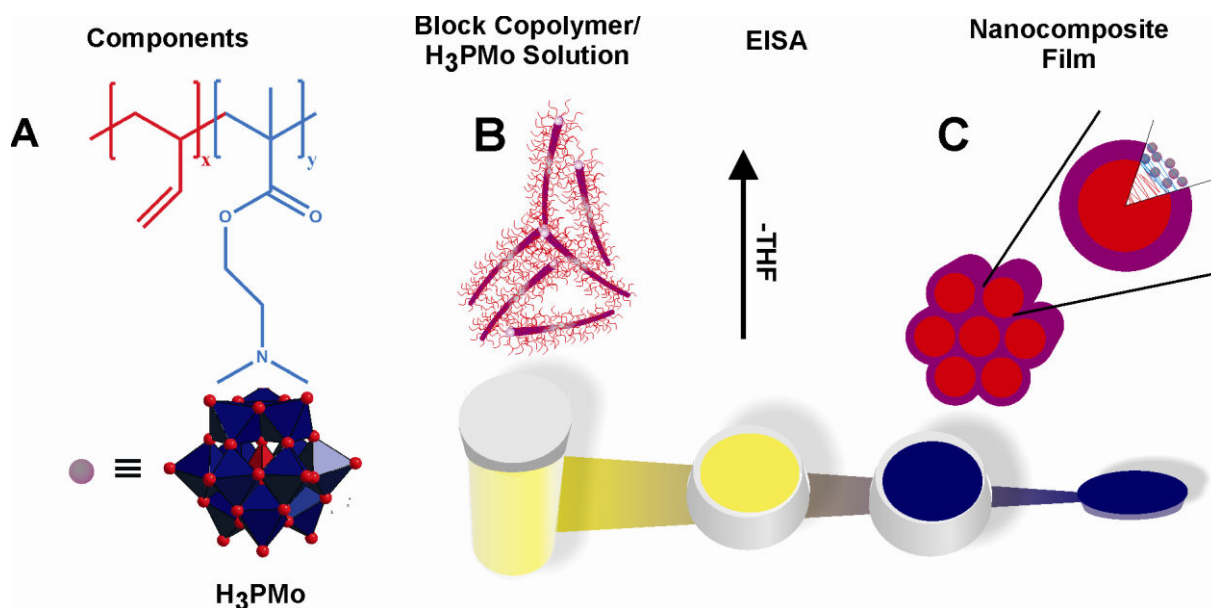
Fourier-transformed infrared (FTIR) data were collected on a Bruker IFS66V using KBr pellets.

Powder X-Ray Diffraction (PXRD) patterns were obtained using nickel filtered Cu-K $\alpha$  radiation ( $\lambda = 1.54187$  Å) on a Bragg-Brentano-type diffractometer (XPERT-PRO, PANalytical B.V.) equipped with an X'Celerator Scientific RTMS detector. All patterns were analyzed using Panalytical's Highscore Plus software.

## Results and Discussion

Scheme 1 summarizes the one-pot route to inverse hexagonally ordered diblock copolymer/POM nanocomposite films. Well-ordered homogeneous nanocomposites can only be obtained if POMs are preferentially incorporated to one domain of the block copolymer and macrophase separation during self assembly is prevented by assuring good solubility of the composite even at high polymer and POM concentrations. To meet these requirements it was important to characterize the solution (Scheme 1B) to be able to optimize the process parameters.

**Scheme 1: Illustration of one-pot direct synthesis of PB-b-PDMAEMA/H<sub>3</sub>PMo nanocomposite films.**



A) Chemical structure of PB-b-PDMAEMA (top) and H<sub>3</sub>PMo (bottom). DP: x = 411 and y = 40. B) Micelle formation in solution with PB chains assuring solubility. C) Inverse hexagonally ordered PB-b-PDMAEMA/H<sub>3</sub>PMo nanocomposite film with PB cylinders in a PDMAEMA/H<sub>3</sub>PMo matrix.

*Characterization of the solution.* PB-b-PDMAEMA was selected as structure directing agent (SDA). The amine function of the PDMAEMA block is sufficiently basic to be protonated by H<sub>3</sub>PMo.<sup>36</sup> THF was selected as solvent since both, the diblock copolymer and H<sub>3</sub>PMo are soluble in it. Moreover, as will be discussed later, THF also is a good solvent for the second block (PB) which is not involved in the composite formation and thus assures the solubility of the PB-b-PDMAEMA/H<sub>3</sub>PMo complex. PB<sub>411</sub>-b-PDMAEMA<sub>40</sub> was synthesized by sequential living anionic polymerization. The subscripts denote the degree of polymerization (DP) of the corresponding blocks.

Both H<sub>3</sub>PMo (diameter: 1.0 – 1.1 nm<sup>2;21</sup>) and PDMAEMA homopolymer ( $\chi_{\text{PDMAEMA-THF}} = 0.003$ , for details of the calculation of Flory-Huggins interactions parameters,  $\chi$ , see SI, chapter III) are highly soluble in THF.<sup>37</sup> First, a diblock copolymer solution in THF was added slowly to the H<sub>3</sub>PMo solution in THF while stirring at RT. This solution stayed clear even at high composite concentrations (90 wt %) containing 83 wt % of H<sub>3</sub>PMo

(Figure SI 3). After proton transfer, triply charged  $\text{PMo}^{3-}$  strongly interacted with the PDMAEMA cations.<sup>38;39</sup> These electrostatic interactions result in the formation of collapsed and insoluble PDMAEMA/ $\text{H}_3\text{PMo}$  complexes.<sup>38;39</sup> When  $\text{H}_3\text{PMo}$  was added to a PDMAEMA homopolymer solution in THF instant precipitation of the complex was observed (Figure 1A). Contrary to this, no precipitate is formed when adding  $\text{H}_3\text{PMo}$  to PB-b-PDMAEMA. This is because the hydrophobic PB block is also highly soluble in THF ( $\chi_{\text{PB-THF}} = 0.11$ ) and therefore capable of keeping the attached PDMAEMA/ $\text{H}_3\text{PMo}$  complex in solution (Figure 1B and Figure SI 4). Clearly, the solvent plays a key role. For instance acetone, a slightly poorer solvent for PB ( $\chi_{\text{PB-acetone}} = 0.36$ ), was already no longer capable to dissolve PB-b-PDMAEMA/ $\text{H}_3\text{PMo}$  complexes (Figure 1C). Furthermore, the DP of the PB had to be higher than the one for the hydrophilic block to keep the complex in solutionI (Figure SI 5).

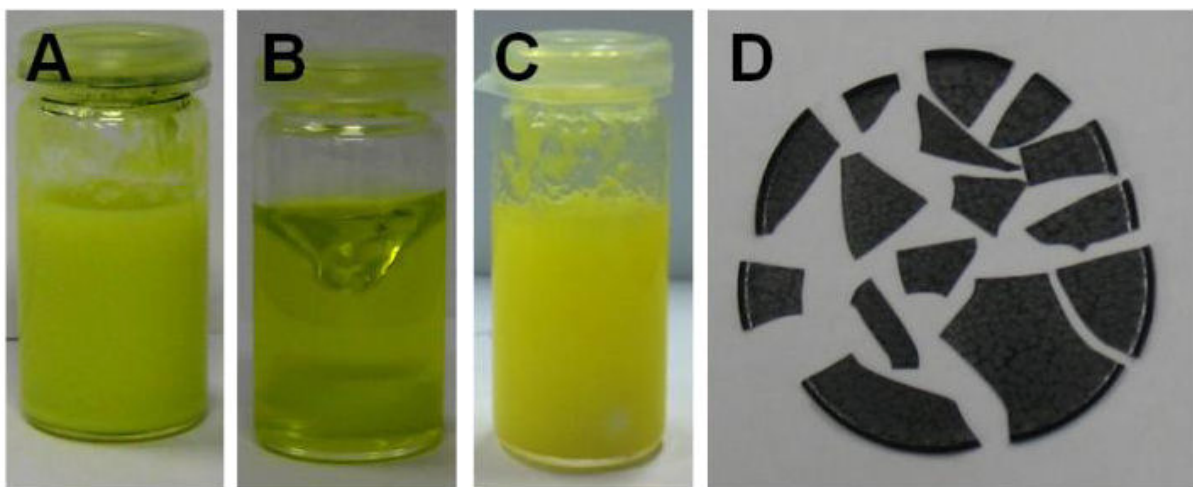


Figure 1: Photographs of: A) PDMAEMA homopolymer in the presence of  $\text{H}_3\text{PMo}$  in THF, B) PB-b-PDMAEMA with  $\text{H}_3\text{PMo}$  in THF and C) PB-b-PDMAEMA with  $\text{H}_3\text{PMo}$  in acetone. In all cases the  $\text{H}_3\text{PMo}$  content was 70 wt % related to the amount of diblock copolymer and the overall concentration of the PB-b-PDMAEMA/ $\text{H}_3\text{PMo}$  complex was 80 g/L. D) As-synthesized PB-b-PDMAEMA/ $\text{H}_3\text{PMo}$  composite film as obtained for a  $\text{H}_3\text{PMo}$  loading of 70 wt %.

Micelle formation in THF-solutions was systematically studied by cryo-TEM imaging as a function of  $\text{H}_3\text{PMo}$  loading of the PB-b-PDMAEMA/ $\text{H}_3\text{PMo}$  complex. Representative micrographs of three solutions containing complexes with decreasing PB-b-

PDMAEMA/H<sub>3</sub>PMo ratio are shown (3.23, 1.08 and 0.54) in Figure , dimensions of the solution structures are given in Table 1. Contrast in TEM micrographs arises from electron density differences between PB and PDMAEMA/H<sub>3</sub>PMo domains. The insoluble PDMAEMA/H<sub>3</sub>PMo domains appear dark and PB domains grayish or undistinguishable from THF inclusions. Figure 2A corresponds to an H<sub>3</sub>PMo content of 44 wt % and shows spherical micelles. The PDMAEMA/H<sub>3</sub>PMo core diameter was 17 ± 3 nm and was stabilized by the PB chains. The PB-b-PDMAEMA/H<sub>3</sub>PMo composite with a higher H<sub>3</sub>PMo content of 70 wt % showed a 3D bicontinuous network (BCN) with typical 3- and 4- fold network junctions, loops and end-caps (Figure 2B and Figure SI 6). The observed core diameter was slightly decreased (13 ± 3 nm) compared to the spherical micelles. Further increase of H<sub>3</sub>PMo content to 83 wt % resulted in a transition to vesicles (Figure 2C). The vesicles had PDMAEMA/H<sub>3</sub>PMo wall thicknesses of 8 ± 2 nm and were fairly monodisperse with inner diameters of 22 to 30 nm.

The sequence of morphologies observed in solution upon mixing H<sub>3</sub>PMo with PB-b-PDMAEMA was in line with the expected preferential electrostatic interaction of H<sub>3</sub>PMo with the PDMAEMA domains of the block copolymer inducing the phase transitions with increasing loadings.

The morphological changes resemble those previously documented for selective diblock copolymers<sup>40</sup> (with one solvophilic and one solvophobic block) and can be explained by molecular packing considerations. That is, with increasing H<sub>3</sub>PMo content, the solvophilic and solvophobic volumes become more symmetric, leading to diminished chain stretching,  $S_c$  (see Table 1), and decreased interfacial curvature. To quantitatively compare the results to known block copolymer phase behavior in selective solvents, effective volume fractions were calculated, taking PB as the solvophilic block and PDMAEMA/H<sub>3</sub>PMo as the solvophobic block (SI chapter V). The resulting PDMAEMA/H<sub>3</sub>PMo volume fractions of 0.27, 0.42, and 0.56 showing spherical micelles, networks, and vesicles, respectively, were considerably lower than what has been observed for selective, strongly segregated diblock copolymers, i.e. PB-b-PEO in water.<sup>41</sup> The volume fraction calculation was based on the assumption that the core domain density is the weighted average of the densities of PDMAEMA and H<sub>3</sub>PMo. This assumption may be incorrect, because the strong electrostatic interactions between PDMAEMA and H<sub>3</sub>PMo may have lead to a denser material. However, this would result in

even lower volume fractions as compared to the reported values for PB-b-PEO in water.

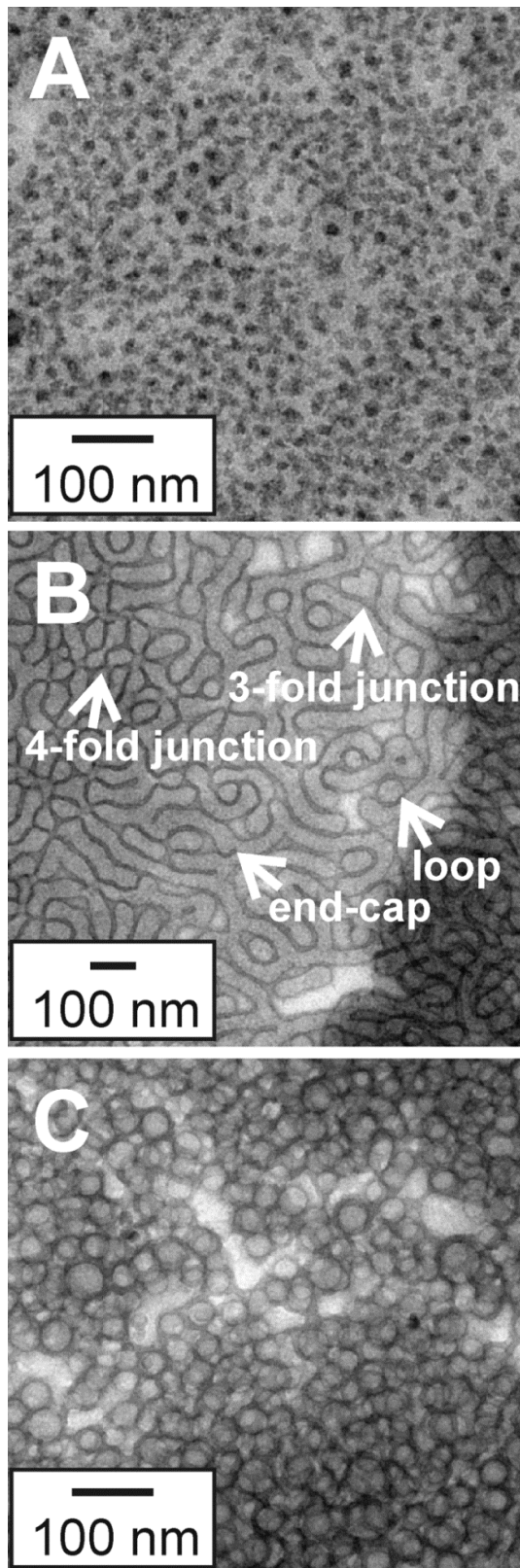


Figure 2: Cryo-TEM images in THF of nanostructures from varying PB-b-PDMAEMA/H<sub>3</sub>PMo ratios: A) 3.23, B) 1.08, and C) 0.54.

A more likely explanation is the high affinity of H<sub>3</sub>PMo to bind THF molecules, which is described in the literature<sup>42</sup> and is consistent with our own observations (SI, chapter VI, Figure SI 7 and SI 8). Up to 20 THF molecules can adsorb to a single H<sub>3</sub>PMo cluster, which is more than enough to explain the discrepancy in expected and observed volume fractions.<sup>42</sup> Whereas strongly segregated block copolymers have core domains that are absolutely free of solvent, the PDMAEMA/H<sub>3</sub>PMo core domains may contain considerable amounts of THF ( $V_{THF} = 0.153 \text{ nm}^3$ ), which effectively increases the core volume fraction.

Table 1: Characteristics of PB-b-PDMAEMA/H<sub>3</sub>PMo complexes in THF as observed by cryo-TEM.

PB-b-PDMAEMA/H <sub>3</sub> PMo ratio	morphology	$d_c^a$ /nm	$S_c^b$
3.23	spheroidal	16.93±3.37	0.85
1.08	3D bicontinuous network	13.08±2.89	0.65
0.54	vesicles	8.37±1.67	0.42

<sup>a</sup>Core diameter of PB-b-PDMAEMA/H<sub>3</sub>PMo domain in THF solution.

<sup>b</sup>Stretching degree of PB-b-PDMAEMA/H<sub>3</sub>PMo domain in THF solution.

The characterization of PB-b-PDMAEMA/H<sub>3</sub>PMo solutions in THF revealed considerable differences compared to the EISA process reported by Brinker et al.<sup>30</sup> While in EISA, the hybrid block interacts with the solvent, here the PB block is better soluble and stabilizes the generated micelles.

*Film casting.* For film casting the clear colloidal solutions were poured into a Teflon petri dish and volatiles were allowed to evaporate at RT and 32 % RH. PB-b-PDMAEMA/H<sub>3</sub>PMo composite films with eight different compositions were prepared (Table 2). At low H<sub>3</sub>PMo content films were transparent with green color. As the H<sub>3</sub>PMo content increased, film colors gradually intensified into a dark blue. The color may be explained by a minute reduction and hydrolysis of H<sub>3</sub>PMo to form the so-called molybdenum blues which have a very high extinction coefficient.<sup>3;6</sup> For all eight

compositions, no precipitation was observed during casting. Moreover, films were homogeneous and did not show any signs of macrophase separation (see Figure 1D).

Table 2: PB-b-PDMAEMA/H<sub>3</sub>PMo composites.

sample	Keggin	wt % Keggin	block copolymer	H <sup>+</sup> /N <sup>a</sup>	r <sup>b</sup>	M <sup>c</sup>	d <sub>spacing</sub> <sup>d</sup> /nm	A <sup>e</sup> /nm	B <sup>f</sup> /nm	f <sub>S,calc</sub> <sup>g</sup>	f <sub>S,TEM</sub> <sup>h</sup>
POM1	H <sub>3</sub> PMo	28	PB-b-PDMAEMA	0.46	6.52	M/D	31	nd	nd	0.22	nd
POM2	H <sub>3</sub> PMo	44	PB-b-PDMAEMA	0.93	3.23	M/D	29	nd	nd	0.27	nd
POM3	H <sub>3</sub> PMo	54	PB-b-PDMAEMA	1.39	2.16	M/D	nd	nd	nd	0.31	nd
POM4	H <sub>3</sub> PMo	61	PB-b-PDMAEMA	1.85	1.62	Hex	42	28.9±2.7	7.9±1.1	0.35	0.44
POM5	H <sub>3</sub> PMo	70	PB-b-PDMAEMA	2.78	1.08	Hex	45	32.4±2.5	10.2±1.7	0.42	0.48
POM6	H <sub>3</sub> PMo	76	PB-b-PDMAEMA	3.71	0.81	Hex	51	35.6±2.8	9.2±2.1	0.47	0.43
POM7	H <sub>3</sub> PMo	80	PB-b-PDMAEMA	4.63	0.65	Hex/D	45	32.0±3.9	6.8±1.5	0.52	0.38
POM8	H <sub>3</sub> PMo	83	PB-b-PDMAEMA	5.59	0.54	Hex/D	31	nd	nd	0.56	nd
POM9	H <sub>3</sub> PMo	70	PB-b-P2VP	1.57	1.91	Hex	39	27.0±1.6	8.98±1.1	0.46	0.49
POM10	H <sub>3</sub> PW	79	PB-b-P2VP	1.61	1.86	Hex	41	29.9±2.1	9.11±1.3	0.46	0.47

<sup>a</sup> Molar ratio of H<sup>+</sup> to DMAEMA units.

<sup>b</sup> Molar ratio of DMAEMA units to H<sub>3</sub>PMo.

<sup>c</sup> Morphology of the mesostructured films: M: micellar; D: disordered; Hex: inverse hexagonal.

<sup>d</sup> Determined from SAXS measurements.

<sup>e</sup> PB cylinder diameter as obtained from TEM micrographs.

<sup>f</sup> PDMAEMA/H<sub>3</sub>PMo matrix thickness as obtained from TEM micrographs.

<sup>g</sup> Calculated solvophobic volume fraction (SI, chapter V).

<sup>h</sup> Solvophobic volume as obtained by TEM measurements.

Nanocomposite films were characterized using combinations of FTIR spectroscopy, PXRD, SAXS, and TEM. FTIR spectra of PB-b-PDMAEMA diblock copolymer, the parent H<sub>3</sub>PMo, and the PB-b-PDMAEMA/H<sub>3</sub>PMo nanocomposites are shown in Figure 3A and Figure SI 9. H<sub>3</sub>PMo shows four characteristic bands, which are the fingerprint of the

Keggin structure.<sup>43,44</sup> There are four kinds of oxygen atoms in H<sub>3</sub>PMo (O<sub>a</sub> – oxygen in PO<sub>4</sub> tetrahedra, O<sub>d</sub> – terminal oxygen atom to Mo, O<sub>b</sub> – corner sharing oxygen and O<sub>c</sub> – edge sharing oxygen) giving rise to characteristic bands at ν<sub>as</sub> (Mo-O<sub>d</sub>) – 960 cm<sup>-1</sup>, ν<sub>as</sub> (Mo-O<sub>b</sub>-Mo) – 870 cm<sup>-1</sup>, ν<sub>as</sub> (Mo-O<sub>c</sub>-Mo) – 785 cm<sup>-1</sup>, and ν<sub>as</sub> (P-O<sub>a</sub>) – 1065 cm<sup>-1</sup> (Figure 3Ae). The FTIR spectra of all nanocomposite films (POM1 – 8) were in good agreement with a superposition of the spectra of parent H<sub>3</sub>PMo and PB-b-PDMAEMA polymer suggesting that the Keggin structure stayed intact upon nanocomposite formation. A summary of observed peak positions of the various materials is given in Table SI 3.

The slight shift in wavenumbers observed for both Mo-O-Mo vibrations (corner and edge shared) is likely due to a change in the environment of the Keggin anions incorporated in the PDMAEMA block. Thus the shift in the frequencies was indicating Coulomb interactions between PB-b-PDMAEMA and H<sub>3</sub>PMo.

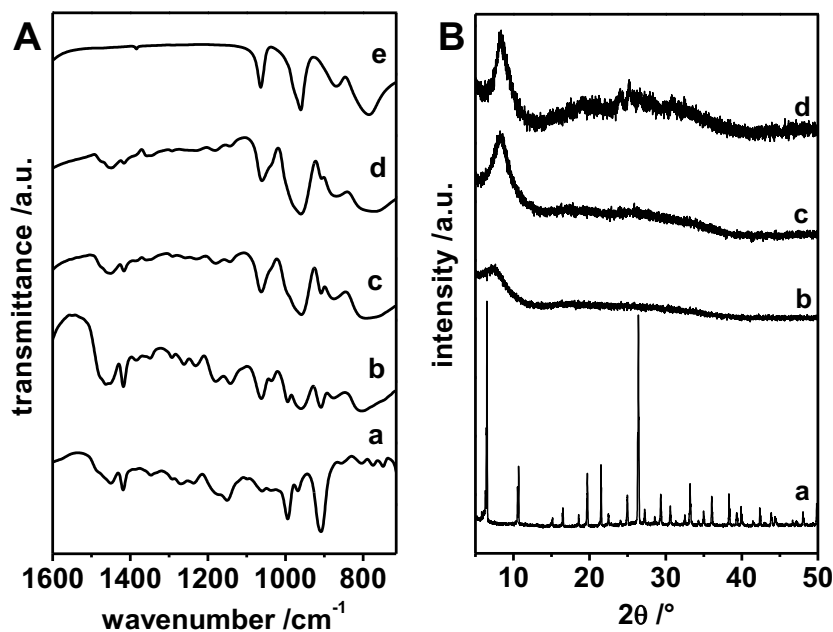


Figure 3: FTIR spectra (A) and PXRD patterns (B) of b) POM2 (44 wt %), c) POM5 (70 wt %), and d) POM8 (83 wt %). For comparison, FTIR spectra of PB-b-PDMAEMA (Aa), parent H<sub>3</sub>PMo (Ae) and the PXRD pattern of H<sub>3</sub>PMo (Ba) are given.

PB-b-PDMAEMA/H<sub>3</sub>PMo nanocomposite films were amorphous and PXRD patterns showed no peaks being characteristic for the parent crystalline H<sub>3</sub>PMo (Figure 3B and Figure SI 10), which again suggested a homogenous dispersion of H<sub>3</sub>PMo in the polymer matrix.

Structural assignment of the nanocomposite films was accomplished by a combination of SAXS measurements (only for selected samples, Figure 4) and TEM images (Figure 5). The SAXS traces of POM1 (28 wt %) and POM2 (44 wt %) (Figure 4A and Figure 4B) showed broad first order peaks centered around values of the scattering wave vector  $q$  corresponding to a  $d$ -spacing of approximately 31 nm and 29 nm, respectively, indicating the absence of long range order.

SAXS patterns obtained for POM4 – POM7 (Figure 4C-F, Figure SI 11, and Figure SI 12) exhibited distinguishable higher-order reflections indicative of cylinders packed in a hexagonal lattice. The main peaks correspond to  $d$ -spacings of 42, 45, 51 and 42 nm for samples POM4, 5, 6, and 7, respectively.

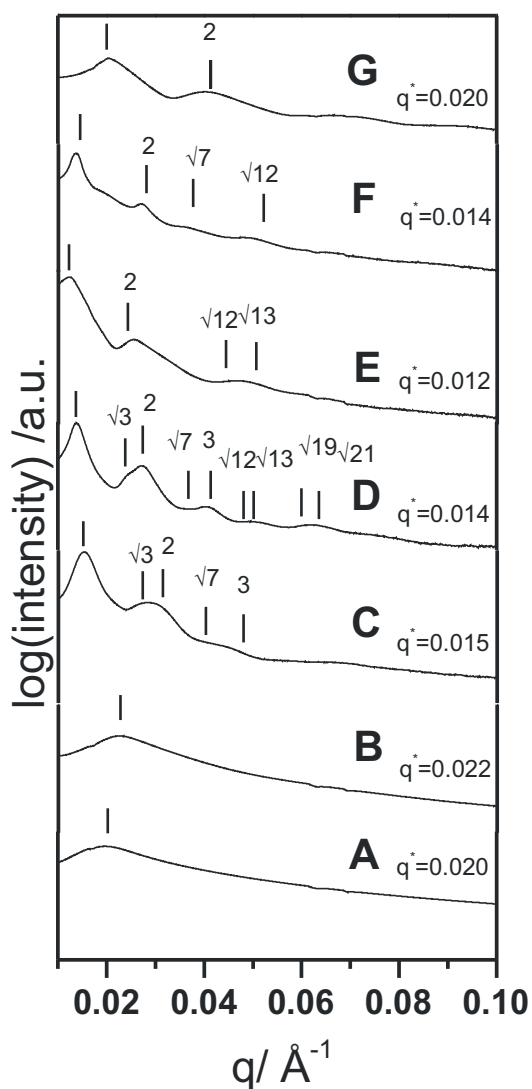


Figure 4: SAXS patterns of PB-b-PDMAEMA/H<sub>3</sub>PMo nanocomposites: A) POM1 (28 wt %), B) POM2 (44 wt %), C) POM4 (61 wt %), D) POM5 (70 wt %), E) POM6 (76 wt %), F) POM7 (80 wt %) and G) POM8 (83 wt %).

Note that the *d*-spacing first increased with increasing H<sub>3</sub>PMo content but then decreased again. This unexpected behavior will be discussed later. The scattering curve of POM8 (83 wt %, Figure 4G) possessed one broad, unstructured higher order reflection at angular position of 2 of the first order maximum, which is typical for short-range-ordered structures. The broad first order maximum corresponded to a *d*-spacing of 31 nm.

Bright-field TEM micrographs (Figure 5) of the nanocomposites corroborate the structural assignments based on SAXS experiments. For POM2 (Figure 5A) micellar disordered mesostructures were observed. Highly ordered hexagonally packed light cylinders in a dark matrix were found for POM4 and POM5 (Figure 5B and C) which translates to PB cylinders in a PDMAEMA/H<sub>3</sub>PMo matrix. Further increase of the H<sub>3</sub>PMo loading led to small regions with less order for POM6 and POM7 (Figure 5D and E) while for POM8 a further significant decrease of order was observed (see Figure 5F). In order to understand the trends of *d*-spacings observed by SAXS, the volume fractions of PB- and PDMAEMA/H<sub>3</sub>PMo-blocks were determined from TEM images ( $f_{s,TEM}$ , see Table 2) for the inverse hexagonally ordered nanocomposite films and compared with calculated ( $f_{s,calc}$ ) volume fractions (for details of calculation see SI chapter V).

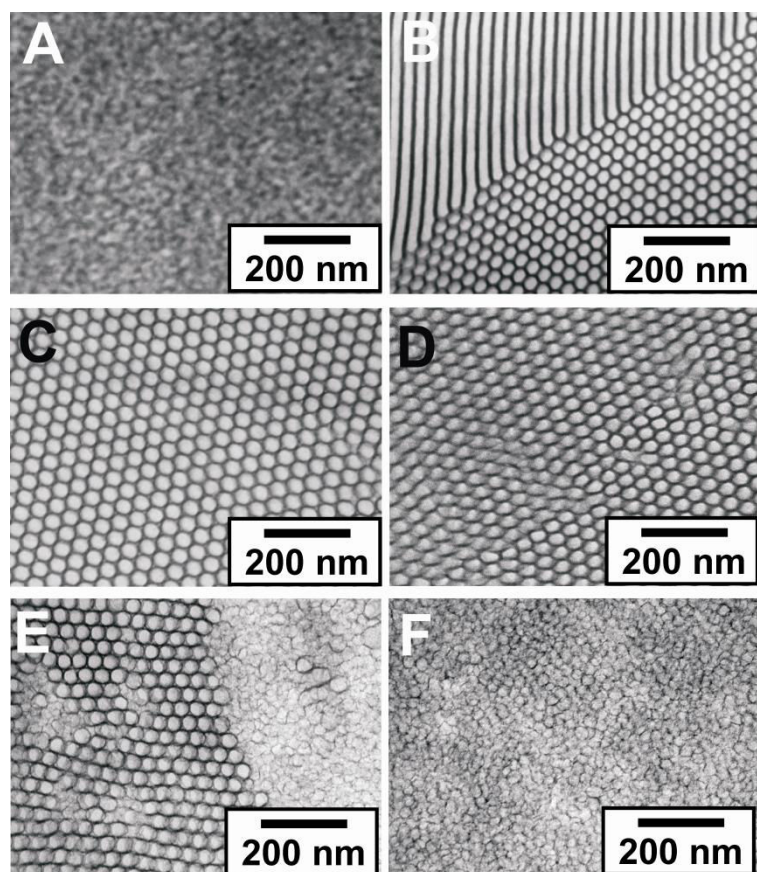


Figure 5: Representative bright-field TEM images of the as-synthesized PB-b-PDMAEMA/H<sub>3</sub>PMo nanocomposites at different magnifications: A) POM2 (44 wt %), B) POM4 (61 wt %), C) POM5 (70 wt %), D) POM6 (76 wt %), E) POM7 (80 wt %) and F) POM8 (83 wt %).

In line with the SAXS observations,  $f_{s,TEM}$  first increased with increasing H<sub>3</sub>PMo loading and then decreased again. As described above, H<sub>3</sub>PMo is expected to preferentially enter the PDMAEMA domains. Therefore, increasing the H<sub>3</sub>PMo content is expected to increase the solvophobic volume fraction (see  $f_{s,calc}$  in Table 2, which is calculated on the basis of this assumption). However, at a certain stoichiometry, when the number of H<sub>3</sub>PMo exceeds the number of DMAEMA units ( $r = \text{DMAEMA}/\text{H}_3\text{PMo} < 1$ , Table 2), the solvophobic volume fraction and the diameter of the cylinders for POM7 decreases. There are two possible explanations:

1. Additional H<sub>3</sub>PMo still enters the DMAEMA block and stronger hydrogen bonding resembling the crystalline state induces denser packing.
2. PDMAEMA domains cannot accommodate additional H<sub>3</sub>PMo and it may become more favourable for H<sub>3</sub>PMo to segregate to the interface. Segregation to the interface leads to a decrease in interfacial tension and a corresponding decrease in domain size, allowing the stretching of the blocks to be decreased.<sup>45-47</sup> Since segregation to the interface is expected to be detrimental to ordering, the experimental observations (compare Figure 5C-F) are more in line with the second reasoning.

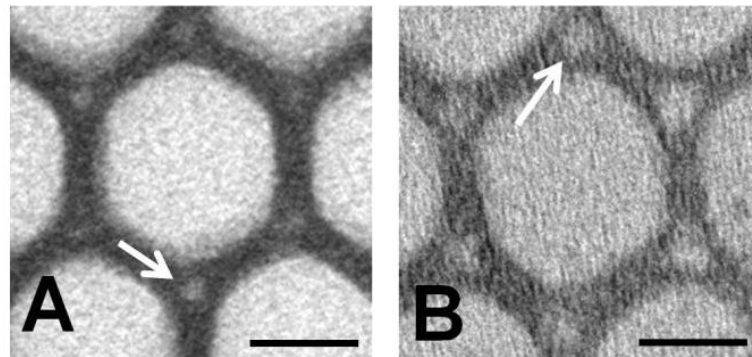


Figure 6: High-resolution TEM images of hexagonal mesostructures for A) POM5 and B) POM9. The arrows denote areas with low electron densities within the matrix. The scale bars are 20 nm.

A second observation resembled solution behavior inasmuch as morphologies were obtained for smaller solvophobic volume fractions than expected from molecular packing arguments. It appeared that inverse hexagonal cylinders were obtained for

unusual large PB volume fractions ranging from 0.51 to 0.66. Following the same line of argument discussed previously, relatively strong adsorption of THF to H<sub>3</sub>PMo lead to temporarily swelling of the PDMAEMA/H<sub>3</sub>PMo domains, thereby increasing the PDMAEMA/H<sub>3</sub>PMo volume fraction. Free THF in the solvophilic PB-block is expected to evaporate first, while the PDMAEMA/H<sub>3</sub>PMo domains remain swollen. Consequently, the volume fraction of the PB block at intermediate stages of the EISA where the hexagonal morphology develops will be much smaller as the volume fraction determined for fully dried, solvent free nanocomposite samples investigated by TEM. When finally the PDMAEMA/H<sub>3</sub>PMo domains shrink upon evaporation of adsorbed THF, the mobility is already significantly reduced. Therefore the system can only rearrange on a very local scale and the hexagonal morphology is retained. This might explain why inverse hexagonal morphologies with PB cylinders in a PDMAEMA/H<sub>3</sub>PMo matrix were obtained for rather large  $f_{s,TEM}$  of the PB block. Indirect proof for the shrinkage of PDMAEMA/H<sub>3</sub>PMo domains at the final stages of film formation, is given by TEM micrographs at higher magnifications, which show light areas in the matrix at the corner of the hexagons, as depicted in Figure . It appears that these light areas are voids induced by drying. It is obvious that the formation of voids is energetically unfavourable. However, the interface region has to find a delicate balance between minimizing the interfacial tension and chain stretching. Voids are not uncommon and have been reported for inverse hexagonal arrays of lipids and charged surfactants.<sup>48,49</sup>

Finally we illustrate the general applicability of this novel approach for producing block copolymer/heteropolyoxometalate nanocomposites. Hexagonally ordered mesostructured films were also obtained applying a different block copolymer (poly(butadiene-block-2-vinylpyridine) (POM9) or other HPAs like phosphotungstic acid (H<sub>3</sub>[PW<sub>12</sub>O<sub>40</sub>], POM10) (Table 1 and Figure SI 13).

## Conclusion

In summary, we presented a general one pot synthesis towards highly ordered inverse hexagonal block copolymer/heteropolyoxometalate nanocomposites. PB-b-PDMAEMA was chosen as SDA with a short ionizable block and a long solvophilic PB block. H<sub>3</sub>PMo protonates the polymer and the polyanions selectively enter the PDMAEMA units. Macrophase separation was never observed. The PB-b-PDMAEMA/H<sub>3</sub>PMo complex remains dissolved in THF even at high concentrations and H<sub>3</sub>PMo loadings. At optimized H<sub>3</sub>PMo loadings, inverse hexagonal mesophases were obtained by EISA. The general applicability of the method for mesostructuring was proven by extending it to other block copolymers and HPAs.

**Acknowledgment.** This work was supported by the Deutsche Forschungsgemeinschaft (DFG) within the Collaborative Research Center (SFB) 840. T. L. thanks the international graduate school of the ENB “Structures, Reactivity and Properties of Metal Oxides” for a fellowship. M.K. was supported by the Netherlands Organization for Scientific Research (NWO, VENI-700.10.404). Z. L was supported by the U.S. Department of Homeland Security under Cooperative Agreement Number 2009-ST-108-LR0004. The X-ray equipment was supported by Department of Energy grant DEFG-02-97ER62443. CHESS was supported by the NSF and NIH-NIGMS via DMR-0225180.

**Supporting Information.** Detailed equations, Table SI 1 – SI 3 and Figures SI 1 – SI 11. This material is available free of charge via the Internet at <http://pubs.acs.org>.

## References

- (1) Berzelius, J. J. *Pogg. Ann. Phys. Chem.* **1826**, *6*, 369-380.
- (2) Pope, M. T. *Heteropoly and Isopoly Oxometalates* Springer-Verlag: Berlin, 1983.
- (3) Pope, M. T.; Müller, A. *Polyoxometalate Chemistry From Topology via Self-Assembly to Applications* Kluwer Academic Publishers: Netherlands, 2001.
- (4) Johannson, G. *Acta Chem. Scand.* **1960**, *14*, 771-773.
- (5) Keggin, J. F. *Nature* **1933**, *131*, 908-909.
- (6) Moffat, J. B. *Metal-Oxygen Clusters - The Surface and Catalytic Properties of Heteropoly Oxometalates* Kluwer Academic/Plenum Publishers: New York, 2001.
- (7) Katsoulis, D. E. *Chem. Rev.* **1998**, *98*, 359-387.

- (8) Nomiya, K.; Murasaki, H.; Miwa, M. *Polyhedron* **1986**, *5*, 1031-1033.
- (9) Misono, M. *Catal. Rev. Sci. Eng.* **1987**, *29*, 269-321.
- (10) Pope, M. T.; Müller, A. *Angew. Chem. Int. Ed.* **1991**, *30*, 34-48.
- (11) Long, D. L.; Tsunashima, R.; Cronin, L. *Angew. Chem. Int. Ed.* **2010**, *49*, 1736-1758.
- (12) Song, Y. F.; Long, D. L.; Ritchie, C.; Cronin, L. *Chem. Record* **2011**, *11*, 158-171.
- (13) Kurth, D. G.; Lehmann, P.; Volkmer, D.; Cölfen, H.; Koop, M. J.; Müller, A.; Du Chesne, A. *Chem. Eur. J.* **2000**, *6*, 385-393.
- (14) Li, H.; Qi, W.; Li, W.; Sun, H.; Bu, W.; Wu, L. *Adv. Mater.* **2005**, *17*, 2688-2692.
- (15) Li, W.; Bu, W.; Li, H.; Wu, L.; Li, M. *Chem. Commun.* **2005**, 3785-3787.
- (16) Wang, Y. L.; Li, W.; Wu, L. X. *Langmuir* **2009**, *25*, 13194-13200.
- (17) Lin, X. K.; Wang, Y. L.; Wu, L. X. *Langmuir* **2009**, *25*, 6081-6087.
- (18) Wang, H. B.; Yan, Y.; Li, B.; Bi, L. H.; Wu, L. X. *Chem. A Eur. J.* **2011**, *17*, 4273-4282.
- (19) Han, Y. K.; Zhang, Z. J.; Wang, Y. L.; Xia, N.; Liu, B.; Xiao, Y.; Jin, L. X.; Zheng, P.; Wang, W. *Macromol. Chem. Phys.* **2011**, *212*, 81-87.
- (20) Polarz, S.; Smarsly, B.; Antonietti, M. *Chem. Phys. Chem* **2001**, *2*, 457-461.
- (21) Stein, A.; Fendorf, M.; Jarvie, T. P.; Müller, K. T.; Benesi, A. J.; Mallouk, T. E. *Chem. Mater.* **1995**, *7*, 304-313.
- (22) Landsmann, S.; Lizandara-Pueyo, C.; Polarz, S. *J. Am. Chem. Soc.* **2010**, *132*, 5315-5321.
- (23) Giner-Casares, J. J.; Brezesinski, G.; Möhwald, H.; Landsmann, S.; Polarz, S. *J. Phys. Chem. Lett.* **2012**, *3*, 322-326.
- (24) Bu, W.; Uchida, S.; Mizuno, N. *Angew. Chem. Int. Ed.* **2009**, *48*, 8281-8284.
- (25) Lin, X.; Liu, F.; Li, H.; Yan, Y.; Bi, L.; Bu, W.; Wu, L. *Chem. Commun.* **2011**, *47*, 10019-10021.
- (26) Yelamanchili, R. S.; Walther, A.; Müller, A. H. E.; Breu, J. *Chem. Commun.* **2008**, 489-491.
- (27) Lee, J.; Orilall, M. C.; Warren, S. C.; Kamperman, M.; Disalvo, F. J.; Wiesner, U. *Nature Mater.* **2008**, *7*, 222-228.

- (28) Liu, S.; Tang, Z. *Nano Today* **2010**, *5*, 267-281.
- (29) Lunkenbein, T.; Cotter, T.; Zihui, L.; Bojer, C.; Trunschke, A.; Müller, A. H. E.; Wiesner, U.; Schlögl, R.; Breu, J. *unpublished results* **2012**.
- (30) Brinker, C. J.; Lu, Y. F.; Sellinger, A.; Fan, H. Y. *Adv. Mater.* **1999**, *11*, 579-585.
- (31) Templin, M.; Franck, A.; Du Chesne, A.; Leist, H.; Zhang, Y.; Ulrich, R.; Schädler, V.; Wiesner, U. *Science* **1997**, *278*, 1795-1798.
- (32) Schacher, F.; Müllner, M.; Schmalz, H.; Müller, A. H. E. *Macromol. Chem. Phys.* **2009**, *210*, 256-262.
- (33) Nakamura, O.; Ogino, I.; Kodama, T. *Solid State Ionics* **1981**, *3-4*, 347-351.
- (34) Förster, S.; Burger, C. *Macromolecules* **1998**, *31*, 879-891.
- (35) Förster, S.; Timmann, A.; Konrad, M.; Schellbach, C.; Meyer, A.; Funari, S. S.; Mulvaney, P.; Knott, R. *J. Phys. Chem. B* **2005**, *109*, 1347-1360.
- (36) Luo, C.; Liu, Y.; Li, Z. *Soft Matter* **2012**, *8*, 2618-2626.
- (37) Kozhevnikov, I. V. *Chem. Rev.* **1998**, *98*, 171-198.
- (38) Mei, Y.; Lauterbach, K.; Hoffmann, M.; Borisov, O. V.; Ballauff, M.; Jusufi, A. *Phys. Rev. Lett.* **2006**, *97*, 158301.
- (39) Plamper, F. A.; Walther, A.; Müller, A. H. E.; Ballauff, M. *Nano Lett.* **2007**, *7*, 167-171.
- (40) Bang, J.; Jain, S.; Li, Z.; Lodge, T. P.; Pedersen, J. S.; Kesselman, E.; Talmon, Y. *Macromolecules* **2006**, *39*, 1199-1208.
- (41) Jain, S.; Gong, X.; Scriven, L. E.; Bates, F. S. *Phys. Rev. Lett.* **2006**, *96*, 138304.
- (42) Aoshima, A.; Tonomura, S.; Yamamatsu, S. *Polymer. Adv. Tech.* **1990**, *2*, 127-132.
- (43) Rocchicciolieltcheff, C.; Fournier, M.; Franck, R.; Thouvenot, R. *Inorg. Chem.* **1983**, *22*, 207-216.
- (44) Rocchicciolieltcheff, C.; Aouissi, A.; Bettahar, M.; Launay, S.; Fournier, M. *J. Catal.* **1996**, *164*, 16-27.
- (45) Kim, B. J.; Fredrickson, G. H.; Bang, J.; Hawker, C. J.; Kramer, E. J. *Macromolecules* **2009**, *42*, 6193-6201.

- (46) Kim, B. J.; Bang, J.; Hawker, C. J.; Chiu, J. J.; Pine, D. J.; Jang, S. G.; Yang, S. M.; Kramer, E. J. *Langmuir* **2007**, *23*, 12693-12703.
- (47) Jang, S. G.; Kim, B. J.; Hawker, C. J.; Kramer, E. J. *Macromolecules* **2011**, *44*, 9366-9373.
- (48) Shearman, G. C.; Ces, O.; Templer, R. H.; Seddon, J. M. *J. Phys.: Condens. Matter* **2006**, *18*, S1105.
- (49) Shearman, G. C.; Tyler, A. I. I.; Brooks, N. J.; Templer, R. H.; Ces, O.; Law, R. V.; Seddon, J. M. *Liq. Cryst.* **2010**, *37*, 679-694.

## Supporting Information

### I. Pre-treatment of Molybdophosphoric acid ( $H_3[PMo_{12}O_{40}]$ , $H_3PMo$ )

Heteropoly acids (HPA) tend to change their degree of hydration and therefore their crystal structure depending on the relative humidity (RH).<sup>1</sup> In order to generate a defined and reproducible stoichiometry of the  $H_3PMo$  precursor, the Keggin was recrystallized from water. Thermogravimetric analysis (TGA) shows the presence of 27  $H_2O$  molecules per formula unit (see Figure SI ).

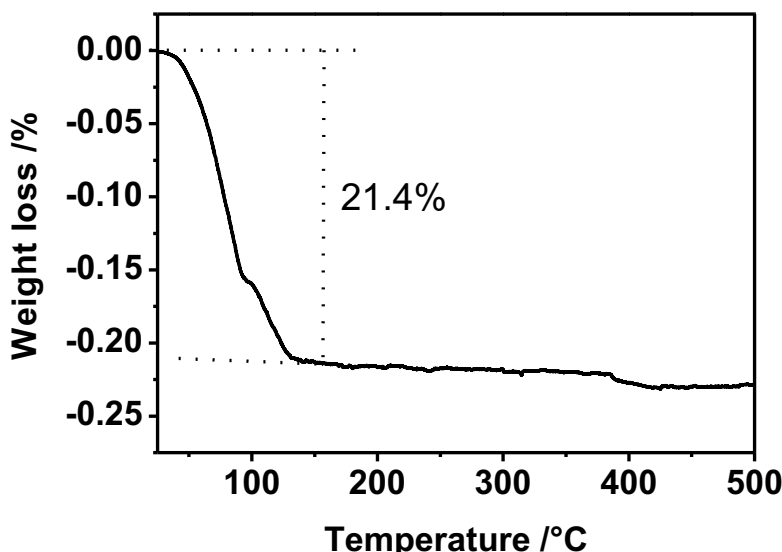


Figure SI 1: TGA measurements of  $H_3PMo$  recrystallized from water and stored 86 % r.H.. Evaluation of the mass loss equals the loss of 27 water molecules per  $H_3PMo$  unit.

## II. Film casting reactor.

Well-ordered poly(butadiene-*block*-2-dimethylaminethyl methacrylate) (PB-b-PDMAEMA) mesostructures were observed when the solvent was allowed to evaporate at 32 % RH. Hence, we engineered a film casting reactor to adjust the desired RH (see Figure SI ). It is known that a defined RH adjusts above a saturated salt solution in solution. In our case a saturated  $\text{CaCl}_2$  yields 32 % RH. An aquarium pump delivers the moisturized air into the reactor. After equilibration, volatiles are allowed to evaporate.



Figure SI 2: Photograph of the self-built film casting reactor.

### III. Calculation of the Florry-Huggins interaction parameter $\chi$

The Florry-Huggins interaction parameter  $\chi$  represents the quality of a solvent to dissolve a polymer and can be calculated as follows:

$$\chi = \frac{V_M}{RT} (\delta_{polymer} - \delta_{solvent}) \quad I$$

where  $V_M$  is molar volume, R represents the ideal gas constant ( $1.9 \text{ calJK}^{-1}\text{mol}^{-1}$ ), T is the casting temperature ( $T=298 \text{ K}$ ) and  $\delta$  is solubility parameter. The values of  $V_M$  and  $\delta^2$  values are given in Table SI 1:

Table SI 1: Molar volume  $V_M$  and solubility parameter  $\delta$  of PB, PDMAEMA, THF and acetone.

polymer	solvent	$V_M^2 / \text{cm}^3\text{mol}^{-1}$	$\delta^2 / \text{calcm}^{-1}$
PB		58.85	8.05
PDMAEMA		136.17	9.21
	THF		9.1
	acetone		9.9

#### IV. Colloidal Solution

In order to check the stability of the solution even at higher concentration and high loadings, photographs were taken at different states of evaporation and the corresponding concentration was calculated. The inorganic H<sub>3</sub>PMo loading was 83 wt % with respect to the amount of diblock copolymer. The corresponding photographs are depicted in Figure SI 3. For the sake of clarity glass vials were taken instead of the TEFLO<sup>N</sup> dishes.

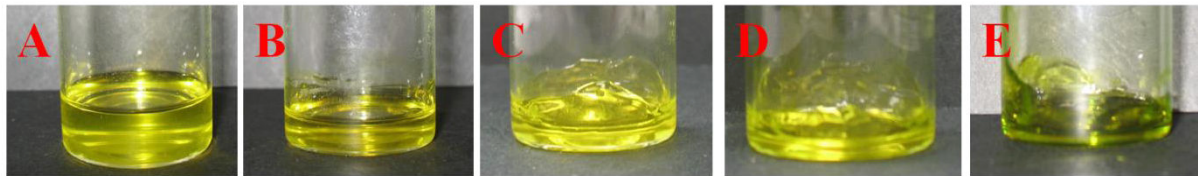


Figure SI 3: Photographs of PB-b-PDMAEMA/H<sub>3</sub>PMo solution in THF (H<sub>3</sub>PMo loading 83 wt % with respect to the diblock copolymer) at different states of evaporation and concentration: A) initial solution (13 wt %), B) 28 wt %, C) 40 wt %, D) 69 wt % and E) 90 wt %.

The presence of colloids in solution was proven by a simple laser experiment ( $\lambda = \sim 540$  nm). A solution of PB-b-DMAEMA/H<sub>3</sub>PMo (70 wt % H<sub>3</sub>PMo) was irradiated by a laser. The photograph in Figure SI clearly shows Tyndall scattering, originating from PB-b-PDMAEMA/H<sub>3</sub>PMo complexes in THF solution. The image exemplarily indicates Tyndall scattering.

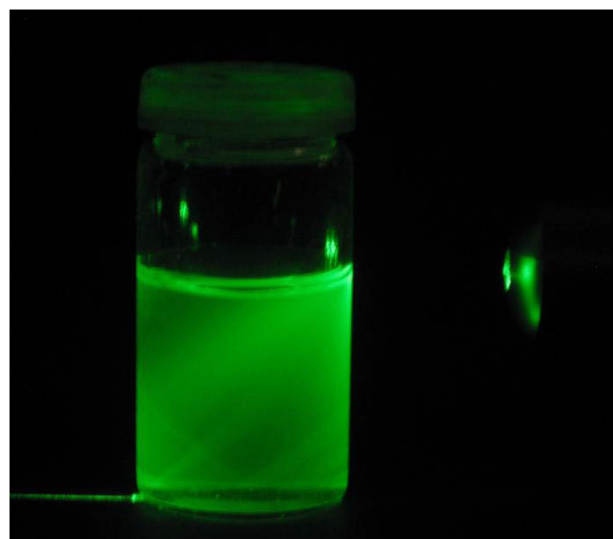


Figure SI 4: Photograph of PB-b-PDMAEMA/H<sub>3</sub>PMo complex in solution (70 wt % H<sub>3</sub>PMo) irradiated by a laser.

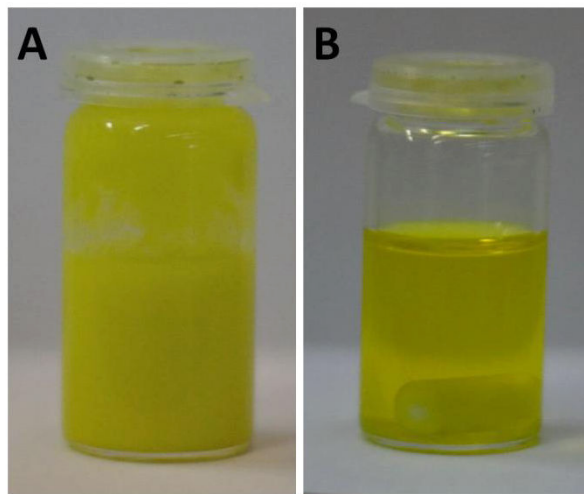


Figure SI 5: Images of ionizable diblock copolymers/ $H_3PMo$  solutions with varying degree of polymerization: A)  $PB_{288}$ -b-PDMAEMA<sub>244</sub> and B)  $PB_{476}$ -b-P2VP<sub>126</sub>. The indices denote the degree of polymerization. In all cases the concentration was 80 g/L and the  $H_3PMo$  content was 70 wt %.

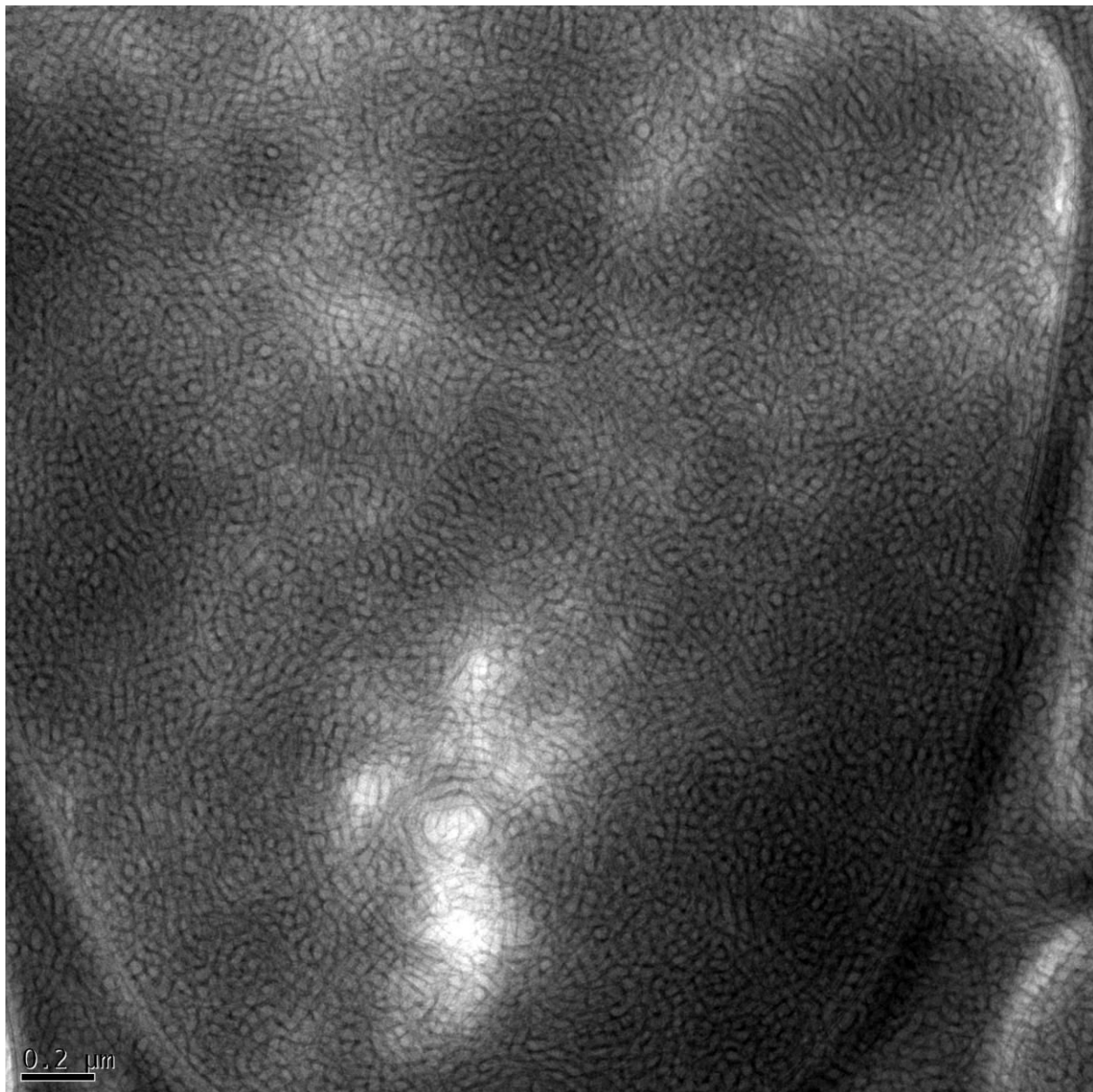


Figure SI 6: Cryo-TEM of 3D bicontinuous network vitrified in THF.

## V. Calculation of the packing parameter

$$V_{PB} = \frac{M_{PB}}{N_A \rho_{PB}} \quad II$$

$$V_{PDMAEMA} = \frac{M_{PDMAEMA}}{N_A \rho_{PDMAEMA}} \quad III$$

$$f_{PDMAEMA} = \frac{V_{PDMAEMA}}{V_{PB} + V_{PDMAEMA}} \quad IV$$

$$V_s = V_{PDMAEMA} + 40 \frac{V_{POM}}{r} \quad V$$

$$f_{s,calc} = \frac{V_s}{V_s + V_{PB}} \quad VI$$

$$f_{s,TEM} = \frac{\frac{\sqrt{3}}{2} (A+B)^2 - \left(\frac{1}{2} \cdot B\right)^2 \cdot \pi}{\frac{\sqrt{3}}{2} (A+B)^2} \quad VII$$

$$S_c = \frac{d_c}{2L_{PDMAEMA}} \quad VIII$$

Here V, M,  $\rho$  and f are the volume, molecular mass, density and volume fraction of the corresponding block denoted by subscripts, respectively.  $N_A$  is the Avogadro number ( $N_A=6.022 \cdot 10^{23}$  mol<sup>-1</sup>).  $V_s$  represents the solvophobic volume and  $f_{s,calc}$  denotes the calculated theoretical volume fraction of the solvophobic block.  $f_{s,TEM}$  is the calculated solvophobic volume based on the dimensions of the PB block (A) and PDMAEMA/H<sub>3</sub>PMo matrix (B) obtained from TEM images.  $V_{POM}$  is calculated by the knowledge of the anionic radius of H<sub>3</sub>PMo ( $V_{H_3PMo} = 0.596$  nm<sup>3</sup>) and tungtophosphoric acid (H<sub>3</sub>PW,  $V_{H_3PW}=0.599$  nm<sup>3</sup>).<sup>3</sup>  $S_c$  shows the stretching degree of the core block in THF solution. It is directly proportional to the core diameter,  $d_c$ , in solution. L indicates the contour length ( $L=DP \cdot 0.25$  nm) where DP is the degree of polymerization of the PDMAEMA block.

Table SI 2: Characteristic values of the different diblock copolymers considered for the calculation of the packing parameters.

diblock copolymer	block	M /gmol <sup>-1</sup>	ρ /gcm <sup>-3</sup>	DP
PB-b-PDMAEMA	PB	22620	0.902 <sup>4</sup>	418
	PDMAEMA	6380	1.318 <sup>5</sup>	40
PB-b-P2VP	PB	22200	0.902 <sup>4</sup>	411
	P2VP	7800	1.145 <sup>2</sup>	75

## VI. Affinity of THF to H<sub>3</sub>PMo

The following experiment was conducted in order to study the high affinity of H<sub>3</sub>PMo crystals to adsorb THF. 300 mg of recrystallized H<sub>3</sub>PMo were placed separately from 3 mL distilled THF in an exsiccator as depicted in Figure SI7 A and C. The closed system was allowed to equilibrate for 30 min. During this time the H<sub>3</sub>PMo starts to liquefy upon adsorbing of gaseous THF (see Figure SI B and C). The very high adsorbing affinity tends to break up lattice energy and dissolves the H<sub>3</sub>PMo in THF. Please note, that this effect is not observed in the presence of water, DMF or acetone.

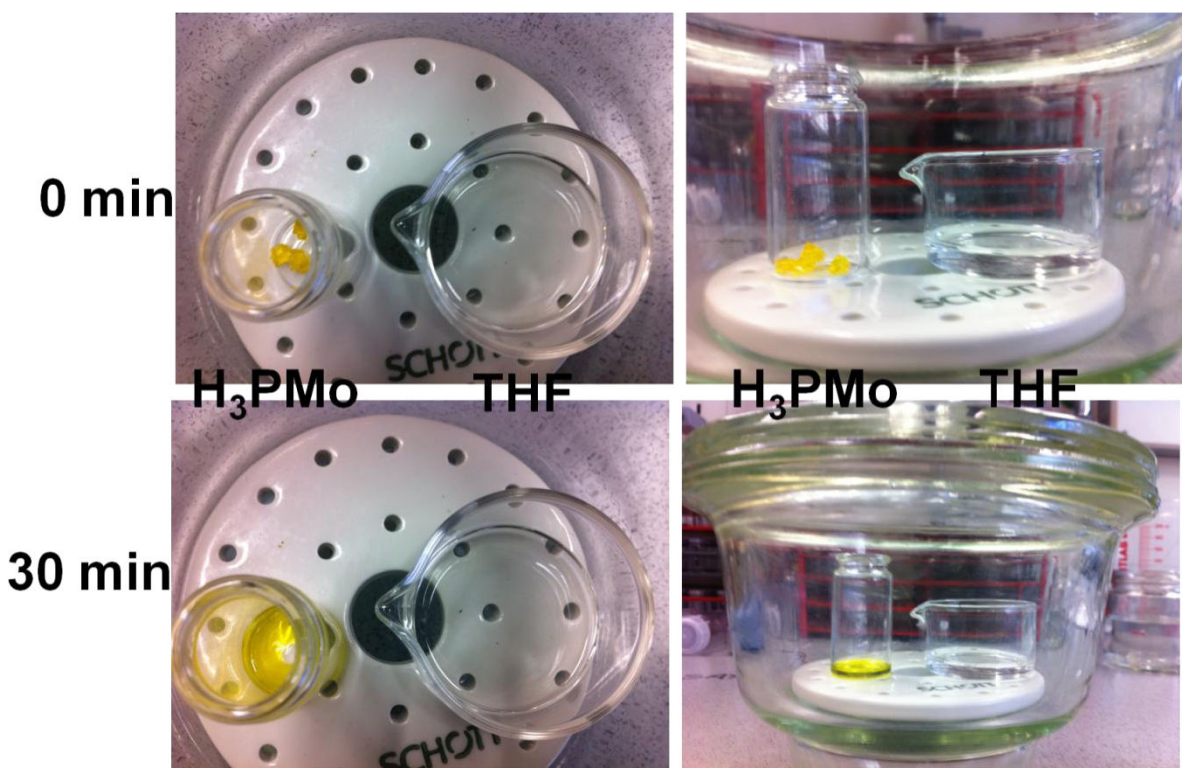


Figure SI 7: Visualization of the high affinity of H<sub>3</sub>PMo to adsorb THF. A) and C) show the initial state with solid H<sub>3</sub>PMo, whereas B) and D) represent the H<sub>3</sub>PMo/THF system after allowing to equilibrate for 30 min. in an exiccator. The liquefaction of the H<sub>3</sub>PMo crystals is clearly observable.

To further proof the strong adsorption of THF over H<sub>3</sub>PMo two <sup>1</sup>H-NMR experiments in d<sup>6</sup>-acetone were conducted (see Figure SI 8). In Figure SI 6A pristine recrystallized H<sub>3</sub>PMo was directly dissolved in d<sup>6</sup>-acetone. The blue arrows denote the

hydrogen bonding to bridge oxygen ( $\delta=2.10$  ppm) and to terminal oxygen ( $\delta=5.32$  ppm), respectively.<sup>6</sup> After film casting from THF and re-dissolving in  $d^6$ -acetone these peaks are gone, but a new triplette arises at  $\delta =3.64$  ppm and a quintette arises at  $\delta =1.80$  ppm, corresponding to THF.

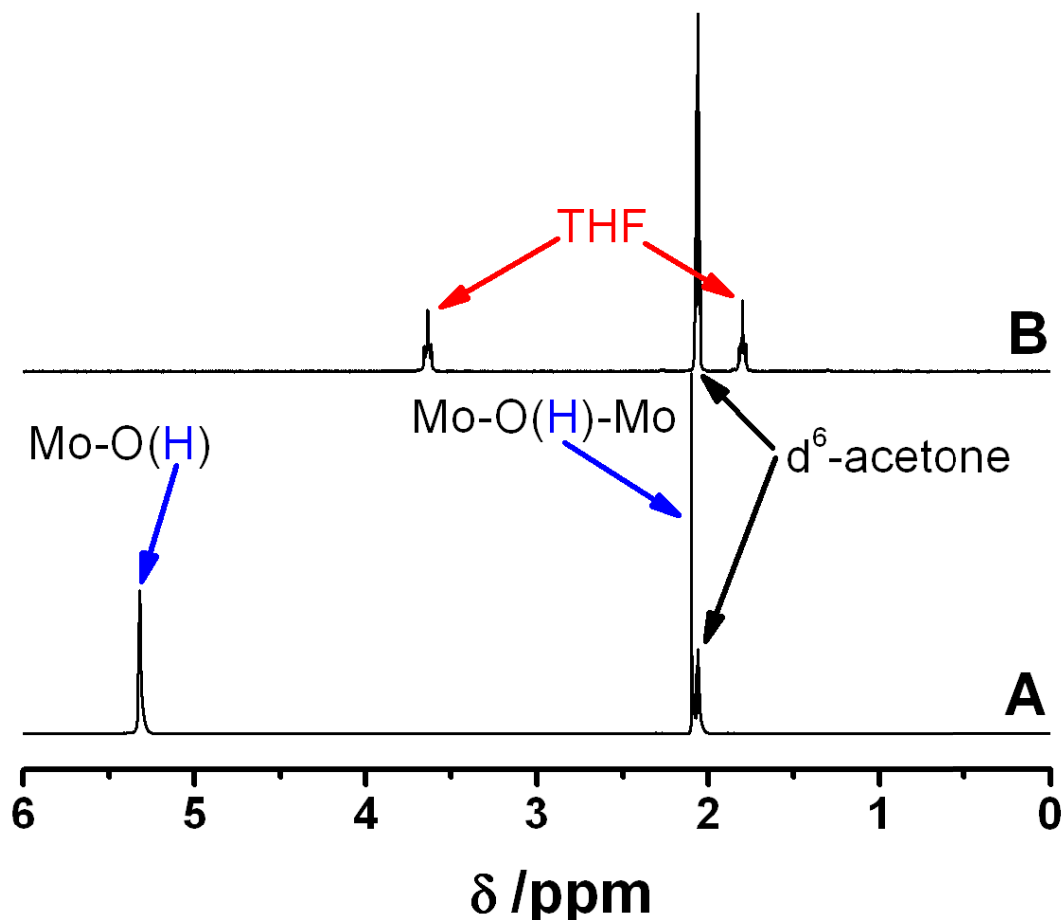


Figure SI 8:  $^1\text{H}$ -NMR spectra of A) pristine  $\text{H}_3\text{PMo}$  in  $d^6$ -acetone and B) after  $\text{H}_3\text{PMo}$  film casting and re-dissolution in  $d^6$ -acetone.

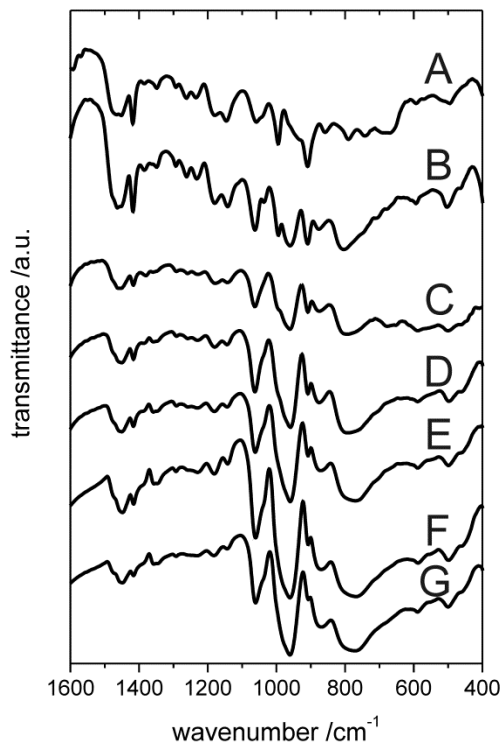
**VII. FTIR and PXRD**

Figure SI 9: FTIR- spectra of PB-b-PDMAEMA/H<sub>3</sub>PMo nanocomposites with different HPMo loading A) 28 wt %, B) 44 wt %, C) 61 wt %, D) 70 wt %, E) 76 wt %, F) 80 wt %, and G) 83 wt %.

Table SI3: Characteristic asymmetric vibrations of the four different oxygen bonds in H<sub>3</sub>PMo obtained from FTIR spectra of the different composite films.

	$\nu_{as}$ (P-O <sub>a</sub> )	$\nu_{as}$ (Mo-O <sub>b</sub> )	$\nu_{as}$ (Mo-O <sub>c</sub> -Mo)	$\nu_{as}$ (Mo-O <sub>d</sub> -Mo)
Reference <sup>7</sup>	1064	962	869	787
H <sub>3</sub> PMo	1064	960	869	784
1:0.5	1061	952 (sh)	858	790
1:1	1062	960	877	804
1:2	1063	961	875	794
1:3	1063	959	876	794
1:4	1062	960	871	770
1:5	1061	960	869	768
1:6	1061	961	869	771

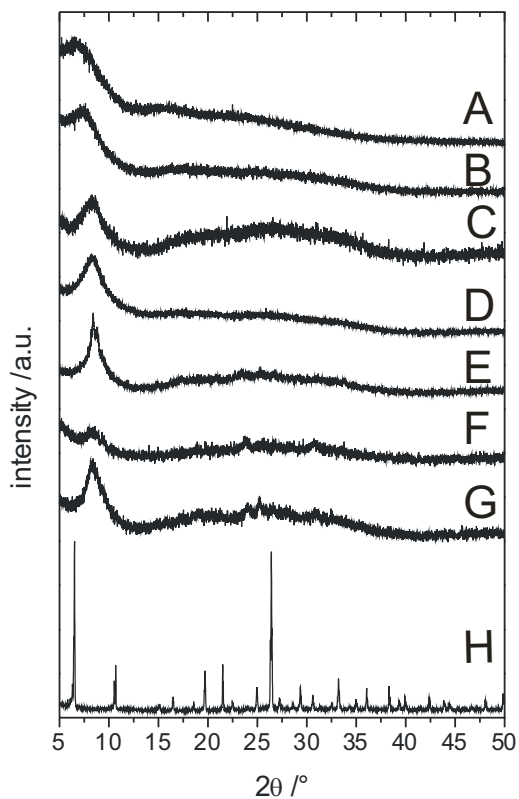


Figure SI 10: PXRD patterns of PB-b-PDMAEMA/H<sub>3</sub>PMo nanocomposites with different HPMo loading: A) 28 wt %, B) 44 wt %, C) 61 wt %, D) 70 wt %, E) 76 wt %, F) 80 wt %, G) 83 wt %, and H) parent H<sub>3</sub>PMo.

VIII. Mesophase behavior

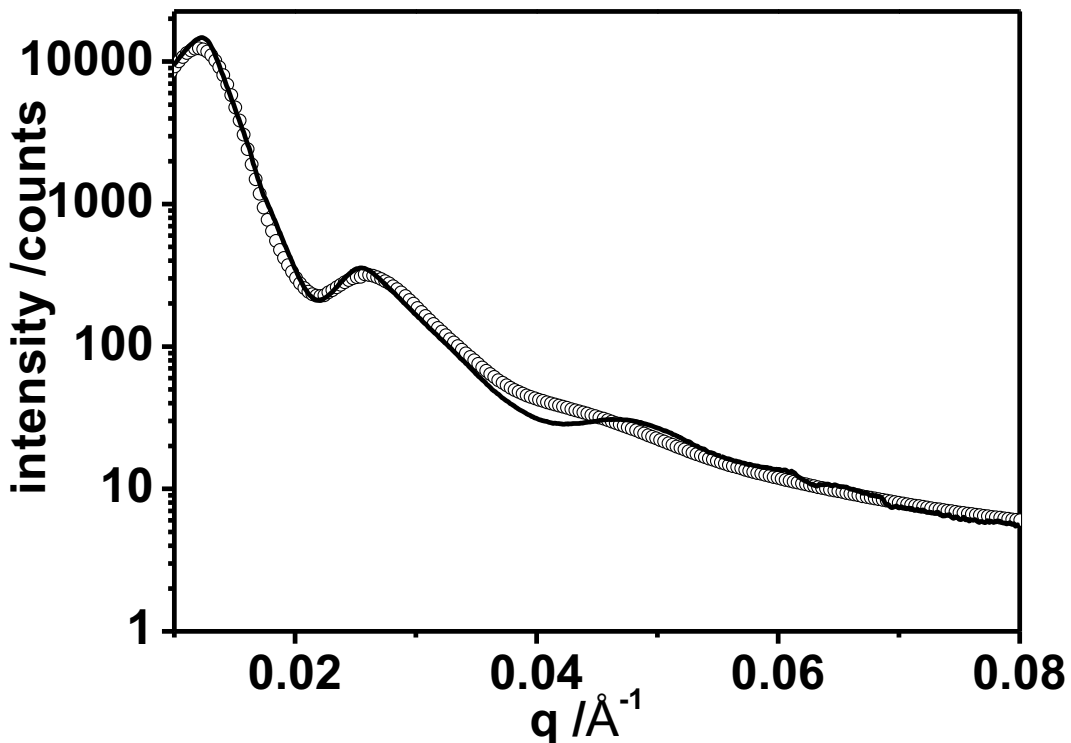


Figure SI 11: SAXS traces of PB-b-PDMAEMA/ $\text{H}_3\text{PMo}$  with  $\text{H}_3\text{PMo}$  loading of 76 wt %. The dotted line denotes a fit to a hexagonal lattice. Please note, that the absence of the  $\sqrt{3}$  reflex in the SAXS pattern is due to a minimum of the cylinder form factor at this position.

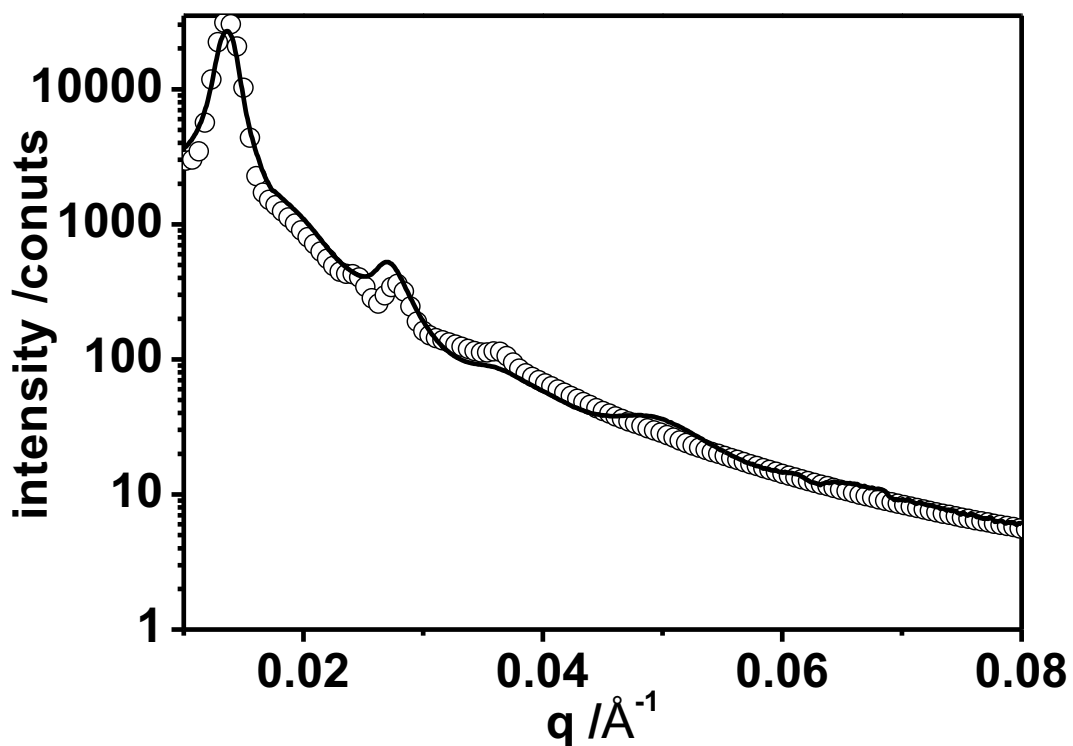


Figure SI 12: SAXS traces of PB-b-PDMAEMA/H<sub>3</sub>PMo with H<sub>3</sub>PMo loading of 80 wt %. The dots denote a fit to a hexagonal lattice.

## IX. Genarlization

In order to show that our approach towards inverse hexagonal PB-b-PDMAEMA/H<sub>3</sub>PMo nanocomposites is a more general approach, two additional experiments were conducted. First, PB-b-P2VP was used as ionizable diblock copolymer instead of PB-b-PDMAEMA. The SAXS and TEM results below on the resulting composites (Figure SI 13 A and B) clearly indicate an inverse hexagonal morphology. Second, the Keggin source was changed to H<sub>3</sub>PW resulting in inverse hexagonal PB-b-P2VP/H<sub>3</sub>PW nanocomposites (Figure SI 13 D and F). Please note, for the latter approach the weight content of H<sub>3</sub>PW was adjusted due to the much higher molecular weight of the Keggin unit.

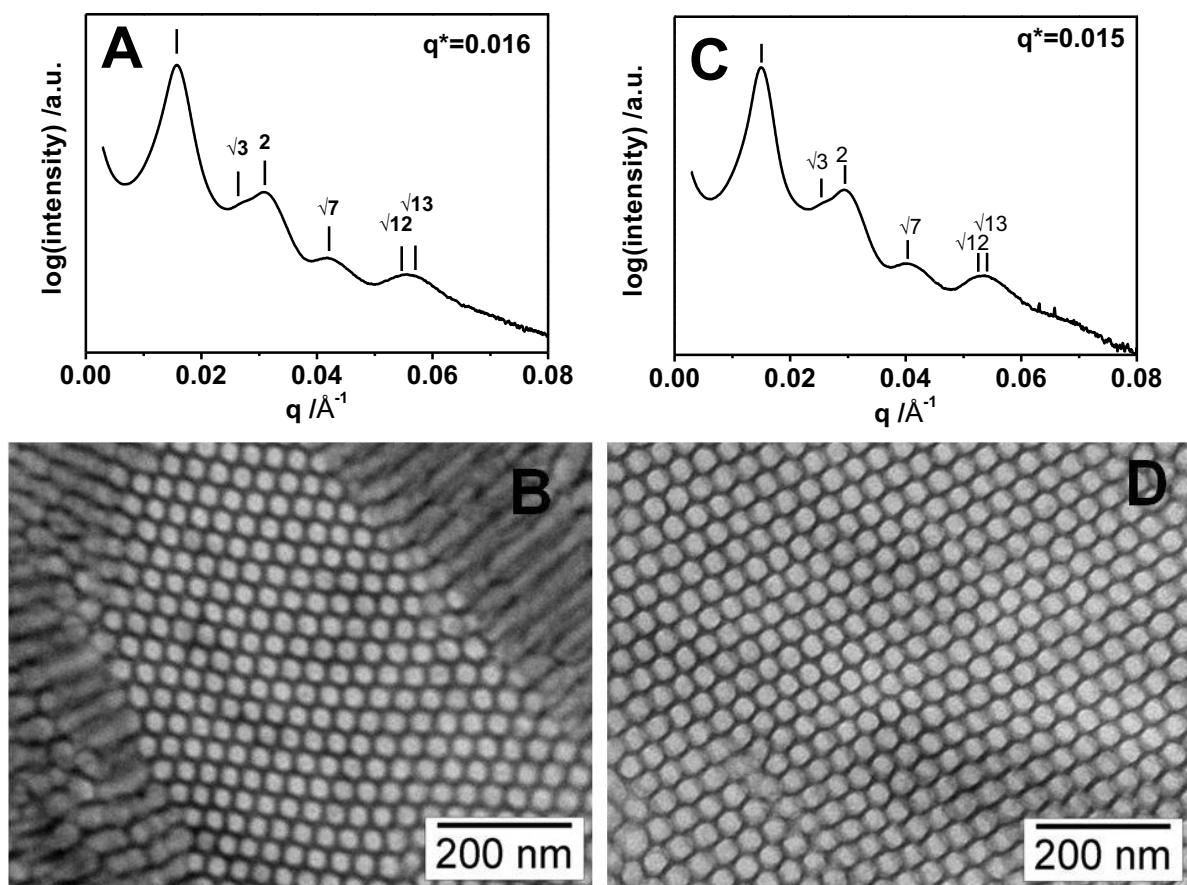


Figure SI 13: Inverse hexagonal mesostructure of PB-b-P2VP/H<sub>3</sub>PMo as evidenced by A) SAXS and B) a TEM micrograph obtained from a microtomed film sample. Inverse hexagonal mesostructure of PB-b-P2VP/H<sub>3</sub>PW as evidenced by D) SAXS and E) a TEM micrograph of a microtomed film sample.

## X. References

- (1) Nakamura, O.; Ogino, I.; Kodama, T. *Solid State Ionics* **1981**, *3-4*, 347-351.
- (2) Brandrup, J.; Immergut, E. H.; Grulke, E. A. *Polymer Handbook* Wiley: Weinheim, 1999.
- (3) Rocchicciolieltcheff, C.; Fournier, M.; Franck, R.; Thouvenot, R. *Inorg. Chem.* **1983**, *22*, 207-216.
- (4) Ko, J. H. *Polymer Data Handbook* Oxford University Press: Oxford, 1999.
- (5) Slim, C.; Tran, Y.; Chehimi, M. M.; Garraud, N.; Roger, J. P.; Combella, C.; Kanoufi, F. *Chem. Mater.* **2008**, *20*, 6677-6685.
- (6) Chen, D.; Xue, Z.; Su, Z. *J. Mol. Catal. A: Chem.* **2003**, *203*, 307-312.
- (7) Rocchicciolieltcheff, C.; Aouissi, A.; Bettahar, M.; Launay, S.; Fournier, M. *J. Catal.* **1996**, *164*, 16-27.

## 7.6 Towards Mesoporous Keggin-Type Polyoxometalate –Systematic Removal of Organic Templates

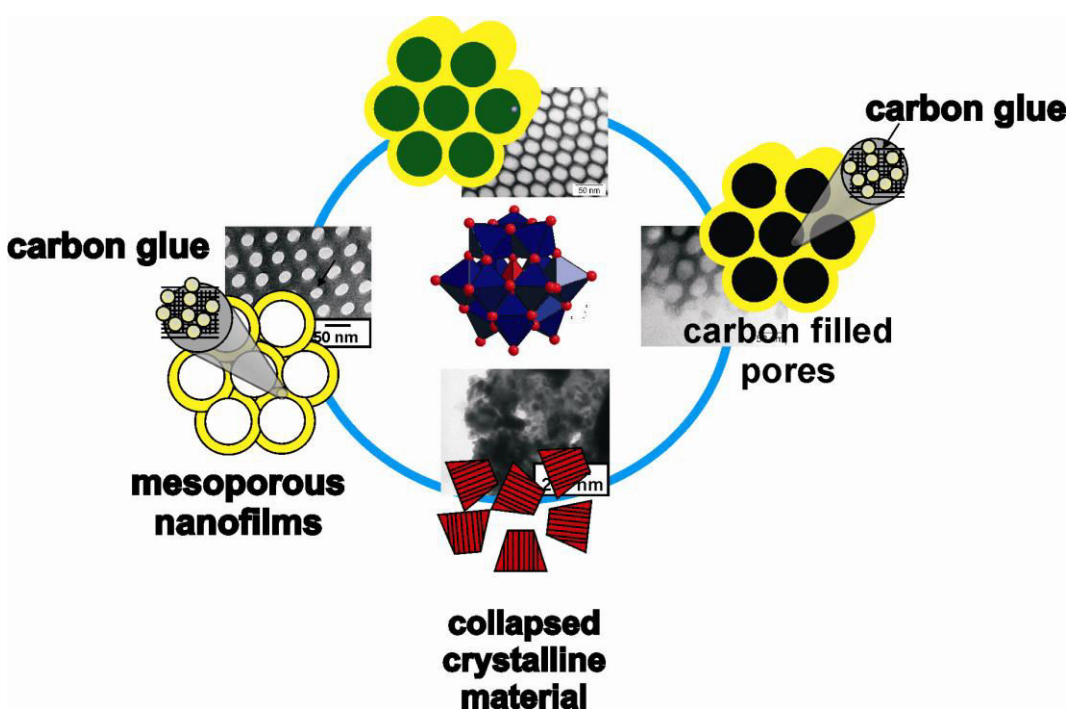
Thomas Lunkenbein,<sup>1</sup> Marleen Kamperman,<sup>2</sup> Martin Schieder,<sup>1</sup> Sebastian With,<sup>3</sup> Zihui Li,<sup>4</sup> Stephan Förster,<sup>3</sup> Ulrich Wiesner,<sup>4</sup> Josef Breu<sup>1,\*</sup>

<sup>1</sup>Lehrstuhl für Anorganische Chemie I, Universität Bayreuth, 95440 Bayreuth, Germany;

<sup>2</sup>Physical Chemistry and Colloid Science, Wageningen University, NL-6703 HB Wageningen, Netherlands;

<sup>3</sup>Lehrstuhl für Physikalische Chemie I, Universität Bayreuth, 95440 Bayreuth, Germany;

<sup>4</sup>Materials Science & Engineering, Cornell University, Ithaca, NY 14853, USA.



### Abstract

Here, we describe a systematic study on the removal of polymer template from inverse hexagonal ordered poly(butadiene)-*block*-poly(2-dimethylaminoethyl methacrylate) / phosphomolybdic acid ( $H_3PMo_{12}O_{40}$ ). Highly ordered mesophases were obtained *via* an evaporation-induced self assembly process. Different techniques were used to remove the organic template: Direct calcinations in air, a two-step heat treatment (1. argon atmosphere, 2. oxidative atmosphere), and a combination of heat and plasma treatment. Our study shows that direct calcination in air and two-step heat treatment led to a collapse of mesostructure before complete removal of carbon was accomplished. Plasma etching of heat treated samples resulted in the accessibility of the pores of ultra-microtomed films, while keeping the mesostructure intact.

**Keywords.** calcination, diblock copolymer, polyoxometalate, evaporation induced self assembly, heteropoly acid

## Introduction

Since the discovery of the first heteropoly compound by Berzelius in 1826 the research on polyoxometalate (POM) chemistry developed to an emerging field in chemistry.<sup>1-3</sup> In particular, POMs of the Keggin-type (Keggin POM) have encountered world-wide attention, due to their unique properties in fields like catalysis, electrochemistry and host guest chemistry.<sup>4-8</sup> Up until today, however, their applications are limited caused by the relatively small surface areas of Keggin POMs ( $3\text{ m}^2\text{g}^{-1}$  for commercial phosphomolybdic acid,  $\text{H}_3\text{PMo}_{12}\text{O}_{40}$ ,  $\text{H}_3\text{PMo}$ ) which hinders the accessibility of the active sides.<sup>4</sup> It has been shown that the activity of heterogeneous catalysts predominantly depends on the surface area of the catalytic active material.<sup>6-8</sup>

Since the pioneering work of scientists from the Mobile Oil cooperation in 1992 a run on mesoporous metal oxides has begun.<sup>9</sup> Extension of the template assisted preparation of mesoporous metal oxides on diblock copolymers enables a variety of smart mesophases with pore sizes of up to several tens of nanometers.<sup>10</sup>

Mesoporous metal oxides with increased surface areas have been successfully prepared exo- and endotempalting methods.<sup>11-15</sup> Since the first preparation of mesoporous silica MCM-41<sup>9</sup>, and SBA-15<sup>10</sup>, these high surface area solids were used for the dispersion and/or encapsulation of Keggin POM.<sup>16-18</sup> Even though the accessible surface area of Keggin POMs can be increased by these templating methods, limitations result from low Keggin POM loading, leaching of the active sites into the reaction medium and pore blocking in porous supports.<sup>4</sup>

However, incorporation of hydrophilic Keggin POM units into hydrophobic organic matrices was challenging. In the last few years this problem has been solved for instance by replacing the counterions with cationic surfactants forming the so called surface encapsulated POMs (SECs). The organophilized Keggin POMs were than soluble in organic solvents and can self-assemble into a variety of discrete nanoobjects that possess high catalytic activity.<sup>3,19-21</sup> An extension of the concept to ionizable diblock copolymers yielded to discrete Keggin POM rod-like, micellar or vesicular nanoobjects.<sup>22-26</sup> Recently, we presented a synthesis protocol towards invers hexagonal ordered diblock copolymer/ Keggin POMs nanocomposites. However, the complete functionality of those ordered nanocomposites can only be achieved if the polymer matrix can be removed to leave ordered mesoporous Keggin POM. Until now, the organic template of

mesostructured Keggin POM was removed by direct heat treatment in air. This in turn resulted in the collapse of the mesostructure indicated by a low accessible surface area or crystalline metal oxide species.<sup>27-30</sup>

In this manuscript we explored several strategies to remove the organic template of the inverse hexagonal ordered diblock copolymer/ H<sub>3</sub>PMo nanocomposites with retaining the ordered mesostructure. Ordered nanocomposites were synthesized using the amphiphilic, ionizable diblock copolymer, poly(butadiene-*block*-dimethylaminoethyl methacrylate) (PB-PDMAEMA) as structure directing agent. Subsequent systematic calcination studies were divided into three sections: First, direct calcinations in air. Second, two step heat treatment first in argon atmosphere followed by calcinations in oxidative atmosphere. This concept is further denoted as combined assembly of soft and hard (CASH). Third, plasma treatment of argon calcined materials.

## Materials and Methods

If not mentioned explicitly the reactants were used without further purification.

### *Synthesis of PB-PDMAEMA.*

The diblock copolymer PB -PDMAEMA was synthesized by sequential living anionic polymerization in tetrahydrofuran (THF) as published elsewhere.<sup>31</sup> THF- Gel permeation chromatography (GPC) was used to determine the molecular weight of the first block (polybutadiene, PB). GPC measurements were performed in the presence of 0.25 wt % tributylammonium bromide (TBAB) to determine the polydispersity index (PDI) of the diblock copolymer. <sup>1</sup>H-NMR was used to determine the overall molecular weight and composition of the diblock copolymer. The resulting PB-PDMAEMA polymer had a molecular weight of 29 kg/mol and a weight content of 22 wt % of PDMAEMA with a PDI of 1.03.

### *Preparation of inverse hexagonal PB-PDMAEMA/H<sub>3</sub>PMo nanocomposites films.*

The diblock copolymer/H<sub>3</sub>PMo composite films were prepared by adding a filtered (0.2 µm, PTFE filter) PB-PDMAEMA polymer solution in tetrahydrofuran (THF, Aldrich, p.a.) to a separate THF solution of H<sub>3</sub>PMo (Aldrich) under continuous stirring. In a typical synthesis of a 1:3 diblock copolymer: H<sub>3</sub>PMo composite film, 500 mg of the diblock copolymer were dissolved in 10 mL of THF. This solution was added dropwise to the H<sub>3</sub>PMo solution in THF solution (1.5 g HPMo in 15 mL of THF) at room temperature

(RT) under continuous stirring. After 30 min, the solution was subsequently poured into a Teflon petri dish (diameter: 7 cm) and a film was cast by evaporation of the solvent in air at RT under a relative humidity of 33 %.

#### *Organic template removal of composite films.*

The removal of diblock copolymer from inverse hexagonal ordered nanocomposite films was performed using three different techniques:

##### *1. Direct calcination in air*

Direct calcination in air was accomplished in a tube furnace under stepwise heating (150 °C – 5 h, 250 °C – 3 h, and 375 °C – 10 h) with a heating and cooling rate of 3 °C/min and constant air flow.

##### *2. CASH method*

Applying the CASH method, as-synthesized nanocomposite films were first heat treated in argon atmosphere (150 °C – 5 h, 250 °C – 3 h, and 375 °C – 10 h). Subsequent, calcination was performed by a systematic variation of the reactive atmospheres (air, oxygen), the temperature, and dwell time according to Table SI1. In all cases heating rate (3 °C/min) and gas flow was kept constant. Sample mass was determined before and after the calcination steps in a glove box. Samples were stored over P<sub>2</sub>O<sub>5</sub> in an exsiccator to minimize the error in weighing due to moisture exposure.

##### *3. Plasma treatment of argon calcined composite films.*

Argon heat treated nanocomposite films were exposed to H-O-plasma for 5 min under reduced atmospheric pressure (70 mTorr) using a SOLARUS 950 Gatan Advanced Plasma System. The power was set to 50 W. The ratio of H<sub>2</sub> to O<sub>2</sub> gas composition was adjusted to 1:4.3 (v/v).

#### *Characterization.*

Fourier transformed infrared (FTIR) data were collected on a Bruker IFS66V using KBr pellets.

Ambient-temperature Raman spectroscopy experiments were performed using a Jobin Yvon Labram spectrometer with a 632.8 nm He-Ne excitation line and a laser output power of 8 mW. The laser beam was focused using a 50x objective, resulting in a spot having a diameter of approx. 5 µm.

Powder X-ray diffraction (PXRD) measurements were performed at RT on a Panalytical XPERT-PRO diffractometer in reflection mode using CuK $\alpha$  radiation.

N<sub>2</sub> physisorption was conducted at 77 K on a Quantachrome Autosorb 1 instrument. Prior to measurements, the samples were degassed at 373 K for 24 h.

Transmission electron microscopy (TEM) micrographs were recorded on a Zeiss CEM 902 with an acceleration voltage of 80 kV. Prior to measurement the samples were embedded into an Epon resin, microtomed into 50 nm thick slices and deposited on a carbon coated copper grid or on a lacey carbon copper grid.

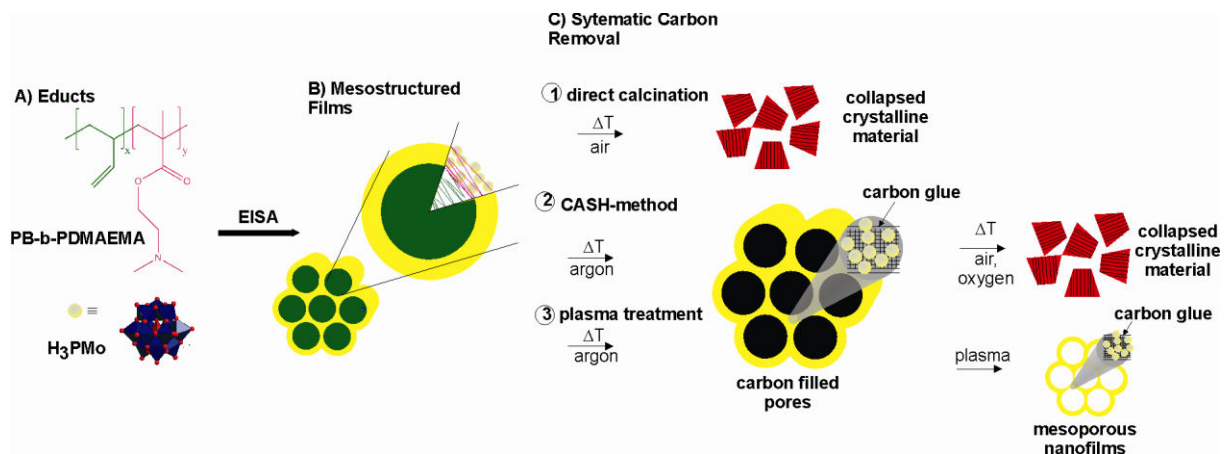
Field emission scanning electron microscopy (FESEM) was performed using a LEO Gemini microscope equipped with a field emission cathode.

Small angle X-ray scattering (SAXS) data were collected at the Cornell High Energy Synchrotron Source (CHESS) applying a CCD 2-D detector. X-ray wavelength of 1.378 Å was used and the sample-to-detector distance was 352.02 cm. Furthermore, SAXS measurements were accomplished at the DESY/HASYLAB with a X-ray wavelength of 0.095 nm and a detector distance of 4.52 m.

## Results and Discussions

We investigated the removal of the polymeric template from inverse hexagonal PB-b-PDMAEMA/H<sub>3</sub>PMo nanocomposites. Over 20 different calcination conditions have been conducted. They were derived from a variation of calcination atmosphere, temperature, and time. A detailed characteristical overview of all samples is given in Table SI 1. Scheme 1 summarizes our approach. Direct calcination of as-synthesized PB-b-PDMAEMA/H<sub>3</sub>PMo nanocomposite in air led to the formation of crystalline MoO<sub>3</sub> and the loss of the hexagonal order (Scheme 1c route 1). To remove the organic template and prevent structural collapse we focused on a two step heat treatment (Scheme 1c route 2): First, heat treatment in an inert environment converts parts of the sp<sup>2</sup> hybridized carbons in the PB block into amorphous carbon. This *in-situ* formed carbon acted as glue for H<sub>3</sub>PMo units and hampered structural collapse during heat treatment.<sup>12;32</sup> Second, calcination in air and oxygen atmosphere at different temperatures and dwell times targeted the removal of the carbon. Additionally we exposed argon treated samples to H-O-plasma (Scheme 1c route 3). Structural assignments of as-synthesized, heat treated, and calcined nanocomposite films were accomplished by a combination of SAXS and

TEM. The chemistry of the walls for all films were investigated by a combination of PXRD and FTIR spectroscopy.



Scheme 1: A) Structure of H<sub>3</sub>PMo and PB-b-PDMAEMA. x denotes the degree of polymerization (DP) for the PB block (x= 411), and y the DP of the PDMAEMA block (y=40). B) Within the PDMAEMA matrix the H<sub>3</sub>PMo clusters were selectively incorporated. C) Systematic calcination studies were conducted either direct in air (route 1) or applying a two step heat treatment (route 2): first in argon and second in oxidative atmosphere. Additional argon heat treated samples were exposed to H<sub>2</sub>O plasma (route 3).

*As-synthesized PB-b-PDMAEMA/H<sub>3</sub>PMo nanocomposites.* Inverse hexagonal PB-b-PDMAEMA/H<sub>3</sub>PMo nanocomposite films were prepared as reported previously.<sup>33</sup> The inverse hexagonal mesostructure was evidenced by TEM images (Figure 1A) and SAXS measurements (Figure SI 1Aa). The corresponding PXRD pattern (Figure 2Aa) showed an amorphous material indicating well dispersed H<sub>3</sub>PMo units within the composite matrix. FTIR spectra (Figure 3Aa and 3Ab) H<sub>3</sub>PMo and PB-b-PDMAEMA/H<sub>3</sub>PMo composite, respectively, illustrated the four characteristic bands of H<sub>3</sub>PMo. FTIR spectra of PB-b-P2VP diblock copolymer, the commercial H<sub>3</sub>PMo and the as-synthesized PB-b-P2VP/H<sub>3</sub>PMo composite were shown in Figure SI 2. It has been widely reported that H<sub>3</sub>PMo unit shows four characteristic bands, which are the fingerprint of the Keggin structure.<sup>34;35</sup> There are four kinds of oxygen atoms in H<sub>3</sub>PMo. H<sub>3</sub>PMo exhibits these characteristic bands at  $\nu_{as}$  (Mo-O<sub>d</sub>) – 960 cm<sup>-1</sup>,  $\nu_{as}$  (Mo-O<sub>b</sub>-Mo) – 870 cm<sup>-1</sup>,  $\nu_{as}$  (Mo-O<sub>c</sub>-Mo) – 785 cm<sup>-1</sup>, and  $\nu_{as}$  (P-O<sub>a</sub>) – 1065 cm<sup>-1</sup>. The FTIR spectrum of the PB-PDMAEMA composite corresponds well to the superposition of the spectrum of the commercial

$\text{H}_3\text{PMo}$  and PB-PDMAEMA polymer template which is an indication that the Keggin structure stayed intact when being incorporated in the polymer matrix. However, there is a shift observed in the frequencies for Mo-O-Mo (corner and edge shared) vibrations (Table SI1). The vibration corresponds to the basic oxygens concerned in the interaction of the  $\text{PMo}^{3-}$  anions and the positive template. The change in the environment of the  $\text{H}_3\text{PMo}$  is a hint for electrostatic interactions between the PB-b-PDMAEMA diblock copolymer and the  $\text{H}_3\text{PMo}$  units.

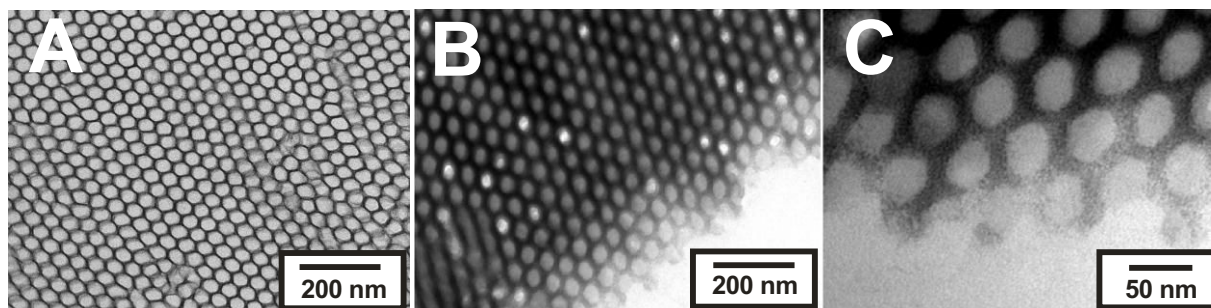


Figure 1: TEM micrographs of A) as-synthesized PB-b-PDMAEMA/ $\text{H}_3\text{PMo}$  nanocomposite, and B) and C) argon heat treated material (carbon/ $\text{H}_3\text{PMo}$  nanocomposite) at different magnifications.

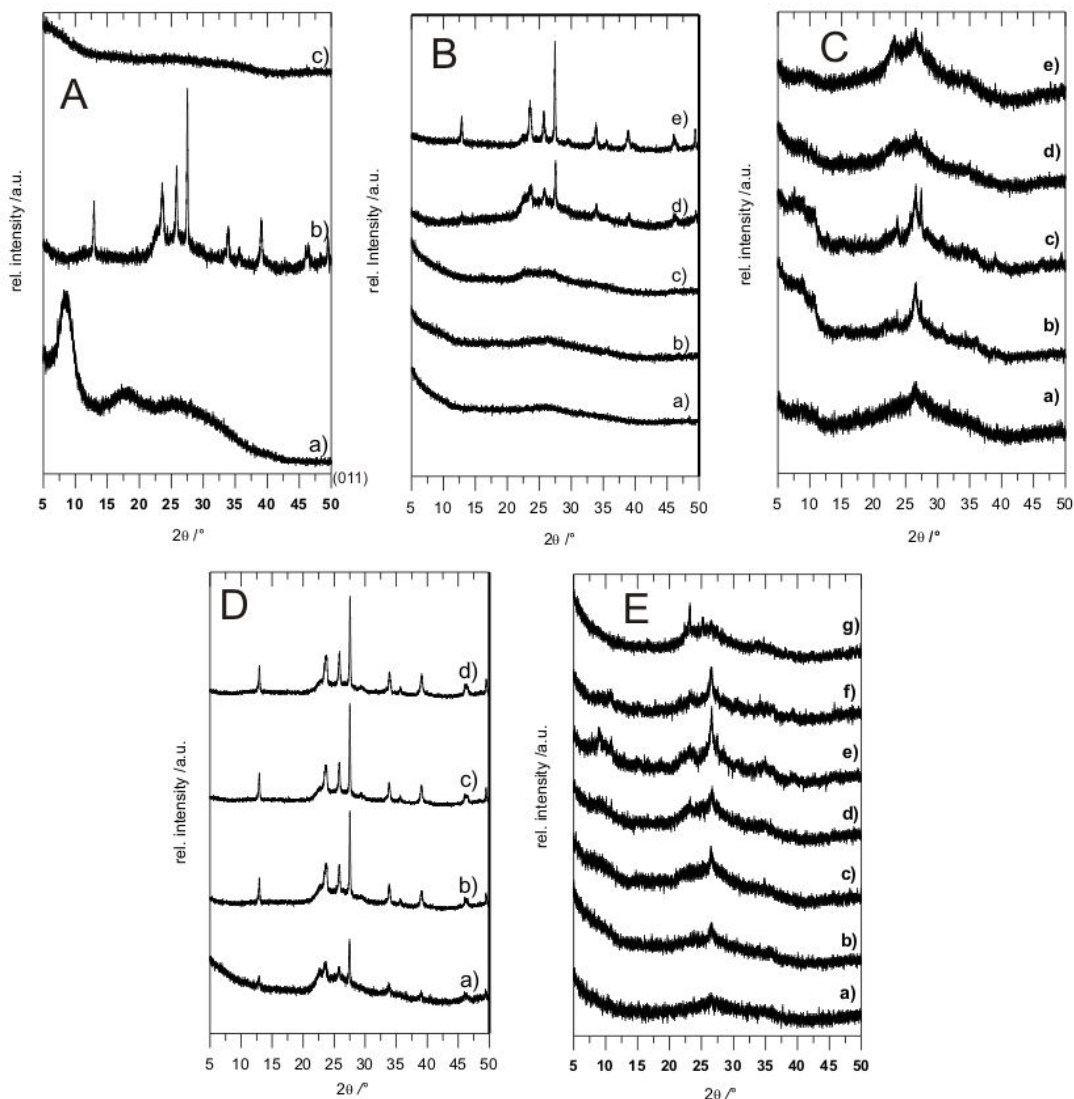


Figure 2: PXRD patterns of the nanocomposites as obtained after different heat treatments. A) PXRD patterns of direct calcined composites: a) as-synthesized, b) calcined direct in air (POM1) and c) heat treated in argon. B) PXRD curves of carbon/H<sub>3</sub>PMo nanocomposites calcined in air for 1 h at different temperatures: a) 300 °C, b) 320 °C, c) 340 °C, d) 360 °C, and e) 380 °C. C) PXRD data obtained from carbon/H<sub>3</sub>PMo nanocomposites calcined in air at 320 °C and different times: a) 3 h, b) 5 h, c) 10 h, d) 15 h, and e) 20 h. D) PXRD graphs corresponding to carbon/H<sub>3</sub>PMo nanocomposites calcined at 360 °C and different times: 5 h, b) 10 h, c) 15 h, and d) 20 h. E) PXRD patterns of oxygen calcined carbon/H<sub>3</sub>PMo nanocomposites at 320 °C and different times: a) 1h, b) 5h, c) 10 h, d) 15 h, e) 20 h, and f) 48 h.

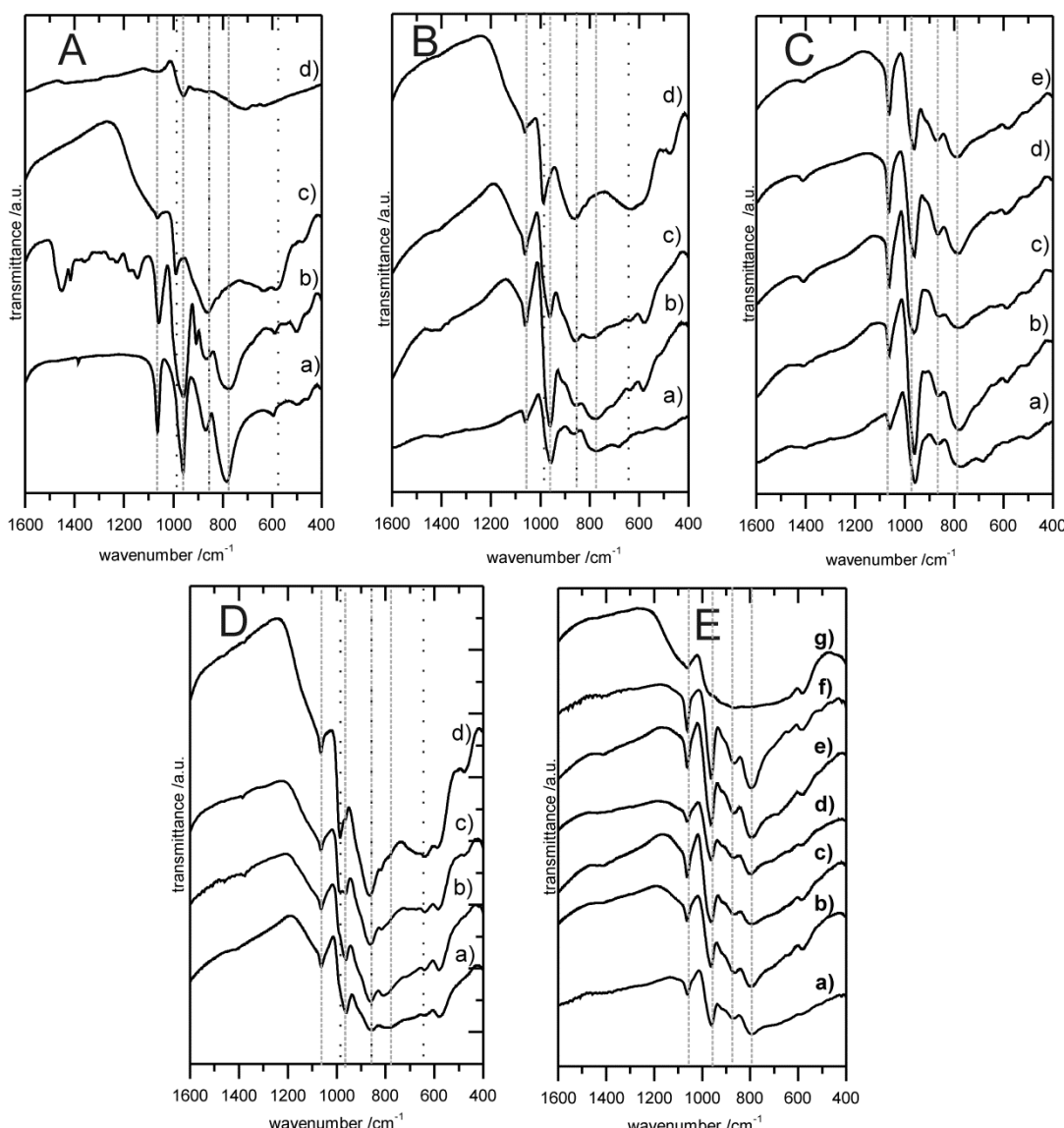


Figure 3: Evolution of FTIR spectra of PB-PDMAEMA/Keggin POM nanocomposites.

The dashed grayish lines denote the four characteristic vibrations attributed to  $\text{H}_3\text{PMo}$ . The black dotted lines are indicative for  $\text{MoO}_3$ . A) FTIR spectra of PB-PDMAEMA/Keggin POM composites: a) as-synthesized, b) calcined direct in air and c) heat treated in argon. B) FTIR spectra of carbon/ $\text{H}_3\text{PMo}$  nanocomposites calcined in air for 1 h at different temperatures: a) 300 °C, b) 320 °C, c) 340 °C, d) 360 °C, and e) 380 °C. C) FTIR spectra obtained from carbon/ $\text{H}_3\text{PMo}$  nanocomposites calcined in air at 320 °C and times: a) 3 h, b) 5 h, c) 10 h, d) 15 h, and e) 20 h. D) FTIR spectra corresponding to carbon/ $\text{H}_3\text{PMo}$  nanocomposites calcined at 360 °C and times: a) 5 h, b) 10 h, c) 15 h, and d) 20 h. E) FTIR spectra of oxygen calcined carbon/ $\text{H}_3\text{PMo}$  nanocomposites at 320 °C and times: a) 1 h, b) 5 h, c) 10 h, d) 15 h, e) 20 h, and f) 48 h.

*Systematic heat treatment.* First, as-synthesized PB-PDMAEMA/ H<sub>3</sub>PMo nanocomposite was calcined directly in air. The PXRD patterns revealed a crystalline MoO<sub>3</sub> phase (Figure 2 Ab) which is in line with the observation made by the FTIR measurements (Figure 3c). The band that corresponded to the terminal Mo-O<sub>t</sub> vibration shifted from 960 cm<sup>-1</sup> to 990 cm<sup>-1</sup> and at the same time the corner-sharing vibration (Mo-O<sub>c</sub>-Mo) at 785 cm<sup>-1</sup> was completely vanished. The structural assignments corroborated the loss of mesostructure (see also SAXS: Figure SI 1Ab and TEM: Figure SI 2 POM1 ). Carbon elemental analysis showed that 1.6 wt % were carbonaceous. These results suggested that the PMo<sup>3-</sup> anions decompose even at relative low temperatures. Furthermore the low carbon content could not stabilize the inorganic walls. Additional decomposition and crystallization of the H<sub>3</sub>PMo units promote the loss of mesostructure.

Second, as-synthesized PB-PDMAEMA/H<sub>3</sub>PMo nanocomposite was heat treated in argon which is further denoted as carbon/H<sub>3</sub>PMo nanocomposite. While heat treated in inert atmosphere at 375 °C PMo<sup>3-</sup>- anions were glued into a rigid carbon matrix resulting in an amorphous material (Figure 2Ac). The disappearance of the  $\nu_{as}(\text{Mo-O}_b\text{-Mo})$  and  $\nu_{as}(\text{Mo-O}_b\text{-Mo})$  vibrations in the FTIR spectra (Figure 3Ad) indicated that parts of the Mo(VI) were reduced, while the Keggin structure was maintained.<sup>36</sup> Raman spectroscopy of carbon/H<sub>3</sub>PMo nanocomposite is shown in Figure a. Two bands around 1600 cm<sup>-1</sup> and 1350 cm<sup>-1</sup> were attributed to graphitic (G-band) and disordered carbon (D-band), respectively, typical for amorphous carbon materials.<sup>12;37</sup> Elemental analysis of carbon/H<sub>3</sub>PMo nanocomposite proofed that 28 wt % were carbon. The *in-situ* formed carbon/H<sub>3</sub>PMo nanocomposites maintained the hexagonal order as evidenced by TEM (Figure 1B and C) and SAXS patterns (Figure SI 1Ac). SEM images showed that the outer surface of the carbon/H<sub>3</sub>PMo nanocomposite was covered (Figure 5). The nature of this material is unclear. We assume that polymeric fragments upon decomposition of the diblock copolymer might cover the material.

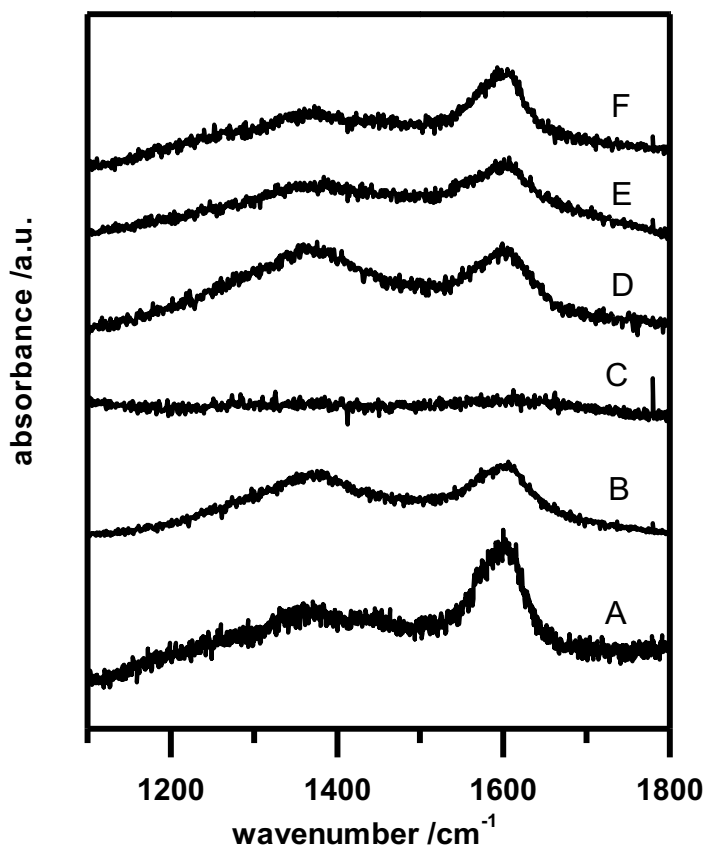


Figure 4: Raman spectra of carbon/H<sub>3</sub>PMo nanocomposite A), and carbon/H<sub>3</sub>PMo nanocomposite after different subsequent calcinations: B) air; 320 °C, 20 h; C) air; 360 °C, 20 h, D) oxygen, 320 °C, 20 h, E) oxygen, 320 °C, 48 h, F) carbon/H<sub>3</sub>PMo nanocomposite after plasma treatment.

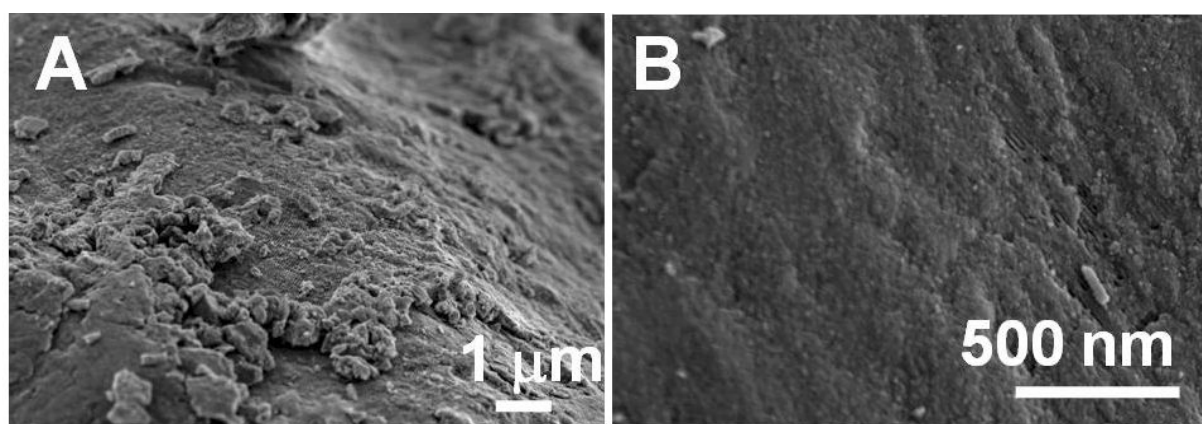


Figure 5: SEM images of carbon/H<sub>3</sub>PMo nanocomposite.

To remove the amorphous carbon calcination in air normally at temperatures around 500 to 600 °C were conducted in the literature.<sup>12;13;38;39</sup> At this relatively high temperatures the H<sub>3</sub>PMo unit decomposed into crystalline MoO<sub>3</sub>.<sup>4;40-42</sup> Hence, carbon/H<sub>3</sub>PMo nanocomposites were subjected to systematic calcination studies in oxidative atmosphere (air, oxygen) to find the appropriate temperature and dwell time for complete carbon removal. In this context we define mild, medium, and harsh calcination conditions depending on the evolution of crystalline phases after calcinations (see Table 1).

Table 1: Definition of calcination conditions.

calcination condition	atmosphere	T /°C	t /h	crystallinity <sup>a</sup>	morphology <sup>b</sup>
mild	air	300	1	A	hex
		320	1	A	hex
		320	3	A	hex
medium	air	320	5	SC	hex
			10	SC	hex
			15	SC	hex
			20	SC	hex
		340	1	SC	hex
		360	1	SC	hex
			5	SC	hex
	oxygen	320	1	SC	hex
			3	SC	hex
			5	SC	hex
			10	SC	hex
			15	SC	hex
			20	SC	hex
harsh	air	360	10	C	D
			15	C	D
			20	C	D
		380	1	C	D
	oxygen	320	48	C	D

<sup>a</sup> as obtained from PXRD measurements: A: amorphous, SC: semicrystalline, C: crystalline.

<sup>b</sup> mesostructure obtained from a combination of TEM and SAXS measurements: hex: invers hexagonal, D: disordered.

The phase evolution of the oxidic walls after subsequent systematic calcinations of

carbon/H<sub>3</sub>PMo nanocomposites were investigated by PXRD measurements (Figure 2) and FTIR spectra (Figure 3). For mild calcination conditions amorphous walls were observed (Figure 2Ac, Ba and Bc). Moreover, medium conditions rendered the formation of semicrystalline walls (Figure 2C and Ea-f). Under harsh calcination temperatures the PXRD patterns shifted to motives resembling those of crystalline MoO<sub>3</sub> (Figure 2Bc-d, D, and Eg). PXRD patterns of crystalline materials (Figure SI 3) revealed the presence of at least four different phases: amorphous phases, one phase that can be assigned to cubic H<sub>3</sub>PMo, and at least two polymorphs of MoO<sub>3</sub>, monoclinic and orthorhombic, respectively.

The PXRD patterns were in line with the FTIR spectra (Figure 3). The FTIR spectra of carbon/H<sub>3</sub>PMo nanocomposite for mild and medium calcination conditions (Figure 3C and E) showed the presence of the four characteristic H<sub>3</sub>PMo vibrations. Both Mo-O-Mo vibrations became more intense indicating the re-oxidation of the H<sub>3</sub>PMo units. However, only under harsh conditions the vibration in the FTIR spectra were shifted (Figure 3D, Bd, and Eg). New peaks at 990 cm<sup>-1</sup> and 650 cm<sup>-1</sup> resemble those of MoO<sub>3</sub>.

Mesostructural changes during the calcination studies of carbon/H<sub>3</sub>PMo nanocomposites were assigned by a combination of SAXS (Figure SI 1) and TEM (Figure SI 2) measurements. Inverse hexagonal mesophases were still present while calcinations under mild and medium conditions. An order/disorder transition could only be observed after applying harsh calcination conditions (Table 1). In contrary to the degree of crystallinity of the chemistry of the walls, the mesophase seemed to be almost unaffected up to harsh calcination conditions. The amorphous carbon acted as glue for the discrete nanoparticles. The enduring existence of the carbon material over the whole range of calcination conditions could be followed by Raman measurements (Figure 4).. Two peaks appeared at around 1350 cm<sup>-1</sup> and 1600 cm<sup>-1</sup> that evidenced the presence of carbonaceous materials.<sup>43</sup> However, under harsh conditions the carbon glue was assumed to be insufficiently low to compensate the decomposition of the H<sub>3</sub>PMo units and the density changes upon crystallization of the walls supporting the collapse of the mesostructure.

Furthermore leaching experiments were conducted for carbon/H<sub>3</sub>PMo nanocomposites calcined under medium conditions to show the influence of an inorganic network formation on retaining the inverse hexagonal mesostructure. The

results were surprising since over 70 % of the material were soluble in water. Indeed, this experiment showed that H<sub>3</sub>PMo units do not condense within the walls. Hence, retaining the mesostructure was ascribed to the presence of the carbon glue.

Hence, a further characterization method was considered that was directly related to the carbon content. Thus, after each calcination step the weight loss of the material (Table SI 1) was determined. The phases obtained from the PXRD measurements could be expressed as function of weight loss and calcinations times (Figure 6) and gave rise to the existence of domains of amorphous (A), semicrystalline (SC), and crystalline (C) phases. The order/ disorder transition could be visualized (Figure 7, grey area) and attributed to a high weight loss and crystalline materials.

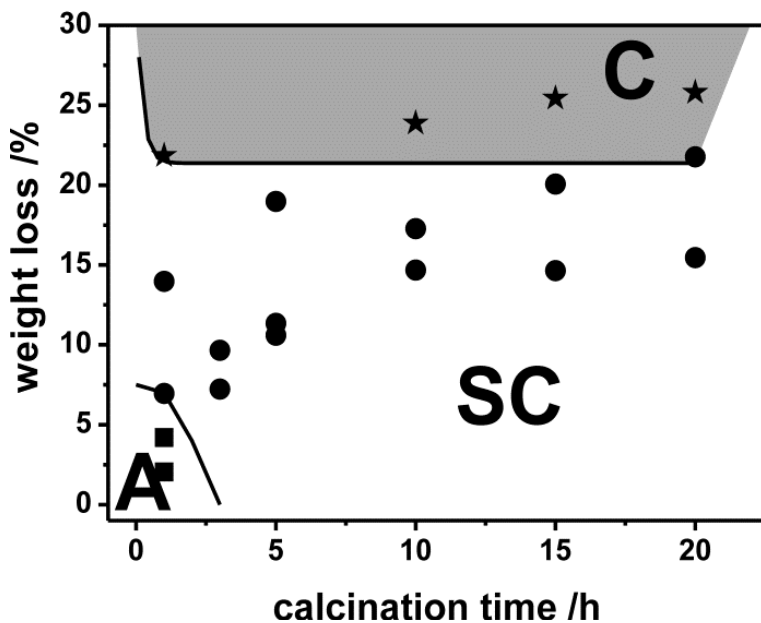


Figure 6: The degree of crystallinity expressed as function of weight loss and calcinations times. The squares denote the amorphous regime (A), the spheres represent semicrystalline materials (SC), and the stars show crystalline material (C). The grey area depicts conditions where disordered nanocomposites were obtained.

*Plasma treatment.* Third, mechanical methods such as plasma treatment were considered in order to gain access to the ordered mesopores, alternatively. Recently, we described the efficiency of plasma in opening the pores of a hexagonally ordered composite.<sup>44</sup> Hence, we exposed ultra-thin microtomed slices (50 nm) of carbon/H<sub>3</sub>PMo

nanocomposites to H<sub>2</sub>O-plasma. The corresponding TEM and SEM images are depicted in Figure 7A to E and Figure SI 4. These micrographs illustrate that plasma treatment opened almost all mesopores. The contrast modulation in Figure 7C suggested that carbon (grey) still covered the material that proved the assumption of a rigid carbon glue material. Additional plasma treatment of a carbon/H<sub>3</sub>PMo nanocomposite bulk material was accomplished to achieve mesoporous Keggin POM. The corresponding FE-SEM image (Figure 7F) showed the presence of hexagonally ordered cylinders. However, the absence of porosity as obtained from physisorption measurements and the presence of D- and G- mode within the corresponding Raman spectra (Figure F) indicated that the pores were still filled with carbon. The destroyed outer cylinders in Figure 7F revealed that plasma treatment removed the outer carbon crust and had no influence on removing the carbon comprised inside the pores.

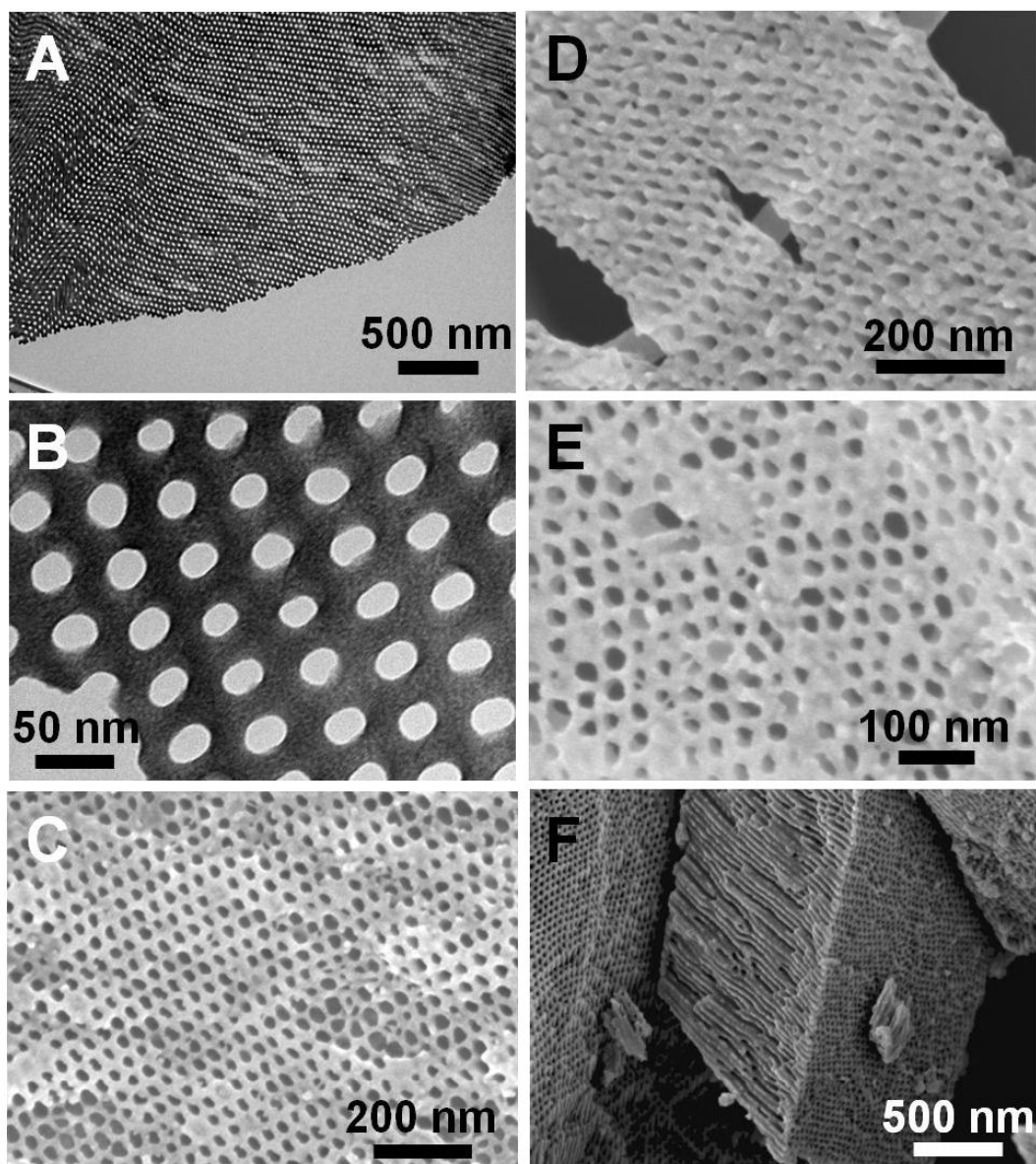


Figure 7: Electronic microscopy images of plasma treated POM-cash: A) and B) TEM micrographs and C) to E) FE-SEM images of H-O-plasma treated POM-cash microtomed films at different magnifications. F) Representative FE-SEM image of plasma treated bulk samples.

## Conclusion

In summary, this work demonstrated that the preparation of mesoporous H<sub>3</sub>PMo is rather complex. In particular, this consideration is based on three pillars: the lack of condensation and the insufficient thermal stability of the H<sub>3</sub>PMo units. The CASH-method is inappropriate for this system due to the thermal instability of H<sub>3</sub>PMo units and the relative inertness of *in-situ* formed graphitic carbon at temperatures below 400 °C. Moreover, plasma etching has been introduced to be a suitable method in order to remove organic material in thin films. Future work might focus on the improvement of carbon removal and condensation of the H<sub>3</sub>PMo units. Further research could introduce a diblock copolymer as SDA that depolymerized at temperatures far below 400 °C. Moreover, cross-linking of the inorganic matrix could be achieved by adding alkali or lanthanoid salts. Replacing the Zündel-cation against metal cations might form an inorganic network and remove the water of constitution. This in turn might lead to enhanced thermal stability and finally to the realization of mesoporous H<sub>3</sub>PMo.

**Acknowledgment.** This work was supported by the Deutsche Forschungsgemeinschaft (DFG) within the Collaborative Research Center (SFB) 840. T. L. thanks the international graduate school of the ENB “Structures, Reactivity and Properties of Metal Oxides” for a fellowship. M.K. was supported by the Netherlands Organization for Scientific Research (NWO, VENI-700.10.404). Z. L was supported by the U.S. Department of Homeland Security under Cooperative Agreement Number 2009-ST-108-LR0004. The X-ray equipment was supported by Department of Energy grant DEFG-02-97ER62443. CHESS was supported by the NSF and NIH-NIGMS via DMR-0225180.

**Supporting Information.** Supporting Information is available in the www.

## References

- (1) Berzelius, J. J. *Pogg. Ann. Phys. Chem.* **1826**, 6, 369-380.
- (2) Long, D. L.; Tsunashima, R.; Cronin, L. *Angew. Chem. Int. Ed.* **2010**, 49, 1736-1758.
- (3) Song, Y. F.; Long, D. L.; Ritchie, C.; Cronin, L. *Chem. Record* **2011**, 11, 158-171.
- (4) Moffat, J. B. *Metal-Oxygen Clusters - The Surface and Catalytic Properties of Heteropoly Oxometalates*; Kluwer Academic/Plenum Publishers: New York, 2001.

- (5) Pope, M. T.; Müller, A. *Polyoxometalate Chemistry From Topology via Self-Assembly to Applications*; Kluwer Academic Publishers: Dordrecht, 2001.
- (6) Nomiya, K.; Murasaki, H.; Miwa, M. *Polyhedron* **1986**, *5*, 1031-1033.
- (7) Katsoulis, D. E. *Chem. Rev.* **1998**, *98*, 359-387.
- (8) Rhule, J. T.; Hill, C. L.; Judd, D. A. *Chem. Rev.* **1998**, *98*, 327-357.
- (9) Kresge, C. T.; Leonowicz, M. E.; Roth, W. J.; Vartuli, J. C.; Beck, J. S. *Nature* **1992**, *359*, 710-712.
- (10) Zhao, D. Y.; Feng, J. L.; Huo, Q. S.; Melosh, N.; Fredrickson, G. H.; Chmelka, B. F.; Stucky, G. D. *Science* **1998**, *279*, 548-552.
- (11) Brezesinski, T.; Wang, J.; Tolbert, S. H.; Dunn, B. *Nature Mater.* **2010**, *9*, 146-151.
- (12) Lee, J.; Orilall, M. C.; Warren, S. C.; Kamperman, M.; Disalvo, F. J.; Wiesner, U. *Nature Mater.* **2008**, *7*, 222-228.
- (13) Yang, P. D.; Zhao, D. Y.; Margolese, D. I.; Chmelka, B. F.; Stucky, G. D. *Nature* **1998**, *396*, 152-155.
- (14) Kang, M.; Kim, D.; Yi, S. H.; Han, J. U.; Yie, J. E.; Kim, J. M. *Catal. Today* **2004**, *93*-*95*, 695-699.
- (15) Lu, A. H.; Schüth, F. *Adv. Mater.* **2006**, *18*, 1793-1805.
- (16) Inumaru, K.; Ishihara, T.; Kamiya, Y.; Okuhara, T.; Yamanaka, S. *Angew. Chem. Int. Ed.* **2007**, *46*, 7625-7628.
- (17) Shi, C. F.; Wang, R. W.; Zhu, G. S.; Qiu, S. L.; Long, J. *Eur. J. Inorg. Chem.* **2005**, 4801-4807.
- (18) Blasco, T.; Corma, A.; Martinez, A.; Martinez-Escalano, P. *J. Catal.* **1998**, *177*, 306-313.
- (19) Nisar, A.; Lu, Y.; Zhuang, J.; Wang, X. *Angew. Chem. Int. Ed.* **2011**, *50*, 3187-3192.
- (20) Yan, Y.; Wu, L. *Isr. J. Chem.* **2011**, *51*, 181-190.
- (21) Li, D.; Yin, P.; Liu, T. *Dalton Trans.* **2012**, *41*, 2853-2861.
- (22) Maayan, G.; Popovitz-Biro, R.; Neumann, R. *J. Am. Chem. Soc.* **2006**, *128*, 4968-4969.

- (23) Bu, W.; Uchida, S.; Mizuno, N. *Angew. Chem. Int. Ed.* **2009**, *48*, 8281-8284.
- (24) Lin, X. K.; Wang, Y. L.; Wu, L. X. *Langmuir* **2009**, *25*, 6081-6087.
- (25) Bu, W. F.; Li, H. L.; Sun, H.; Yin, S. Y.; Wu, L. X. *J. Am. Chem. Soc.* **2005**, *127*, 8016-8017.
- (26) Yelamanchili, R. S.; Walther, A.; Muller, A. H. E.; Breu, J. *Chem. Commun.* **2008**, *4*, 489-491.
- (27) Janauer, G. G.; Doble, A.; Guo, J. D.; Zavalij, P.; Whittingham, M. S. *Chem. Mater.* **1996**, *8*, 2096-2101.
- (28) Stein, A.; Fendorf, M.; Jarvie, T. P.; Mueller, K. T.; Benesi, A. J.; Mallouk, T. E. *Chem. Mater.* **1995**, *7*, 304-313.
- (29) Taguchi, A.; Abe, T.; Iwamoto, M. *Adv. Mater.* **1998**, *10*, 667-669.
- (30) Yun, H. S.; Kuwabara, M.; Zhou, H. S.; Honma, I. *Thin Solid Films* **2007**, *515*, 2842-2846.
- (31) Schacher, F.; Müllner, M.; Schmalz, H.; Müller, A. H. E. *Macromol. Chem. Phys.* **2009**, *210*, 256-262.
- (32) Li, D. L.; Zhou, H. S.; Honma, I. *Nature Mater.* **2004**, *3*, 65-72.
- (33) Lunkenbein, T.; Kamperman, M.; Zihui, L.; Bojer, C.; Förster, S.; Wiesner, U.; Müller, A. H. E.; Breu J. *J. Am. Chem. Soc.* **2012**, submitted.
- (34) Rocchicciolieltcheff, C.; Fournier, M.; Franck, R.; Thouvenot, R. *Inorg. Chem.* **1983**, *22*, 207-216.
- (35) Rocchicciolieltcheff, C.; Aouissi, A.; Bettahar, M.; Launay, S.; Fournier, M. *J. Catal.* **1996**, *164*, 16-27.
- (36) Neier, R.; Trojanowski, C.; Mattes, R. *Dalton Trans.* **1995**, 2521-2528.
- (37) Liang, C.; Hong, K.; Guiochon, G. A.; Mays, J. W.; Dai, S. *Angew. Chem. Int. Ed.* **2004**, *43*, 5785-5789.
- (38) Brezesinski, T.; Wang, J.; Tolbert, S. H.; Dunn, B. *Nature Mater.* **2010**, *9*, 146-151.
- (39) Yelamanchili, R. S.; Lu, Y.; Lunkenbein, T.; Miyajima, N.; Yan L.-T.; Ballauff, M.; Breu, J. *Small* **2009**, *5*, 1326-1333.

- (40) Misono, M. *Catal. Rev. Sci. Eng.* **1987**, *29*, 269-321.
- (41) Rocchicciolieltcheff, C.; Aouissi, A.; Bettahar, M.; Launay, S.; Fournier, M. *J.Catal.* **1996**, *164*, 16-27.
- (42) Mestl, G.; Ilkenhans, T.; Spielbauer, D.; Dieterle, M.; Timpe, O.; Krohnert, J.; Jentoft, F.; Knozinger, H.; Schlogl, R. *Appl. Catal. A Gen.* **2001**, *210*, 13-34.
- (43) Sadezky, A.; Muckenhuber, H.; Grothe, H.; Niessner, R.; Pöschl, U. *Carbon* **2005**, *43*, 1731-1742.
- (44) Warren, S. C.; Messina, L. C.; Slaughter, L. S.; Kamperman, M.; Zhou, Q.; Gruner, S. M.; Disalvo, F. J.; Wiesner, U. *Science* **2008**, *320*, 1748-1752.

## Supporting Information

Table SI 1: Summary of calcination parameters and data obtained for different pyrolyzed PB-*b*-PDMAEMA/Keggin POM composites.

Sample	atmosphere of calcination	T <sub>calc</sub> /°C	t <sub>calc</sub> /h	CASH method +/-	wt loss /%	Hex <sup>a</sup> +/-	intact Keggin POM cluster	cryst. <sup>b</sup>	surface area <sup>b</sup> /m <sup>2</sup> g <sup>-1c</sup>
POM-cash	Argon	375	10	+		+	-	-	-
POM1	Air	375	10	-		-	-	MoO <sub>3</sub>	12
POM2	Air	300	1	+	0	+	+	-	-
POM3	Air	320	1	+	2.1	+	+	-	-
POM4	Air	320	3	+	7.2	+	+	HPMo	-
POM5	Air	320	5	+	10.6	+	+	HPMo	-
POM6	Air	320	10	+	17.3	+	+	HPMo	-
POM7	Air	320	15	+	14.7	+	+	HPMo	-
POM8	Air	320	20	+	15.5	+	+	HPMo	-
POM9	Air	340	1	+	7.0	+		MoO <sub>3</sub>	8
POM10	Air	360	1	+	14.0	+	+	MoO <sub>3</sub>	10
POM11	Air	360	5	+	19.0	+	+	MoO <sub>3</sub>	9
POM12	Air	360	10	+	23.9	-	-	MoO <sub>3</sub>	8
POM13	Air	360	15	+	25.4	-	-	MoO <sub>3</sub>	11
POM14	Air	360	20	+	25.8	-	-	MoO <sub>3</sub>	9
POM15	Air	380	1	+	21.9	-		MoO <sub>3</sub>	8
POM16	Oxygen	320	1	+	4.2	+	+	HPMo	3
POM17	Oxygen	320	3	+	9.7	+	+	HPMo	7
POM18	Oxygen	320	5	+	11.3	+	+	HPMo	-
POM19	Oxygen	320	10	+	14.7	+	+	HPMo	7
POM20	Oxygen	320	15	+	20.1	+/-	+	HPMo	7
POM21	Oxygen	320	20	+	21.8	+/-	+	HPMo	9

<sup>a</sup> hexagonal mesostructure according to TEM images

<sup>b</sup> crystallinity according to PXRD measurements

<sup>c</sup>obtained from 5 point BET analysis at 77K with nitrogen

## SAXS measurements

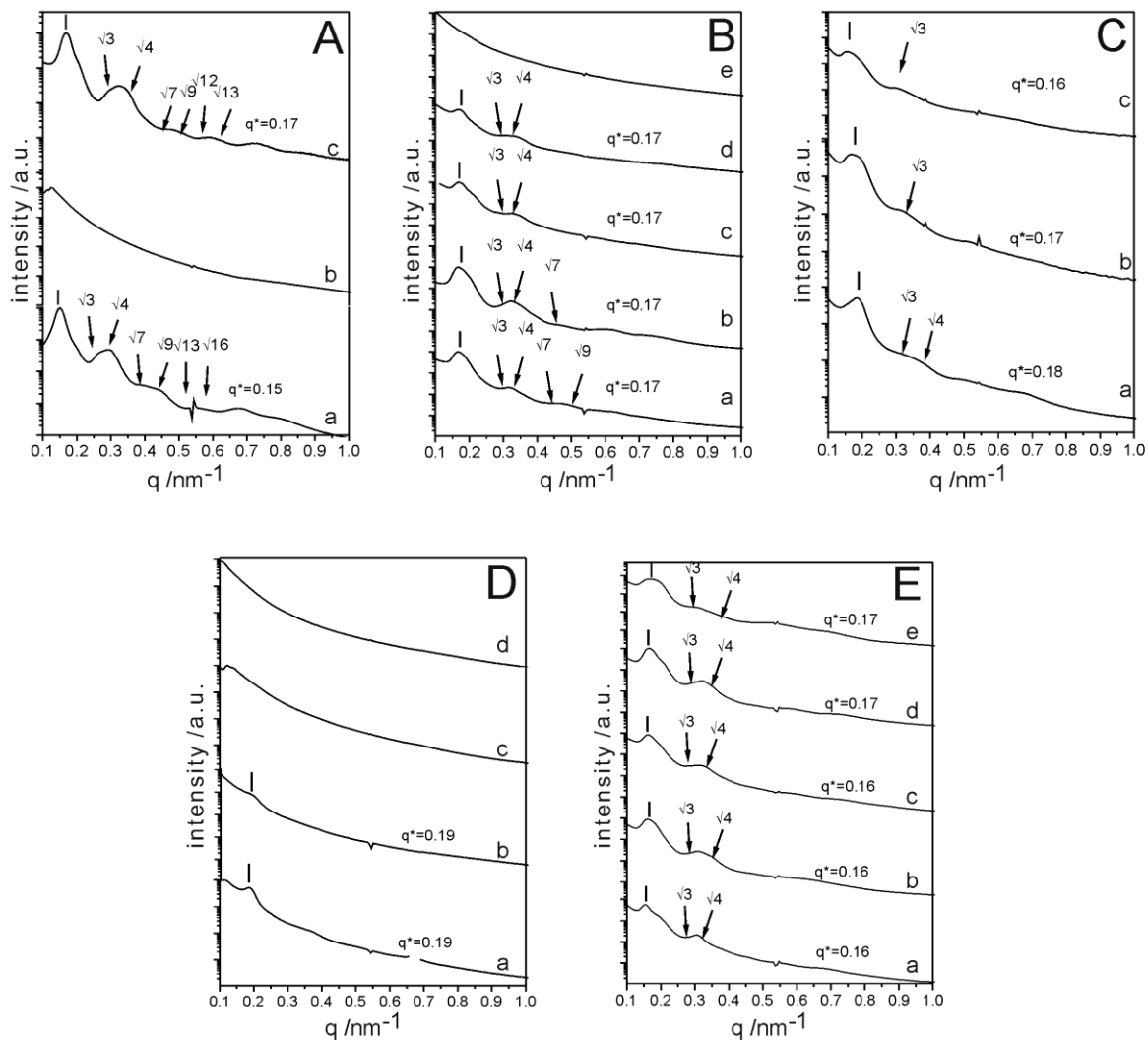


Figure SI 1: SAXS patterns of: A) as-synthesized (a), direct in air b), and c) carbon/H<sub>3</sub>PMo nanocomposite. B) The curves represent carbon/H<sub>3</sub>PMo nanocomposite after heat treatment in air for 1 h at different temperatures: a) 300 °C, b) 320 °C, c) 340 °C, d) 360 °C, and e) 380 °C. C) The graphs denote carbon/H<sub>3</sub>PMo nanocomposite pyrolyzed in air at 320 °C for different times: a) 10 h, b) 15 h, and c) 20 h. D) Calcination of carbon/H<sub>3</sub>PMo nanocomposite in air at 360 °C for different times: a) 5 h, b) 10 h, c) 15 h, and d) 20 h. E) Oxygen calcination of carbon/H<sub>3</sub>PMo nanocomposite at 320 °C for different times: a) 1 h, b) 5 h, c) 10 h, 15 h, and 20 h.

TEM images

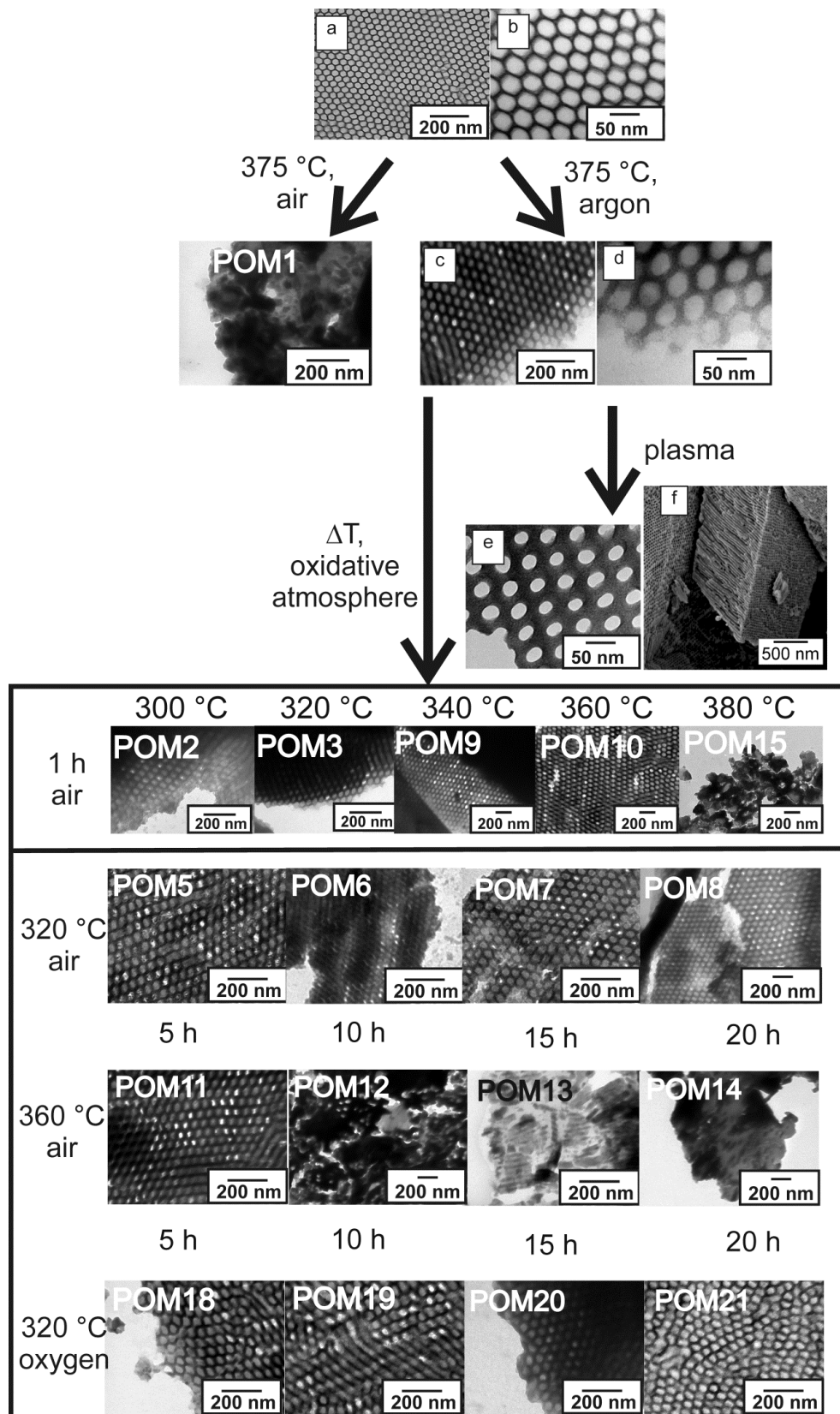


Figure SI 2: Representative TEM images.

## PXRD patterns

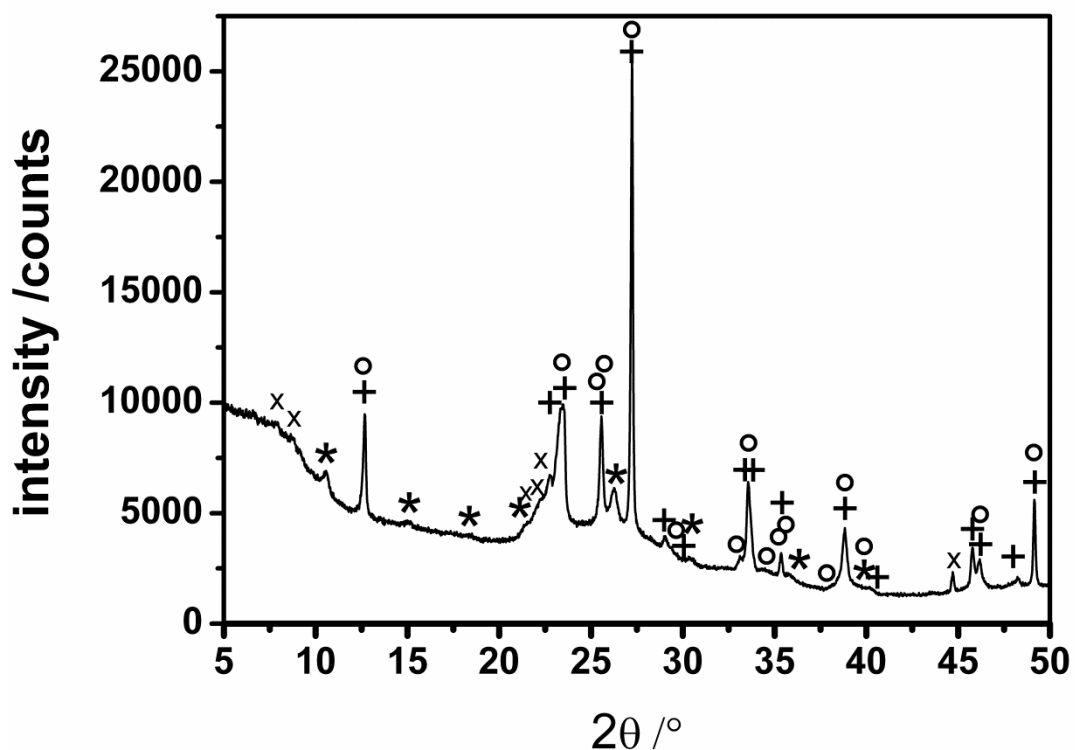


Figure SI 3: PXRD patterns for carbon/H<sub>3</sub>PMo composite calcined at 360 °C for 20 h in air. (+), (°), (\*) denote expected reflex positions for monoclinic, orthorhombic MoO<sub>3</sub>, cubic H<sub>3</sub>PMo and partially reduced molybdenum oxides such as (Mo<sub>4</sub>O<sub>11</sub>, Mo<sub>8</sub>O<sub>23</sub>, respectively.

**Plasma treatment**

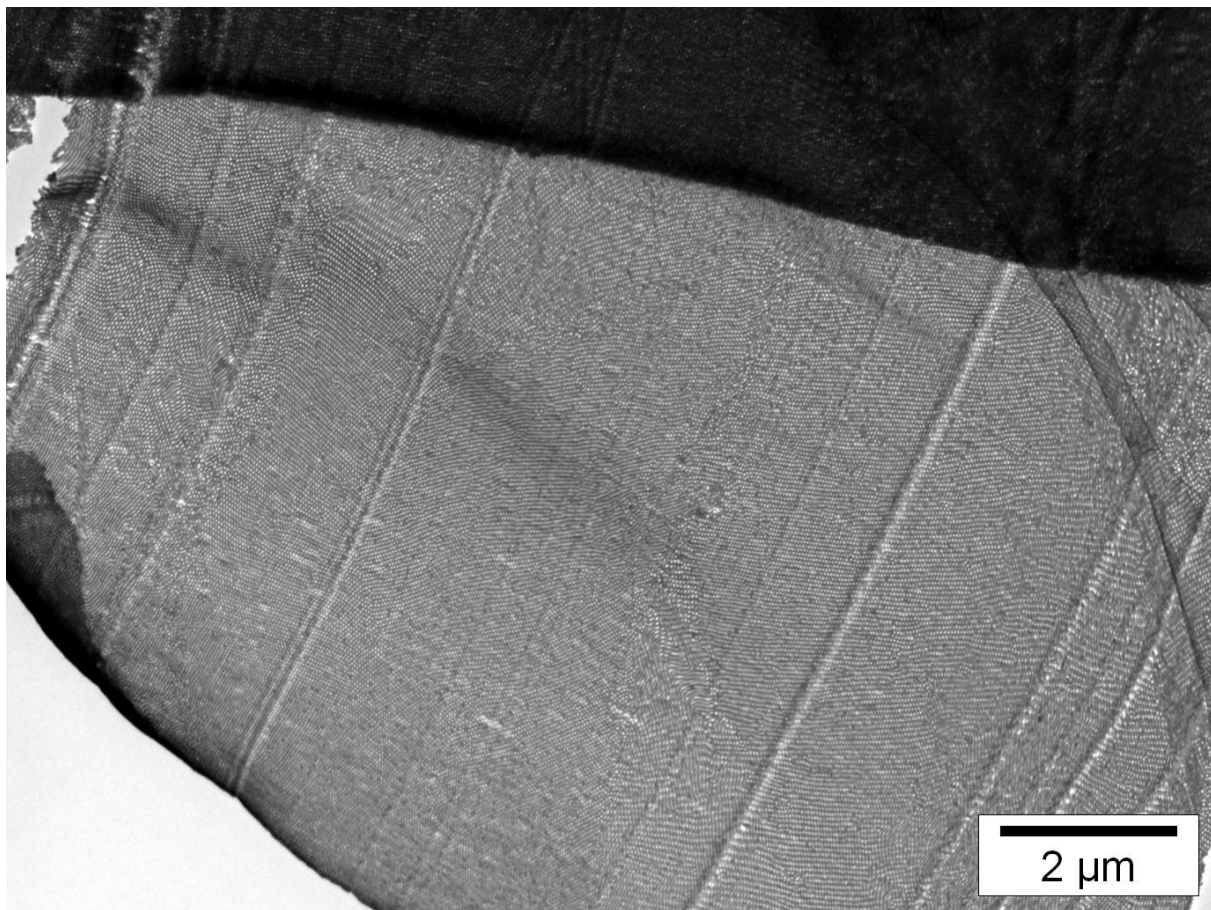


Figure SI 4: TEM micrograph of POM-plasma at low magnification.

## 7.7 Direct Access to Ordered Porous Molybdenum Oxycarbide/ Carbon Nanocomposites

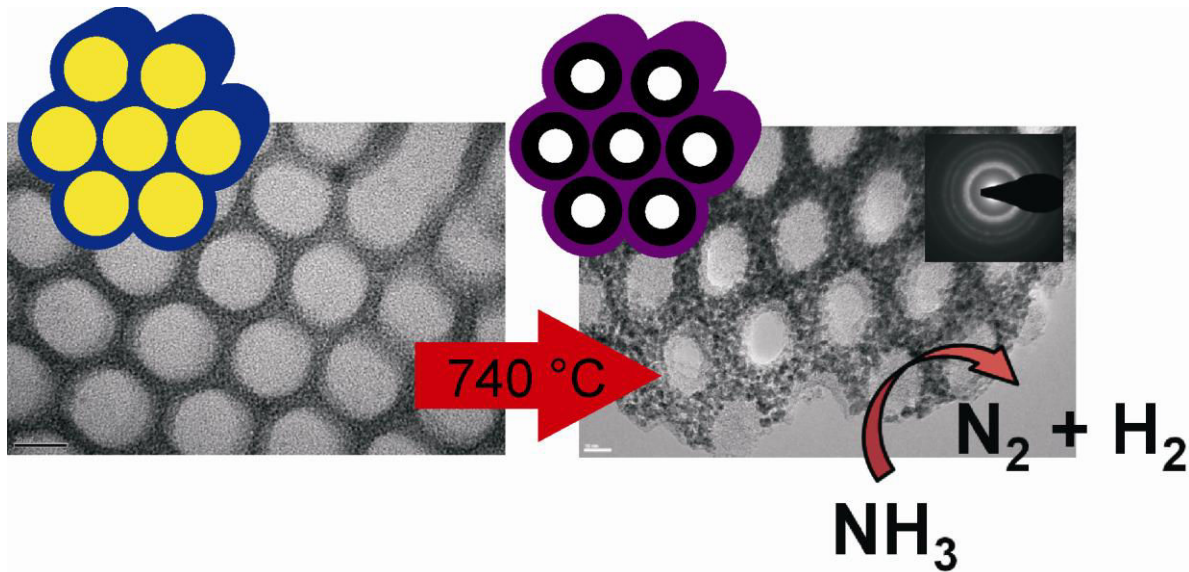
Thomas Lunkenbein,<sup>1</sup> Dirk Rosenthal,<sup>2</sup> Torsten Otromba,<sup>3</sup> Zihui Li,<sup>4</sup> Hiroaki Sai,<sup>4</sup> Carina Bojer,<sup>1</sup> Ulrich Wiesner,<sup>4</sup> Annette Trunschke,<sup>2</sup> Robert Schlögl,<sup>2</sup> Josef Breu<sup>1,\*</sup>

<sup>1</sup>Lehrstuhl für Anorganische Chemie I, Universität Bayreuth, 95440 Bayreuth, Germany;

<sup>2</sup>Abteilung für Anorganische Chemie, Fritz-Haber-Institut der Max-Planck-Gesellschaft, 14195 Berlin, Germany;

<sup>3</sup>Institut für Chemie, Technische Universität Berlin, 10623 Berlin, Germany.

<sup>4</sup>Materials Science & Engineering, Cornell University, Ithaca, NY 14853, USA.



**Abstract.**

Hexagonally ordered mesoporous molybdenum oxycarbide/carbon nanocomposites (MoC/C) were directly accessed by mild heat treatment of mesostructured of poly(butadiene-*block*-2-vinylpyridine) (PB-b-P2VP) and molybdophosphoric acid. PB-b-P2VP serves as structure directing agent and as carbon source in the carburization allowing the hybrid to be converted to MoC/C nanocomposite in one step. The in-situ formed carbon scaffold stabilized the hexagonal mesostructure and served as matrix for MoC nanocrystals (4 nm). The high specific surface area ( $133\text{ m}^2\text{g}^{-1}$ ) obtained for MoC/C nanocomposites renders the materials interesting for potential applications as super capacitors. MoC/C showed promising results in the catalytic decomposition of  $\text{NH}_3$ .

**Keywords.** polyoxometalate, carbides, self-assembly, heterogeneous catalysis, physisorption

## Introduction.

Heterogeneous catalysis is still predominated by metals, metal oxides, and metal sulfides.<sup>[1]</sup> However, additional demands for more sophisticated, efficient, and economical processes, require alternative catalytic materials. For instance, in industrial catalytic processes there is a growing interest in substituting rare and expensive noble metal catalysts by cheap and abundant transition metal carbides (TC) materials. Among others, TCs have attracted considerable interest in current academic catalytic research. It has been demonstrated by Levy and Boudart that the combination of group VI transition metals and carbon can result in Pt-like properties with respect to activity, selectivity, and resistance against poisoning.<sup>[1,2]</sup> In particular, in catalytic reactions involving the transformation of C-H bonds of hydrocarbons, i.e. dehydrogenation, hydrogenation, and hydrogenolysis, the TCs received a great deal of attention.<sup>[3]</sup>

However, applying conventional carburization methods, TCs showing porosity and high specific surface areas are difficult to obtain. Standard metallurgy approaches involve reaction of the metals with carbon at temperatures above 1200 °C.<sup>[4]</sup> This inevitably yields bulk TCs with low surface area and mediocre catalytic activity. Exploration of the true potential of TCs, requires the development of appropriate techniques to synthesize TCs with nanoscale particle size, high surface area and large pores.<sup>[5]</sup> High surface area TCs have been reported using a temperature programmed reduction,<sup>[6]</sup> high-temperature decomposition,<sup>[7]</sup> or carbothermal reduction.<sup>[8]</sup> Although these preparation methods deliver high surface area and catalytical active TCs,<sup>[9]</sup> the obtained carbides do not feature ordered and uniform pores that might optimize mass transport.<sup>[10]</sup>

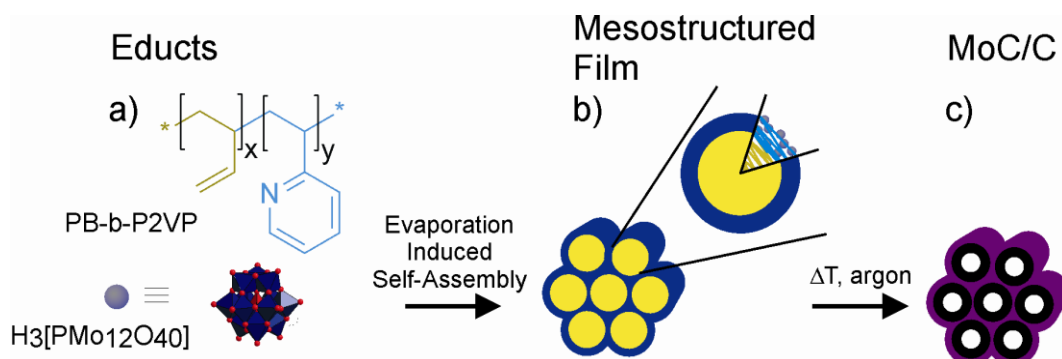
Techniques for organizing TCs on the mesoscale using inorganic or organic matrices are scarce. Ordered mesoporous TCs have been reported by exotemplating of polyoxometalates into mesoporous silica followed by carburization using an additional carbon source like CO or CH<sub>4</sub>.<sup>[11]</sup> Ordered micro-/mesoporous TC/carbon (TC/C) nanocomposites were synthesized by endotemplating of pre-synthesized, stabilized T<sub>O</sub>x nanoparticle suspension into a pluronic template followed by carbothermal reduction.<sup>[12]</sup> For successful carburization additional carbon sources and/or curing steps were required rendering the process rather complex.

Aside from catalysis, such hierarchical porous TC/C nanocomposites (micropores in the wall of mesopores) have been shown to be excellent super capacitor.<sup>[12d,13]</sup> In brief, ordered mesoporous channels support penetration and transportation of the electrolyte. The open space is an essential feature for highly efficient capacitors. Simultaneously, micropores embedded in the walls of mesopores provide additional space for charge storage.

TC/C nanocomposites are, however, not only superior to pure TCs in supercapacitor applications, their catalytic activity and stability had also been shown to be advanced.<sup>[14]</sup> The development of a direct and general access to ordered mesoporous TC/C nanocomposite with TC walls, uniform large pores, and high porosity is consequently highly desirable.

Here we describe a direct route towards hexagonally ordered mesoporous molybdenum carbide/carbon (MoC/C) nanocomposite by endotemplating followed by subsequent carbothermal reduction in inert atmosphere. Molybdophosphoric acid ( $\text{H}_3\text{PMo}_{12}\text{O}_{40}$ ;  $\text{H}_3\text{PMo}$ ) was adopted as molybdenum precursor. A structure directing agent (SDA) particular rich in  $\text{sp}^2$ -carbon was applied, poly(butadiene-*block*-2-vinylpyridine) (PB-*b*-P2VP), which at the same time served as carbon source in the carburization reaction.

## Results and Discussion



**Scheme 1.** Illustration of the synthesis scheme of MoC/C: a) Chemical structure of PB-*b*-P2VP (above) and  $\text{H}_3\text{PMo}$  (bottom). The index  $x$  denotes the degree of polymerization (DP) of the PB block ( $x=411$ ) and  $y$  represents the DP of the P2VP units ( $y=75$ ). b) Inverse hexagonal mesophase obtained after solvent evaporation. c) MoC/C with retained mesostructure after mild heat treatment ( $740^\circ\text{C}$ ) in argon atmosphere.

Scheme 1 summarizes our approach. Evaporation induced self-assembly of H<sub>3</sub>PMo in the presence of PB-b-P2VP lead to inverse hexagonal ordered PB cylinders in a P2VP/H<sub>3</sub>PMo matrix as reported recently.<sup>[15]</sup> Structural assignment of the mesostructured PB-b-P2VP/H<sub>3</sub>PMo nanocomposite was accomplished by SAXS measurements (Figure 1a). At least 6 high order Bragg reflections centered around the first order maximum at angular positions equal to the ratio of 1: $\sqrt{3}$ :2: $\sqrt{7}$ :3: $\sqrt{12}$ : $\sqrt{13}$  are indicative for hexagonal ordered cylinders. The corresponding spacing ( $d_{spacing}$ ) is 39 nm. The hexagonal mesostructure was further corroborated by brightfield TEM measurements (Figure 2a-c). The TEM images evidence the inverse hexagonal mesostructure of the PB-b-P2VP/H<sub>3</sub>PMo nanocomposite with a PB pore diameter of 27.0  $\pm$  1.6 nm and a wall thickness of 9.0  $\pm$  1.1 nm. The high resolution (HR)-TEM image in Figure 2c shows the good dispersion of discrete H<sub>3</sub>PMo units which were selectively incorporated into the P2VP walls. The diameter of the monodispers dark dots was estimated to be 1.2 nm, in agreement with the reported diameter of H<sub>3</sub>PMo clusters (1.1 nm).<sup>[16]</sup> The good dispersion of the H<sub>3</sub>PMo units within the polymeric matrix could further be corroborated by the amorphous nature of the powder patterns of the as-synthesized PB-b-P2VP/H<sub>3</sub>PMo nanocomposites (Figure 1bB).

The as-synthesized inverse hexagonal PB-b-P2VP/H<sub>3</sub>PMo nanocomposite was subsequently heat treated under argon atmosphere in a tube furnace to 740 °C. During this process, the sp<sup>2</sup> hybridized carbon was partially converted into a rigid carbon scaffold (C)<sup>[17]</sup> while the H<sub>3</sub>PMo cluster decomposed. At the same time parts of the carbonaceous material are supposed to react with the molybdenum centers to form molybdenum carbides.

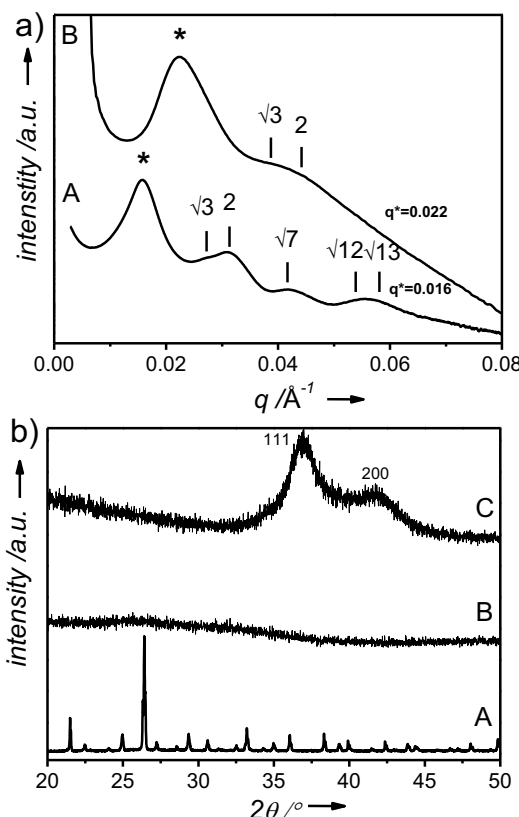


**Figure 1.** a) SAXS patterns of (A) as-synthesized PB-b-P2VP/H<sub>3</sub>PMo nanocomposite and (B) MoC/C. b) PXRD patterns of (A) parent H<sub>3</sub>PMo, (B) PB-b-P2VP/H<sub>3</sub>PMo nanocomposite, and (C) MoC/C.

Structural characterization of MoC/C proved preservation of the ordered mesostructure. SAXS patterns (Figure 1aB) of heat-treated composite show a first-order maximum with corresponding  $d_{\text{spacing}}$  of 28.6 nm. At least two higher order reflections at angular position of  $\sqrt{3}$  and 2 of the first-order maximum were consistent with a hexagonal lattice. The absence of higher order reflections suggested a certain degree of disorder in the regular mesostructure. The shift of the 10 reflection to higher  $q$  values correlated with a decrease of the cell parameters of 28 %. The *in-situ* formed rigid carbon scaffold (Figure SI 3), however, was capable of preventing collapse of the mesostructures on heat treatment and carbide formation. The structural assignment was further corroborated by TEM studies (Figure 2c and d).

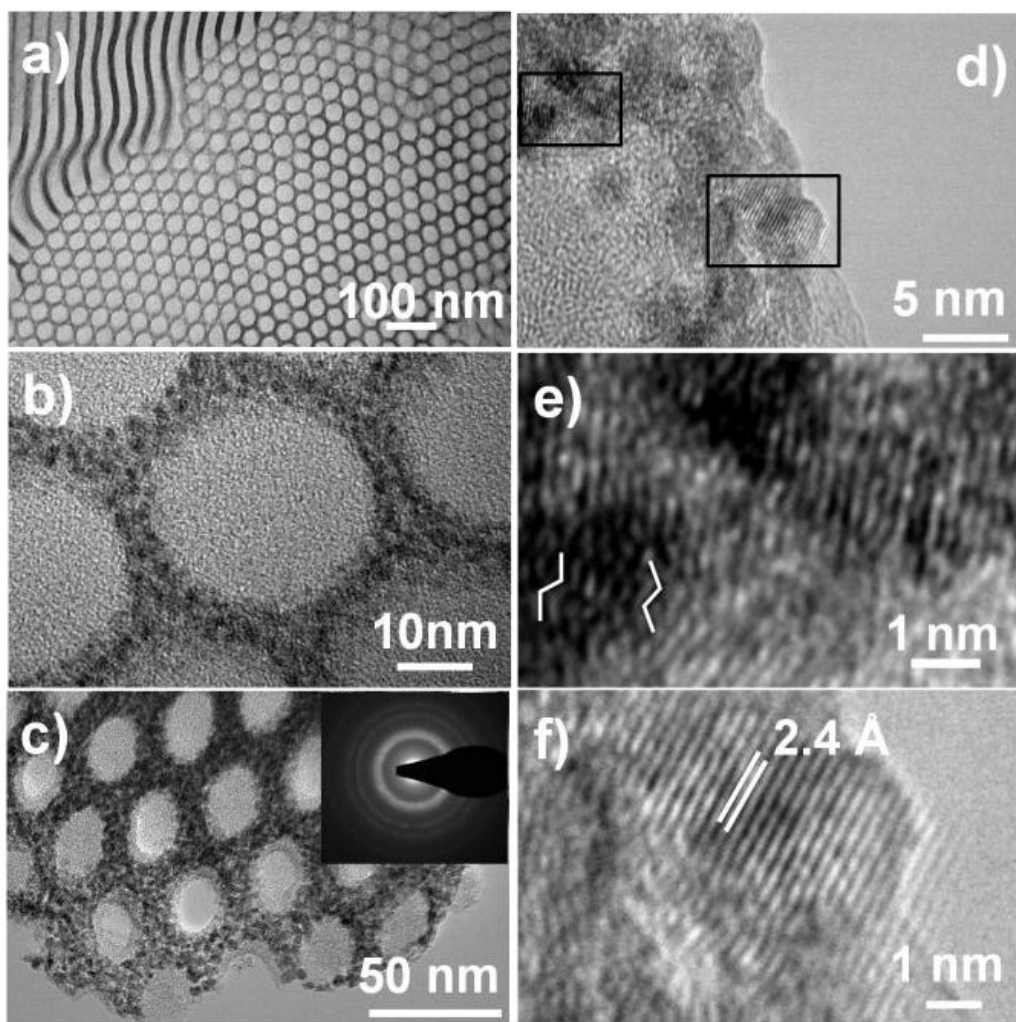


**Figure 2.** Representative bright-field TEM images of PB-b-P2VP/H<sub>3</sub>PMo nanocomposite (a and b) and of MoC/C at different magnifications (c-f). The inset in (c) represents a SAED pattern indicative for nanocrystalline MoO<sub>x</sub>C<sub>y</sub>. e) and f) are HR-TEM images of d). e) displays the chevron-like structure of the vacancies of MoO<sub>x</sub>C<sub>y</sub> along the [010] zone axis. f) shows a HR-TEM image of a single nanocrystal. The spacing of 2.4 Å corresponds well with the (111) plane of MoO<sub>x</sub>C<sub>y</sub>.

TEM micrographs of MoC/C exhibit a well-defined 2D hexagonal mesostructure with pore diameters of  $19.3 \pm 4.0$  nm and wall thicknesses of  $13.1 \pm 1.6$  nm in agreement with the observed  $d_{\text{spacing}}$  of the SAXS patterns (28.0 nm). TEM images also revealed the presence of quite monodispers carbide nanoparticles exhibiting an average diameter of roughly 4 nm which are well dispersed in the carbon matrix. During heat treatment the randomly distributed H<sub>3</sub>PMo units within the P2VP matrix produced a large number of carbide nuclei leading to rather small particle sizes.

The diffraction patterns showed two broad reflections at angular positions of 37° and 43° (Figure 1bC, Figure SI 4aA) attributed to the (111) and (200) plane of a face centered cubic (fcc) arrangement of  $\text{MoC}_{1-x}$  or molybdenum oxycarbide ( $\text{MoO}_x\text{C}_y$ ). The diffusive selected area electron diffraction pattern (SAED, inset: Figure 2C) further corroborated the formation of fcc-type carbide species. It has recently been highlighted that oxycarbides and fcc-  $\text{MoC}_{1-x}$  possess similar PXRD patterns.<sup>[18]</sup> Figure 2G shows a HR-TEM image of a single nanocrystal. The spacing of 2.4 Å corresponds well with the (111) plane of both,  $\text{MoC}_{1-x}$  or  $\text{MoO}_x\text{C}_y$ . To clarify the nature of the carbide phase formed a combined analytical sequence of elemental analysis (EA), thermogravimetric analysis coupled with mass spectrometry (TGA-MS) in a hydrogen argon mixture (5 vol % H<sub>2</sub>), and HR-TEM measurements of MoC/C were conducted. The presence of considerable amounts of oxygen (EA, Table S1) and the concomitant release of CO and CH<sub>4</sub> in the TG as detected by MS profiles (Figure SI 5) were more in line with an oxycarbide species. In addition, HR-TEM images showed a chevron-like structure (Figure 2g). This structure is well known to result from atom vacancies in the [010] zone axis of crystalline  $\text{MoO}_x\text{C}_y$ .<sup>[19]</sup>

Nitrogen physisorption measurements (Figure 3a) of porous MoC/C exhibited a type I isotherm with a type H4 hysteresis. The specific surface area of 133 m<sup>2</sup>/g was determined by applying the BET equation. Since micropores were detected, the recommendations of Rouquerol *et al.* were followed for calculating the BET surface area.<sup>[20]</sup> Non local density functional theory (NLDFT, slit/cylindrical pore kernel) was adopted to determine the pore size distribution and pore volumes. NLDFT analysis of nitrogen physisorption isotherms Figure 3b showed the presence of both, micro- and mesopores in MoC/C. The estimated cumulative pore volume was 0.085 cm<sup>3</sup>/g. Approximately the half, 0.043 cm<sup>3</sup>/g, of the total volume could be attributed to micropores (Figure SI 4). Four peaks at diameters of 0.68 nm, 1.27 nm, 3.79 nm, and 5.30 nm were observed. Most likely, the micropore peak was related to holes in the carbon scaffold. On a first sight, the TEM images might suggest a rather uniform pore size of mesopores in the range of 19.3 nm. The pore size distribution, however, rapidly decayed after 5.3 nm. Only very little pore volume stretches the range up to a maximum of 17.5 nm. The size limitation and the broad mesopore distribution denoted a partially blocking of the voids by the rigid carbon scaffold lining the pores as clearly indicated by the contrast modulation in Figure 2c and Figure SI 3. The hierarchical pore structure in

which micropores are drilled into the walls of ordered mesopores provided high specific surface area.

To further proof the concept of pore blocking by rigid carbon linings Raman spectroscopy was performed. The spectrum of MoC/C is shown in Figure 3c. Two bands appeared at  $1599\text{ cm}^{-1}$  and  $1333\text{ cm}^{-1}$  which are typical for carbonaceous materials.<sup>[21]</sup> The rigid carbon scaffold not only embedded the large number of  $\text{MoO}_x\text{C}_y$  nanocrystals, but also retained the hexagonal order of mesopores. However, it also passivated the molybdenum oxycarbide centers by acting as barrier to reaction environment as shown by chemisorption experiments (Figure 3d). When MoC/C is pre-treated in He atmosphere no CO uptake was detectable (Figure 3d, squares). However, exposure of the composite to hydrogen atmosphere at  $450\text{ }^\circ\text{C}$  (Figure 3d, circles) and  $600\text{ }^\circ\text{C}$  (Figure 3d, triangles) before the experiment led to an irreversible CO uptake of  $84\text{ }\mu\text{mol/g}$  and  $165\text{ }\mu\text{mol/g}$ , respectively. Hydrogenation and removal of carbon that covered the surface may facilitate diffusion of CO molecules and allow adsorption. At the time a small reflection arose in the PXRD patterns at  $39^\circ 2\theta$  (Figure SI 3aB) which could be assigned to  $\text{Mo}_2\text{C}$ . Thus,  $\text{H}_2$  pre-treatment resulted also in the modification of the chemisorption properties of the material that may be caused by partial reduction of the oxycarbide surface under formation of  $\text{Mo}_2\text{C}$ . The hexagonal mesostructure was maintained as evidenced by TEM investigations (Figure SI 6b). Hence, appropriate pre-treatment in reductive atmosphere could enable a way to uncover some carbide centers activating the material for catalysis. To proof this hypothesis activated MoC/C was tested as catalyst in the decomposition of  $\text{NH}_3$ . Preliminary investigations revealed activity of MoC/C in the decomposition reaction of  $\text{NH}_3$  (Figure SI 7). The activation energy was estimated to be  $37\text{ kcal/mol}$  (Figure SI 7b) which is in close agreement with the results reported earlier for other molybdenum carbides ( $36\text{ kcal/mol}$ ).<sup>[22]</sup>

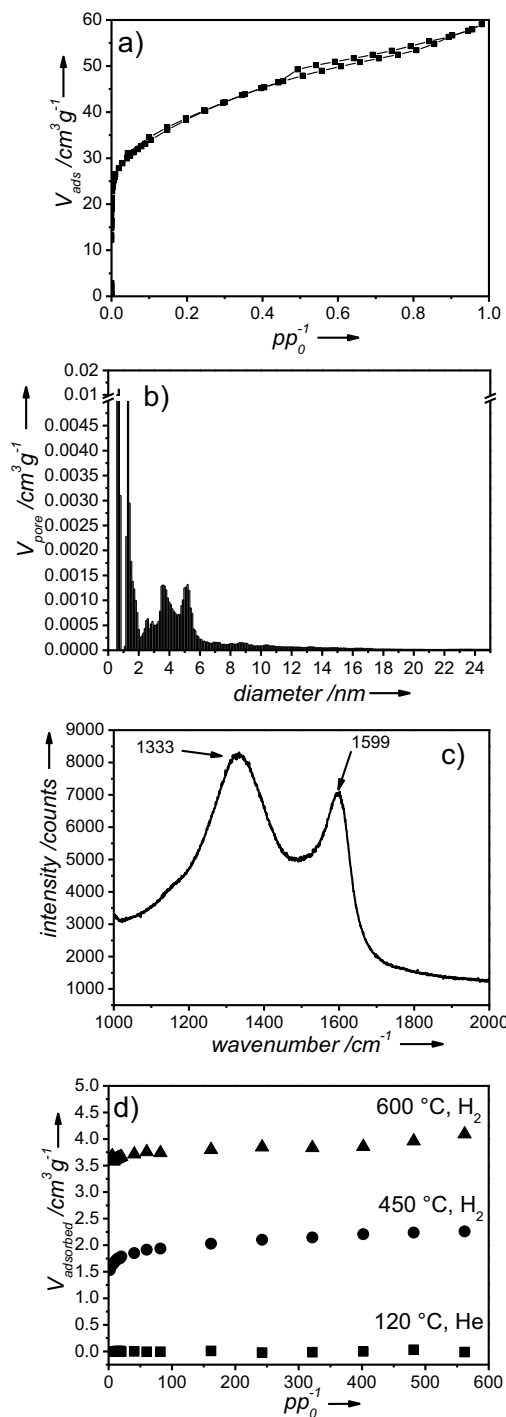


**Figure 3.** a) Nitrogen physisorption isotherm of MoC/C. b) NLDFT analysis of nitrogen adsorption isotherms of the micropore and mesopore distribution of MoC/C. c) Raman spectrum of MoC/C. The peaks at 1333 cm<sup>-1</sup> and 1599 cm<sup>-1</sup> are typical for carbonaceous materials. d) Chemisorption curves for the irreversible CO uptake of MoC/C after different pre-treatment: in He atmosphere at 120 °C (squares), in H<sub>2</sub> atmosphere at 450 °C (circles) and in H<sub>2</sub> atmosphere at 600 °C (triangles). In all cases holding times were 2h.

## Conclusion

In summary, we have established a direct path to mesoporous MoC/C nanocomposites by simple heat treatment of a hexagonally ordered diblock copolymer/heteropoly acid nanocomposite in argon atmosphere. The diblock copolymer served multiple tasks as SDA and carbon source. The H<sub>3</sub>PMo units could easily be converted into MoO<sub>x</sub>C<sub>y</sub> nanoparticles that were embedded in a porous carbon matrix. The resulting MoC/C nanocomposite exhibited inverse hexagonal order, hierarchical pore structure, and high surface area. These MoO<sub>x</sub>C<sub>y</sub> nanoparticles could be activated by uncovering them by pre-treatment in H<sub>2</sub>. MoC/C nanocomposites showed not only activity in catalysis, such as NH<sub>3</sub> decomposition, but the hierarchical pore structure might also render them interesting for super capacitor applications.

**Acknowledgment.** This work was supported by the Deutsche Forschungsgemeinschaft (DFG) within the Collaborative Research Center (SFB) 840. T. L. acknowledges the international graduate school of the ENB “Structures, Reactivity and Properties of Metal Oxides” for a fellowship. Z. L was supported by the U.S. Department of Homeland Security under Cooperative Agreement Number 2009-ST-108-LR0004. H.S. was supported by a Grant Number R21DE018335 from the National Institute of Dental and Craniofacial Research. The X-ray equipment was supported by Department of Energy grant DEFG-02-97ER62443. CHESS was supported by the NSF and NIH-NIGMS via DMR-0225180. Prof. Dr. Rüdiger Kniep is gratefully acknowledged for the support with elemental analysis. We also thank Prof. Dr. Axel H. E. Müller for ensuring easy access to its anionic polymerization reactors. Dr. Andrey Tarasov is acknowledged for thermogravimetric measurements.

**Supporting Information.** Supporting Informations is available in the www.

## References

- [1] A. M. Alexander, J. S. J. Hargreaves, *Chem. Soc. Rev.* **2010**, 39.
- [2] R. B. Levy, M. Boudart, *Science* **1973**, 181, 547-549.
- [3] a) H. H. Hwu, J. G. Chen, *Chem. Rev.* **2004**, 105, 185-212; b) J. G. Chen, *Chem. Rev.* **1996**, 96, 1477-1498.
- [4] A. Hanif, T. Xiao, A. P. E. York, J. Sloan, M. L. H. Green, *Chem. Mater.* **2002**, 14, 1009-1015.

- [5] C. Giordano, C. Erpen, W. Yao, M. Antonietti, *Nano Lett.* **2008**, *8*, 4659-4663.
- [6] J. S. Lee, S. T. Oyama, M. Boudart, *J. Catal.* **1987**, *106*, 125-133.
- [7] H. Preiss, B. Meyer, C. Olschewski, *J. Mater. Sci.* **1998**, *33*, 713-722.
- [8] a) M. J. Ledoux, S. Hantzer, C. P. Huu, J. Guille, M. P. Desaneaux, *J. Catal.* **1988**, *114*, 176-185; b) D. Mordenti, D. Brodzki, G. Djega-Mariadassou, *J. Solid State Chem.* **1998**, *141*, 114-120.
- [9] a) T. c. Xiao, A. P. E. York, V. C. Williams, H. Al Megren, A. Hanif, X. y. Zhou, M. L. H. Green, *Chem. Mater.* **2000**, *12*, 3896-3905; b) T. Xiao, H. Wang, J. Da, K. S. Coleman, M. L. H. Green, *J. Catal.* **2002**, *211*, 183-191; c) M. A. Ecormier, K. Wilson, A. F. Lee, *J. Catal.* **2003**, *215*, 57-65.
- [10] a) D. L. Li, H. S. Zhou, I. Honma, *Nature Mater.* **2004**, *3*, 65-72; b) F. Hoffmann, M. Cornelius, J. Morell, M. Fröba, *Angew. Chem.* **2006**, *118*, 3290-3328; *Angew. Chem. Int. Ed.* **2006**, *45*, 3216-3251; c) M. C. Orilall, U. Wiesner, *Chem. Soc. Rev.* **2011**, *40*, 520-535; d) F. Schüth, *Angew. Chem.* **2003**, *115*, 3730-3750; *Angew. Chem. Int. Ed.* **2003**, *42*, 3604-3622, e) M. Hartmann, *Angew. Chem.* **2004**, *116*, 6004-6006; *Angew. Chem. Int. Ed.* **2004**, *43*, 5880-5882.
- [11] a) X. Cui, H. Li, L. Guo, D. He, H. Chen, J. Shi, *Dalton Trans.* **2008**; b) Z. Wu, Y. Yang, D. Gu, Q. Li, D. Feng, Z. Chen, B. Tu, P. A. Webley, D. Zhao, *Small* **2009**, *5*, 2738-2749.
- [12] a) J. Han, J. Duan, P. Chen, H. Lou, X. Zheng, H. Hong, *Chem. Sus. Chem* **2012**, *5*, 727-733; b) C. H. Huang, D. Gu, D. Zhao, R. A. Doong, *Chem. Mater.* **2010**, *22*, 1760-1767, c) T. Yu, Y. Deng, L. Wang, R. Liu, L. Zhang, B. Tu, D. Zhao, *Adv. Mater.* **2007**, *19*, 2301-2306; d) H. J. Liu, J. Wang, C. X. Wang, Y. Y. Xia, *Adv. Energy Mater.* **2011**, *1*, 1101-1108.
- [13] J. Chmiola, G. Yushin, Y. Gogotsi, C. Portet, P. Simon, P. L. Taberna, *Science* **2006**, *313*, 1760-1763.
- [14.] D. Mordenti, D. Brodzki, G. Djega-Mariadassou, *J. Solid State Chem.* **1998**, *141*, 114-120.
- [15] T. Lunkenbein, M. Kamperman, L. Zihui, C. Bojer, S. Förster, U. Wiesner, A. H. E. Müller, Breu J., *J. Am. Chem. Soc.* **2012**, submitted.
- [16] A. Stein, M. Fendorf, T. P. Jarvie, K. T. Mueller, A. J. Benesi, T. E. Mallouk, *Chem. Mater.* **1995**, *7*, 304-313.

- [17] J. Lee, M. C. Orilall, S. C. Warren, M. Kamperman, F. J. Disalvo, U. Wiesner, *Nature Mater.* **2008**, *7*, 222-228.
- [18] T. C. Xiao, A. P. E. York, V. C. Williams, H. Al Megren, A. Hanif, X. y. Zhou, M. L. H. Green, *Chem. Mater.* **2000**, *12*, 3896-3905.
- [19] S. T. Oyama, C. Delporte, C. Pham-Huu, M. J. Ledoux, *Chem. Lett.* **1997**, *9*, 949-950.
- [20] J. Rouquerol, P. Llewellyn, F. Rouquerol, in *Studies in Surface Science and Catalysis Characterization of Porous Solids VII Proceedings of the 7th International Symposium on the Characterization of Porous Solids (COPS-VII), Aix-en-Provence, France, 26-28 May 2005* Ed.: P. L. Llewellyn), Elsevier, **2007**, pp. 49-56.
- [21] A. Sadezky, H. Muckenhuber, H. Grothe, R. Niessner, U. Pöschl, *Carbon* **2005**, *43*, 1731-1742.
- [22] C. Jeong-Gil, *J. Catal.* **1999**, *182*, 104-116.

## Supporting Information

### I. Materials and Methods.

#### *Synthesis of poly(butadiene-block-2-vinylpyridine) (PB-b-P2VP) diblock copolymer.*

The diblock copolymer PB-b-P2VP was synthesized by sequential living anionic polymerization in tetrahydrofuran (THF) as published elsewhere.<sup>[1]</sup> Gel permeation chromatography (GPC) in THF was used to determine the molecular weight of the first block (polybutadiene, PB) and to determine the polydispersity index (PDI) of the diblock copolymer. <sup>1</sup>H-NMR was used to calculate the overall molecular weight and composition of the diblock copolymer. The resulting PB-b-P2VP polymer had a molecular weight of 30 kg/mol and a weight content of 26 wt % of P2VP with a PDI of 1.02.

*Synthesis of composites.* The polymer/polyoxometalate composite films were prepared following the same preparation method as published previously.<sup>[2]</sup> A filtered (0.2 µm, PTFE) PB-b-P2VP polymer solution in distilled THF (Aldrich) was added dropwise to a separate solution of molybdophosphoric acid (H<sub>3</sub>PMo; Aldrich) in distilled THF under continuous stirring. Prior dissolution in THF, the H<sub>3</sub>PMo was recrystallized from water and stored at 86% relative humidity (RH) inspired by the approach of Nakamura et al.<sup>[3]</sup> According to TGA analysis 27 water molecules per formula unit are present.

Typically, 0.1 g of the block copolymer was dissolved in THF (2 mL). This solution was added to a THF solution of H<sub>3</sub>PMo (0.3 g H<sub>3</sub>PMo in 3 mL of THF) at room temperature (RT) under continuous stirring. After 30 min, the solution was subsequently poured into a Teflon Petri dish (diameter: 3.2 cm) and a film was cast by evaporation of the solvent in air at 32 % RH and RT in a dessicator (Figure SI 1A). The solution was covered by a hemispherical glass cab during the evaporation process. A small slit between the bottom of the desiccators and the glass cab was maintained to adjust slow evaporation rates.

*Carburization.* Carburization of the as-synthesized hexagonally ordered PB-b-P2VP/H<sub>3</sub>PMo composite was accomplished in a tube furnace in argon atmosphere (100 ml/min). The composite was heated to 740 °C with a heating rate of 1 K/min and kept at this temperature for 2 h.

*Catalytic Studies.* Prior to catalysis studies 100 mg as-synthesized PB-b-P2VP/H<sub>3</sub>PMo composite (grain size: 200 to 300 µm) was carburized as described above and subsequent activated in H<sub>2</sub> atmosphere at 600 °C for 2h. Ammonia decomposition was accomplished in SiO<sub>2</sub>- fixed bed reactor exhibiting an inner diameter of 0.8 cm and a length of 40 cm. The catalyst was diluted with SiO<sub>2</sub>- pearls to a volume of 1.25 mL. Hence, was placed in isothermal area of the furnace (HTM Reetz). The volume flow was adjusted from 50 to 150 mls/min. The concentration of ammonia was kept constant at 2%. Catalytic studies were accomplished at seven different temperatures between 300 °C and 600 °C for 2.5 h each. Gas analytics consisted of an IR-spectrometer (Rosemount BINOS 1.2; Messbereich 0 - 20% NH<sub>3</sub>) and GC Varian CP-3800 equipped with a 5 Å molecular sieve and a Carboplot Q column. The carrier gas was argon.

*Characterization.* Small-angle x-ray scattering (SAXS) patterns of samples were obtained at Cornell High Energy Synchrotron Source (CHESS) G1 station with a beam energy of 9 keV (X-ray wavelength of 1.452 Å, and sample-to-detector distance of 359.41 cm) as well as at a home-built Rigaku RU300 CuK $\alpha$  rotating anode beamline. The details of both SAXS beamline configurations are described elsewhere.<sup>[4]</sup> Acquired 2D patterns were azimuthally integrated around the beam center to produce intensity versus scattering vector magnitude,  $q$ , defined as  $q=4\pi\sin\theta/\lambda$  where  $2\theta$  is the total scattering angle and  $\lambda$  is the x-ray wavelength.

Brightfield transmission electron microscopy (TEM) and high resolution TEM (HRTEM) images were performed on a Philips CM200 FEG operated at an acceleration voltage of 200 kV. As-synthesized films were microtomed at cryogenic conditions and placed on a Lacey carbon copper grid. Lacey carbon copper grids were dipped into heat treated powder.

Fourier Transform Infrared spectroscopy (FTIR) data was collected on a Bruker IFS66V using KBr pellets.

Powder X-Ray Diffraction (PXRD) patterns were obtained using nickel filtered Cu-K $\alpha$  radiation ( $\lambda = 1.54187$  Å) on a Bragg-Brentano-type diffractometer (XPERT-PRO, PANalytical B.V.) equipped with an X'Celerator Scientific RTMS detector. All patterns were analyzed using Panalytical's Highscore Plus software.

Ambient-temperature Raman spectroscopy experiments were performed using a Jobin Yvon Labram spectrometer with a 632.8 nm He-Ne excitation line and a laser

output power of 8 mW. The laser beam was focused using a 100x objective, resulting in a spot having a diameter of approx. 5  $\mu\text{m}$ .

$\text{N}_2$  physisorption was conducted at 77 K on a Quantachrome Autosorb 1 instrument. Prior to measurements, the samples were degassed at 473 K for 24 h.

CO-chemisorption was carried out with the static volumetric method in a Quantachrome Autosorb 1C. Two isotherms at 303 K in the pressure range of 2 – 560 Torr were measured, the first with both the reversible and irreversible part and the second with the reversible part only. In all cases the irreversibly chemisorbed CO amount is used. The MoC/C composite was treated in flowing argon at 393 K, hydrogen at 673 K and 873 K, respectively and dwelled for 2 h (ramp 2 K/min).

Thermogravimetric analysis (TGA) was conducted on a Netzsch STA 449C Jupiter coupled with a mass spectrometry (Pfeiffer Omnistar) in a 5 vol %  $\text{H}_2$  atmosphere and a heating rate of 5 K/min.

## II. Film casting reactor.

It has been found that best distinct mesostructures are observed when the solvent was allowed to evaporate at 32 % RH. Hence we build ourselves a film casting reactor to adjust the desired RH. (Figure SI ). It is known that a defined RH adjusts above a saturated salt solution in solution. In our case a saturated  $\text{CaCl}_2$  yields to 32 % RH. An aquarium pump delivers the moisturized air into the reactor. After equilibration, volatiles are allowed to evaporate.

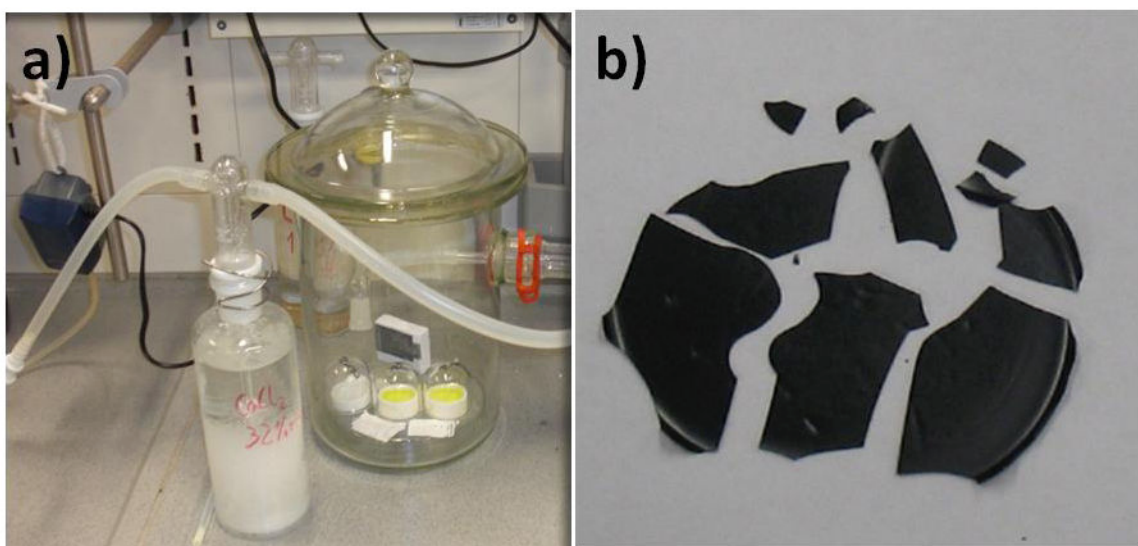


Figure SI 1: (a) Photograph of the self build film casting reactor and (b) image of a PB-b-P2VP/H<sub>3</sub>PMo composite film.

### III. Inverse hexagonal PB-b-P2VP/H<sub>3</sub>PMo composites

PB-b-P2VP/H<sub>3</sub>PMo composite films were solvent casted from THF and exhibited an H<sub>3</sub>PMo content of 70 wt.-%. The dried composite film turned dark blue. The dark blue colour of the film arise from the partial reduction and hydrolysis of the H<sub>3</sub>PMo cluster and the formation of the so-called molybdenum blues.<sup>[5,6]</sup> The composite film was homogeneous and did not show any kind of macrophase separation (see Figure SI 3B).

In addition, wide-angle powder XRD patterns of the H<sub>3</sub>PMo and as-synthesized PB-b-P2VP/H<sub>3</sub>PMo composites were recorded (see Figure 3). In contrast to the parent H<sub>3</sub>PMo (see Figure 3A), XRD patterns of the PB-b-P2VP composite (Figure 3B) do not show any characteristic peaks for crystalline H<sub>3</sub>PMo which is also an indication of the very high dispersion of H<sub>3</sub>PMo in the polymer matrix.

The grafting of H<sub>3</sub>PMo over the PB-b-P2VP template was further verified by FTIR measurements (Figure SI 4). FTIR spectra of PB-b-P2VP diblock copolymer, the commercial H<sub>3</sub>PMo and the as-synthesized PB-b-P2VP/H<sub>3</sub>PMo composite were shown in Figure SI 2. It has been widely reported that the H<sub>3</sub>PMo show four characteristic bands, which are the fingerprint of the Keggin structure.<sup>[7,8]</sup> There are four kinds of oxygen atoms in H<sub>3</sub>PMo. H<sub>3</sub>PMo exhibits these characteristic bands at  $\nu_{as}$  (Mo-O<sub>d</sub>) – 960 cm<sup>-1</sup>,  $\nu_{as}$  (Mo-O<sub>b</sub>-Mo) – 870 cm<sup>-1</sup>,  $\nu_{as}$  (Mo-O<sub>c</sub>-Mo) – 785 cm<sup>-1</sup>, and  $\nu_{as}$  (P-O<sub>a</sub>) – 1065 cm<sup>-1</sup>. The FTIR spectrum of the PB-b-P2VP composite corresponds well to the superposition of the spectrum of the commercial H<sub>3</sub>PMo and PB-b-P2VP polymer template which is an indication that the Keggin structure stayed intact when being grafted in the polymer matrix. However, there is a shift observed in the frequencies for Mo-O-Mo (corner and edge shared) vibrations (see Table SI1). The vibration corresponds to the basic oxygens concerned in the protonation of H<sub>3</sub>PMo anions indicating that there is a change in the environment of the H<sub>3</sub>PMo anions dispersed in the polymer matrix in comparison to commercial H<sub>3</sub>PMo. The change in the environment of the H<sub>3</sub>PMo is a hint for electrostatic interaction between the PB-b-P2VP diblock copolymer and the H<sub>3</sub>PMo units.

## IV. FTIR spectrum

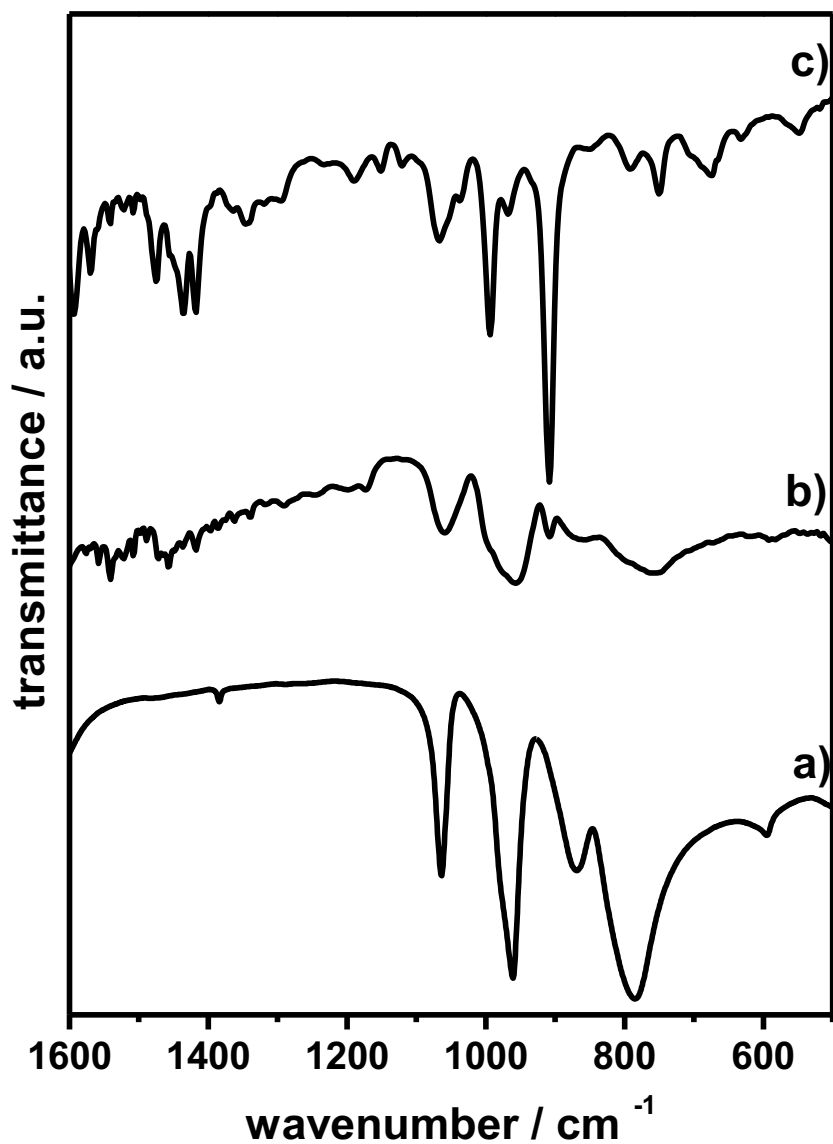


Figure SI 2: FTIR spectrum of parent H<sub>3</sub>PMo (a) PB-b-P2VP nanocomposite (b) and PB-b-P2VP diblock copolymer (c).

V. TEM

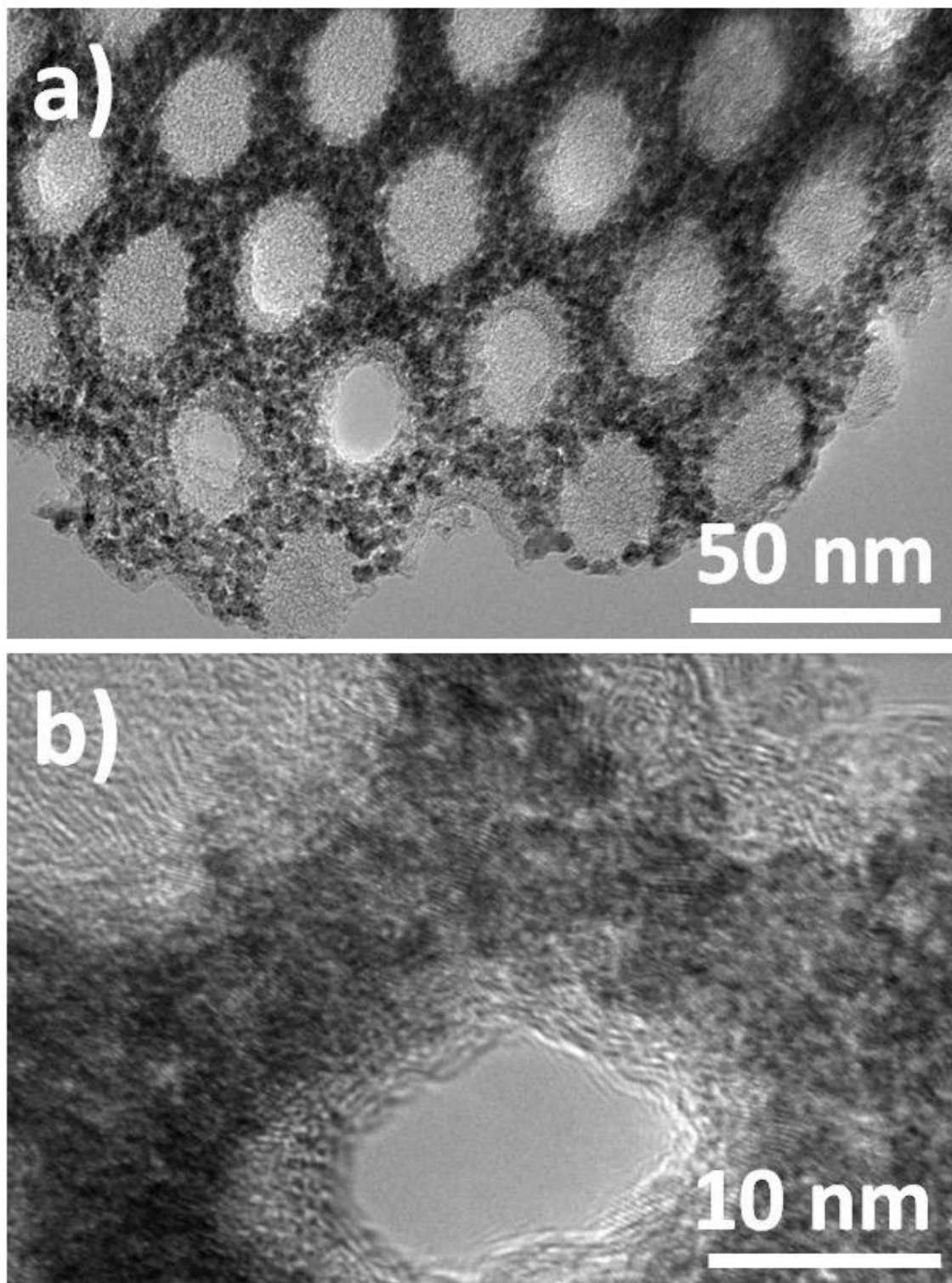


Figure SI 3: TEM micrographs of MoC/C at different magnifications showing the carbon scaffold.

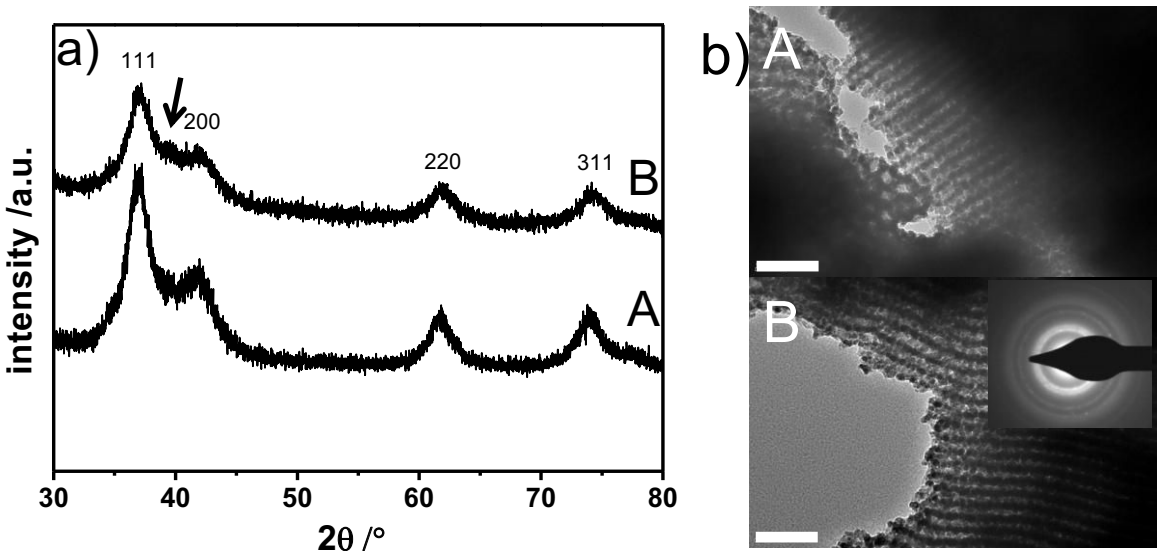
**VI. Assignments after chemisorption measurements**

Figure SI 4: a) PXRD patterns of MoC/C (A) and after chemisorption experiments with pretreatment at 600 °C for 2 h in H<sub>2</sub> atmosphere (B). The arrow denote a small reflection that can be attributed to Mo<sub>2</sub>C. b) TEM images of MoC/C after chemisorption pretreated at 600 °C for 2h in H<sub>2</sub>. The scale bar is 50 nm. (A) and (B) represent representative images taken for different grains. The inset in (B) shows the corresponding SAED pattern indicating a fcc molybdenum carbide. The TEM images show that the mesostructure of MoC/C is retained after exposuring to 600°C in H<sub>2</sub> atmosphere.

## VII. TG-MS of MoC/C

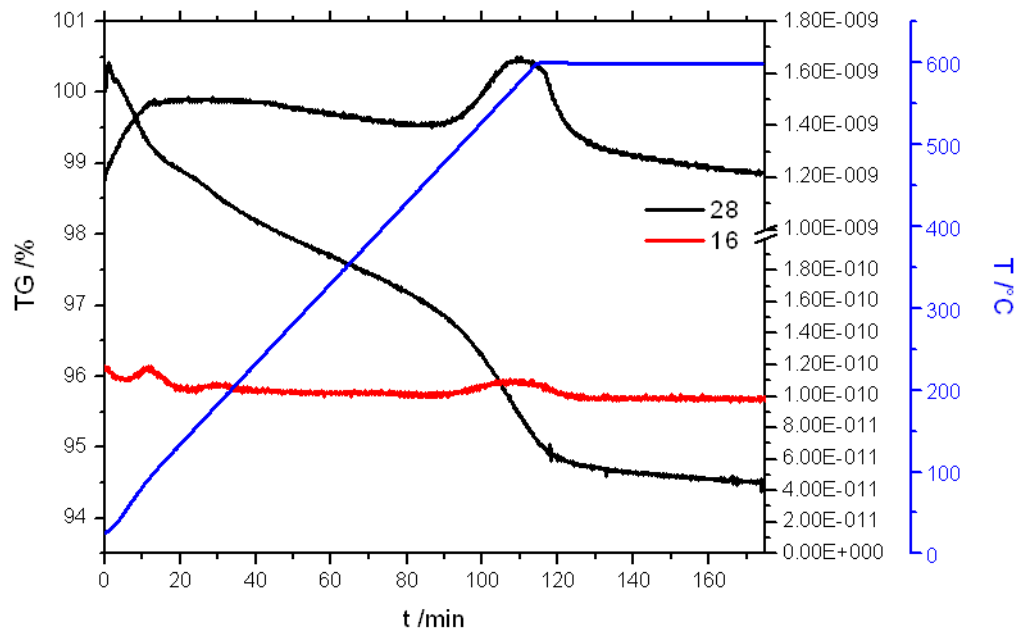


Figure SI 5: TGA-MS profiles of MoC/C. The black curve denotes the TG-signal. Green is the ion current corresponding to CO and red corresponds to  $\text{CH}_4$ . The temperature profile is also given (blue). The gas mixture was 5 vol.-%  $\text{H}_2$  in argon.

Table S2: Results of the EA for PB-b-P2VP/ $\text{H}_3\text{PMo}$  composite and MoC/C in wt %.

	O	N	H	C	P	Mo <sup>a</sup>
PB-b-P2VP/ $\text{H}_3\text{PMo}$	24.9	1.2	3.7	31.4	1.2	37.7
MoC/C	12.4	0.2	0.4	25.4	1.8	59.8

<sup>a</sup> Calculated as difference of the sum of all measured elements to 100 wt %.

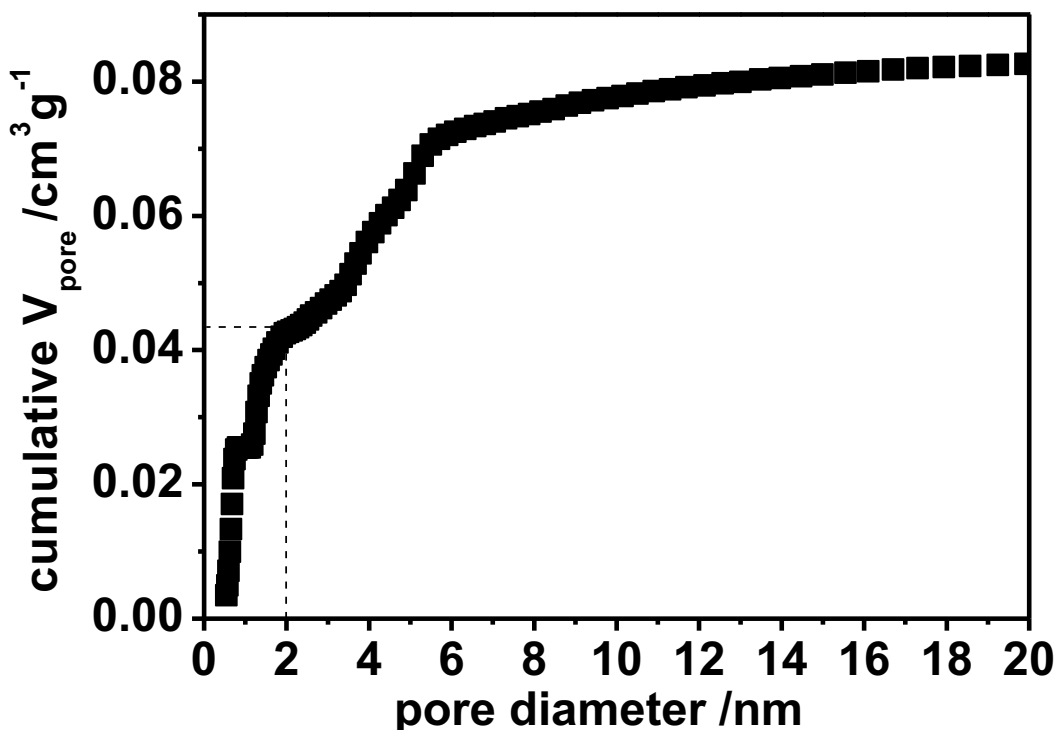
**VIII. Physisorption**

Figure SI 6: Cumulative Pore volume of MoC/C nanocomposite as obtained from non local density functional theory (NLDFT, slit/cylindrical pore kernel). The total pore volume was 0.085 cm<sup>3</sup>/g. The micropore volume was 0.043 cm<sup>3</sup>/g (dashed line).

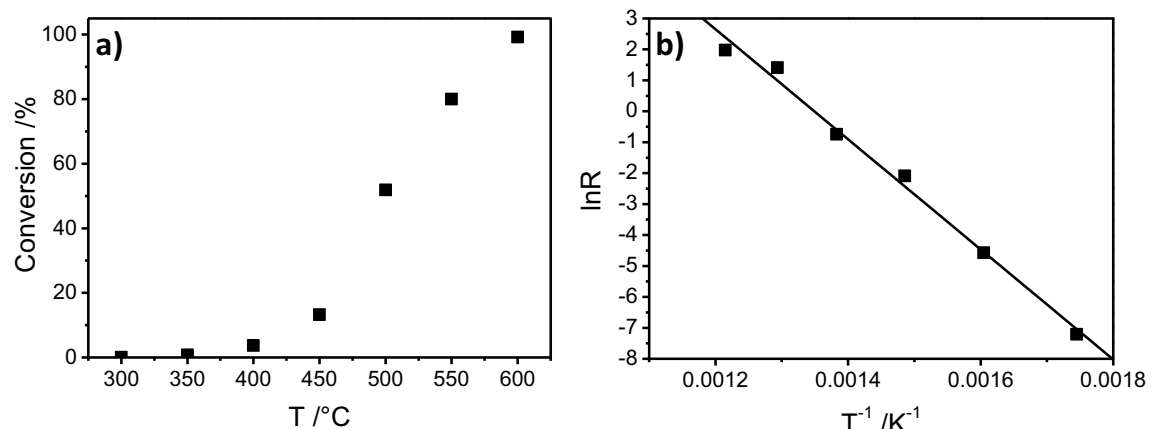
**IX. Catalytic Studies**

Figure SI 7: Catalytic decomposition of  $\text{NH}_3$  over activated MoC/C: a)  $\text{NH}_3$  conversion versus temperature. b) Arrhenius Plot obtained for the decomposition of ammonia over MoC/C. The activation energy was estimated to 156 kJ/mol that translates to 37 kcal/mol.

## X. TPR

Moreover, temperature programmed reduction (TPR) experiments (Figure SI 5A) in a hydrogen/argon mixture (5 vol.-% hydrogen) of MoC/C revealed that hydrogen was consumed in three discrete steps with maxima arising at 180 °C, 480 °C and 710 °C, respectively. The reason of the discontinuous nature of the carbon reactivity remains unclear. However, even after exposing the material to hydrogen at 800 °C some rigid carbon residues could be confirmed by Raman measurements (Figure SI 7B).

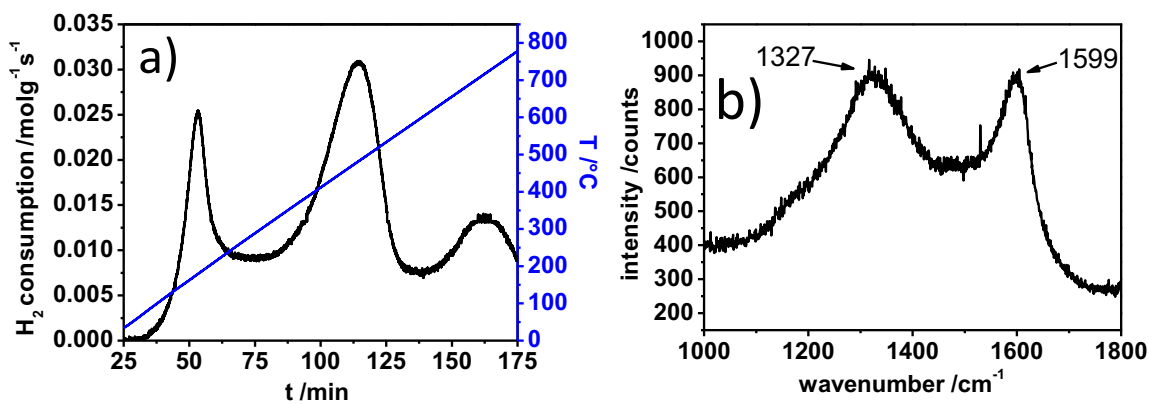


Figure SI 8: A) TPR traces of MoC/C in Ar/H<sub>2</sub> mixture (95/5 v/v) from 25 °C to 800 °C and heating rate of 1 K/min and B) corresponding Raman spectrum.

**XI. References**

- [1.] A. Walther, A. S. Goldmann, R. S. Yelamanchili, M. Drechsler, H. Schmalz, A. Eisenberg, A. H. E. Müller, *Macromolecules* **2008**, *41*, 3254-3260.
- [2.] T. Lunkenbein, M. Kamperman, L. Zihui, C. Bojer, S. Förster, U. Wiesner, A. H. E. Müller, *Breu J., J. Am. Chem. Soc.* **2012**, submitted.
- [3.] O. Nakamura, I. Ogino, T. Kodama, *Solid State Ionics* **1981**, *3-4*, 347-351.
- [4.] A. C. Finnefrock, R. Ulrich, G. E. S. Toombes, S. M. Gruner, U. Wiesner, *J. Am. Chem. Soc.* **2003**, *125*, 13084-13093.
- [5.] M. T. Pope, A. Müller, *Polyoxometalate Chemistry From Topology via Self-Assembly to Applications*, Kluwer Academic Publishers, Dordrecht **2001**.
- [6.] M. T. Pope, *Heteropoly and Isopoly Oxometalates*, Springer-Verlag, Berlin **1983**.
- [7.] C. Rocchicciolieltcheff, M. Fournier, R. Franck, R. Thouvenot, *Inorg. Chem.* **1983**, *22*, 207-216.
- [8.] C. Rocchicciolieltcheff, A. Aouissi, M. Bettahar, S. Launay, M. Fournier, *J. Catal.* **1996**, *164*, 16-27.

## 8. Referenz

- [1.] G. E. Moore, *Electronics* **1965**, *38*, 114-116.
- [2.] R. P. Feynman, *Caltech Engineering and Science* **1960**, *23*, 22-36.
- [3.] G. Gao, *Nanostructures & Nanomaterials*, Imperial College Press, London **2004**.
- [4.] X. Gao, Y. Cui, R. M. Levenson, L. W. K. Chung, S. Nie, *Nat. Biotechnol.* **2004**, *22*, 969-976.
- [5.] A. N. Shipway, E. Katz, I. Willner, *Chem. Phys. Chem* **2000**, *1*, 18-52.
- [6.] C. Sanchez, P. Belleville, M. Popall, L. Nicole, *Chem. Soc. Rev.* **2011**, *40*, 696-753.
- [7.] C. N. R. Rao, A. K. Cheetham, *J. Mater. Chem.* **2001**, *11*, 2887-2894.
- [8.] C. N. R. Rao, S. R. C. Vivekchand, K. Biswasa, A. Govindaraja, *Dalton Trans.* **2007**, 3728-3749.
- [9.] A. G. Davies, J. M. T. Thompson, *Advances in Nanoengineering*, Imperial College Press, London **2007**.
- [10.] C. B. Murray, D. J. Norris, M. G. Bawendi, *J. Am. Chem. Soc.* **1993**, *115*, 8706-8715.
- [11.] G. Sukhorukov, A. Fery, H. M+Ähwald, *Prog. Polym. Sci.* **2005**, *30*, 885-897.
- [12.] P. Yang, H. Yan, S. Mao, R. Russo, J. Johnson, R. Saykally, N. Morris, J. Pham, R. He, H. J. Choi, *Adv. Funct. Mater.* **2002**, *12*, 323-331.
- [13.] Y. Xia, P. Yang, Y. Sun, Y. Wu, B. Mayers, B. Gates, Y. Yin, F. Kim, H. Yan, *Adv. Mater.* **2003**, *15*, 353-389.
- [14.] S. Y. Zhao, S. H. Chen, S. Y. Wang, D. G. Li, H. Y. Ma, *Langmuir* **2002**, *18*, 3315-3318.
- [15.] L. Chen, J. Xu, J. D. Holmes, M. A. Morris, *J. Phys. Chem. C* **2010**, *114*, 2003-2011.
- [16.] Y. Gogotsi, *Nanomaterials Handbook*, CRC Press, Boca Raton **2006**.
- [17.] M. Haruta, N. Yamada, T. Kobayashi, S. Iijima, *J. Catal.* **1989**, *115*, 301-309.
- [18.] H. N. Aiyer, V. Vijayakrishnan, G. N. Subbanna, C. N. R. Rao, *Surf. Sci.* **1994**, *313*, 392-398.
- [19.] Y. W. Jun, Y. M. Huh, J. S. Choi, J. H. Lee, H. T. Song, S. Kim, S. Kim, S. Yoon, K. S. Kim, J. S. Shin, J. S. Suh, J. Cheon, *J. Am. Chem. Soc.* **2005**, *127*, 5732-5733.
- [20.] E. Roduner, *Chem. Soc. Rev.* **2006**, *35*, 583-592.

- [21.] M. Antonietti, G. A. Ozin, *Chem. Eur. J.* **2004**, *10*, 29-41.
- [22.] M. D. Cobb, J. Macoubrie, *J. Nanopart. Res.* **2004**, *6*, 395-405.
- [23.] J. Rouquerol, D. Avnir, C. W. Fairbridge, D. H. Everett, J. H. Haynes, N. Pernicone, J. D. F. Ramsay, K. S. W. Sing, K. K. Unger, *Pure Appl. Chem.* **1994**, *66*, 1739-1758.
- [24.] H. Cölfen, S. Mann, *Angew. Chem. Int. Ed.* **2003**, *42*, 2350-2365.
- [25.] M. C. Orilall, U. Wiesner, *Chem. Soc. Rev.* **2011**, *40*, 520-535.
- [26.] S. Vignolini, N. A. Yufa, P. S. Cunha, S. Guldin, I. Rushkin, M. Steifik, K. Hur, U. Wiesner, J. J. Baumberg, U. Steiner, *Adv. Mater.* **2012**, *24*, OP23-OP27.
- [27.] C. Sanchez, B. Julian, P. Belleville, M. Popall, *J. Mater. Chem.* **2005**, *15*, 3559-3592.
- [28.] M. José-Yacamón, L. Rendón, J. Arenas, M. C. S. Puche, *Science* **1996**, *273*, 223-225.
- [29.] B. Teo, X. Sun, *J Cluster Sci.* **2006**, *17*, 529-540.
- [30.] J. Y. Cheng, C. A. Ross, H. I. Smith, E. L. Thomas, *Adv. Mater.* **2006**, *18*, 2505-2521.
- [31.] W. Lu, C. M. Lieber, *Nature Mater.* **2007**, *6*, 841-850.
- [32.] M. Templin, A. Franck, A. Du Chesne, H. Leist, Y. Zhang, R. Ulrich, V. Sch+ñdler, U. Wiesner, *Science* **1997**, *278*, 1795-1798.
- [33.] R. Ulrich, J. W. Zwanziger, S. M. De Paul, A. Reiche, H. Leuninger, H. W. Spiess, U. Wiesner, *Adv. Mater.* **2002**, *14*, 1134-1137.
- [34.] E. J. W. Crossland, M. Kamperman, M. Nedelcu, C. Ducati, U. Wiesner, D. Smilgies, G. E. S. Toombes, M. A. Hillmyer, S. Ludwigs, U. Steiner, H. J. Snaith, *Nano Lett.* **2008**, *9*, 2807-2812.
- [35.] F. Schüth, *Angew. Chem. Int. Ed.* **2003**, *42*, 3604-3622.
- [36.] F. Hoffmann, M. Cornelius, J. Morell, M. Fröba, *Angew. Chem. Int. Ed.* **2006**, *45*, 3216-3251.
- [37.] T. J. Barton, L. M. Bull, W. G. Klemperer, D. A. Loy, B. McEnaney, M. Misono, P. A. Monson, G. Pez, G. W. Scherer, J. C. Vartuli, O. M. Yaghi, *Chem. Mater.* **1999**, *11*, 2633-2656.
- [38.] S. Polarz, M. Antonietti, *Chem. Commun.* **2002**, 2593-2604.
- [39.] M. Lazzari, G. Liu, *Block Copolymers in Nanoscience*, (Eds.: M. Lazzari, G. Liu) Wiley-VCH, Weinheim **2006**.

- [40.] R. S. Yelamanchili, A. Walther, A. H. E. Müller, J. Breu, *Chem. Commun.* **2008**, 489-491.
- [41.] S. C. Warren, F. J. Disalvo, U. Wiesner, *Nature Mater.* **2007**, *6*, 248.
- [42.] S. C. Warren, L. C. Messina, L. S. Slaughter, M. Kamperman, Q. Zhou, S. M. Gruner, F. J. Disalvo, U. Wiesner, *Science* **2008**, *320*, 1748-1752.
- [43.] D. R. Rolison, *Science* **2003**, *299*, 1698-1701.
- [44.] M. Hartmann, *Angew. Chem. Int. Ed.* **2004**, *43*, 5880-5882.
- [45.] J. Chmiola, G. Yushin, Y. Gogotsi, C. Portet, P. Simon, P. L. Taberna, *Science* **2006**, *313*, 1760-1763.
- [46.] M. Lazzari, C. Rodriguez-Abreu, J. Rivas, M. A. Lopez-Quintela, *J. Nanosci. Nanotechnol.* **2006**, *6*, 892-905.
- [47.] S. Förster, T. Plantenberg, *Angew. Chem. Int. Ed.* **2002**, *41*, 688-714.
- [48.] G. J. D. Soler-Illia, C. Sanchez, B. Lebeau, J. Patarin, *Chem. Rev.* **2002**, *102*, 4093-4138.
- [49.] G. J. D. Soler-Illia, C. Sanchez, B. Lebeau, J. Patarin, *Chem. Rev.* **2002**, *102*, 4093-4138.
- [50.] A. Walther, A. S. Goldmann, R. S. Yelamanchili, M. Drechsler, H. Schmalz, A. Eisenberg, A. H. E. Müller, *Macromolecules* **2008**, *41*, 3254-3260.
- [51.] *The Colloidal Domain where Physics, Chemistry, Biology and Technology Meet*, (Eds.: D. F. Evans, H. Wennerström) Wiley-VCH, Weinheim **1994**.
- [52.] S. Förster, V. Abetz, A. H. E. Müller, in *Polyelectrolytes with Defined Molecular Architecture II* (Ed.: M. Schmidt), Springer Berlin / Heidelberg, **2004**, pp. 267-277.
- [53.] M. Moffitt, K. Khougaz, A. Eisenberg, *Acc. Chem. Res.* **1996**, *29*, 95-102.
- [54.] E. L. Thomas, D. M. Anderson, C. S. Henkee, D. Hoffman, *Nature* **1988**, *334*, 598-601.
- [55.] M. Szwarc, *Nature* **1956**, *178*, 1168-1169.
- [56.] M. W. Matsen, F. S. Bates, *Macromolecules* **1996**, *29*, 1091-1098.
- [57.] J. Lee, M. C. Orilall, S. C. Warren, M. Kamperman, F. J. Disalvo, U. Wiesner, *Nature Mater.* **2008**, *7*, 222-228.
- [58.] T. Brezesinski, B. Smarsly, K. Iimura, D. Gross, C. Boissiere, H. Amenitsch, M. Antonietti, C. Sanchez, *Small* **2005**, *1*, 889-898.
- [59.] T. Brezesinski, M. Groenewolt, A. Gibaud, N. Pinna, M. Antonietti, B. M. Smarsly, *Adv. Mater.* **2006**, *18*, 2260-2263.

- [60.] C. T. Kresge, M. E. Leonowicz, W. J. Roth, J. C. Vartuli, J. S. Beck, *Nature* **1992**, *359*, 710-712.
- [61.] D. Y. Zhao, J. L. Feng, Q. S. Huo, N. Melosh, G. H. Fredrickson, B. F. Chmelka, G. D. Stucky, *Science* **1998**, *279*, 548-552.
- [62.] S. Ruthstein, J. Schmidt, E. Kesselman, Y. Talmon, D. Goldfarb, *J. Am. Chem. Soc.* **2006**, *128*, 3366-3374.
- [63.] S. Polarz, A. V. Orlov, F. Schüth, A. H. Lu, *Chem. Eur. J.* **2007**, *13*, 592-597.
- [64.] T. Ressler, A. Walter, Z. D. Huang, W. Bensch, *J. Catal.* **2008**, *254*, 170-179.
- [65.] V. F. Stone, R. J. Davis, *Chem. Mater.* **1998**, *10*, 1468-1474.
- [66.] J. G. Yu, W. Liu, H. G. Yu, *Cryst. Growth .Des.* **2008**, *8*, 930-934.
- [67.] A. Hardwick, P. G. Dickens, R. C. T. Slade, *Solid State Ionics* **1984**, *13*, 345-350.
- [68.] C. X. Li, Y. Zhang, K. P. O'Halloran, H. Y. Ma, *J. Appl. Electrochem.* **2009**, *39*, 1011-1015.
- [69.] T. Brezesinski, J. Wang, R. Senter, K. Brezesinski, B. Dunn, S. H. Tolbert, *ACS Nano* **2010**, *4*, 967-977.
- [70.] C. Reitz, C. Suchomski, C. Weidmann, T. Brezesinski, *Nano Res.* **2011**, *4*, 414-424.
- [71.] T. Wagner, C. D. Kohl, M. Froba, M. Tiemann, *Sensors* **2006**, *6*, 318-323.
- [72.] T. Wagner, T. Waitz, J. Roggenbuck, M. Froba, C. D. Kohl, M. Tiemann, *Thin Solid Films* **2007**, *515*, 8360-8363.
- [73.] S. Badilescu, P. V. Ashrit, *Solid State Ionics* **2003**, *158*, 187-197.
- [74.] A. Sayari, P. Liu, *Microporous Mater.* **1997**, *12*, 149-177.
- [75.] C. Sanchez, C. Boissiere, D. Grosso, C. Laberty, L. Nicole, *Chem. Mater.* **2008**, *20*, 682-737.
- [76.] C. J. Brinker, *Mater. Res. Bull.* **2004**, *29*, 631-640.
- [77.] W. Fan, M. A. Snyder, S. Kumar, P. S. Lee, W. C. Yoo, A. V. McCormick, R. L. Penn, A. Stein, M. Tsapatsis, *Nature Mater.* **2008**, *7*, 984-991.
- [78.] J. N. Kondo, K. Domen, *Chem. Mater.* **2008**, *20*, 835-847.
- [79.] Z. R. Zhang, T. J. Pinnavaia, *Angew. Chem. Int. Ed.* **2008**, *47*, 7501-7504.
- [80.] R. S. Yelamanchili, Y. Lu, T. Lunkenbein, N. Miyajima, Y. L. Tang, M. Ballauff, J. Breu, *Small* **2009**, *5*, 1326-1333.
- [81.] M. T. Pope, *Heteropoly and Isopoly Oxometalates*, Springer-Verlag, Berlin **1983**.

- [82.] R. K. Murmann, K. C. Giese, *Inorg. Chem.* **1978**, *17*, 1160-1166.
- [83.] R. D. Shannon, C. T. Prewitt, *Acta Crystallogr. B.* **1969**, *B 25*, 925-946.
- [84.] Y. Z. Gao, Y. Q. Xu, Z. G. Han, C. H. Li, F. Y. Cui, Y. N. Chi, C. W. Hu, *J. Solid State Chem.* **2010**, *183*, 1000-1006.
- [85.] F. Chai, D. L. Li, H. B. Wu, C. L. Zhang, X. H. Wang, *J. Solid State Chem.* **2009**, *182*, 1661-1665.
- [86.] Berzelius, J.J., *Pogg. Ann. Phys. Chem.* **1826**, *6*, 369-3.
- [87.] Y. Jeannin, M. Fournier, *Pure Appl. Chem.* **1987**, *59*, 1529-1548.
- [88.] J. F. Keggin, *Nature* **1933**, *131*, 908-909.
- [89.] M. T. Pope, A. Müller, *Angew. Chem. Int. Ed.* **1991**, *30*, 34-48.
- [90.] M. T. Pope, A. Müller, *Polyoxometalate Chemistry From Topology via Self-Assembly to Applications*, Kluwer Academic Publishers, Dordrecht **2001**.
- [91.] J. B. Moffat, *Metal-Oxygen Clusters - The Surface and Catalytic Properties of Heteropoly Oxometalates*, Kluwer Academic/Plenum Publishers, New York **2001**.
- [92.] D. E. Katsoulis, *Chem. Rev.* **1998**, *98*, 359-387.
- [93.] K. Nomiya, H. Murasaki, M. Miwa, *Polyhedron* **1986**, *5*, 1031-1033.
- [94.] M. Misono, *Catal. Rev. Sci. Eng.* **1987**, *29*, 269-321.
- [95.] S. Liu, Z. Tang, *Nano Today* **2010**, *5*, 267-281.
- [96.] S. Landsmann, C. Lizandara-Pueyo, S. Polarz, *J. Am. Chem. Soc.* **2010**, *132*, 5315-5321.
- [97.] D. G. Kurth, P. Lehmann, D. Volkmer, H. Colfen, M. J. Koop, A. Müller, A. Du Chesne, *Chem. Eur. J.* **2000**, *6*, 385-393.
- [98.] W. Li, W. Bu, H. Li, L. Wu, M. Li, *Chem. Commun.* **2005**, 3785-3787.
- [99.] H. Li, W. Qi, W. Li, H. Sun, W. Bu, L. Wu, *Adv. Mater.* **2005**, *17*, 2688-2692.
- [100.] Y. L. Wang, W. Li, L. X. Wu, *Langmuir* **2009**, *25*, 13194-13200.
- [101.] S. Polarz, B. Smarsly, M. Antonietti, *Chem. Phys. Chem.* **2001**, *2*, 457-461.
- [102.] Y. K. Han, Z. J. Zhang, Y. L. Wang, N. Xia, B. Liu, Y. Xiao, L. X. Jin, P. Zheng, W. Wang, *Macromol. Chem. Phys.* **2011**, *212*, 81-87.
- [103.] X. K. Lin, Y. L. Wang, L. X. Wu, *Langmuir* **2009**, *25*, 6081-6087.
- [104.] A. Nisar, Y. Lu, J. Zhuang, X. Wang, *Angew. Chem. Int. Ed.* **2011**, *50*, 3187-3192.

- [105.] Y. Yan, L. Wu, *Isr. J. Chem.* **2011**, *51*, 181-190.
- [106.] W. Bu, S. Uchida, N. Mizuno, *Angew. Chem. Int. Ed.* **2009**, *48*, 8281-8284.
- [107.] X. Lin, F. Liu, H. Li, Y. Yan, L. Bi, W. Bu, L. Wu, *Chem. Commun.* **2011**, *47*, 10019-10021.
- [108.] A. Gervasini, A. Auroux, *J. Catal.* **1991**, *131*, 190-198.
- [109.] A. Bernheim-Groswasser, E. Wachtel, Y. Talmon, *Langmuir* **2000**, *16*, 4131-4140.
- [110.] S. T. Oyama, C. Delporte, C. Pham-Huu, M. J. Ledoux, *Chem. Lett.* **1997**, *9*, 949-950.

## 9. Publikationsliste

### 9.1 Publikationen

#### [1] Shaping Colloidal Rutile into Thermally Stable and Porous Mesoscopic Titania Balls

R. S. Yelamanchili, Y. Lu, T. Lunkenbein, N. Miyajima, L. T. Yan, M. Ballauff, J. Breu.

*Small* **2009**, *5*, 1326-1333.

#### [2] Deformation Measurements on Thin Clay Tactoids

D. A. Kunz, E. Max, R. Weinkamer, T. Lunkenbein, J. Breu, A. Fery.

*Small* **2009**, *5*, 1816-1820.

#### [3] Template-Directed Synthesis of Hybrid Titania Nanowires within Core-Shell Bishydrophilic Cylindrical Polymer Brushes

J. Yuan, Y. Lu, F. Schacher, T. Lunkenbein, S. Weiss, H. Schmalz, A. H. E. Müller.

*Chemistry of Materials* **2009**, *21*, 4146-4154.

#### [4] Tailoring Shear-Stiff, Mica-like Nanoplatelets

M. W. Möller, U. A. Handge, D. A. Kunz, T. Lunkenbein, V. Altstädt, J. Breu.

*ACS Nano* **2010**, *4*, 717-724.

#### [5] Composites of Metal Nanoparticles and TiO<sub>2</sub> Immobilized in Spherical Polyelectrolyte Brushes

Y. Lu, T. Lunkenbein, J. Preussner, S. Proch, J. Breu, R. Kempe, M. Ballauff.

*Langmuir* **2010**, *26*, 4176-4183.

**[6] Barrier Properties of Synthetic Clay with a Kilo-Aspect Ratio**

M. W. Möller, T. Lunkenbein, H. Kalo, M. Schieder, D. A. Kunz, J. Breu.

*Advanced Materials* **2010**, *22*, 5245-5249.

**[7] Kilo Aspect Ratio Clay Platelets**

M. W. Möller, T. Lunkenbein, D. A. Kunz, H. Kalo, M. Schieder, J. Breu.

*Zeitschrift für Anorganische und Allgemeine Chemie* **2010**, *636*, 2113.

**[8] Shear Stiff, Surface Modified, Mica-like Nanoplatelets: a Novel Filler for Polymer Nanocomposites**

M. R. Schütz, H. Kalo, T. Lunkenbein, A. H. Gröschel, A. H. E Müller, C. A. Wilkie, J. Breu.

*Journal of Materials Chemistry* **2011**, *21*, 12110-12116.

**[9] Intumescence-like Behavior of Polystyrene Synthetic Clay Nanocomposites**

M. R. Schütz, H. Kalo, T. Lunkenbein, J. Breu, C. A. Wilkie.

*Polymer* **2011**, *52*, 3288-3294.

**[10] Particle Nanosomes with Tailored Silhouettes**

C. S. Wagner, A. Fortini, E. Hofmann, T. Lunkenbein, M. Schmidt, A. Wittemann.

*Soft Matter* **2012**, *8*, 1928-1933.

**[11] Catalytic activity of nanoalloys from gold and palladium**

J. Kaiser, L. Leppert, H. Welz, F. Polzer, S. Wunder, N. Wanderka, M. Albrecht, T. Lunkenbein, J. Breu, S. Kümmel, Y. Lu, M. Ballauff.

*Physical Chemistry Chemical Physics* **2012**, *14*, 6487-6495.

**[12] UV-Cured, Flexible, and Transparent Nanocomposite-Coating with Remarkable Oxygen Barrier**

M. W. Möller, D. A. Kunz, T. Lunkenbein, S. Sommer, A. Nennemann, J. Breu.

*Advanced Materials* **2012**, *24*, 2142-2147.

**[13] Template-Directed Synthesis of Hollow Silica Nanowires and Nanotubes from Cylindrical Core-Shell Polymer Brushes**

M. Müllner, T. Lunkenbein, J. Breu, F. Caruso, A. H. E. Müller.

*Chemistry of Materials* **2012**, *24*, 1802-1810.

**[14] A Facile Polymer Templating Route Towards High Aspect Ratio Crystalline Titania Nanostructures**

M. Müllner, T. Lunkenbein, N. Miyajima, J. Breu, A. H. E. Müller.

*Small*, DOI: 10.1002/smll.201200738.

(Aktuell: *Small* **2012**, *8*, 2636-2640.)

**[15] Template-Directed Mild Synthesis of Anatase Nanotubes within Cylindrical Core-Shell-Corona Polymer Brushes**

M. Müllner, T. Lunkenbein, M. Schieder, N. Miyajima, M. Förtsch, J. Breu, F. Caruso, A. H. E. Müller.

*ACS Nano*, submitted.

(Aktuell: *Macromolecules*, **2012**, *45*, 6981-6988.)

[16] Direct Synthesis of Inverse Hexagonally Ordered Diblock Copolymer/Polyoxometalate Nanocomposite Films

T. Lunkenbein, M. Kamperman, Z. Li, H. Sai, C. Bojer, S. Förster, U. Wiesner, A. H. E. Müller, J. Breu.

*Journal of the American Chemical Society*, submitted.

(Aktuell: *Journal of the American Chemical Society* **2012**, *134*, 12685-12692.)

[17] Packing of Cylindrical Keggin-Type Polyoxometalate Hybrid Micelles as a Function of Aspect Ratio

T. Lunkenben, M. Schieder, C. Bojer, A. H. E. Müller, J. Breu

*Zeitschrift für Physikalische Chemie*, submitted.

(Aktuell: *Zeitschrift für Physikalische Chemie* **2012**, *226*, 815-826.)

[18] Direct Access to Ordered Porous Molybdenum Oxycarbide/Carbon Nanocomposites

T. Lunkenbein, D. Rosenthal, T. Otremba, Z. Li, H. Sai, C. Bojer, U. Wiesner, A. Trunschke, R. Schlögl, J. Breu.

*Angewandte Chemie- International Edition*, to be submitted.

(Aktuell: *Angewandte Chemie* **2012**, *124*, 13066-13070; *Angewandte Chemie- International Edition* **2012**, *51*, 12892-12896.)

**[19] Towards Mesoporous Keggin-Type Polyoxometalate -Systematic Removal of Organic Templates**

T. Lunkenstein, M. Kamperman, M. Schieder, S. With, Z. Li, S. Förster, U. Wiesner, J. Breu.

*Chemistry- An Asian Journal*, to be submitted.

(Aktuell: *Journal of Materials Chemistry A*, to be submitted.)

**[20] High Surface Area Keggin-Type Polyoxometalates Nanorods and their Catalytic Performance in the Isopropanol Decomposition**

T. Lunkenstein, K. Friedel-Ortega, R. S. Yelamanchili, A. Trunschke, R. Schlögl, J. Breu

*Langmuir*, to be submitted.

**[21] Controlled Preparation of Highly Crystalline Tungsten Oxide Nanotubes**

M. Schieder, T. Lunkenstein, T. Martin, W. Milius, J. Breu.

*in preparation.*

(Aktuell: *Journal of Materials Chemistry A* **2013**, *1*, 381-387.)

## 9.2 Posterbeiträge

### [1] Core-Crosslinked Block Copolymers as Templates for Grafting Keggin Polyoxometalates

T. Lunkenbein, R. S. Yelamanchili, A. Walther, A. H. E. Müller, J. Breu.

*14. Vortragstagung der Fachgruppe Festkörperchemie und Materialforschung, Bayreuth, 2008.*

### [2] Ionizable Amphiphilic Core-Crosslinked Diblock Copolymer for the Synthesis of Mesostructured Keggin-Type Polyoxometalate

T. Lunkenbein, R. S. Yelamanchili, A. Walther, A. H. E. Müller, J. Breu.

*21. Deutsche Zeolith-Tagung, Kiel, 2009.*

### [3] Shaping Colloidal Rutile into Thermally Stable and Porous Mesoscopic Titania-Spheres Templatated by Spherical Polyelectrolyte Brushes

T. Lunkenbein, R. S. Yelamanchili, Y. Lu, N. Miyajima, L. T. Yan, M. Ballauff, J. Breu.

*11. Bayreuther Polymer Symposium, Bayreuth, 2009.*

### [4] Anisotropic Colloidal Rutile-Nanowires Templatated by Cylindrical Polyelectrolyte Brushes

T. Lunkenbein, M. Müllner, N. Miyajima, A. H. E. Müller, J. Breu.

*12. Bayreuther Polymer Symposium, Bayreuth, 2011.*

### [5] Control of Mesostructure of Keggin Polyoxometalate Hybrid Materials Templatated by Ionizable Amphiphilic Diblock Copolymers

T. Lunkenbein, M. Kamperman, Z. Li, M. Drechsler, U. Wiesner, A. H. E. Müller, J. Breu.

*MRS Directed Self-Assembly of Materials Workshop, Nashville, 2011.*

## 10. Danksagung

Viele kleine Leute, an vielen kleinen Orten, die viele kleine Dinge tun, können das Gesicht der Welt verändern. Passender kann man diese Doktorarbeit nicht zusammenfassen. Alleine hätte ich diese Arbeit niemals bewerkstelligen können. Daher möchte ich mich bei allen bedanken, die mich auf den Weg bis hierhin bekleidet haben.

Meinen Doktorvater Josef Breu bin ich dankbar für die anspruchsvolle Themenstellung, für das Vertrauen, das er mir geschenkt hat und für die Hilfe und Unterstützung, wenn ich mal wieder „gegen die Wand gefahren“ bin. Die Zeit hier am Lehrstuhl hat mich in jeglicher Hinsicht geprägt und reifen lassen. Lieber Josef, ich danke dir für drei Jahre gemeinsames Forschen und Arbeiten, energisches Diskutieren (;-)), Kompetenz, Verständnis, gemeinsamer Spaß, Freude und auch für die privaten Momente.

Ich bedanke mich zudem bei meinen Mentoren Axel H. E. Müller, Jürgen Senker und Hans Keppler für die Zeit und Mühen, die Diskussionen und die Korrekturen der Manuskripte.

Explizit möchte ich mich noch einmal bei Axel H. E. Müller bedanken, der es mir ermöglichte, die Synthesen der Diblockcopolymere an seinem Lehrstuhl durchzuführen.

Ich danke der internationalen Graduiertenschule des Elitenetzwerkes Bayern „Structure, Reactivity and Properties of Oxide Materials“ und der Bayreuther Graduiertenschule für Mathematik und Naturwissenschaft für meine Mitgliedschaft.

Eine wichtige Stütze war auch Marleen Kamperman. Ohne Ihrer Expertise und den guten holländischen „Kips“ wäre der Erfolg wahrscheinlich deutlich geringer ausgefallen. Gastfreundlicher und zuvorkommender kann man Aufenthalte nicht gestalten! Hartstikke bedankt! Viel Glück mit Simon!

Mein herzlichster Dank geht auch an den vielen Kooperationspartnern außerhalb und innerhalb Bayreuths. Robert Schlögl, Annette Trunschke, Dirk Rosenthal, Klaus Firedel-Ortega, Ulrich Wiesner, Zihui Li, Hiroaki Sai, Stephan Förster, Sebastian With, Markus Müllner und alle diejenigen, die mich universitär weitergebracht haben und ich vergessen habe.

Ich danke dem „roten Labor“: Manuela Stirner, Patrick Feicht und Mazen Ziadeh. Vor allem aber Martin Schieder, Carina Bojer und Lena Geiling, die durch Einsatz, Schweiß und Fleiß immer eine gute Hilfe waren.

Weiterhin möchte ich auch nicht vergessen den Kollegen/-innen und Freund/-innen des Lehrstuhls Anorganische Chemie I zu danken. Allen voran Wolfgang Milius, der immer ein offenes Ohr hatte und eine sehr große persönliche Bereicherung war.

Allen Bayreuthern, die ich im Laufe meiner hiesigen Universitätskarriere kennengelernt habe und die Freunde geworden sind, möchte ich außerdem herzlich danke sagen.

Danke auch an den Alumniverein der Chemie der Universität Bayreuth „Chemiker Spass Gesellschaft e.V.“ für die abwechslungsreichen Abendgestaltungen und Programme.

Ich möchte mich auch bei meinen Freunden in der Heimat bedanken, die ihre Lust auf das ein oder andere Bier und die ein oder andere Feier nie verheimlichen konnten und stets für gesellige Abende bereitstanden.

Meiner Verwandtschaft danke ich, die mich in stressigen Zeiten unterstützte, insofern, dass sie mir eine Hilti, eine Motorsäge, einen Baumstamm, Photovoltaik-Platten oder einen Hammer in die Hand drückte, hier und da ein Dach decken ließen, etwas ausgebaut oder renoviert werden musste, den Rucksack packte oder einfach nur etwas Leckeres zum Essen übrig hatte.

Zum Schluss und allermeist möchte ich mich bei meinen Eltern, Geschwistern und meiner Freundin Anita bedanken. Danke dafür, dass ihr immer für mich da gewesen seid, nie aufgehört habt mich zu unterstützen und mir bei allen was ich getan habe immer wieder den Rücken gestärkt habt. Ihr seid die wahren Helden dieser Arbeit!

## **11. Erklärung des Verfassers**

Hiermit bestätige ich, dass ich die vorliegende Arbeit selbst verfasst und keine anderen als die angegebenen Quellen und Hilfsmittel benutzt habe.

Weiterhin bestätige ich, dass ich weder diese noch eine andere Promotion an einer anderen Hochschule endgültig nicht bestanden habe.

Bayreuth, 06. Juni 2012

.....  
Thomas Lunkenbein